Microstructural analysis of upper mantle peridotites: their application in understanding mantle processes during the formation of the Intra-Carpathian Basin System

György Falus

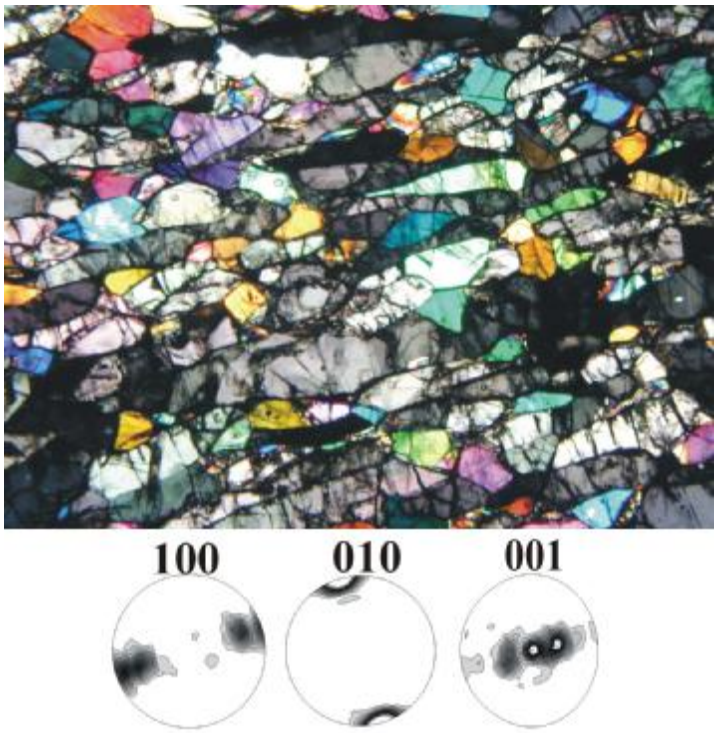

Advisor:

Csaba Szabó

Lithosphere Fluid Research Lab
Department of Petrology and Geochemistry
Eötvös University, Budapest

2004

Table of contents

List of figures and tables

Preface

Physical and chemical state of the upper mantle is among the most important controlling factors in tectonic processes from local to regional scale. Understanding the significance of various processes and the recognition of relation between them provides valuable and essential information to get closer to a more realistic view of plate tectonics, rifting, volcanism, metasomatism and other fundamental processes.

Upper mantle xenoliths hosted in Neogene alkali basalts provide material from the lithospheric upper mantle beneath the Intra-Carpathian Basin System. Their detailed study provides insight into the nature (both physical and chemical) of the underlying lower lithosphere.

The main aim of this thesis is twofold: 1) to describe and quantify deformation of the lithospheric upper mantle beneath the Intra-Carpathian Basin System primarily related to basin formation processes; and 2) to integrate voluminous high quality geochemical data accumulated in the last decades with new, hitherto missing microstructural observations thereby providing a more dynamic, thus more realistic view of lithospheric evolution and response to basin formation.

The integrated analysis of more than 50 mantle peridotite xenoliths from the Intra-Carpathian Basin System revealed that geochemical and structural evolution of the mantle lithosphere is the consequence of multi-stage physico-chemical processes. Moreover, significant relation not only exists between xenolith textures and geochemical characteristics of the mantle xenoliths but an intense linkage with deformation fabrics of olivine - interpreted as which developed in the response if basin forming processes - was also demonstrated. Deformation fabrics of olivine show remarkable connection to estimated equilibrium temperatures and clearly define two distinct vertical units within the lithospheric mantle, at least in the central portion of the basin system studied. Deeper units are characterized by high equilibrium temperatures, relatively fertile major element and depleted trace element compositions, MORB-like radiogenic isotopic compositions and fabric indicating deformation in a constant stress regime with single extension direction. This part of the mantle was attached to the lithosphere during cooling after the cessation of deformation. In contrast, xenoliths from the shallower potion of the mantle exhibit low equilibrium temperatures, depleted major element and enriched trace element and radiogenic isotopic compositions and a fabric indicative of multiple deformation. Alternatively, the development of latter

deformation fabric is interpreted as the consequence of subsequent deformations with principal stress/strain axes at large angles with respect to one-another. They are attributed as being originally part of the lithosphere before and during basin formation A third type of olivine fabric also occurs indicating deformation on a slip system commonly observed in mantle peridotites from mid-ocean ridges. Equilibrium temperatures are intermediate between “deep” and “shallow” mantle derived material. However, this textural type is quite rare.

The structure of subcontinental lithospheric mantle beneath the Intra-Carpathian Basin System is anisotropic with large-scale gradual and local heterogeneities. This structure has remarkable influence on the migration and residence time of percolating fluids/melts regarding their attenuation in the mantle at shallower depth, which results in more intensive reaction of melts/fluids and wall rock peridotite. Moreover, the anisotropy of upper mantle and the distinction of different structural units within the upper mantle is suggested to be detectable with geophysical methods

I. Introduction

The asthenosphere and lithospheric mantle of the Earth are locales of various physico-chemical processes responsible for tectonic and magmatic processes observed at the surface. The majority of scientific works approach the understanding of such processes either from the geochemical or physical side of the problems. In accordance, geochemical and physical processes are deeply understood within the mantle. However, their relation, influence on one-another is poorly understood and integrated approaches are seldom.

The Intra-Carpathian Basin System, was formed at late stages of the Alpine orogeny, the convergence of the Adriatic and European plates (e.g., Kázmér and Kovács, 1985; Balla, 1988; Ratschbacer et al, 1991; Csontos et al., 1992, Csontos, 1995; Fodor et al., 1999, Csontos et al., 2002). The eastward escape of the orogenic wedge from the Alpine collision zone, followed by extensional collapse and the retreat and active pull of the Carpathian subduction zone by subduction roll-back are responsible for the formation of the Pannonian Basin. Significant quantity of lithospheric thinning accompanied basin formation (e.g., Royden et al., 1983; Csontos, 1995; Török, 1995; Fodor et al., 1999; Tari et al., 1999; Falus et al., 2000; Huismans et al, 2001). Plio-Pleistocene alkali basaltic locations occurring dispersed in the basin system (Figure I.1) with abundant mantle fragments provide spectacular opportunity to study the lithospheric upper mantle beneath the region.

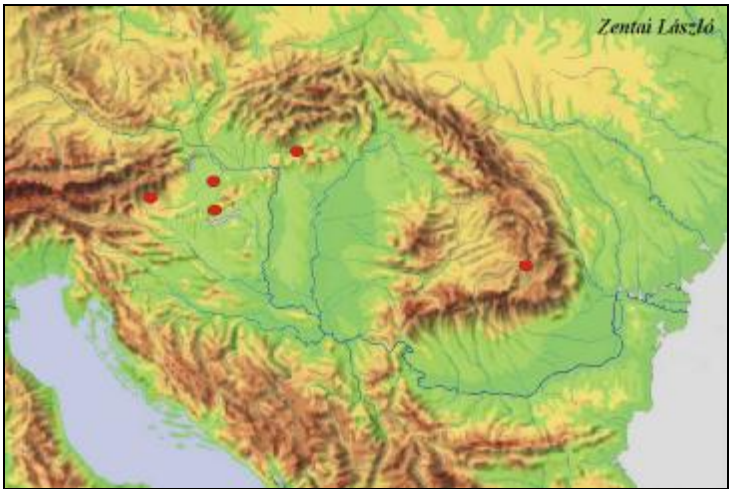

Figure I.1 Topographic map of the Intra-Carpathian Basin System and surroundings. Xenolith locations (red circle) of Neogene-Pleistocene alkali basalts with considerable amount of mantle xenoliths are also indicated. Map of László Zentai, 1996.

Geochemical analysis of the lithospheric upper mantle has a long and continuously developing history. Several hundred (maybe several thousand) studies were carried out on mantle derived material of various origins (xenoliths, ophiolites, peridotite massifs). These early studies revealed that most of the mantle rocks studied represent a residuum after partial melting (e.g., Frey and Green, 1974; Frey and Prinz, 1978).

Geochemical studies on mantle derived xenoliths in the Intra-Carpathian Basin System are numerous and extensive (e.g., Embey-Isztin, 1976, 1984 Embey-Isztin et al., 1989, 2001; Kurat et al., 1991; Downes et al., 1992; Szabó and Taylor, 1994; Downes and Vaselli, 1995, Szabó et al., 1995ab Vaselli et al., 1995, 1996; Rosenbaum et al., 1997; Dobosi et al., 1999; Falus et al., 2000, Bali et al., 2001, 2002; and references therein) regarding their major, trace-element and isotope geochemical compositions. These studies revealed that the lithospheric mantle beneath the region is similar to that observed world wide in shallow subcontinental lithospheric mantle environment. Moreover, marked relation between the composition of mantle xenoliths and xenolith textures (interpreted as indicative of deformation state) was found (e.g., Downes et al., 1992; Szabó et al., 1995a). In fact, some *physical parameters* (equilibrium temperature, oxygen fugacity) also showed remarkable relationship with xenolith textures (Szabó et al., 1995a). However, no consistent kinematic model was found that is able to link texture-forming processes and those driving the evolution of geochemical characteristics without getting in to inconsistency with one of the parameters observed.

Simultaneously to the evolution of geochemical exploration, but essentially independently from that, the analysis and interpretation of deformation and resulting textures and structures (together often addressed as “fabrics”) also largely improved. In fact, not only a large evolution of analytical techniques (from U-stage to EBSD techniques) but also the modern kinematic interpretation of studied microstructures went through significant progress (e.g., Wenk and Christie, 1991). Specific attention has been paid to reveal and understand the behavior of olivine (e.g., Carter and Avé Lallemant, 1970, Mercier and Nicolas, 1975; Nicolas

and Christensen 1987; Mainprice and Nicolas, 1989; Suhr, 1993 Zhang et al., 2000), the most abundant mineral of the upper mantle in lab experiments. Moreover, experimental results were successfully applied to interpret *olivine microstructures* (i.e., lattice preferred orientation) in some natural peridotites (e.g., Van der Wal, 1993; Vissers et al., 1997; Soedjatmiko and Christensen, 2000; Dijkstra et al., 2002). Unfortunately, these works lack

extensive geochemical data and thus the link between deformation, recrystallization and geochemical characteristics was not clarified.

An additional outcome of the recognition of fabric development and anisotropy due to preferred orientation in olivine-dominated rocks is the resulting anisotropy in several physical parameters of the mantle rocks. Among these the best studiable and studied feature is the seismic anisotropy as a consequence of different seismic velocities with respect to crystal axes in the mineral (e.g., Nicolas and Christensen, 1987; Karato, 1992). Resulting seismic anisotropy is a well studied and gradually understood feature world wide. *Measurements of the splitting of the seismic waves* provide information on the anisotropy of the mantle that can be used to unravel the structure and flow pattern of the upper mantle (e.g. Silver, 1996).

Structural anisotropy, besides producing detectable modification in the propagation of seismic waves (e.g., Ribe, 1992), but also influences the migration of percolating fluids and melts (e.g., Waff and Faul, 1992). Conversely, anisotropy of the mantle may considerably influence residence time of magmas in the mantle affecting metasomatic and magmatic processes.

The main aim of this thesis is to describe and quantify deformation of the lithospheric upper mantle beneath the Intra-Carpathian Basin System primarily related to basin formation processes using available orientation analyzing techniques. Results obtained are integrated with voluminous high quality geochemical data accumulated in the last thereby providing a more dynamic, thus more realistic view of lithospheric evolution and response to basin formation.

To accomplish the goal of the thesis several hundred xenoliths, collected earlier or personally were carefully looked through from all xenolith locations of the region. The widest range of deformed xenoliths was selected from the specimen set. Moreover, if possible xenoliths earlier studied in detail, fulfilling textural requirements were selected for microstructural analysis in order to generate a self-consistent-as possible basis for the studies. Naturally, textural types not described so far (e.g., Figure II.2) were also selected and geochemical analysis, with respect to analytical potential were also carried out on them.

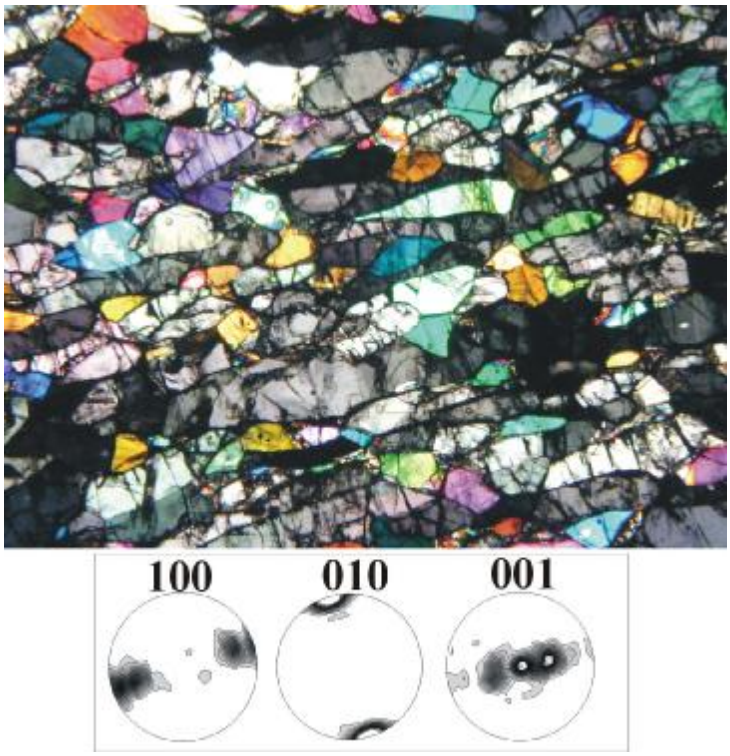

Figure II.2 Tabular equigranular xenolith from the BBHVF. Also shown is the orientation pattern of olivine crystals with respect to crystal axes.

II. Structure and geodynamic evolution of the Intra-Carpathian Basin System

II.1 Structural geological model of the basin formation

The Intra-Carpathian Basin System, a back-arc basin of the Carpathian arc with anomalously thin lithosphere was formed at late stages of the Alpine orogeny, the convergence of the Adriatic and European plates. Extensional tectonics forming the internal part of the basin system was closely related to ongoing thrusting and folding in the surrounding Carpathian belt. The major driving forces of basin formation are believed to be continuous subduction on the northern and eastern interfaces of the forming basin and synchronous extrusion of the basin units from the Alpine compressional belt.

The substratum of the Intra-Carpathian Basin System, composed of pre-Tertiary thrust sheets, is not uniform, but as indicated by paleobiogeographic (e.g., Géczy, 1973; Géczy, 1984; Vörös, 1993; Szente, 1995) and paleomagnetic (e.g., Márton and Márton, 1978; Márton and Márton, 1996) studies, is composed of two major blocks, the ALCAPA block in the north of African affinity and the TISZA-DACIA block in the south of European affinity (Figure II.1).

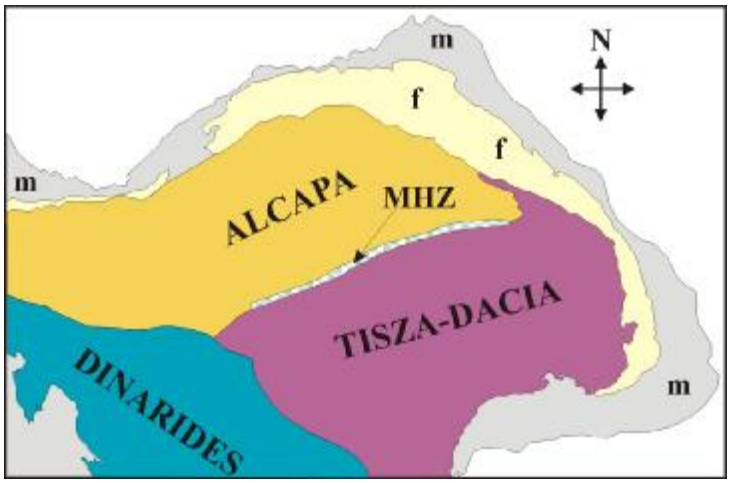

Figure II.1 Simplified geological map indicating recent position of lithospheric blocks (ALCAPA, TISZA-DACIA) in the Intra-Carpathian Basin System. Also shown is the relative position of the Dinarides. MHZ – Mid-Hungarian Zone; f – flysch, m – molasses.

These works have also revealed that the two blocks, now in contact along the Mid-Hungarian Zone (Csontos and Nagymarosy, 1998), had significantly different Mesozoic histories and were assembled in the Middle Miocene after opposite rotation (e.g., Márton and Márton, 1978; Balla, 1984; Csontos, 1992; Kovác et al., 1994; Figure II.2).

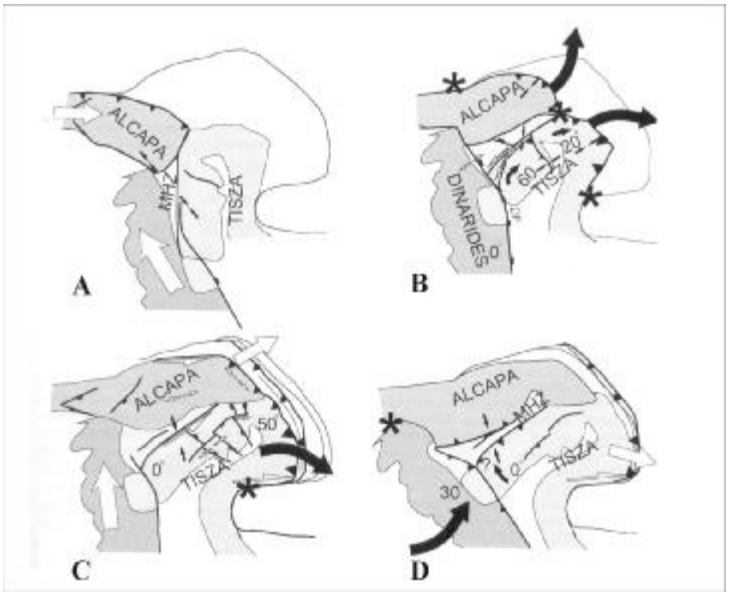

Figure II.2 Schematic tertiary evolution and geodynamic setting of the ALCAPA and the TISZA-DACIA block. The motion of DINARIDES is also shown. **A** – suggested situation in the Ottnangian; **B –** Karpatian rotations (indicated by large black arrows, numbers show quantity of rotation); **C** – Badenian major rifting event (white arrows show major tension orientations; black arrows display compression); **D** – Pliocen-Quaternary inversion due to push by the Dinaridic block. Asterix indicates fix points during rotation (after Csontos et al., 2002). MHZ – Mid Hungarian Zone.

The driving mechanism of rotation and the juxtaposition of the constituent blocks is believed to be the extrusion tectonics generated by the Alpine collision during the Oligocene—Early Miocene (Kázmér anf Kovács, 1985; Balla, 1988; Ratschbacer et al, 1991; Csontos et al., 1992). Extrusion tectonics, described by Tapponier and Molnar (1976), is defined as synchronous interaction between tectonic escape (Burke and Sengör, 1986) and extensional collapse (Dewey, 1988). The key factor of this type of tectonic process is the presence of a subductable oceanic or thinned continental crust at the edge of the escaping units. The Outer Carpathian flysch basins, which were opened by Jurassic-Early Cretaceous rifting (Csontos,

1995), with weakened lithosphere served as such "free space", which could be later occupied by the escaping ALCAPA and TISZA-DACIA blocks (Csontos, 1995). The eastward escape of the orogenic wedge from the Alpine collision zone, followed by extensional collapse and the retreat and active pull of the Carpathian subduction zone by subduction roll-back are responsible for the formation of the Pannonian Basin.

II.2 Timing of tectonic events during basin formation

Surface and subsurface tectonic observations, together with seismic profiles led to the recognition of major tectonic phases, which led to the formation and recent structure of the Intra-Carpathian Basin System. These phases are discussed in detail below:

Paleogene-Early Miocene event:

This interval is characterized by large opposed rotations of the two major constituent blocks as indicated by paleomagnetic data (Figure II.2A; e.g., Balla, 1984). Lateral faults and thrust faults characterize the tectonic pattern of this period (Fodor et al., 1992; Tari et al., 1993). Transtensional structures are often observed in the TISZA-DACIA block. Basin formation in the northern part of the TISZA-DACIA block also takes place during this tectonic period (Ciulavu et al, 1994).

The Early Miocene was the period when rotational contact of the two continental blocks took place (Balla, 1984; Kovác et al., 1994). Radial shortening and lateral faults between major thrusts are found both on the ALCAPA and TISZA-DACIA blocks. Extension with normal faulting in the Vienna basin started in the Eggenburgian and culminated in the Ottnnangian and Karpathian (see later). Volcanic rocks occur sporadically throughout the whole period. Silicic rocks, as thick ignimbrites were erupted along the Mid-Hungarian Zone (e.g., Szabó et al., 1992; Pécskay et al., 1995).

Karpatian event:

Major rotations were achieved till the beginning of the Middle Miocene and rifting (Figure II.2B), associated with significant syn-sedimentary faulting and high subsidence rates (going on from the Ottnangian in the western parts of the Intra-

Carpathian Basin System) started in this period continuing in the Badenian in the central and eastern portions of the Basin (Csontos, 1995; Fodor et al., 1999). Stretching in the basin was coeval with nappe thrusting in the Outer Carpathians (Csontos, 1995). However, nappe formation already ceased in the western part of the Carpathian chain.

Major basin openings (Little Hungarian Plain Tari, 1994; Hód-Békés Györfi and Csontos, 1994) along low angle normal faults are related to the Karpatian tectonic event. Extension was accompanied by rapid uplift of metamorphic core complexes. At the same time the opening of thin-skinned, strike slip basins, the Vienna and East Slovakian Basins took place. The major stress field driving deformation in the crust is the NE-SW to ENE-WSW trending tension (Fodor et al., 1999). The Karpatian was the period of major calc-alkali volcanic activity. Eruption centers are located along the Carpathian arc (e.g., Szabó et al., 1992; Pécskay, 1995).

Badenian event:

This was the period of broad rifting in the gross of the Intra-Carpathian Basin System (Figure II.2C, e.g., Tari, 1994). Lateral faulting, associated with the formation of pull-apart basins characterized the tectonic pattern of this period (e.g., Fodor et al., 1999). A remarkable feature during the Badenian event is the rotation of dominating stress fields from that characterizing the Karpatian deformation. The rotation of major tension direction from NE to E occurred before or within the Middle Badenian (Fodor et al., 1999) due to fixation of the subduction front in the northwesternmost part of the Carpathians.

Similar structural geological results, although occurring temporally somewhat shifted, can be obtained mostly from seismic sections within the TISZA-DACIA unit Györfi and Csontos, 1994). Although the Transylvanian Basin also subsided, no extensional structures have yet been found (e.g., Ciulavu et al., 1994). The end of rifting in the western parts of the Pannonian Basin (Tari, 1994) is shown on seismic sections. Large volumes of andesites where formed during the Badenian. Eruption centers are located along the Carpathian arc (Szakács and Seghedi, 1995).

Late Miocene event (Sarmata, Pannonian, Pontian):

The period is considered to be the thermal cooling phase of the Middle Miocene rifting (Horváth and Royden, 1981). In the late Sarmatian overall inversion in the basin system can be observed. Recent subsidence model calculations, however assume a second, active mantle upwelling during the earliest Pannonian (Huismans et al., 2001). The upwelling of the asthenosphere resulted in extreme thinning (γ~8) of the sub-continental lithosphere beneath the central part of the region. Most of the basin system is characterized by tectonic subsidence, however minor inversion of earlier graben structures (Horváth, 1995) and erosion in the Sarmatian can also be observed. The Sarmatian erosional event is explained by the combination of increase of intraplate compressional stress (Horváth, 1995) and global sea level fall at the end of the Sarmatian (Vakarcs et al., 1994). The Pannonian was characterized by post-rift subsidence, as indicated by widespread and thick Pannonian sediments, often onlaping the pre-Miocene basement (Csontos, 1995). The basin system was filled up by the end of the Pontian by large delta system. Calc alkaline and coexisting alkali magmatism is observed in this period (e.g., Szabó et al., 1992)

Late Miocene-Recent:

The tectonic period is characterized by the complete termination of the subduction of the European foreland beneath the Carpathians followed by the detachment of the subducting slab in a scissor-like nature from west to east (Spakman, 1990). The ongoing convergence between the Adriatic and European plates at the Dinaric front resulted in compression of the lithosphere beneath the Intra-Carpathian Basin System (Horváth and Cloething, 1996). This caused repeated positive structural inversions within the basin system. Compressive stress field resulted in uplift in the peripheral and western parts of the basin and subsidence is only observed in parts of the Great Hungarian Plain (Figure II.2D, Horváth and Cloething, 1996; Bada et al., 1999)

Alkali (and ultra potassic) volcanic activity is known from several parts of the basin system (e.g., Embey-Isztin et al., 1993; Harangi, 2001). Alkali basaltic activity was associated with deep seated earthquakes as demonstrated by Falus et al. (2004). Synsedimentary rocks in the vicinity of the basaltic volcanic areas also display evidence for such tectonic events (Sacchi et al., 1999).

II.3 Structure and thickness of the lithosphere beneath the Intra-Carpathian Basin System

Early seismic experiments exploring the structure of the Intra-Carpathian Basin System carried out beneath the Great Hungarian Plain revealed that the area is underlain by anomalously thin continental crust and lithosphere (Figure II.3). Stegena et al. (1975) suggested the presence of a mantle diapir, which was formed during the early Tertiary and which eroded the crust from below resulting in isostatic subsidence.

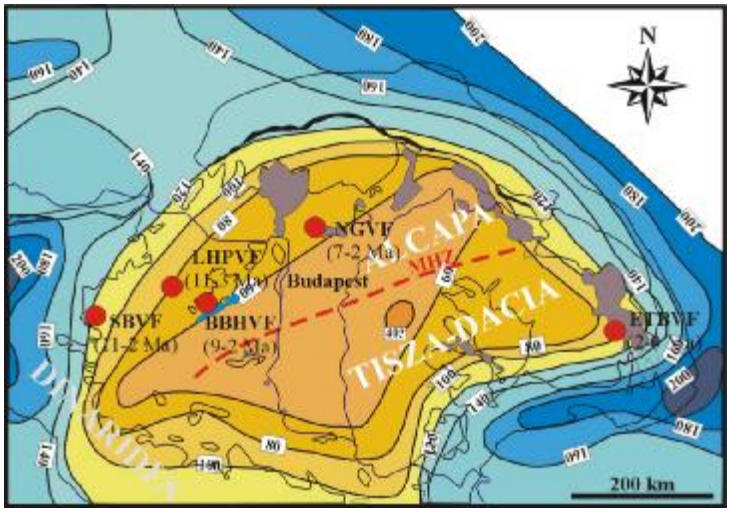

Figure II.3. Lithospheric thickness of the Intra-Carpathian Basin System after Lenkey (1999; and references therein). Calk-alkaline volcanic fields (gray patches) and major upper mantle xenolith localities in the Neogene-Pleistocene alkali basaltic occurrences (red circles) are also indicated with period of volcanic activity (Balogh et al., 1986): SBVF - Styrian Basin Volcanic Field; LHPV – Little Hungarian Plain Volcanic Field; BBHVF – Bakony – Balaton Highland Volcanic Field; NGVF – Nógrád-Gömör Volcanic Field; ETBVF – Eastern Transylvanian Basin Volcanic Field; MHZ – Mid-Hungarian Zone

Crustal structure and crustal thickness of the basin system is well defined due to structural geological field studies, paleostress data (e.g., Csontos et al., 1992; Fodor et al., 1999 and the analysis of numerous seismic profiles (reflection, refraction and wide-angle reflection) taken in the area (e.g., Ibrmajer et al., 1994; Posgay et al., 1995). Seismic studies showed that with the exception of the Transdanubian Central Range (TCR) the basin system is characterized by 30-22.5 km crustal thickness being

the thinnest in the central part of the basin and thickening towards the margins. The anomalously thin crust is suggested to be the result of Neogene extension (e.g., Horváth, 1993).

The structure of the upper crust reflects brittle deformation occurring as normal faults that frequently reactivated nappe surfaces and strike-slip tectonic movements. The faults are often syn-sedimentary and never cut through the lower crust, which shows strong layering (e.g., Posgay et al., 1990) and is suggested to deform in the ductile regime. Normal faulting and contemporaneous strike slip tectonic movements as well as the layering (sub-horizontal reflectors) in the lower crust are related to the major extension of the Intra-Carpathian Basin System in the Middle Miocene (e.g., Horváth, 1993).

The nature of the mantle lithosphere, however is poorly constrained. Only few seismic studies with weak resolution (e.g., Babuška et al., 1988; Posgay et al, 1995)., magnetotelluric soundings (e.g., Ádám et al., 1996) and gravity anomaly profiles (e.g., Szafián et al., 1997) explored the deep lithosphere beneath the basin system. The main aim of these studies was to determine the asthenosphere-lithosphere and crust-mantle boundaries, whereas the internal structure of the mantle lithosphere was not investigated. All of the geophysical studies carried out, dealing with the lithosphere reflect updoming of the asthenosphere and indicate that it is also anomalously thin beneath the region. Lithospheric thickness minimums (~60 km) correlate well with crustal minimums (Posgay et al., 1995) and heat flow maximums (e.g., Ádám, 1978; Lenkey, 1999).

Besides the geophysical information mantle xenoliths, hosted in alkali basalts (see details later) provide direct evidence of the nature of the subcontinental lithospheric mantle beneath the Intra-Carpathian Basin System.

II.4 Neogene-Quaternary volcanic activity

Development of the Intra-Carpathian Basin System, as well as the thrusting and folding of the Carpathians was accompanied by widespread and various volcanic activities during the period from the Neogene to Quaternary. The volcanic products can be subdivided into four major genetic types: 1) Miocene silicic volcanism; 2) Miocene to Pliocene potassic and ultrapotassic volcanism; 3) Miocene to Quaternary calc-alkaline volcanism and 4) Late Miocene to Quaternary alkaline volcanism (Szabó et al., 1992; Harangi, 2001).

These volcanic rocks cover considerable areas of the Intra-Carpathian Basin System, however the majority of the magmatic products is covered by young sediments (Harangi, 2001). In the following section, timing, geodynamic position and major chemical characteristics of the different magma types will be shown.

Miocene silicic volcanism

Silicic pyroclastic rocks were the first volcanic products during the Miocene evolution of the Intra-Carpathian Basin System. These volcanic products originated by voluminous explosive eruptions. The volcanic activity occurred repeatedly resulting in large volume of ignimbrites (e.g., Szakács et al., 1998). The volcanic series is traditionally subdivided in to three units, however recent studies showed that age and paleomagnetic data give large scatter. The volcanic rocks are produced by a more or less continuous volcanism from multiple eruption centers.

The petrogenesis of Miocene silicic magmas is believed to be related to intermixing of mantle derived melts and crustal origin partial melts. According to Harangi (2001) their recent position (along the margin of the ALCAPA and the TISZA-DACIA blocks – Mid Hungarian Zone) suggests that at least the early part of the volcanism resulted because of strike-slip tectonic movements along the margin of the two microplates.

Miocene-Pliocene potassic and ultrapotassic volcanism

Rocks related to these magmatic processes are minor among other Neogene volcanic products of the Intra-Carpathian Basin System. Their formation, partial melting of metasomatized lithospheric mantle, worldwide is suggested to be related to lithospheric stretching or upwelling of hot asthenospheric material as demonstrated by Thompson et al. (1989). The spatial distribution of these rock types is restricted to the central and south-western portion of the basin system (e.g., Harangi et al., 1995).

The occurrence of these rocks indicates partial melting of a strongly metasomatized, phlogopite bearing mantle. According to Harangi (2001) the main period of the formation of potassic and ultrapotassic rocks on the ALCAPA-block is coeval with the main rifting period of the Intra-Carpathian Basin System (Harangi, 2001).

Miocene-Quaternary calc-alkali volcanism

Calc-alkali volcanic complexes surround the Intra-Carpathian Basin System. Most of the calc-alkali volcanic products, however, are buried in the central and eastern Pannonian Basin (e.g., Széky-Fux and Pécskay, 1991). The age distribution of calc-alkali volcanic complexes is strikingly systematic: being oldest in the westernmost parts of the Basin system from 16.5 Ma in the northern part to 0.15 Ma in the southeastern edge of the basin system (e.g., Pécskay et al., 1995).

The composition of these calc-alkali magmatites is typical of subduction related magmas (Harangi, 2001). Their generation is originally interpreted as the result of introduction of fluids to the mantle wedge from the subducted slab and sediments (e.g., Harangi, 2001). Recently, however, the production of calc-alkali melts in extensional regions has been also pointed out (Hawkesworth et al., 1995; Wilson et al., 1997). In this case the partial melting takes place due to decompression in an earlier metasomatized lithospheric mantle. This model was suggested for calc-alkaline volcanic rocks in the Northern Pannonian Basin (e.g., Konečný et al., 1995). Chemical composition of the rocks suggests mixing between enriched-asthenosphere derived magmas and metasedimentary lower crust. In contrast, calc-alkali rocks at the eastern Carpathians show evidence for direct relationship with subduction along the Carpathian Arc (e.g., Szabó et al., 1992) Their evolution is suggested to be complex process involving subduction enriched mantle source and upper crustal contamination (Harangi and Downes (2000).

Late Miocene-Quaternary alkali volcanism (mantle xenolith bearing)

The volcanism produced mafic rocks (e.g., Embey-Isztin and Dobosi, 1995), occurring in several isolated fields in the Intra-Carpathian Basin System (Styrian Basin Volcanic Field-SBVF, Little Hungarian Plain Volcanic Field-LHPVF, Bakony—Balaton Highland Volcanic Field-BBHVF, Nógrád-Gömör Volcanic Field-NGVF, Persány Mountains (Eastern Transylvanian Basin) Volcanic Field-ETBVF; Figure II.3). The volcanism began first (10-12 Ma) in the western (Styrian Basin) part of the Intra-Carpathian Basin System (e.g., Balogh et al., 1986, 1994). It culminated in all volcanic fields at 3-5 Ma. The last eruptions yielding mantle xenolith-bearing volcanic products occurred around 0.8 Ma in the Persány area (Mihaila and Kreutzer, 1981). Phreatomagmatic to magmatic eruptions characterized the volcanism resulting

in various volcanic forms (e.g., Harangi and Harangi, 1995; Németh and Martin, 1999).

Major element composition of the mantle derived melts implies that they represent primary magmas. Trace element composition indicates subduction related component in the source region of most of the magmas (Downes et al., 1995; Harangi, 2001). Partial melting occurred at 80-100 km mantle depth, in the garnet stability zone (Embey-Isztin and Dobosi, 1995; Harangi et al., 1995).

The volcanism can be classified as post-extensional volcanic activity (Embey-Isztin and Dobosi, 1995; Harangi, 2001) and was generated due to the upwelling of EAR-type asthenospheric material, possibly induced by thin-spot effect (Thompson and Gibson, 1991) of the thin lithosphere beneath the Intra-Carpathian Basin System.

Alkali basaltic magmas themselves reflect nature and characteristics of the mantle source they have been derived from. Nevertheless, the curiosity of some of the Intra-Carpathian Basin System alkali basalts is the high abundance of upper mantle wall-rock fragments, i.e., mantle xenoliths. They occur both in pyroclasts and lava flows.

III. Textural evolution, fabric development and the nature of deformation in the upper mantle

III.1 Textural nomenclature of mantle xenoliths

Structural studies of mantle-derived peridotite fragments, i.e., peridotite massifs and mantle xenoliths, revealed that these rocks have distinctive textures and adjoining structures. Early studies on mantle rocks (e.g., Mercier and Nicolas, 1975; Pike and Schwartman, 1977; Harte, 1977) suggested that observed textures represent deformation history and evolution of the mantle fragment the rock has been derived from.

Mantle deformation is reflected as the continuous and systematic changes in grain size, geometry of the grain boundaries, dislocation density (e.g., Mercier and Nicolas, 1975). These factors are controlled by recrystallization, which involves the growth of new, relatively strain free grains (neoblasts) lowering the strain energy of the aggregate (Ross et al., 1980). It should be noted that recrystallization might occur under both static (annealing) and dynamic conditions. The appearance of spinel, the most sensitive to stress, also provides valuable information on the deformation state of the studied mantle section.

Mercier and Nicolas (1975) distinguished three main textural groups with respect to the state of recrystallization (i.e., the factors mentioned above). *Protogranular* textural group (Figure III.1) is characterized by coarse grain size (2-5 mm), curvilinear grain boundaries.

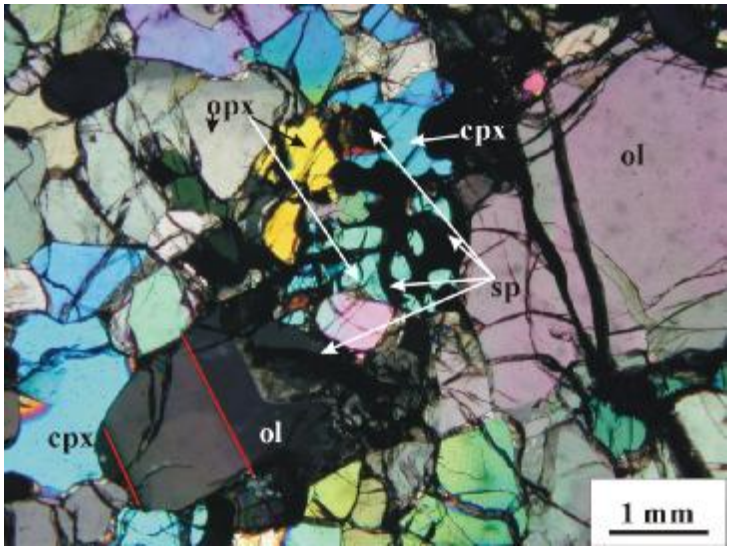

Figure III.1 Protogranular spinel lherzolite from the SBVF with curvilinear grain boundaries and coarse spaced subgrain walls – indicated with red line. Note vermicular shape of spinel and its intimate textural relation with pyroxenes. ol – olivine; opx – orthopyroxene; cpx – clinopyroxene; sp – spinel. Cross polarized light image.

Olivine crystals contain well-recovered kink-bands (low dislocation density), which are generally parallel to (100). Spinels are around 1 mm in grain size and show intimate textural relation with clinpyroxene and orthopyroxene. Only weak lattice preferred orientation (LPO) is observed on the olivine and orthopyroxene crystals. This textural group in accordance with its geochemical characteristics (see Chapter VI.) is presumed to represent the most undeformed, most pristine mantle among the studied mantle fragments. The *porphyroclastic* textural group (Figure III.2) represents mantle material, which is characterized by a double maximum in grain size distribution of constituent olivine, orthopyroxene and rarely clinopyroxene. Internal strain features (weakly recovered kink-bands) in the coarse grains, related to large dislocation density are often observed. The coarser grains (i.e., porphyroclasts) are generally characterized by considerable aspect ratios. The long axes of the porphyroclasts are generally sub-parallel if observed, to the foliation. Lattice preferred orientation in the porphyroclasts is moderate to strong. Matrix grains, surrounding the porphyroclasts are fine-grained, generally isometric and lack internal strain features. These matrix grains are addressed as neoblasts. The generation of neoblasts is believed to be related to recrystallization related to recovery processes. However, orientation analysis in neoblasts next to porphyroclasts, showing

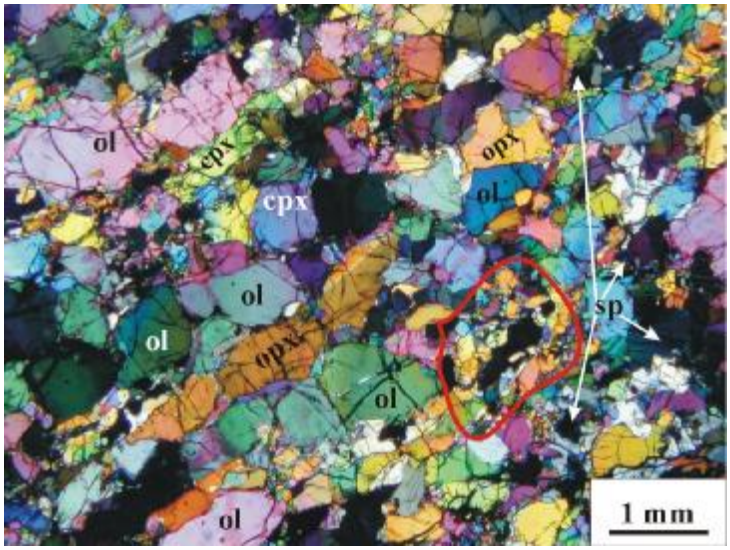

Figure III.2 Porphyroclastic spinel lherzolite from the LHPVF with elongated porphyroclasts and isometric recrystallized grains (in the highlighted area) displaying significant grain size reduction. ol – olivine; opx – orthopyroxene; cpx – clinopyroxene; sp – spinel. Cross polarized light image.

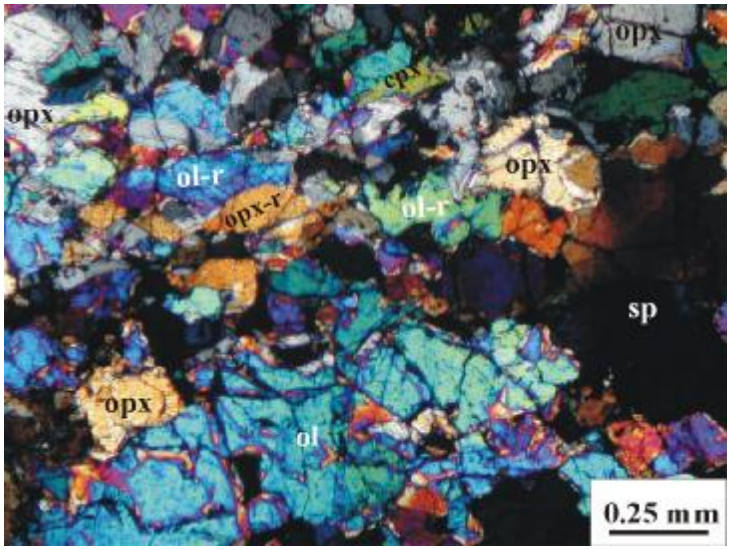

Figure III.3 Porphyroclastic spinel lherzolite from the ETBVF with elongated porphyroclasts and recrystallized grains (-r). ol – olivine; opx – orthopyroxene; cpx – clinopyroxene; sp – spinel. Cross polarized light image.

orientation similar to the porphyroclasts, revealed that neoblast formation, at least partly, maybe a syn-kinematic process (Mercier and Nicolas, 1975). Some rare xenoliths, however contain elongated matrix grains sub-parallel to the long axis of elongated porphyroclasts (Figure III.3). These matrix grains often display undulouse extinction reflecting the distortion of the crystal lattice related to large dislocation density. These crystals are presumably syn-kinematic and were formed due to dynamic recrystallization. Lattice preferred orientation (LPO) of such matrix grains is strong and is often similar to the LPO of porphyroclasts, however significant differences may also arise (e.g., Zhang et al., 2000) It is still a question of debate how these matrix grains escaped annealing. Spinel crystals exhibit the characteristic holly-leaf structures and are strongly elongated sub-parallel to the main lineation determined by elongation of porphyroclasts (Mercier and Nicolas, 1975).

The increasing ratio of recrystallized (and annealed) grains is characteristic of the equigranular textural group. This group is traditionally subdivided in to two subgroups with respect to grain dimensions. Texture of equi-axed grains is addressed as mosaic-equigranular (Figure, III.4), whereas that with flattened or elongated grains is called tabular equigranular (Figure III.5). Tabular equigranular xenoliths are suggested to represent static recrystallization process of originally foliated material (Passchier and Trouw, 1995), whereas mosaic equigranular texture could develop after tabular equigranular texture or directly from porphyroclastic texture through static recrystallization. Grain boundaries are generally straight or gently curved. Triple junctions in both types often occur, indicating textural equilibrium and annealing. Spinel is scattered in the rock and occurs either as inclusions or in triple junctions, generally as small rounded crystals. Annealing, governing grain growth produces secondary textural types, which based solely on structural analyses are difficult to distinguish from primary textures. Spinel, occurring as inclusion may be the only evidence for the secondary nature of the observed texture.

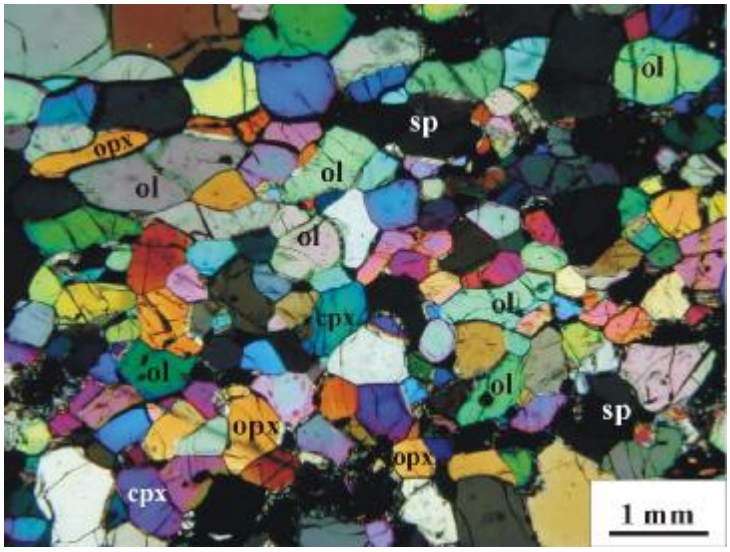

Figure III.4 Mosaic equigranular spinel lherzolite with equi-axed (isometric) grains from the BBHVF. Grain boundaries are convex, straight or gently curved. Note large grain size with respect to recrystallized grains in the porphyroclastic lherzolite (Figure III.2). ol – olivine; opx – orthopyroxene; cpx – clinopyroxene; sp – spinel. Cross polarized light image.

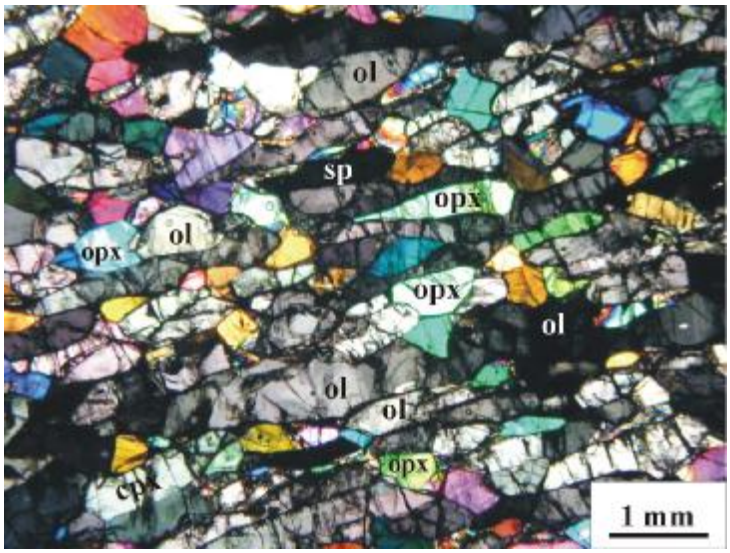

Figure III.5 Tabular equigranular spinel lherzolite from the BBHVF with flat grains. Section prepared perpendicular to the foliation, subparallel to the macroscopic lineation. ol – olivine; opx – orthopyroxene; cpx – clinopyroxene; sp – spinel. Cross polarized light image.

Poikilitic texture (Figure III.6) is suggested to be a secondary textural type (e.g., Mercier and Nicolas, 1975) . It is characterized by coarse grains (~2-4 mm) with straight or gently curved grain boundaries and often-occurring triple junctions. Neither undulouse extinction nor kink bands occur in this textural type. Spinel crystals are generally small rounded or euhedral inclusions in olivine and orthopyroxene.

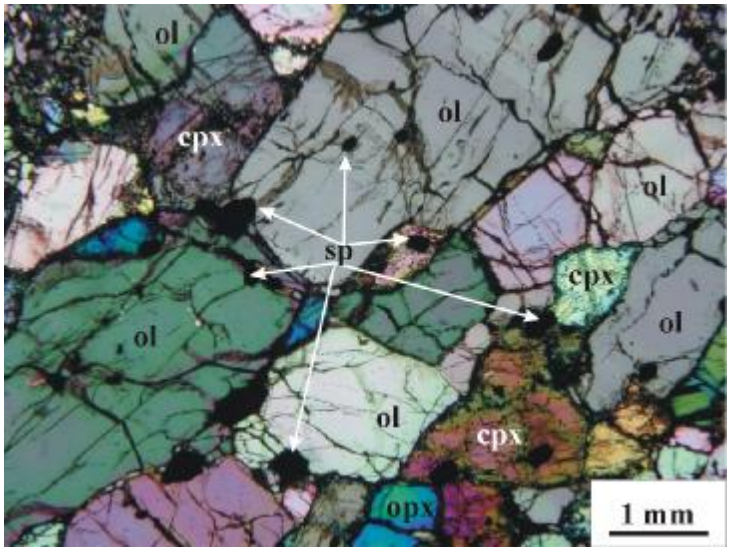

Figure III.6 Secondary recrystallized ("poikilitic") spinel harzburgite from the BBHVF with coarse grains and curvilinear (!) grain boundaries. Spinel crystals only occur as isometric or spherical inclusions in silicate phases. ol – olivine; opx – orthopyroxene; cpx – clinopyroxene; sp – spinel. Cross polarized light image.

III.2 Intracrystalline deformation

Deformation in rocks is achieved by a large number of processes on the scale of individual grains (Passchier and Trouw, 1995). The actual processes involved depend on *lithological (internal) controlling factors such as mineralogy, presence and composition of the intergranular fluid, grain size, lattice-preferred orientation (LPO), porosity and permeability; and on external controls such as temperature, lithostatic pressure, differential stress, fluid pressure and externally imposed strain rate.* In the following section the influence of both internal and external factors will be highlighted, which drive textural and structural development of the observed

microstructures in the mantle peridotites studied in this work through *olivine*, the dominant mineral phase in the mantle.

Numerous experimental studies (e.g., Carter and Avé Lallement, 1970) and the analysis of natural samples (e.g., Mercier and Nicolas, 1975) revealed that olivines, major constituents of peridotitic rocks, respond to stress with intracrystalline deformation at mantle conditions and realistic strain rates ($<10^{-8}$). Intracrystalline deformation is related to the motion of crystal lattice defects (i.e., vacancies, dislocations). Among intracrystalline deformation types in the shallow mantle dislocation plastic mechanisms are the most common. During this type of intracrystalline deformation strain is achieved by the slip of dislocations within grains.

Dislocations, linear defects in the crystal lattice are generated around impurities in the crystal, i.e., fluid or solid inclusions, microcracks, etc. Dislocations are generated by stress and form dislocation loops, which are the source of subsequent dislocations (Figure III.7) called a *Frank-Read source* (Weertman & Weertman 1964). Such sources are essential for significant plastic deformation.

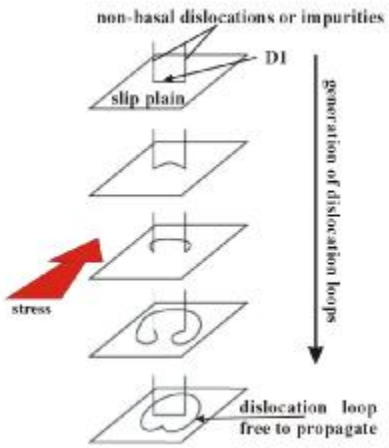

Figure III.7 A Frank-Read source for the multiple initiation of dislocation loops. A dislocation is pinned in the basal plane at two ends by either impurities or an immobile non-basal dislocation. If a shear stress is resolved onto the basal plane, the dislocation line becomes unstable and begins to bow. With increasing stress, the line bows back onto itself to produce a new loop that is free to propagate, and a section that remains pinned, which may initiate more loops.

Generation and motion of dislocations is crystallographically controlled. Dislocations are usually represented by dislocation lines, which delineate the core of dislocations and the Burgers vector, which describes both the magnitude and the direction of slip (Figure III.8). An alternative way of describing dislocation motion is using slip plane instead of dislocation lines (Figure III.8). The slip plane and the Burgers vector define a slip system, which may be characteristic for a mineral at

certain physical conditions (Passchier and Trouw, 1995). Slip systems are marked in the following way: (slip plane)[slip direction].

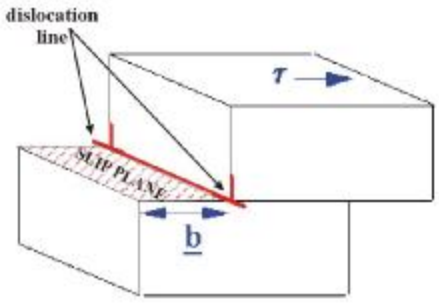

Figure III.8 Simplified cartoon describing intracrystalline slip with dislocation line + Burgess-vector (**b**) and with slip plane + Burgess-vector (**b**). τ – stress direction.

Slip systems of olivine crystals, being the subject of many deformation experiments (e.g., Carter and Avé Lallement, 1970, Boullier and Nicolas, 1973; Nicolas and Christensen, 1987; Suhr, 1993) are well defined. The activation and dominance of slip systems in olivine are strongly temperature dependent (e.g., Avé Lallement and Carter, 1970). At 'low' temperature (700-900 ^{o}C), slip systems (010)[001] (Nicolas and Christensen 1987) or {110}[001] (Carter and Avé Lallement 1970) have been reported (Figure III.9a). At medium temperatures (~1000 ^{o}C) the {0kl}[100] slip system, i.e., "pencil glide" is dominant (Figure III:9b). At high temperatures, above 1000 ^{o}C (010)[100] is the only active slip system (Figure III:9c).

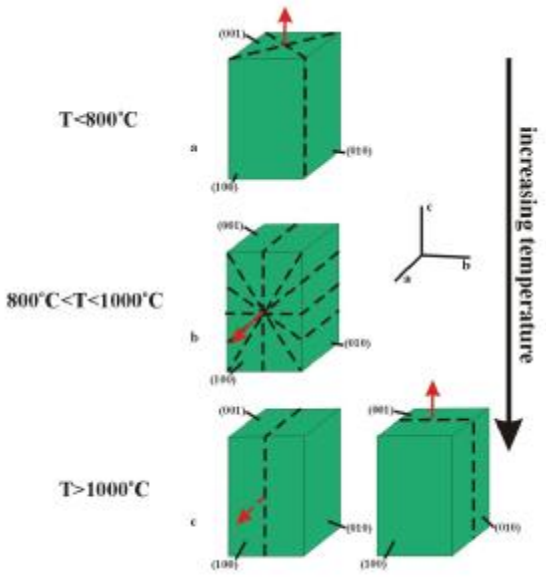

Figure III.9 Simplified cartoon displaying olivine slip systems with respect to temperature (at strain rate ~ $1x10^{-6}$; Carter and Avé Lallemant, 1970). **a**) low temperature {110}[001]-slip; **b**) medium temperature {0kl}[100]-slip – "pencil glide"; **c**) high temperature (010)[100]-slip and (100)[001]-slip, however the activation of the latter is often attributed to H_2O activity or simple geometrical reasons (see text for details).

The activation of (100)[001] slip system was observed in high-temperature (>1000 ^{o}C) deformation experiments (e.g., Zhang et al., 2000). Its activation is either related to H_2O activity but may be also dependent on geometrical reasons (e.g., highest Schmid-factor*; Figure III.10).

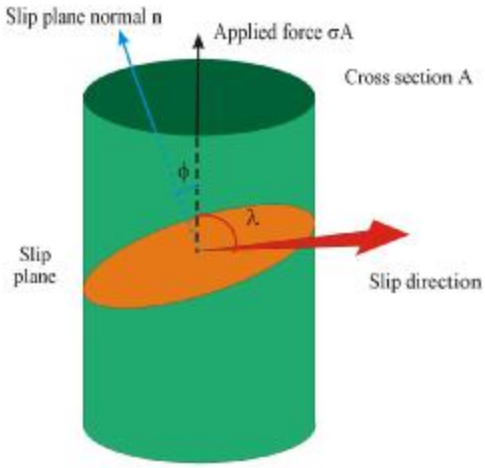

Figure III.10 Geometrical constrains of the Schmid-factor on a simplified cartoon. ϕ - angle between slip plane normal (**n**) and the applied force; λ – angle between slip direction and applied force.

One important effect of intracrystalline slip deformation is the development lattice preferred orientation (LPO; e.g., Mercier and Nicolas, 1975). Even if microscopic features indicating deformation are not visible, lattice preferred orientation might be treated as a strong evidence for intracrystalline deformation in the studied rock (e.g., Vauchez and Tommasi, 2003), which demonstrates that the deformation of the given material took place in the dislocation creep regime.

---

*The applied force along the tensile axis is F=σA. If slip occurs on the slip plane shown in **Figure III.10**, with plane normal **n**, then the slip direction will lie in this plane. We can calculate the *resolved shear stress* acting parallel to the slip direction on the slip plane as follows.

The area of the slip plane is A/cosϕ, where ϕ is the angle between the tensile axis and the slip plane normal.

The component of the axial force F that lies parallel to the slip direction is F cos λ. The resolved shear stress on the slip plane parallel to the slip direction is therefore given by:

$$t_R = \frac{\text{resolved force acting on slip plane}}{\text{area of slip plane}} = \frac{F\cos l}{A/\cos f} = \frac{F}{A}\cos f \cos l$$

It is found that the value of t_R at which slip occurs in a given material with specified dislocation density and purity is a constant, known as the *critical resolved shear stress* t_C. This is **Schmid's Law**.

The quantity cos f cos l is called the *Schmid factor*. The tensile stress at which the crystal starts to slip is known as the yield stress s_y, and corresponds to the quantity F/A in the above equation.

Symbolically, therefore, Schmid's Law can be written:

$$\tau_C = \sigma_y \cos\phi \cos\lambda$$

In a given crystal, there may be many available slip systems. As the tensile load is increased, the resolved shear stress on each system increases until eventually τ_C is reached on one system. The crystal begins to plastically deform by slip on this system, known as the *primary slip system*. The stress required to cause slip on the primary slip system is the *yield stress* of the single crystal. As the load is increased further, τ_C may be reached on other slip systems; these then begin to operate.

From Schmid's Law, it is apparent that the primary slip system will be the system with the *greatest Schmid factor*. It is possible to calculate the values of cos ϕ cos λ for every slip system and subsequently determine which slip system operates first. http://www.msm.cam.ac.uk/doitpoms/tlplib/BD4/slip_geometry.php

III.3 Recovery and recrystallization

During deformation the free dislocations nucleate and migrate in the crystal lattice, which increases the "internal strain energy" (elastic strain energy) of the system. Internal strain energy is proportional to dislocation density, which means the number of dislocations per unit volume in the crystal lattice (Passchier and Trouw, 1995). Certain processes, however in the crystals can decrease dislocation density, i.e., the internal strain energy by ordering and annihilating dislocations, following the thermodynamic principle to minimize total free energy in a system. Dislocations in the crystal lattice can be grouped into planar networks. These networks may be addressed as subgrain walls, which separate crystal fragments, i.e., subgrains (Figure III.11). These grains are slightly misoriented with respect to the host grains. The orientation of subgrain walls strongly depends on the slip system of dislocation, which accumulate in it (Trepied et al., 1980).

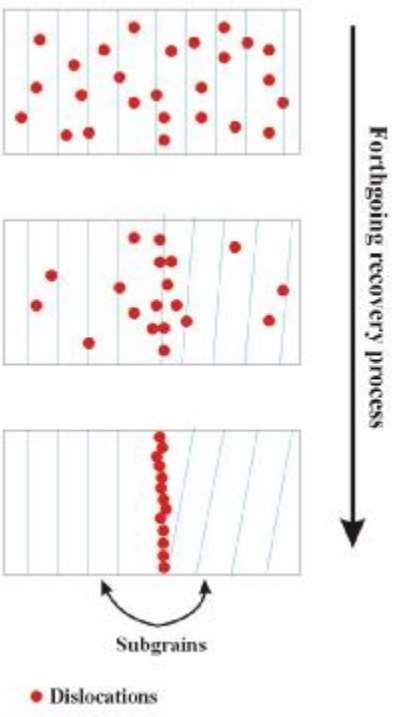

Figure III.11 Schematic representation of recovery. During recovery dislocations (marked by red spheres) order in to subgrain walls separating subgrains, simultaneously their number decreases due to their annihilation. Note angular deviancy between subgrains (indicated by subparallel blue lines).

Another way of lowering internal strain energy in a system of crystal lattices is to generate or increase the ratio of crystals with lower internal strain energy (lower dislocation density, i.e., to recrystallize the mineral assemblage during deformation.

Dynamic recrystallization occurs during deformation, which reworks an existing grain texture. Dynamic recrystallization may be separated into two end-member processes: rotational- and migration dynamic recrystallization. Rotational recrystallization involves progressive crystallographic misorientation without significant migration of the grain boundary. Moreover, orientation relationships with the parental grain can still be recognized (Urai, 1983; Lloyd et al., 1997). Grain boundary migration recrystallization conversely is driven by strain energy differences between adjacent grains (Lloyd et al., 1997). Grains with lower internal strain energy grow at the expense of those with larger dislocation density. Orientation relationships with the parental grains (if it is correct to call them like this) are not recognizable. Rotational and migration recrystallization are related and often cyclical processes, which drive dynamic recrystallization during deformation. Dynamic recrystallization is suggested to be extremely important in overlapping gaps generated during heterogeneous deformation (Zhang et al., 2000).

Dynamic recrystallization (e.g., induced by rifting) is replaced by static recrystallization after the ceasing of deformation (e.g., thermal phase after rifting). Static recrystallization is a thermally induced process. It is suggested to occur during annealing following the deformation (Lloyd et al., 1997). However the presence of intracrystalline melt/fluid may also considerably facilitate static recrystallization and grain growth (e.g., Bussod and Christie, 1991). This process involves grain boundary migration and grain growth, thus significant changes in LPO, generated during the dynamic part of the recrystallization are expected. However, in some natural examples static annealing does not considerably change earlier LPO (Vauchez and Garrido, 2001). The preserved lattice preferred orientation may provide valuable information on the physical conditions characterizing deformation.

III.4 Recrystallized grain size

Systematic variations in grain size were recognized early in the study of mantle peridotites and this feature was incorporated into the textural classification of these rocks (e.g., Mercier and Nicolas, 1975). Protogranular peridotites are coarse grained with grain size (for olivine and orthopyroxene) ranging from 2 to 10 mm. Conversely, equigranular peridotites constitute of finer (0.5-1 mm) grains. This clear, continuous decrease in grain size is attributed to recrystallization and the formation of neoblast with lower dislocation density, lowering internal strain energy of the system.

Empirical relationships between differential flow stress and recrystallized grain size in olivine rocks have been formulated using recrystallized grain size distribution in the rocks (e.g., Avé Lallement et al., 1980; Van der Wal, 1993). This correlation provided opportunities to estimate stresses driving deformation and inducing recrystallization. Thus, recrystallized grains size of olivines could be used as paleo-piezometers (Van der Wal, 1993)

However, many technical and fundamental problems arise with these paleo-stress estimations. Several experiments were preformed on single crystals (e.g., Karato et al., 1980), and it is a problem to relate single crystal microstructural data to polycrystalline aggregates. Further problems arise with the presence of second phase, namely orthopyroxene in most of the mantle-derived rocks. Although recently experiments explored the effect of the presence of orthopyroxene (Ji et al., 2001) on the bulk rheological behavior of the rocks, however detailed study of the effect on recrystallized grain size have not been preformed.

Despite the uncertainties in precise estimation of flow stresses, recrystallized grain sizes will be used in this work to compare flow stresses, which developed distinct textural types. It must be noted here that recrystallized grain size not only depends on paleo-flow stresses, but also is dependent on annealing and associated grain growth.

III.5 Melt-rock interaction

Evidence on the presence of partial melts is often observed in upper mantle rocks. Distribution of these liquids is very important. Liquid/solid interfacial geometries are driven towards steady state configuration due to surface tension (Waff and Faul, 1992). If surface energies and tensions were isotropic, constant wetting angles and constant liquid-solid interface curvature would be expected (Bulau et al., 1979; Cooper and Kohlstedt, 1982; Toramaru and Fujii, 1986). However, observations indicate that significant deviations exist from the suggested model (Waff and Faul, 1992).

Detailed study on melt distribution in natural and synthetic samples revealed that deviancy in geometry of liquid-crystal interfaces from the theoretical isotropic is related to the generation and stability of flat, crystal faces. This crystallographically controlled phenomenon results due to low free energy on certain low index crystal

faces. These crystal faces in olivine (in the olivine-basalt system), according to universal stage measurements are perpendicular to the [b]-axis and parallel to (010) (Waff and Faul, 1992). All of the flat (010) faces seemed to be wetted. There were, however, other (010) faces observed that were not wetted. It is suggested that grains only in contact with melt will exhibit such flat (faceted) faces.

Faceted interfaces occur already at low melt fractions, even below 1 vol% (Waff and Faul, 1992). The presence of flat interfaces will increase permeability of the rock parallel to these interfaces. This feature becomes especially important in regions where the lattice preferred orientation of olivine is pronounced, e.g., mid-ocean ridges (e.g., Christensen, 1984), continental rifts (Tommasi and Vauchez, 2001). Due to dominant slip system (010)[100] in olivines at upper mantle conditions (see earlier) in these rift zones olivine 'a' axes ([100]) tend to align sub-parallel to major extension directions (Figure III.12), whereas [b]-axes are dominantly perpendicular to the Earth's surface with the exception of the axial zone below the ridge, where [a]-axes would be perpendicular to the surface and [b]-axes subparallel to it. This geometry aligns (010) faces subparallel to the surface (or perpendicular beneath the axial zone), which enhances permeability sub-parallel to the surface and diminishes it in horizontal direction (Waff and Faul, 1992). The opposite effect is accepted in the axial zone beneath the ridge. This phenomenon would focus melt into the axial zone of the mid-ocean ridge areas but would also inhibit small melt fractions from rising under gravitational buoyancy and, thus, these melt fractions would solidify at the base of the lithosphere.

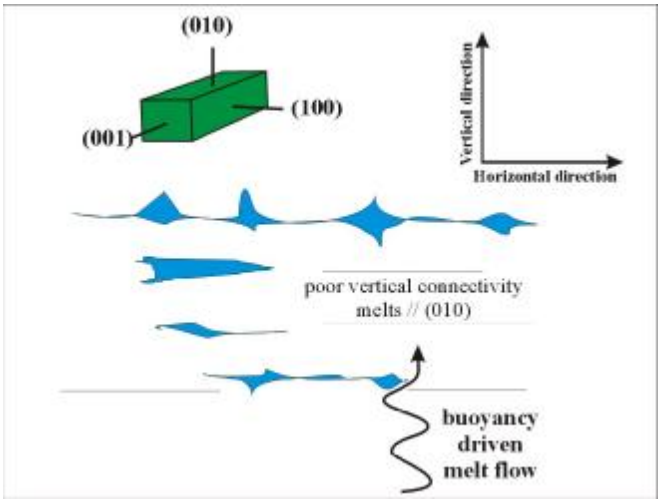

Figure III.12 Lattice preferred orientation of olivine with (010) faces being subhorizontal. Connected melt pores and easy melt migration will also be subhorizontal. Vertical motion of melt is difficult, due to poor vertical connectivity.

IV. Petrographic characterization of mantle xenoliths

Samples selected for this study were analyzed in details under polarized light microscope (Nikon Eclipse 600) and in some special cases (very fine grain size) with scanning electron microscope (SEM-Amray 1810I). SEM was used in those cases where the magnification and/or resolution of the light microscope was insufficient to ascertain textural, mineralogical features (typically below 30-40 micron average grain size). The goal of detailed microscopy was manifold. First to perform "conventional" petrographic observations: modal composition of the studied samples; classical textural classification (using the directives of Mercier and Nicolas [1975]); to detect metasomatic effects, partial melting and mineral reactions. Secondly, detailed microscopy was used to detect and describe deformation features observed in the samples. Special attention was paid to the texture of the mantle derived xenoliths. Moreover, deformation microstructures present in the studied rocks e.g., grain shape (aspect ratio), grain size, the nature of the grain boundary (straight, gently curved, curvilinear, lobated, etc.), geometry of grain contacts (the presence or the absence of triple junctions) were also studied. Optical features of the minerals, especially olivines, which are the dominant phases in the studied mantle derived samples, were analyzed in detail. Undulouse extinction, kink bands and subgrain formation were traced and when possible, were quantified. The nature (dynamic or static; subgrain rotation recrystallization or grain boundary migration recrystallization) and the extent of recrystallization was also studied.

The description of rocks selected for detailed study will be represented based on xenolith locations. Table IV.1 summarizes the most important petrographic features of the analyzed samples.

Styrian Basin Volcanic Field (SBVF)

More than 50 samples were looked through macroscopically from this xenolith location, which lies on the western margin of the Intra-Carpathian Basin System (Figure II.3). Nevertheless, no samples were found indicating any type of macroscopic deformation features. Those xenoliths analyzed in detail (some rock samples [Kf4, Kf5] were studied by Vaselli et al. [1996], whereas Kf3 and Kf17 by Falus et al. [2000]) are all spinel lherzolites (Table IV.1) that have dominantly protogranular texture with only minor recrystallization going on in sample Kf5. Grain size is coarse (2-4 mm), grain boundaries are curvilinear

Location	Sample	Texture	Grain boundary	Modes (vol%) ol	opx	cpx	sp	npp
	Kf3[1]	pr	curv	60	25	13	2	amp
SBVF	Kf4[2]	pr/po	s/gc	50	32	16	2	amp
	Kf5[2]	po	s/gc	70	17	9	4	amp
	Kf17[1]	pr	curv	62	20	16	2	
	GC03-05	po/equ	s/gc	73	17	6	4	
	GC03-06	po	curv	76	18	4	2	
	GC03-10	po/equ	s/gc	90	9	1	0	
	GC03-12	po	curv-s/gc	71	22	6	2	
	GC03-12b	po	curv-s/gc	81	12	5	3	
LHPVF	GC0314	po	curv-s/gc	73	23	3	1	
	ghh02	po/equ	s/gc	90	5	4	1	
	ghh02b	po/equ	s/gc	66	25	8	2	
	gko02	po	s/gc	74	21	4	1	
	GC06	po	s/gc	90	3	5	2	
	GC08	po/equ	s/gc	86	4	8	1	
	Szb03-02	pr	s/gc	58	29	12	2	
	Szb03-04	mos-equ	s/gc	77	16	6	1	
	Szb03-07	poik	curv*	76	21	2	1	mp
	Szb213 TK	mos-equ	s/gc	73	21	5	1	mp
	Szb21	mos-equ	s/gc	72	15	12	1	mp
	Szb28	po	s/gc	74	13	12	2	
	Szb34	tab-equ	s/gc	81	13	6	0	mp
	Szb6	mos-equ	s/gc	86	8	5	1	
	Szba1	tab-equ	s/gc	78	16	5	1	
	Szba2	mos-equ	s/gc	77	14	9	1	mp
	Szba4	poik	s/gc	62	20	12	6	
	Szbd-1	pr	curv	87	9	3	0	
	Szbd-4	po	s/gc	80	17	3	1	
	Szbd-5	tab-equ	s/gc	77	15	7	1	
BBHVF	Szbd-6	po	s/gc	76	15	7	1	
	Szbd-7	mos-equ	s/gc	80	13	6	1	
	Szbd-8	tab-equ	s/gc	77	15	7	1	
	Szbd-9	po	s/gc	82	14	2	1	
	Szbd-10	tab-equ	s/gc	75	17	7	1	mp
	Szbd-11	poik	curv*	80	15	4	1	
	Szbd-13	pr	s/gc	75	14	10	1	
	Szbd-14	tab-equ	s/gc	75	20	4	1	
	Szbd-15	tab-equ	s/gc	86	10	3	1	mp
	Szbd-16	poik	curv*	61	31	6	1	
	SzbP-15	pr	s/gc	81	14	4	1	
	Szb99/26	mos-equ	s/gc	77	12	10	1	
	Szgk03-01	tab-equ	s/gc	78	19	3	1	
	Szgk99/04	po	s/gc	73	18	8	1	
	Tih03-02	mos-equ	s/gc	91	7	2	0	mp
	Tih03-12	poik	curv*	89	9	2	0	
	Tih03-13	poik	curv*	83	16	1	0	
	NBN27[3]	equ	s/gc	76	15	8	1	
	NBN30[3]	equ	s/gc	75	16	7	2	
NGVF	NBN52[3]	equ	s/gc	79	13	7	1	
	NFL15[3]	equ	s/gc	68	16	11	3	amp
	NMS032	po	s/gc	65	20	13	2	
	BG18[4]	pr	curv	61	25	12	2	
	BG15[4]	fol	s/gc	66	19	13	2	
	LGR09[4]	fol	curv	68	17	23	2	amp
ETBVF	LGR03-01	myl	s/gc	60	25	13	2	
	LGR03-04	myl	s/gc	59	23	18	2	
	NVTR03-01	myl	s/gc	64	22	14	2	
	Rk99/04	myl	s/gc	57	25	15	3	amp

Table IV.1 Modal composition of mantle xenoliths studied in detail. Ol – olivine; opx – orthopyroxene; cpx – clinopyroxene; sp – spinel; npp – non primary phases, pr – protogranular, po – porphyroclastic, equ – equigranular, mos – mosaic, tab – tabular, poik – poikilitic, curv – curvilinear; curv* – secondary origin curvilinear, s/gc – straight/gently curved, amp – amphibole, mp – silicate melt pocket. Analyzed earlier by (1) Vaselli et al. (1996); (2) Falus et al. (2000); (3) Szabó and Taylor (1994); Vaselli et al. (1995).

(Figure IV.1). Internal strain features in the coarse grains are relatively seldom. Clinopyroxene lamellae in large orthopyroxenes are rarely observed lamellae (Figure IV.1). Orthopyroxene-clinopyroxene-spinel clusters were found in the studied samples (Figure III.1) occupying 5-7 volume % of the sample. These clusters are believed to represent former garnets (e.g., Smith, 1976; Falus et al., 2000). The subordinate recrystallization, which affected about 3-5 vol% of the xenoliths produced relatively fine grained (300-500 microns) zones. The crystals here are isometric and have straight or gently curve grain boundaries with often developed triple junctions. The crystals lack all types of internal strain features, they display normal extinction.

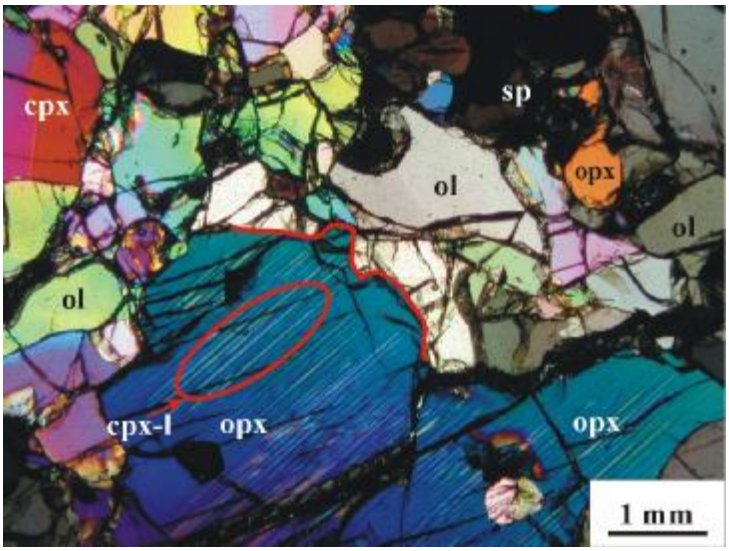

Figure IV.1 Porphyroclastic spinel lherzolite from the SBVF (Kf17). Coarse grains with curvilinear grain boundary (indicated with red ellipse) of orthopyroxene with deformation twins are shown. ol – olivine; opx – orthopyroxene; cpx – clinopyroxene; cpx-l – clinopyroxene lamellae; sp – spinel. Cross polarized light image.

Little Hungarian Plain Volcanic Field (LHPVF)

Detailed study of 12 deformed xenoliths selected after looking through more than 200 hand specimens was carried out in this xenolith location, which lies east, towards the central part of the basin relative to the SBVF (Figure II.3). It is obvious even macroscopically that a marked change exists between grain size and modal composition of mantle derived samples from the SBVF and LHPVF (Table IV.1). Microscopic observations show that grain size reduction is quite pronounced even in the texturally most undeformed xenoliths studied in the LHPVF.

Samples selected for detailed study similarly to the findings of earlier works in the region (e.g., Szabó et al., 1995b; Embey-Isztin et al., 2000) display porphyroclastic, porphyroclastic/equigranular textures. It is important to note that the study of Kurat et al. (1991) mentions also protogranular textured xenoliths. However, this finding was not confirmed by subsequent studies (e.g., Szabó et al., 1995b)

The selected deformed samples show variable modal compositions ranging from pyroxene rich spinel lherzolites to orthopyroxene and especially clinopyroxene poor harzburgites (Table IV.1). Moreover, 1 wehrlite (Table IV.1) was also found. Texturally, the xenoliths can be subdivided in to two major groups with respect to shape and grain boundary of recrystallized grains 1) where the recrystallized grains are elongated subparallel to the long axis of porphyroclasts and often have curvilinear grain boundaries, moreover they generally exhibit undulouse extinction (*group 1*); and 2) where the recrystallized grains are equi-axed have straight/gently curve grain boundaries an lack internal strain features (*group 2*).

In *Group 1* samples (GC03-06, GC03-12; GC03-12/b) porphyroclasts of the constituent phases are generally elongated subparallel to the macroscopic elongation, determined by the elongation of spinel crystals or fine-grained spinel patches, with an average grain size around 1-2 mm (long axis). Aspect ratio of the porphyroclastic grains is around 1:2 to 1:4. Most of the porphyroclasts, display internal strain features in the form of undulatory extinction, finely spaced (5-10 microns) kink bands, which are subparallel to (100) in olivine porphyroclasts and the formation of subgrains (Figure IV.2). A clear difference between undulouse extinction and finely spaced kink bands is only drawn by the resolution of the optical microscope. Orthopyroxenes often exhibit deformation twins and exsolution lamellae of clinopyroxenes. These lamellae are often kinked, bent or curved (Figure IV.3). Orthopyroxenes frequently develop subgrains. Clinopyroxene porphyroclasts are rare, but when present, they also display internal strain features as deformation twins and kinked exsolution lamellae of orthopyroxene. Clinopyroxenes in two special samples of this group (GC03-06, GC03-12) also contain crystallographically oriented spinel inclusions (parallel to (110) of the clinopyroxenes; Figure IV.4). Grain boundaries of the porphyroclasts are irregular, strongly lobated. They display abundant concave embayments, which are related to recrystallized bulging grains that pin inside the large deformed porphyroclasts. Olivine porphyroclasts are generally pinned by recrystallized orthopyroxenes, whereas the deformed orthopyroxene porphyroclasts generally contain embayments of recrystallized olivine grains.

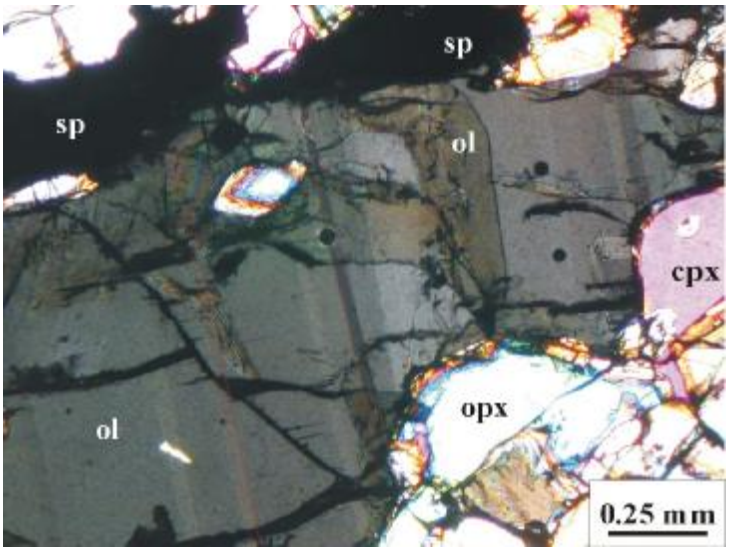

Figure IV.2 Large olivine porphyroclasts with fine spaced kink banding. The average thickness of kink bands (subgrains), indicated by thin red lines, is 10-20 microns. Porphyroclastic spinel lherzolite from the LHPVF (GC03-12). ol – olivine; opx – orthopyroxene; cpx – clinopyroxene; sp – spinel. Cross polarized light image.

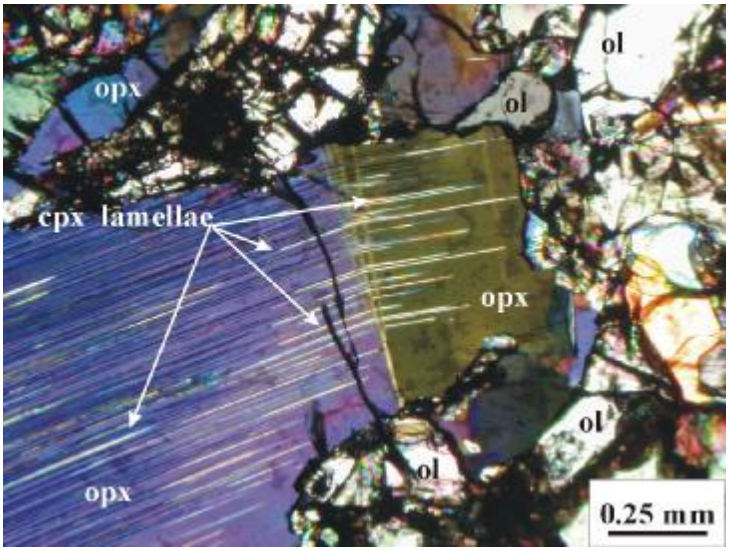

Figure IV.3 Kinked clinopyroxene exsolution lamellae in an orthopyroxene porphyroclast, surrounded by recrystallized grains. Porphyroclastic spinel lherzolite from the LHPVF (GC03-12). ol – olivine; opx – orthopyroxene; cpx – clinopyroxene; sp – spinel. Cross polarized light image.

Recrystallized grains are finer grained than the porphyroclasts and have grain size typically around 100-300 microns. They are generally elongated subparallel to the porphyroclasts and the macroscopic elongation exhibiting aspect ratios around 1:2. It is also often observed that recrystallized grains display internal strain features (mostly the recrystallized olivines), mainly undulouse extinction. Grain boundaries of the recrystallized grains can be irregular, strongly lobated. This feature is especially true for the recrystallized pyroxene grains, although it also frequently observed among olivines. Beside these types of recrystallized grains, those with straight or gently curved grain boundaries may also be subordinately observed. These grains often connect in well developed triple junctions and lack any sign of internal strain features.

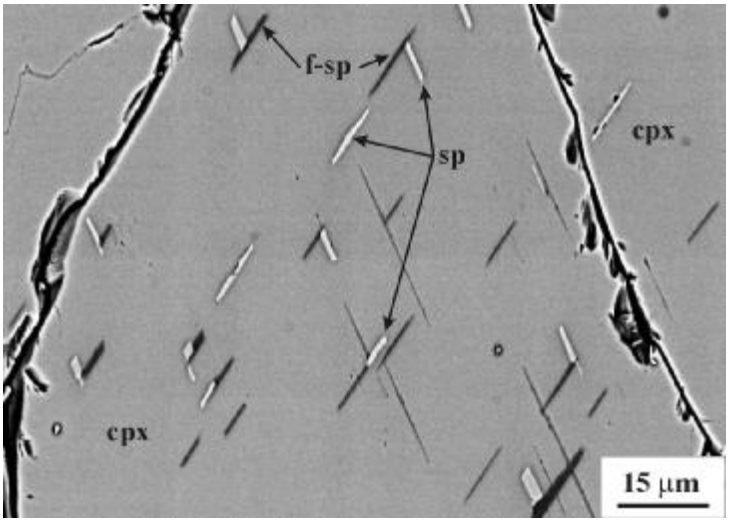

Figure IV.4 Crystallographically oriented spinel rods in a clinopyroxene porphyroclast subparallel to (110) as a result of exsolution. Note that section is not perpendicular to [c]-axis. Porphyroclastic spinel lherzolite from the LHPVF (GC03-06) cpx – clinopyroxene; sp – spinel; f-sp – former spinel lost during sample preparation. SEM image.

A specific, unique feature (described and analyzed in detail by Falus et al. 2004) is observed among some of the *group 1* xenoliths (and not only those selected for study namely in GC03-06 (and two other samples, which did not display macroscopic evidence for deformation). Large (3-4 mm) rounded patches with more or less sharp boundaries were found. These patches occupy 3-5 volume% of the studied samples. These patches are symplectites composed of orthopyroxene, clinopyroxene and spinel that generally occur in the central part of the patches (Figure IV.5). This grain assemblage is surrounded by euhedral

olivine grains and glass that also often infiltrates the symplectites. The symplectites constitute mainly of orthopyroxene, which is the dominant mineral phase and constitutes the mass of the symplectites. Clinopyroxene and spinel in the least recrystallized symplectites occur intimately intergrown in roughly the same volume ratios as elongated, vermicular forms "dispersed" in the mass of orthopyroxene (Figure IV.5).

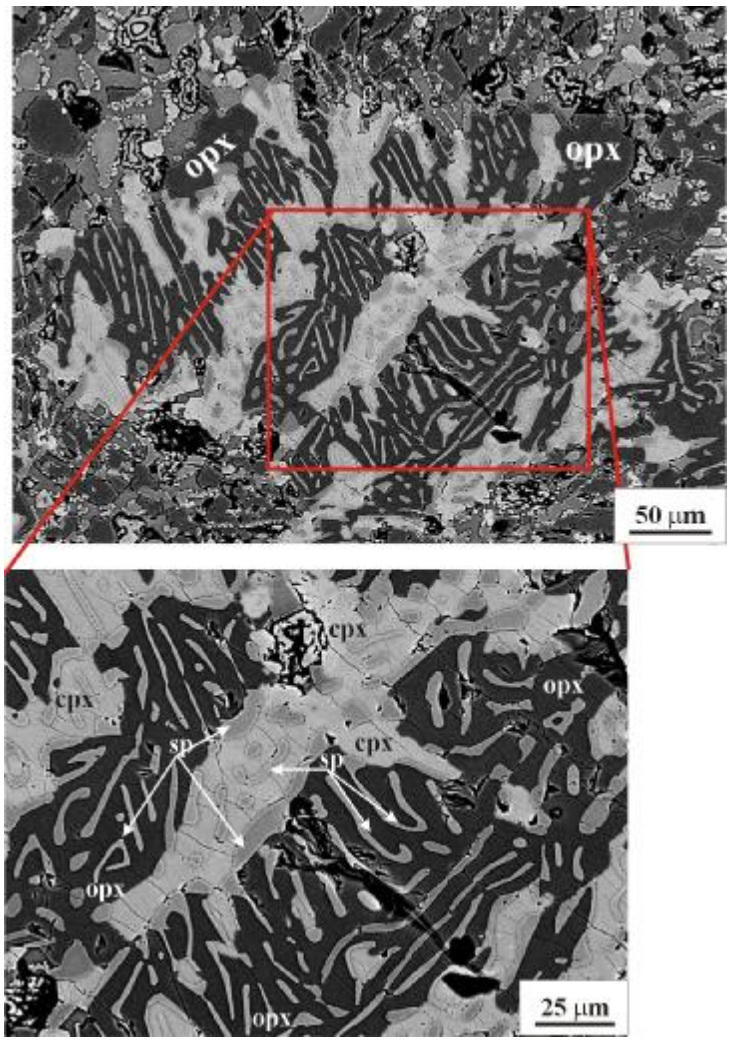

Figure IV.5 Pyroxene spinel symplectite with breakdown products and an enlarged image of the symplectite itself. Intimate intergrowth of clinopyroxene and spinels can also be observed. Porphyroclastic spinel lherzolite from the LHPVF (GC03-06). opx – orthopyroxene; cpx – clinopyroxene; sp – spinel. SEM image.

More intensively recrystallized patches lack the intimate intergrowth of clinopyroxene and spinel. Clinopyroxenes are rather isometric, whereas spinel remains vermicular and is often surrounded by fine grained isometric spinel crystals (Figure IV.6). Surrounding crystals of

the xenolith are generally rich in polyphase melt inclusions. The symplectites are believed to represent former garnets, as shown by their chemical composition (See Chapter VIII. for details)

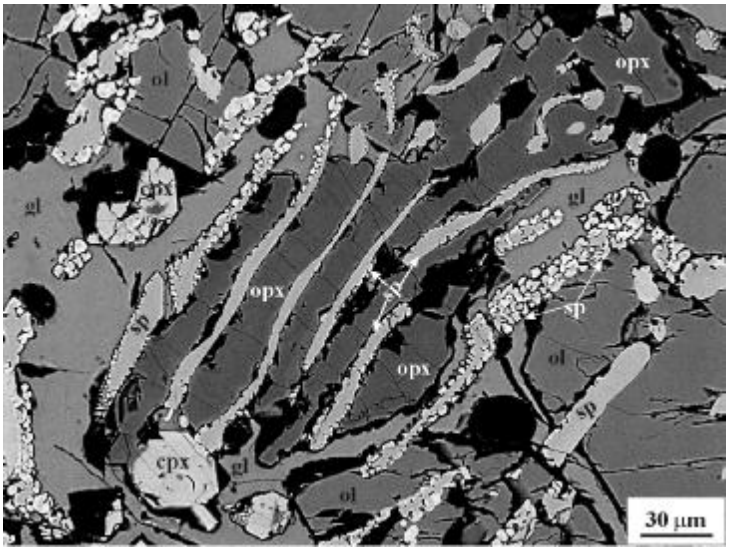

Figure IV.6 Reacted pyroxene spinel symplectite with remnant orthopyroxene and vermicular spinel surrounded by breakdown products of symplectite: glass and euhedral olivine. Note isometric occurrence of clinopyroxenes and spinel "rods" surrounded by isometric spinel grains. Porphyroclastic spinel lherzolite from the LHPVF (GC03-06). ol – olivine; opx – orthopyroxene; cpx – clinopyroxene; sp – spinel; gl - glass. SEM image.

Group II xenoliths from the LHPVF (Gr06, Gr08, Gkh02, Gkh02/b, GC03-04, Gko-07, GC03-05, GC03-10, GC03-14) also fulfill the textural criteria for porphyroclastic xenoliths, using the nomenclature of Mercier and Nicolas (1975). The porphyroclasts in these rocks are somewhat finer grained (1-1.5 mm) than those in *Group I* and are mostly elongated, however, isometric porphyroclasts also occur. Grain boundary of the crystals is curvilinear with pinning of recrystallized grains occurring occasionally. The porphyroclasts display internal strain features, generally kink bands, but compared to those of Group I. these kink bands are much coarser, with average spacing around 40-60 microns. Orthopyroxene porphyroclasts generally lack exsolution lamellae of clinopyroxenes, but may display deformation twins and irregular, lobated grain boundaries. Whereas, clinopyroxene porphyroclasts are rare and occur only as recrystallized grains.

Recrystallized grains are mostly isometric with fine grain size (100-200 microns). Some recrystallized grains are elongated, and may have aspect ratios around 1:2 to 1:4, but these are atypical. Grain boundaries are almost always straight or gently curved. These

grains always lack internal strain features. Some recrystallized grains of olivine, similarly to Group I. xenoliths, may form ribbon structures.

Bakony--Balaton Highland Volcanic Field (BBHVF)

The volcanic field, consisting of more than 200 former eruption centers (Németh and Martin, 2002) is the largest and most spectacular volcanic field of alkali basalts in the Intra-Carpathian Basin System (Figure II.3). Samples from three xenolith locations (Szentbékkálla, Szigliget and Tihany) were studied in detail. Among the studied samples those from Szentbékkálla were selected in the largest number (30) because this location provides the texturally most variable xenoliths and not negligibly these rocks are quite fresh. Two texturally special samples were selected from Szigliget and 3 from Tihany. Although Tihany samples are not "special" texturally, their scarcity and absence from earlier xenolith studies together with their relatively old sampling age, with respect to other, better known locations of the BBHVF justifies their detailed study.

Szentbékkálla

Xenoliths selected from Szentbékkálla are mostly equigranular, but porphyroclastic, protogranular and also secondary recrystallized “poikilitic” ones were studied. All samples display macroscopic deformation features, i.e., lineation formed by elongated crystals, mostly spinels and also rarely compositional layering. In some cases, macroscopic lineation is caused by the elongation of melt pockets.

Several protogranular xenoliths (Szb03-02, Szbd-1, Szbd-13, Szb-P-15) displaying macroscopic deformation were found. The selected xenoliths are pyroxene and spinel rich spinel lherzolites (Table IV.1). Macroscopic deformation features, i.e., compositional layering of pyroxene and spinel and olivine-rich bands, and foliation are frequently observed. The grains are also elongated and exhibit aspect ratios around 1:2. Moreover, spinels may exhibit even more extreme aspect ratios of 1:3-1:4. Average grain size is coarse, most of the grains reach 5 mm in diameter. Grains only very rarely display internal strain features. When so, they occur as widely spaced (~500 microns) kink bands. Furthermore, orthopyroxene grains may contain exsolution lamellae of clinopyroxene (in Szb03-02). Grain boundaries of all constituent phases are curvilinear. Although pinning of these grain boundaries by rare fine grained (400-500 micron) recrystallized grains is also observed. Some recrystallized grains, surrounding the coarse crystals do occur. These grains are isometric and have straight or

gently curved grain boundaries. Triple junctions among the recrystallized grains are also abundant. Although recrystallized grains are subordinate and occupy not more than 5 volume% of the studied sample.

Porphyroclastic xenoliths are the scarcest textural type among the xenoliths from Szentbékkálla. Despite their low abundance, porphyroclastic xenoliths frequently exhibit macroscopic strain features. Five of the hand specimens (Szbd-4, Szbd-6, Szbd-9, Szbd-14 and Szb28) studied display macroscopic strain features and were analyzed further in detail. The selected samples are relatively pyroxene rich spinel lherzolites (Table IV.1). They display bimodal grain size distribution. Porphyroclasts are almost solely orthopyroxenes all other phases are intensively recrystallized. The remnant orthopyroxene porphyroclasts display internal strain features in the form of deformation twins and undulouse extinction. In one of the xenoliths (Szb28) even exsolution lamellae of clinopyroxene in the orthopyroxene is preserved. Olivines in these samples are generally elongated, have grain size around 1-2 mm and may exhibit aspect ratios of 1:3. These elongated grains often contain subgrains or relatively coarse grained kink bands (50-100 microns). Isometric olivine grains regularly form ribbons displaying evidence for the recrystallization of earlier elongated porphyroclasts (Figure IV.7). Grain boundaries of recrystallized grains are generally straight or gently curved. However, in some cases convex grain boundaries, mostly at olivine/orthopyroxene contacts may also occur. Clinopyroxenes in these samples are generally isometric with straight or gently curved grain boundaries.

Spinel, one of the most sensitive and effective macroscopic strain indicators in mantle peridotites is either elongated or, more commonly forms extremely elongated patches (aspect ratio - 1:10 !) consisting of isometric spinel crystals (Figure IV.8). The spinels are mostly intergranular, however they may also be included in the silicate phases (orthopyroxene and olivine) as small (>50 microns) spherical inclusions.

Equigranular xenoliths besides the protogranular ones are the most abundant textural type at Szentbékkálla xenolith location. Several subtypes of the equigranular mantle xenoliths were found. Those with relatively fine grain size and generally equi-axed grain shapes (Figure III.4) and others with relatively coarse grain size with flattened grains (Figure III.5) simultaneously occur. Many of these xenoliths display macroscopic deformation features. Deformed xenoliths were selected from all the ***equigranular*** subtypes to get a comprehensive view of these rocks. Most of the selected samples are spinel harzburgites, but pyroxene rich spinel lherzolites are not rare either (Table IV.1). Moreover, a composite xenolith composed of equigranular spinel lherzolite and dunite bands was also studied in

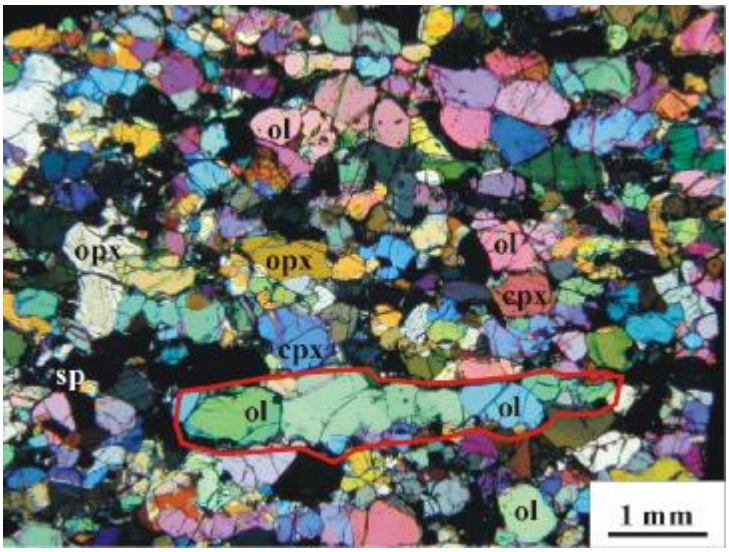

Figure IV.7 "Ribbon" olivine indicated by red contour in a porphyroclastic spinel lherzolite from the BBHVF (Szb28). Aspect ratio of the former grain, now recrystallized, is around 1:6-1:7. ol – olivine; opx – orthopyroxene; cpx – clinopyroxene; sp – spinel. Cross polarized light image.

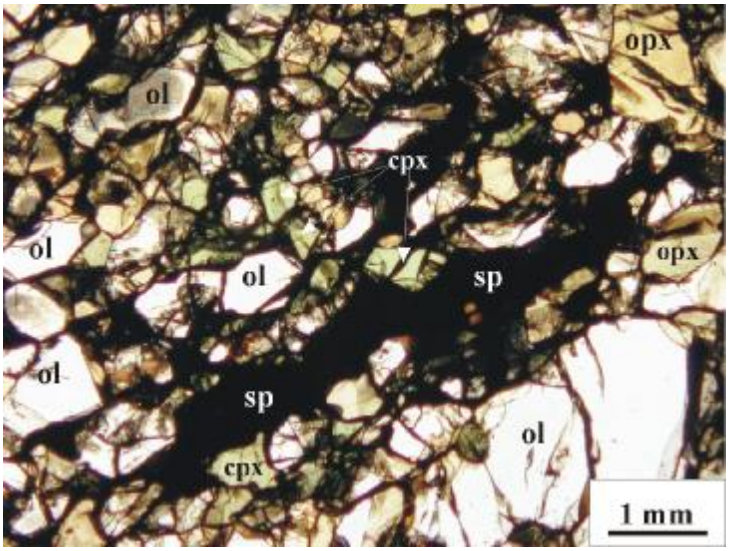

Figure IV.8 Elongated spinel in a porphyroclastic spinel lherzolite from the BBHVF (Szgk99/04). The aspect ratio of spinel is about 1:8-1:10. ol – olivine; opx – orthopyroxene; cpx – clinopyroxene; sp – spinel. Plain polarized light image.

detail (Szb03-04). However, many of the selected equigranular samples contain melt pockets. These melt pockets are characteristic features of this textural type (as described by Bali et al., submitted). They always have sharp, straight or gently curved boundaries. They consist of crystalline phases and glass. Rarely relic clinopyroxenes and corroded amphiboles are found in these pockets.

The selected equigranular samples were further grouped in to two subgroups: in *Group I.* beside the elongated spinel crystals or spinel patches other constituent phases (olivine or orthopyroxene or both) exhibit elongated (flattened) grain shapes. In these xenoliths melt pockets, when present, also often display elongated shapes. This group corresponds to tabular equigranular xenoliths (Mercier and Nicolas, 1975). Whereas, those samples in which only spinel is elongated and all other phases were isometric (mosaic equigranular – Mercier and Nicolas, 1975) were classified in *Group II.*.

Samples that belong to Group I. (Szba1, Szbd-5, Szbd-8, Szbd-10, Szbd-15, Szb34) are generally relatively coarse grained rocks with grain size around 200-300 microns. Olivines and orthopyroxenes, besides the spinels, frequently display elongated grain shapes and can exhibit aspect ratios in extreme cases around 1:8-1:10 (average- 1:3-1:4). The elongated olivine crystals often exhibit internal strain features, generally widely spaced kink bands (average spacing ~30-40 microns) that are perpendicular to the long axis of the olivine grains. Grain boundaries are straight or gently curved and well equilibrated triple junctions at grain contacts are often found. Nevertheless, concave boundaries are also found mostly on orthopyroxene-olivine contacts. Elongated orthopyroxenes and the isometric crystals of the other constituent phases never display internal strain features. Furthermore, in sample Szbd-8 one remnant orthopyroxene porphyroclasts observed has irregular, strongly lobated grain boundary (Figure IV.8). Similar textural features were described in ophiolitic mantle fragments from Othris Massif (Dijkstra et al., 2002). Clinopyroxenes only occur as small isometric phases and are generally quite rare as it is reflected also by the modal compositions (Table IV.1). Some of the spinel crystals are interstitial and in these cases they are often elongated and have similar dimension to the other constituent phases, although they can be extremely elongated and have aspect ratios around 1:5-1:8. However considerable amount of the spinel crystals occur as inclusions in olivine and orthopyroxene. They form small (30-50 microns) spherical or euhedral inclusions. As mentioned earlier melt pockets are common phases in these samples. Their sharp boundaries and dimensions that are similar to those of crystalline phases in the host rock suggest that they are reaction products of former host rock

phases and infiltrated silicate melts (Bali et al., 2001). In some cases besides melt pockets, melt veins connecting these pockets or independently from those, occur in the rocks.

Two of the xenoliths from group I (Szba1 and Szbd-15) and one xenolith from Szigliget (Szgk03-01; described later) show extreme shape preferred orientation (SPO). All constituent phases are extremely flattened and display large aspect ratios (1:4-1:6; Figure III.5). Grain size is relatively coarse, it may reach 1 mm (long axis). Grain boundaries are straight or gently curved and triple junctions often occur at grain contacts. This special group is studied and described in detail by Hidas et al. (in prep.).

Equigranular xenoliths that belong to Group II. (Szb21, Szb99/26, Szba2, Szb6, Szb03-04; Szb213TK, Szbd-7) are dominantly olivine rich and pyroxene (especially clinpyroxene) poor rocks with isometric grains. Although some of the olivines may exhibit weak elongation with aspect ratios 1:2 (as a maximum). Grain size is variable in this group. It may be as low as 100 microns but in some cases average grain size may reach 500 microns. These rocks display relatively weak shape preferred orientation and only the elongation of spinel patches (consisting of isometric spinel grains) or more rarely individual elongated crystals indicate deformation and strain. As a matter of fact rarely ribbon structures of olivine and orthopyroxene, now consisting of isometric grains is observed (Figure IV.7). The aspect ratio of these former porphyroclasts may be very extreme (1:5-1:7). Pyroxenes (both ortho- and clinopyroxene) display isometric grain shapes and all phases almost always lack internal strain features. Exceptionally these rocks may contain 1-2 remnant porphyroclasts of orthopyroxene (Szbd-7), which, similarly to that in Sz-b-d-8 (group I) have lobated grain boundaries (Figure IV.9).

The grain boundaries are dominantly straight or gently curved and grain contacts frequently occur, as well developed triple junctions. Besides the interstitial spinel grains those, included in the silicate phases of the peridotite are very abundant. These spinels are finer grained than the interstitial ones (30-50 microns) and are mostly spherical or euhedral. Radial cracks often surround these inclusions. Melt pockets occupy considerable volume ratio (3-10 vol%) of most of the group II. xenoliths and display similar petrographic features to those melt pockets observed in group I. samples.

Poikilitic xenoliths from Szentbékkálla are solely harzburgites and almost always display isometric grain shapes. Nevertheless, samples selected for detailed study (Szba4, Szbd-16, Szbd-11, Szb03-07) display marked macroscopic strain features with compositional banding of orthopyroxene rich and olivine rich bands or foliation. Grain size is coarse (1-3 mm). The grains themselves can be isometric (Szb03-02) or elongated with typical aspect

ratios 1:3-1:4 (Szba1, Szbd-16). Grain boundaries are straight or gently curved, but may also be curvilinear. Clinopyroxenes are somewhat finer grained than olivine and orthopyroxene and often exhibit spongy textures indicating partial melting. Spinel crystals occur solely as fine grained (30-100 microns), spherical and euhedral inclusions in olivine and orthopyroxene (Figure III.6).

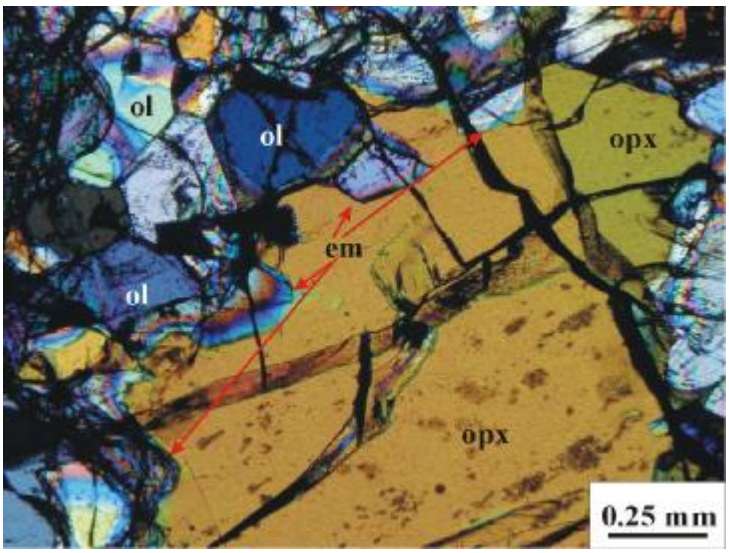

Figure IV.9 A remnant orthopyroxene porphyroclast is an equigranular spinel lherzolite from the BBHVF (Szbd-8). Note lobated grain boundary of the porphyroclast and low index crystal faces of embayed recrystallized olivines. ol – olivine; opx – orthopyroxene; em-embayment. Cross polarized light image.

Tihany

Samples selected from Tihany xenolith location are all olivine rich harzburgites. Four of the five xenoliths that were selected for detailed study (Tih03-04. Tih03-05, Tih03-12 and Tih03-13) are coarse *poikilitic*. These poikilitic xenoliths exhibit grain sizes around 1 mm. Grain boundaries are often corroded, probably due to weathering. When the boundaries are observable, they are straight or gently curved. Orthopyroxenes may display bimodal grain size distribution but fine grains are always subordinate. Spinel crystals always occur as spherical or euhedral inclusions in olivines and orthopyroxenes.

One xenolith among the five selected (Tih03-02) has mosaic equigranular texture. The xenolith shows weak compositional banding of pyroxene rich and olivine rich bands. Grains are isometric or moderately elongated with maximum aspect ratio ~1:2. The grain size is relatively fine (200-300 microns) excluding the rare orthopyroxene porphyroclasts that

have grain size around 1 mm and display undulouse extinction. Most of the grains have straight or gently curved grain boundaries and lack any type of internal strain features. Spinels occur as small spherical inclusions but are also found in intergranular position displaying opaque rims when in contact with interstitial glass.

Szigliget

Two samples, a porphyroclastic (Szgk99/04) and a tabular equigranular (Szgk03-01) from this xenolith location were selected for detailed study. The porphyroclastic sample consists of elongated orthopyroxene porphyroclasts (1-2 mm) with internal strain features and extremely elongated spinel. Recrystallized grains are fine grained (300-400 microns) and equi-axed. The tabular equigranular xenolith is quite similar to those two (Szba1, Szbd-15) found in Szentbékkálla.

Nógrád-Gömör Volcanic Field (NGVF)

The NGVF lies in the northern boundary region of the Intra-Carpathian Basin System (Figure II.3). Several xenolith locations are found in the region. Five samples (NBN27, NBN30, NBN52, NFL15 and NMS032) from three xenolith locations (Maskófalva-Maskova, Fülek-Filakovo at the northern part of the volcanic field and Bárna the southernmost part of the volcanic field) were selected for detailed study.

Only one xenoliths (NMS032) displays porphyroclastic texture among those selected for detailed study. The grains exhibit bimodal grain size distribution. Porphyroclasts of olivine and orthopyroxenes are moderately elongated and display internal strain features. Recrystallized grains are fine grained. The geometry of grain boundaries could not be resolved due to intensive weathering along the grain boundaries. Three samples (NBN27, NBN30, NFL15) are equigranular textured samples. They are all olivine rich spinel lherzolites (Table IV.1) with some rare orthopyroxene porphyroclasts with large grain size (1-3 mm), and which display internal strain features, like deformation twins and undulouse extinction. In one of the samples (NBN30) olivine also displays bimodal grain size distribution, however olivine porphyroclasts (0.5-0.8 mm), elongated and displaying undulouse extinction, are very rare in the sample. Recrystallized grains are finer grained (100-300 microns) and may exhibit isometric grain shapes. However, elongated grain shapes are also not rare, especially in NBN 30, where aspect ratio of the recrystallized olivines may reach 1:4. Grain boundaries of the recrystallized grains are generally straight or gently

curved, with some rare ones displaying lobated boundaries. Triple junctions at grain contacts are regularly developed. Clinopyroxenes are quite rare and when present, they only occur as recrystallized grains. Spinels generally occur as elongated crystals subparallel to the macroscopic lineation, displaying aspect ratios around 1:3-1:5. Some of the spinel grains in NBN27 are spherical and enclosed in olivines and orthopyroxenes. Spinels in NFL15 display opaque rims and are always surrounded by glass and amphiboles. Sample NBN52 is mosaic equigranular xenolith displaying macroscopic banding. The grain size is relatively fine (100-200 microns). Grain boundaries are straight or gently curved. Aspect ratio of the constituent grains is moderate (max. 1:2).

East Transylvanian Basin Volcanic Field (ETBVF) - the Persány Mountains

Mantle material from the easternmost, young alkali basaltic location of the Intra-Carpathian Basin System (Figure II.3) with spectacular xenolith occurrences was also studied. Most of the mantle peridotites found have protogranular or very weakly recrystallized protogranular/porphyroclastic textures (BG18) as already stated by earlier works dealing with this locality (e.g., Vaselli et al., 1995). Nevertheless, these studies failed to identify a very special, rare textural type: the *mylonitic* mantle xenoliths. These xenoliths seem to be quite rare (< 1% of all mantle derived samples) but, due to the extreme high abundance of mantle rocks in the volcanic tuffs of the ETBVF, they are easily found. Such textural types have not been identified from elsewhere in the Intra-Carpathian Basin System, which extends their importance and genetic significance. Four of these mylonites (LGR03-01, LGR03-04, NVTR03-01 and Rk99/04) were studied in detail and also 2 truly porphyroclastic samples (LGR09, BG15 studied in detail also by Vaselli et al., 1995 addressed as “foliated”) were described in detail in this thesis. Several other xenoliths (>200) were carefully looked through in hand specimen, however none of them displayed any type of macroscopic deformation (strain) feature.

All xenoliths studied are pyroxene and spinel rich spinel lherzolites (Table IV.1). The constituent phases in all samples show marked bimodal grain size distribution. In three of the four mylonites (LGR03-01, LGR03-04 and Rk99/04) porphyroclasts and recrystallized grains occupy similar volume ratios, whereas NVTR03-01 is an ultramylonite, because the volume ratio of porphyroclasts is quite low (~10 %). All of the samples display shear banding that is mainly anostomosing (Figure IV.10) although in the ultramylonite they are mostly straight (Figure IV.11). Porphyroclasts are relatively coarse grained (1-3 mm) frequently occur as

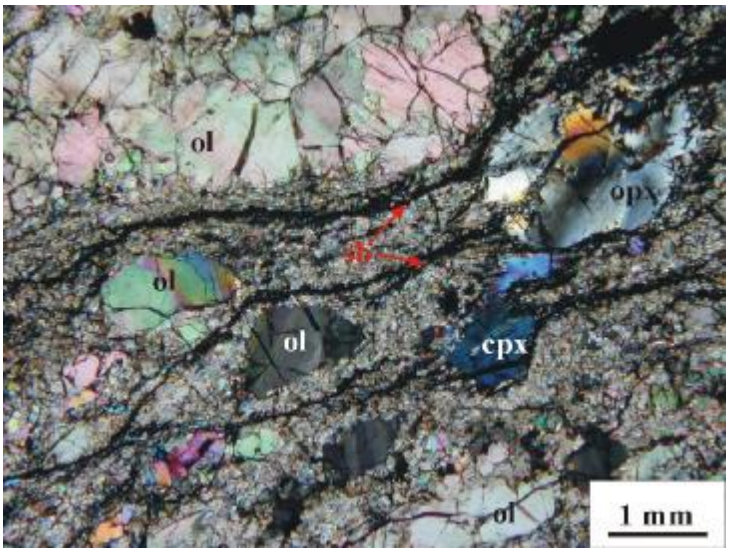

Figure IV.10 Anastomozing shear bands around strongly deformed porphyroclasts in a spinel lherzolite mylonite from the ETBVF (LGR03-01). Note extreme internal strain features in the porphyroclasts. ol – olivine; opx – orthopyroxene; cpx – clinopyroxene; sb – shear band. Cross polarized light image.

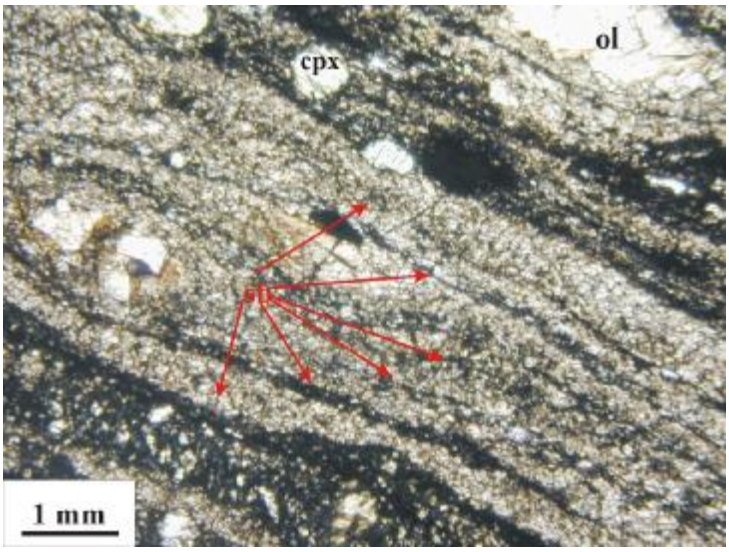

Figure IV.11 Subparallel shear bands in a spinel lherzolite ultramylonite from the ETBVF (NVTR03-01). Note close spacing of the shearbands, the rounded shape of a clinopyroxene porphyroclast and the very fine grained matrix between the bands. ol – olivine; cpx – clinopyroxene; sb – shear band. Plain polarized light image.

sigma clasts (Figure IV.12). Some of the grains (mostly the orthopyroxene porphyroclasts) display extremely elongated grain shapes subparallel to the shear banding (Figure IV.13). Aspect ratios may reach 1:10-1:15. They are similar to the sheared orthopyroxene porphyroclasts of the Horoman peridotite, described by Ishii and Sawaguchi (2002). Sigma (porphyro-) clasts always grow recrystallized tails. Despite the abundance of porphyroclasts in the mylonites (except for NVTR 03-01) olivine porphyroclasts are rarely found. They occur mostly as large patches of equigranular assemblages that mimic former porphyroclasts. When however olivine porphyroclasts are found, they are generally rounded and display undulouse extinction (Figure 14.). Pyroxenes (both ortho- and clinopyroxene) display internal strain features, like undulouse extinction, kinking and folding of exsolved clinopyroxene and orthopyroxene lamellae, respectively. They have strongly lobated grain boundaries that are pinned with embayments of recrystallized grains. However some of the elongated orthopyroxene porphyroclasts display remarkably straight boundaries along their long axes subparallel to the shear banding (Figure IV.13). Spinels also develop porphyroclasts, that may display aspect ratios similar to the pyroxenes. Recrystallized grains are very fine grained compared to other xenolith locations. Average grain size is around 30-50 microns. Most of the recrystallized grains are isometric or only moderately elongated (1:2). The recrystallized grains exhibit straight or gently curved boundaries and triple junctions at grain contacts are frequently developed. Shear bands in all samples studied contain glass. Recrystallized grains in contact with this melt often grow low index faces. One sample of the studied four contains amphibole in a shear band.

Two xenoliths with porphyroclastic texture (LGR09, BG15) are also spinel lherzolites (Table IV.1). Bimodal grain size distribution is obvious, however recrystallized grains are coarser grained than those observed in the mylonites. Porphyroclasts of all constituent phases are mainly elongated subparallel to the macroscopic lineation. Although some of the orthopyroxenes and clinopyroxenes may also be rounded. Average grain size is large 2-4 mm. Grain boundaries are generally lobated, although those parallel to the elongation axis of the porphyroclasts may also be straight in LGR09, whereas they are mainly straight or gently curved in BG15. Internal strain features are spectacular in LGR09. Olivines develop subgrains parallel to (100), but also those parallel to (001) can be observed, thus giving olivine porphyroclasts a chess-board pattern (Figure IV.15). Orthopyroxenes and clinopyroxenes contain exsolution lamellae of the other mineral. These lamellae are mostly folded, bent and kinked. Recrystallized grains are relatively coarse (100-150 microns). They are also often elongated subparallel to the macroscopic elongation of the xenolith and

similarly to some of the recrystallized grains of LHPVF Group I. xenoliths often display undulouse extinction (Figure III.3) Their grain boundaries, similarly to those of LHPVF are mostly lobated. Along some cracks running through porphyroclasts isometric grains (same as the porphyroclasts) with low index crystal faces are developed. Rarely amphiboles may also occur along cracks in orthopyroxene porphyroclasts.

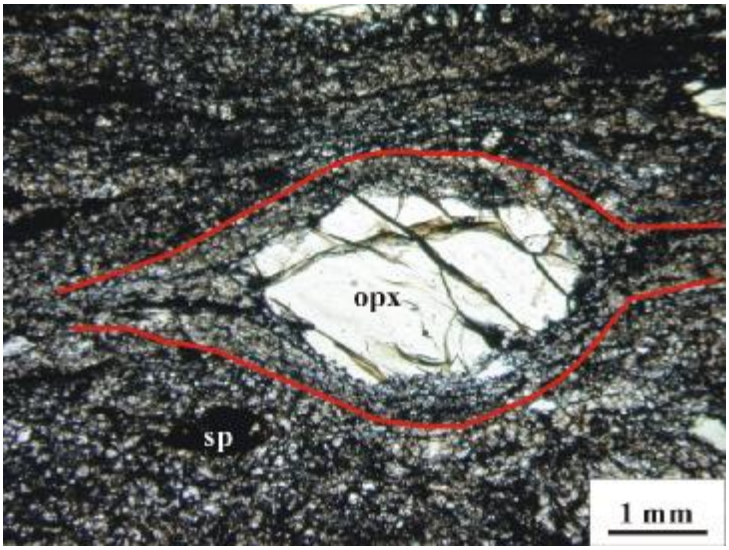

Figure IV.12 Orthopyroxene sigma-clast surrounded by fine grained, recrystallized orthopyroxene (outlined by red line) in a spinel lherzolite mylonite from the ETBVF (NVTR03-01). opx – orthopyroxene; sp – spinel;. Cross polarized light image.

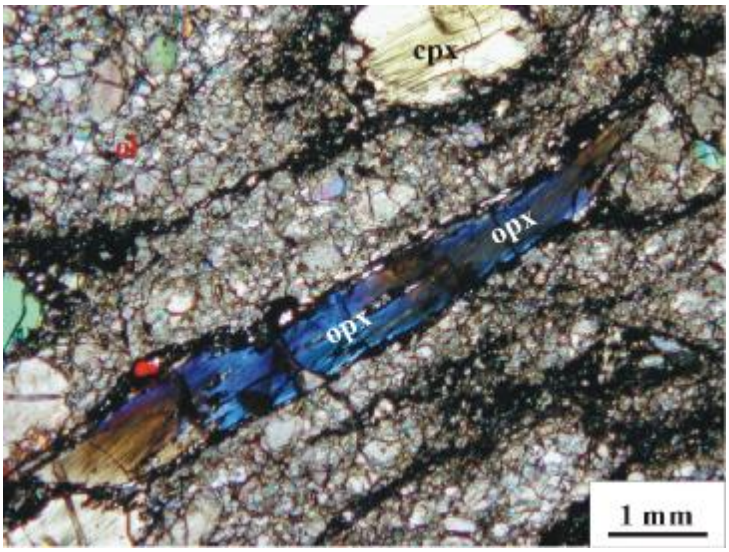

Figure IV.13 Elongated orthopyroxene porphyroclast (aspect ratio- ~1:10) in a spinel lherzolite mylonite from the ETBVF (LGR03-04). Note straight grain boundaries along the long axis of the orthopyroxene. ol – olivine; opx – orthopyroxene; cpx – clinopyroxene. Cross polarized light image

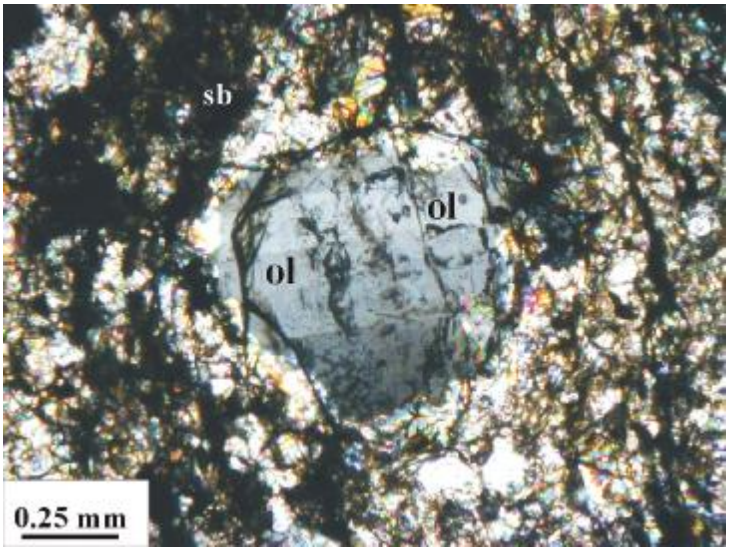

Figure IV.14 Rounded olivine porphyroclast with undulouse extinction surrounded by fine grained, recrystallized olivine in a spinel lherzolite mylonite from the ETBVF (NVTR03-01). ol – olivine; sb – shear band;. Cross polarized light image.

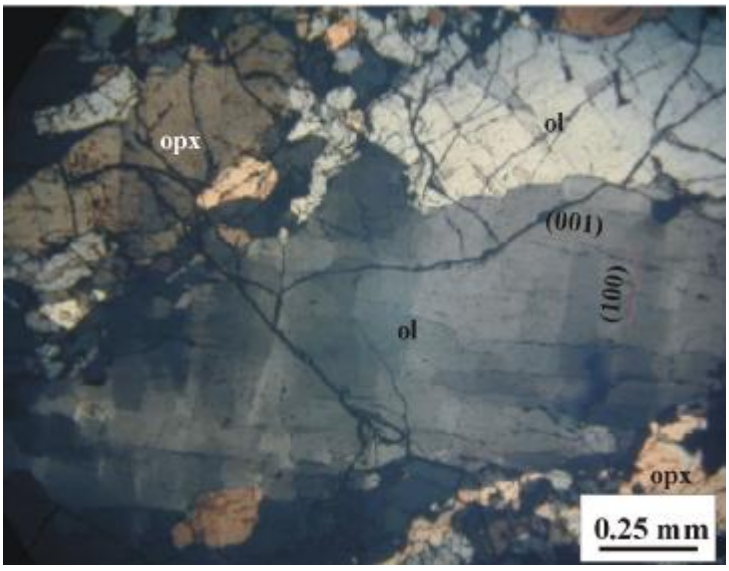

Figure IV.15 "Chess board " pattern of deformed olivine porphyroclast in sample LGR09 from the ETBVF. Subgrain boundaries of (100) and (001) are indicated. ol – olivine; opx – orthopyroxene; cpx – clinopyroxene. Cross polarized light image.

V. Deformation, fabrics and lattice preferred orientation

Constituent grains in rocks that deformed under specific physical conditions may develop specific fabrics (for the theoretical background see Chapter III.). The fabrics (or lattice preferred orientation [LPO]) can be studied with orientation analyzing methods. Detailed petrographic observation of the selected samples from all xenolith locations was followed by orientation analysis. The analyses were carried out on a universal stage (U-stage – Ernst Leitz Wetzlar 2415) mounted on a polarization microscope (Biolar) similarly to many of the published literature dealing with orientation measurement (e.g., Carter and Avé Lallemant, 1971, Mercier and Nicolas, 1975; Van der Wal, 1993; Dijkstra et al., 2002). The U-stage is a conventional and widely used tool for orientation analysis. It is especially effective on samples with coarse grain size (typically above 60-80 microns). The precision of measurements is acceptable (~ 5^{o} according to the literature) for a first good approximation of the orientation analyzed. There are some more advanced methods for orientation analysis (e.g., electron back scattered diffraction [EBSD] and other electron channeling methods and also transmission electron microscopy [TEM]). These are widely applied for fine-grained rocks and specific aims, respectively. Another difficulty of these electron-optical methods is that they require very advanced hardware and software background. Nevertheless, several control measurements were carried out on individual grains and on whole thin sections with the U-stage. The error of reproducibility of the measurements on axes of single grains was below 3^{o}, whereas on whole thin sections the similarities were unambiguous. However, some minor differences undoubtedly existed (Figure V.I).

Primarily the orientation of olivine grains was measured in the selected thin sections. Not only because behavior of olivines and the kinematic meaning of several olivine fabrics is already understood (e.g., Tommasi et al., 2000; Zhang et al., 2000), but also because olivines are the most abundant phases in mantle peridotites. Moreover, they respond very sensitively to any deformation occurring in the mantle. Nevertheless, in some of the xenoliths the orientation and fabric of orthopyroxenes, which are much more "rigid" than olivines (e.g., Soedjatmiko and Christensen, 2000) were also determined (not shown in this work) and are treated by Hidas et al. (submitted).

Orientation distribution of crystal axes with respect to macroscopic deformation features plotted in stereograms is widely used to interpret the slip systems active during crystal plastic deformation. Experimental petrologic works (e.g., Zhang et al., 2000) and

theoretical modeling (e.g., Wenk and Tomé, 1999) that produced numerous fabrics at different physical conditions provide a solid basis for the interpretation of orientation data. The results of these works together with those derived from the study of naturally deformed samples will be applied to interpret our orientation data. It should be noted, however, that most of the data are derived from pure olivine rocks. Nevertheless, studies on natural samples (e.g., Dijkstra et al., 2002) demonstrated that olivines in adjacent dunites and lherzolites display similar fabrics.

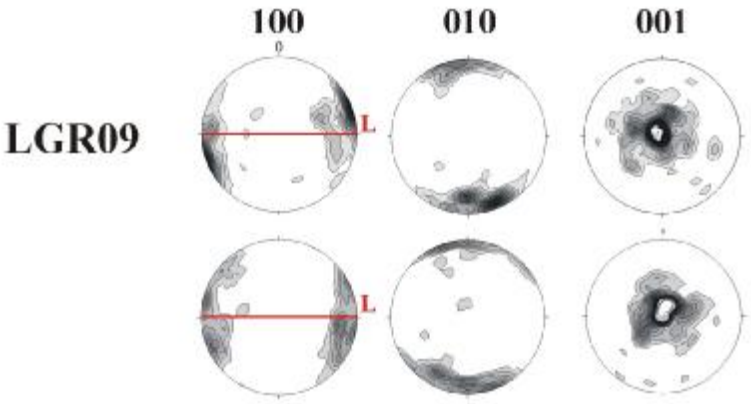

Figure V.1 Stereogram of 100 randomly selected olivine grains in xenolith LGR09 from the ETBVF. Note the similar distribution patterns of the two measurements. Lower hemisphere, equal area projection. Horizontal line denotes macroscopic foliation, L-lineation. Data contoured at 1, 2, 3,… times uniform distribution.

V.1 The orientation analysis method

Since olivine has orthorhombic crystal symmetry its optical axes identified on the U-stage can be directly adapted to the crystal axes of the analyzed minerals (i.e., $\alpha_{olivine}$-010; $\beta_{olivine}$-001; $\gamma_{olivine}$-100). All xenoliths were slide perpendicular to the macroscopic foliation or compositional banding (if observed) and parallel to the lineation. Two of the three optical axes were measured and the third axis was calculated on an EXCEL-sheet constructed for this aim. If the angles of the two measured axes showed too high errors (were below 80^{o}), the measurement was eliminated from the record. The average error of the measurements was about 2-4 degrees, which is within the reproducibility of single axis measurements. Data were visualized on lower hemisphere, equal area stereographic projection. The stereographic projections are oriented parallel to the surface of the thin section. Lineation is horizontal. Because orientations of olivine crystal axes in the literature are always displayed in the same way, they are directly comparable to one another.

Almost 50 samples were selected from the 5 xenolith locations of the Intra-Carpathian Basin System. In most of the samples where the geometry and grain size was optimal 100 olivine orientations were analyzed. Porphyroclasts and recrystallized grains, where present, were measured separately. The orientation of orthopyroxene grains was only measured in some specific samples that showed special textures (for details see Hidas et al., in prep.) and are not discussed in this work. Results of the orientation measurements are presented with respect to xenolith locations.

For the description and separation of orientation subgroups found among the studied mantle xenoliths several methods were applied: 1) visual separation of stereographic projections (most frequently used in the literature); 2) multiples of the uniform distribution and 3) misorientation analysis on special samples.

SBVF

Three samples from the SBVF have been analyzed under the U-stage. No macroscopic deformation signatures (neither foliation, compositional banding, nor lineation was observed in these xenoliths. Without these macroscopic deformation signatures, the geometry of the axes could not be positioned with respect to any macroscopic feature only with respect to the thin section plane. Nevertheless, crystal axes plotted on the stereograms cluster in all studied samples (Kf4, Kf5 and Kf17; Figure V.2; Table V.1). However, due to the geometry of the U-stage and the coarse grain size of the samples, only low number of crystal axe orientations could be measured (~25). The low number of measurements results in multiple maximums of the crystal axes. Although, even such low number of crystal axes plotted suggest the activation of a single slip system most probably the (010)[100] (described by Carter and Avé Lallemant, 1970).

Table V.1. Summary of the active slip systems of randomly selected 100 olivines (if less was studied, indicated in text) in the selected xenoliths from the five xenolith locations with respect to texture. Note remarkable dependence of deformation patterns with texture for xenoliths in the BBHVF (for details see text). c – core; r – rim; n – recrystallized grain T – equilibrium temperatures (^{o}C) calculated using the method of Brey and Köhler (1990); $\Delta \log fO_2$ – oxygen fugacity calculated using the method of Ballhaus et al. (1990). Slip systems described 1 – Carter and Avé Lallemant (1970); 2 – Zhang et al. (2000); 3 – Durham et al. (1977).

Location	Sample	Texture	slip system	T	$\Delta \log fO_2$
	Kf4	pr/po	?(010)[100]?	1076	0.37
SBVF	Kf5	po	?(010)[100]?	1057	0.43
	Kf17	pr	?(010)[100]?	1012	-0.37
	GC03-10	po/equ		960	0.19
	GC0314	po	(010)[100][1]		
	ghh02	po/equ			
	GC03-06 c	po		902	-1.42
	GC03-06 r	po		823	-0.68
	GC03-12 p	po		857	-0.45
	GC03-12 r	po		920	-1.20
	GC03-12 n	po	(010)[100] and possible	864	-1.67
	GC03-12b	po	activation of (100)[001][2] and		
LHPVF	ghh02b	po/equ	slip toward [100]&[001]		
	gko02	po	with twist walls on (010)[3]		
	GC06	po		960	-0.03
	GC08	po/equ		788	-1.41
	GC03-05	po/equ	{0kl}[100][1]	995	-3.24
	Szb03-02	pr			
	Szbd-1	pr			
	Szb6	mos-equ	(010)[100]		
	Szbd-13	pr		1154	-2.19
	SzbP-15	pr		1128	-2.21
	Szgk99/04	po			
	Szb28	po			
	Szb34	tab-equ			
	Szba1	tab-equ	(010)[100] and possible	1017	-0.49
	Szba4	poik	activation of (100)[001] and		
	Szgk03-01	tab-equ	slip toward [100]&[001]	1009	0.09
	Szbd-4	po	with twist walls on (010)		
BBHVF	Szbd-6	po			
	Szbd-14	tab-equ			
	Szbd-15	tab-equ		978	-0.38
	Szbd-9	po	{0kl}[100]	1070	-0.55
	Szb03-07	poik		1082	-0.24
	Szb213 TK	mos-equ			
	Szb21	mos-equ		940	-0.55
	Szba2	mos-equ			
	Szbd-5	tab-equ			
	Szbd-7	mos-equ	mixed slip system & static recrystallization		
	Szbd-8	tab-equ			
	Szbd-10	tab-equ			
	Szbd-11	poik			
	Szbd-16	poik			
	Szb99/26	mos-equ			
	Tih03-02	mos-equ		1071	0.96
	NBN27	equ	(010)[100]	1004	-0.45
	NBN30	equ	(010)[100]	919	-0.50
NGVF	NBN52	equ	(010)[100]	939	-1.02
	NFL15	equ	(010)[100]		
	NMS032	po	(010)[100] and possible activation of (100)[001] and slip toward [100]&[001] with twist walls on (010)		
	BG18	pr	?(010)[100]?	1024	-0.76
	BG15	fol	(010)[100]	805	-0.60
	LGR09 p	fol	(010)[100]	785	-1.22
	LGR09 r	fol	(010)[100]	899	-1.38
ETBVF	LGR03-01 c	myl	?	908	-1.60
	LGR03-01 r	myl		857	-1.09
	LGR03-01 n	myl		864	-1.51
	LGR03-04	myl	?		
	NVTR03-01 c	myl	?	886	-1.98
	NVTR03-01 r	myl		893	-2.63
	NVTR03-01 n	myl		920	-1.78
	Rk99/04 p	myl	?	708	-0.05
	Rk99/04 n	myl		971	-0.05

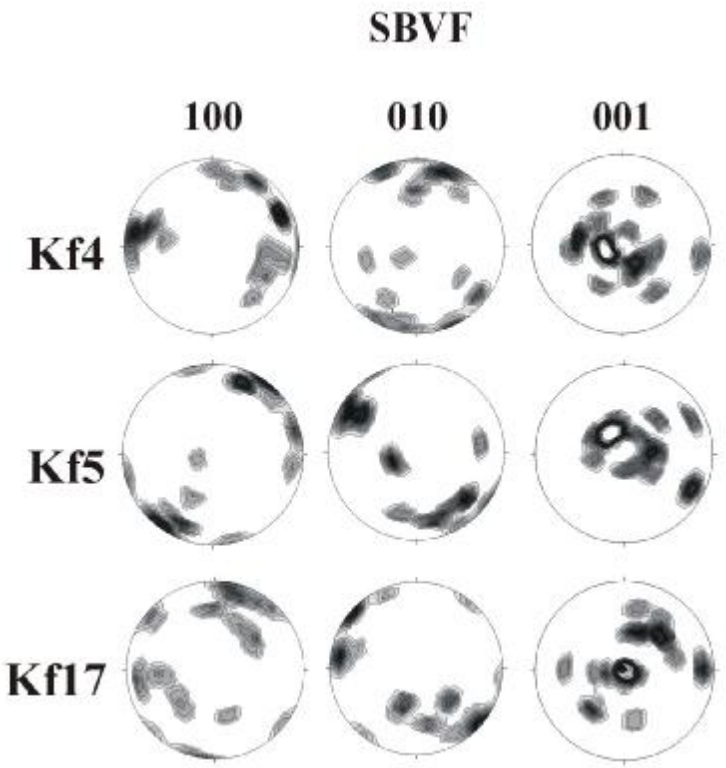

Figure V.2 Stereogram of olivine orientations in three selected xenoliths from the SBVF. 30 grains were analyzed in each sample. Note that orientation patterns could not be fixed to external reference frame (macroscopic lineation, foliation). Lower hemisphere, equal area projection. Data contoured at 1, 2, 3,… times uniform distribution.

LHPVF

Olivine orientations were analyzed in 11 selected xenoliths from the LHPVF (Table V.1). Olivine crystals in all of the samples measured display moderate to marked LPO. The orientation patterns can be subdivided into three main subgroups. In the first subgroup (Ghh02, GC03-10, GC03-14) the orientation of the crystal axes display a single point maximum with high multiples of uniform distribution – [100] at small angles to the lineation in the foliation plane; [001] at high angles to the lineation in the foliation plane and [010] at high angles to the foliation plane and the lineation (Figure V.3). Recrystallized grains and porphyroclasts (although latter are rarely preserved) show similar orientations. Such olivine orientation patterns are attributed to the activation of a single slip system (010)[100] during intracrystalline deformation (e.g., Carter and Avé Lallemant, 1970). The second subgroup consists of 7 xenoliths (GC03-06, GC03-12, GC03-12b, Gr06, Gr08, Gko-02, Ghh02b). In all of the samples [100] displays a maximum at the lineation in the foliation plane, whereas

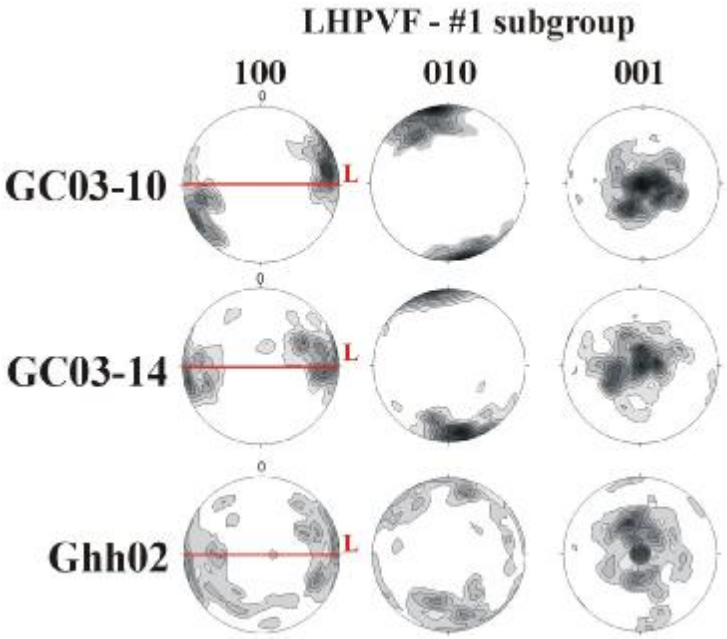

Figure V.3 Stereograms of olivine orientations in three selected xenoliths from the LHPVF. 100 grains were analyzed in each sample. Subgroup with high maximums in all axes orientations. Note marked point maximum in the distribution of mineral axes. Horizontal red line denotes orientation of macroscopic foliation or compositional banding; L – macroscopic lineation. Lower hemisphere, equal area projection. Data contoured at 1, 2, 3,… times uniform distribution.

partial girdles are observed both in the foliation plane (Figure V.4) towards [001] and in some cases towards [010] at high angles to both the lineation and the foliation (Figure V.4). This results in intermediate multiples of uniform distribution at the maximums for [100]. The [001] displays a marked maximum in the foliation plane at high angles to the lineation but a strong girdle towards [100] in the foliation plane is clearly defined (Figure V.4ab). The [001] axes are characterized by high multiples of uniform distribution at the maximums. The [010] shows a point maximum with high multiples of uniform distribution at high angles to the lineation and the foliation plane (Figure V.4a). Although, a weak girdle towards [100] may also be observed (Figure V.4). The orientation of porphyroclasts does not differ significantly from that of recrystallized grains. Similar orientation patterns are quite rare from xenoliths and other mantle derived peridotites worldwide and indicate activation of multiple slip systems (see details later).

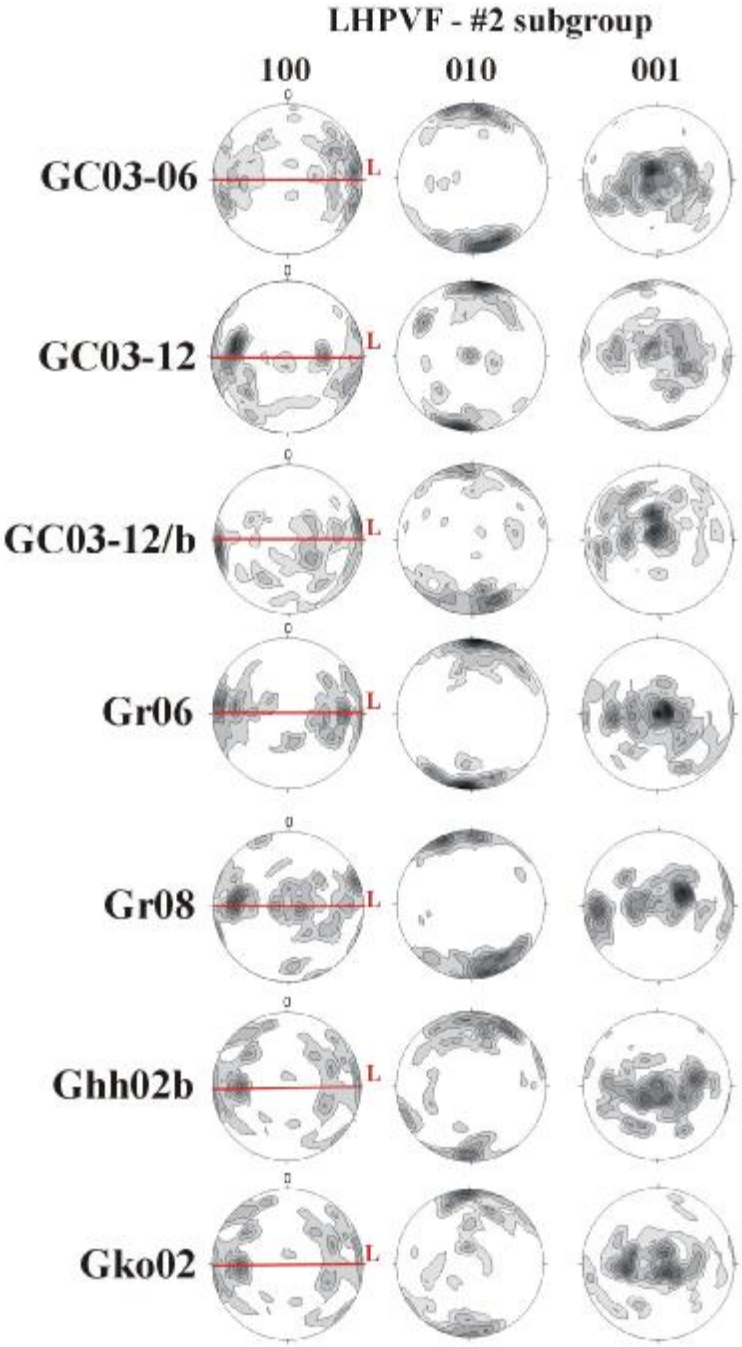

Figure V.4 Stereograms of olivine orientations in seven selected xenoliths from the LHPVF. 100 grains were analyzed in each sample. Subgroup with intermediate maximum of [100]-axes and high maximums for [010] and [001]. Note marked girdle of (100) and (001) in foliation plane. Red line denotes orientation of macroscopic foliation or compositional banding; L – macroscopic lineation. Lower hemisphere, equal area projection. Data contoured at 1, 2, 3,… times uniform distribution.

Olivine grains in one selected sample (GC03-05) from the LHPVF displays distinct fabric from those of the two groups. Olivine [100]-axes show a weak point maximum at the lineation in the foliation plane. The major difference between the orientation of the other groups and this sample is that besides the point maximum of [001] at high angles to the lineation in the foliation plane and the point maximum of [010] at high angles to the lineation and the foliation plane both axes show partial girdle to one-another (Figure V.5) and display intermediate maximums. The orientation of recrystallized grains is similar the orientation of the porphyroclasts. Such olivine fabrics are recognized as the activation of {0kl}[100] slip systems.

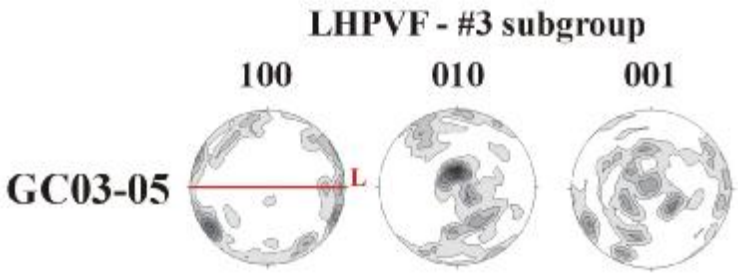

Figure V.5 Stereogram of olivine orientations in a selected xenolith (GC03-05) from the LHPVF. 100 grains were analyzed in each sample. Note marked girdle of (010) and (001) perpendicular to the foliation plane. Red line denotes orientation of macroscopic foliation or compositional banding; L – macroscopic lineation. Lower hemisphere, equal area projection. Data contoured at 1, 2, 3,… times uniform distribution.

BBHVF

Among the studied xenolith locations most of the samples (30) were selected from the BBHVF (Table V.1). Besides analyzing olivine grains, the orientation of orthopyroxenes was also analyzed in some of the samples. Despite the large number of samples analyzed, only three main orientation subgroups can be distinguished. Olivine orientation in the three subgroups is similar to that observed in the LHPVF samples: 1) all crystal axes display one point maximum with high multiples of uniform distributions– [100] subparallel to the lineation in the foliation plane, [001] perpendicular to the lineation in the foliation plane and [010] at high angles to both lineation and foliation (Figure V.6). Six samples (Szbd-1, Szbd-13, Szbp-15, Szb03-02, Szb6, Szgk99-04) among the studied 30 belong to this subgroup. Recrystallized grains display similar orientations to that of porphyroclasts. Such olivine orientation patterns are attributed to the activation of a single slip system (010)[100] during intracrystalline deformation (e.g., Carter and Avé Lallemant, 1970).

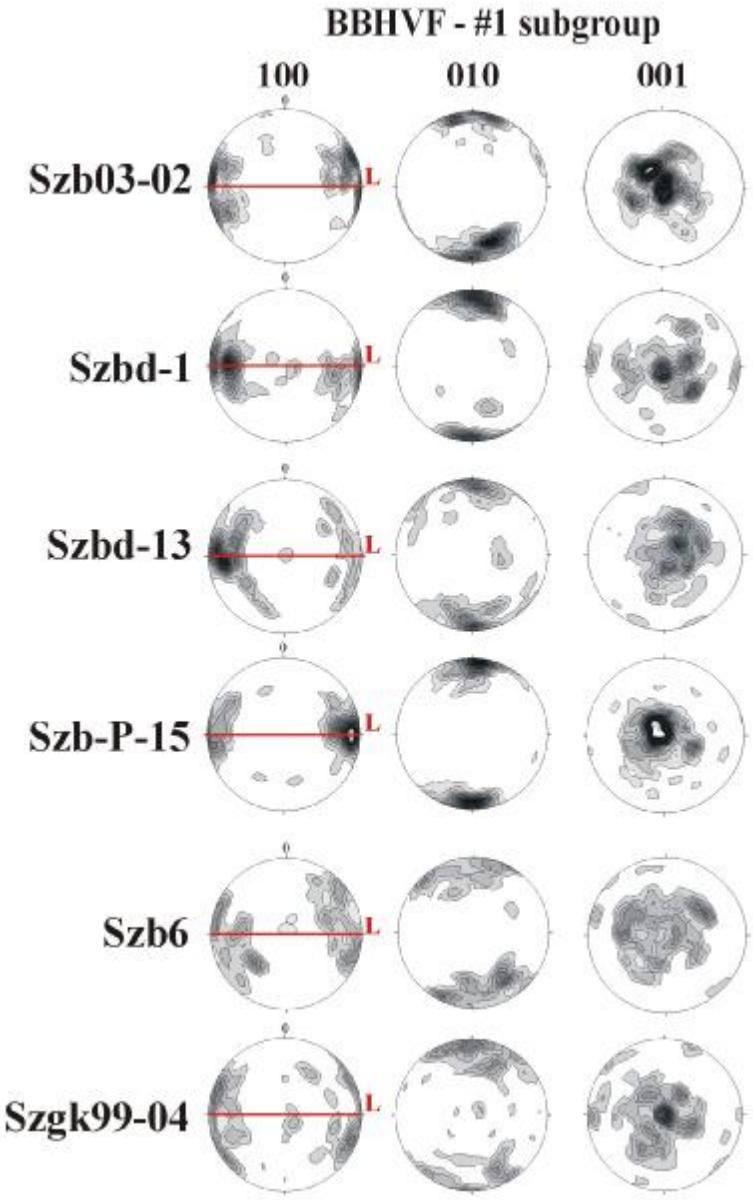

Figure V.6 Stereograms of olivine orientations in six selected xenoliths from the BBHVF. 100 grains were analyzed in each sample, except for Szb03-02 (72 grains). Note marked point maximum in the distribution of mineral axes. All axes orientations are characterized by high maximum distributions. Red line denotes orientation of macroscopic foliation or compositional banding; L – macroscopic lineation. Lower hemisphere, equal area projection. Data contoured at 1, 2, 3,… times uniform distribution.

Subgroup 2) consists of ten samples (Szba1, Szbd-15, Szgk03-01, Szba4, Szb28, Szb34, Szbd-4, Szbd-6, Szbd-11 and Szbd 14) that show a point maximum of [010] perpendicular to the lineation and the foliation plane with high multiples of uniform distribution. The other two axes [100] and [001] besides showing a point maximum

subparallel to the lineation in the foliation plane and perpendicular to the lineation in the foliation plane, respectively, also display partial girdles in the foliation plane (Figure V.7). This results in intermediate values for [100] and high values for [001] of multiples of uniform distribution at the maximums. In some cases (Szba1, Szbd-15 and Szgk03-01; studied in detail by Hidas et al. in prep.) this partial girdle of [100] and [001] is so pronounced that they plot as a continuous subhorizontal band in the stereograms (Figure V.8) Similar orientation patterns are quite rare and indicate activation of multiple slip systems (see details later). One of the samples (Szba4) does not display partial girdles of [100] and [001] but instead they display two maximums: both [100] and [001] subparallel to the lineation in the foliation plane and perpendicular to the lineation in the foliation plane (Figure V.7). The orientation pattern observed in this subgroup is characteristic for the activation of (010)[001] slip system (e.g., Tommasi et al., 2000). In case of the porphyroclastic samples recrystallized olivine grains show similar orientations to that of the porphyroclasts.

Those xenoliths that display a point maximum of [100] subparallel to the lineation in the foliation plane, and a marked partial girdle of [001] towards [010] where classified into group 3). Nevertheless, both [001] and [010] display a strong point maximum at high angles to the lineation in the foliation plane and at high angles to both lineation and foliation, respectively (Figure V.9). It is worth to note that only one clear example of this fabric type was found (Szbd-9). In all the other samples the orientation distribution of olivine axes is scattered and shows similarities with all above mentioned groups (Figure V.10). Such olivine fabrics are recognized as the activation of {0kl}[100] slip systems.

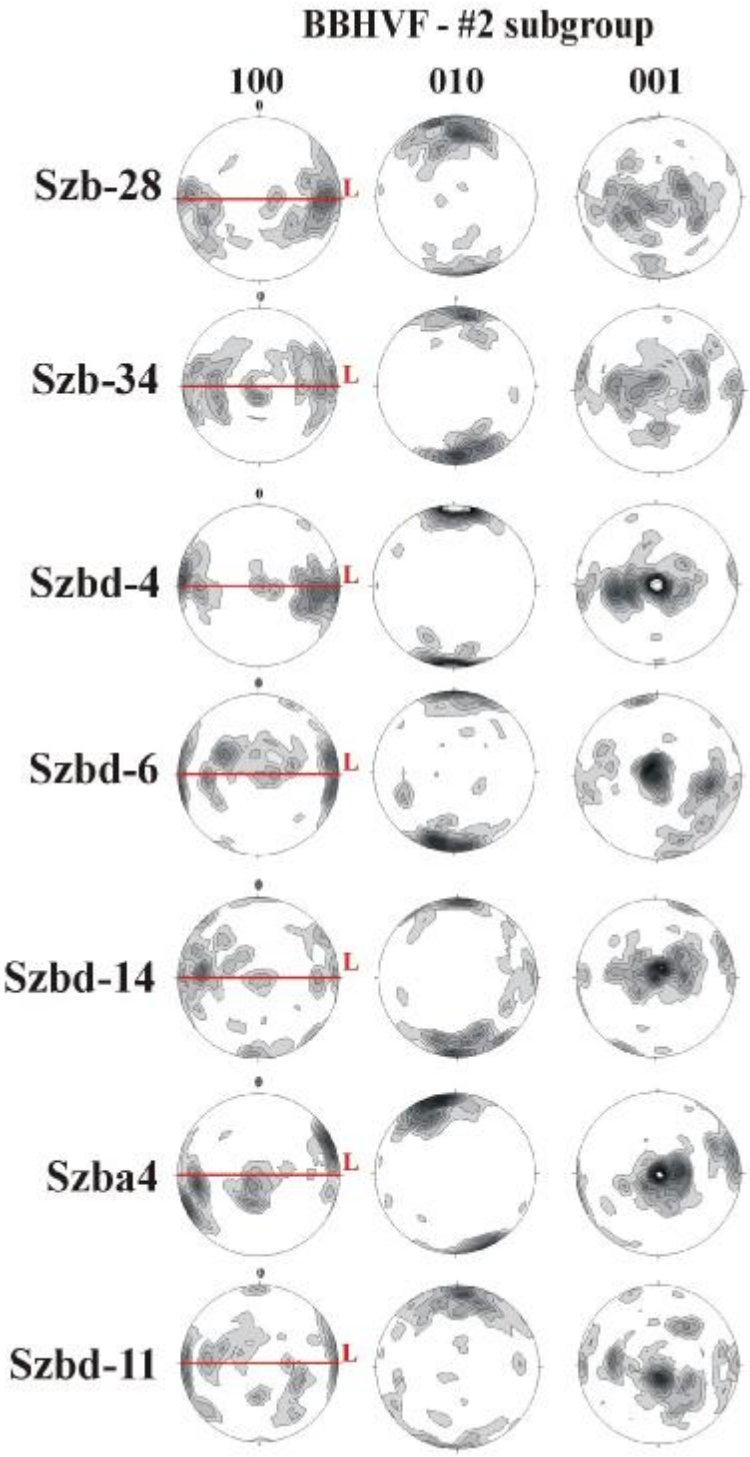

Figure V.7 Stereograms of olivine orientations in seven selected xenoliths from the BBHVF. 100 grains were analyzed in each sample. Note girdle or double maximum of (100) and (001) in the foliation plane. [100]-axes display intermediate maximums, whereas [010] and [001]- axes have high maximums. Red line denotes orientation of macroscopic foliation or compositional banding; L – macroscopic lineation. Lower hemisphere, equal area projection. Data contoured at 1, 2, 3,… times uniform distribution.

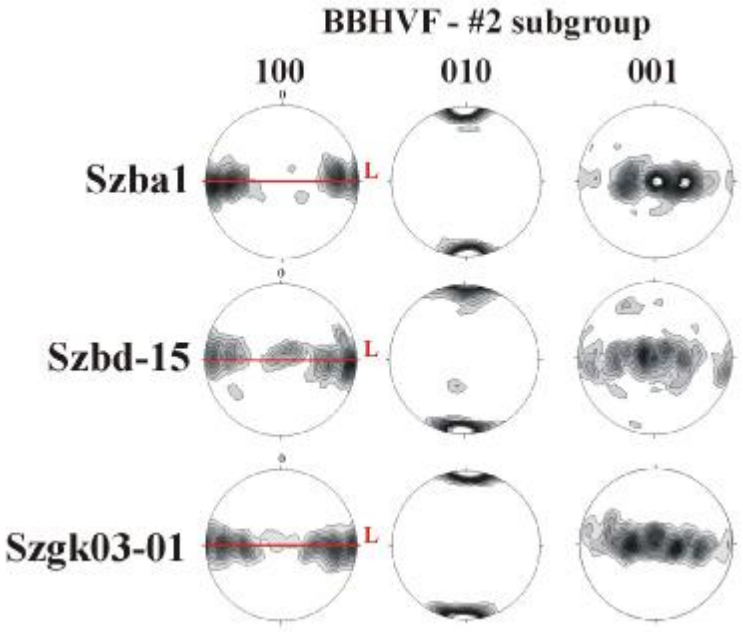

Figure V.8 Stereograms of olivine orientations in the three xenoliths studied in details by Hidas et al. (submitted) from the BBHVF. 100 grains were analyzed in each sample. Note girdle of (100) and (001) in the foliation plane. [100]-axes display intermediate maximums, whereas [010] and [001]- axes have high maximums. Red line denotes orientation of macroscopic foliation or compositional banding; L – macroscopic lineation. Lower hemisphere, equal area projection. Data contoured at 1, 2, 3,… times uniform distribution.

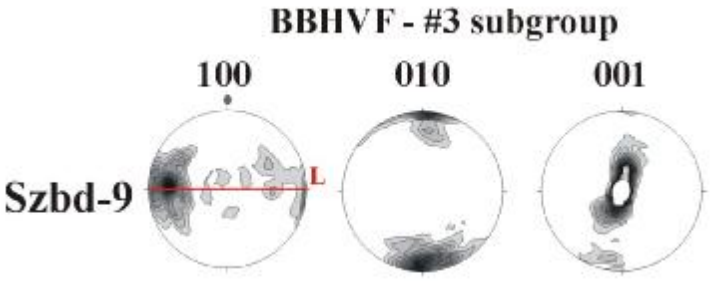

Figure V.9 Stereograms of olivine orientations in xenolith Szbd-9 from the BBHVF. 100 grains were analyzed. Note girdle of (010) and (001) perpendicular to the foliation plane. Red line denotes orientation of macroscopic foliation or compositional banding. Macroscopic lineation at 90°; L – macroscopic lineation. Data contoured at 1, 2, 3,… times uniform distribution.

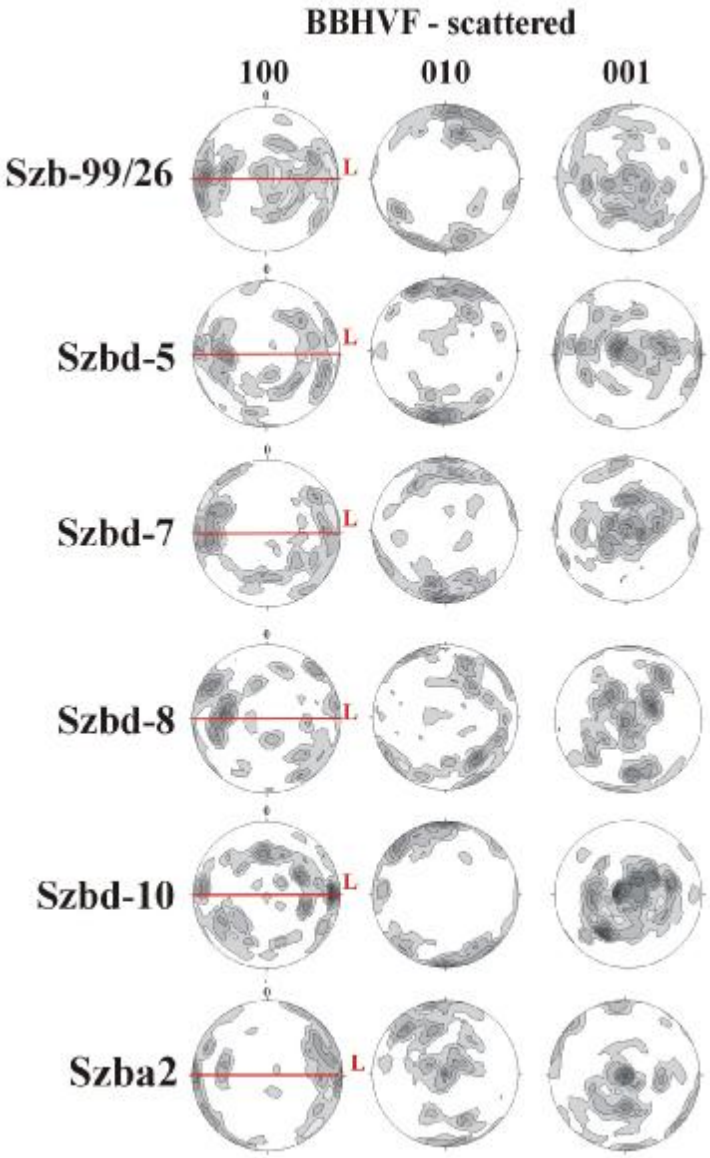

Continued on the next page

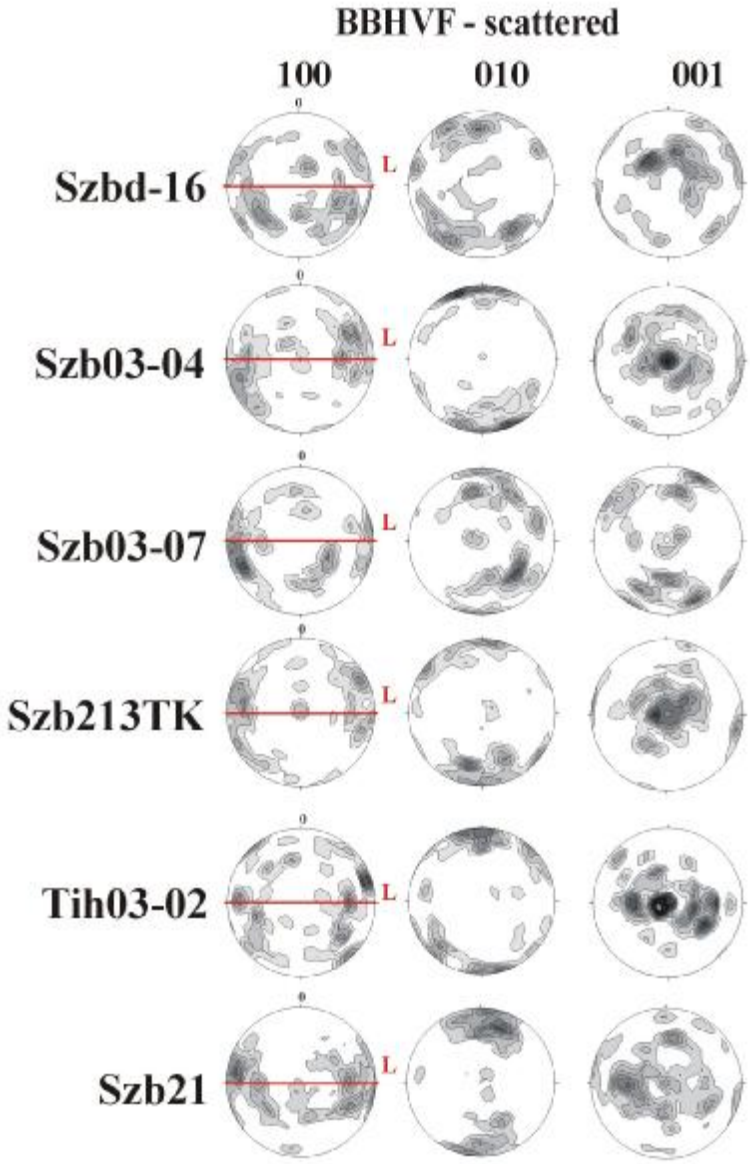

Figure V.10 Stereograms of olivine orientations in 12 studied xenoliths from the BBHVF. 100 grains were analyzed in each sample with the exception of Tih03-02 (50 grains). Note the weak LPO olivines. All axes develop low distribution maximums. Red line denotes orientation of macroscopic foliation or compositional banding; L – macroscopic lineation. Lower hemisphere, equal area projection. Data contoured at 1, 2, 3,… times uniform distribution.

NGVF

Orientation of olivine grains of five xenoliths (NBN27, NBN30, NBN52, NFL15 and NMS032) has been studied (Table V.1). In all five studied samples olivine crystals display moderately strong lattice preferred orientation. In the selected samples [100] axes of olivine show a maximum subparallel to the lineation in the foliation plane although a partial girdle from the lineation toward high angles to the lineation and the foliation towards (010) is observed (Figure V.11). Moreover in NMS032 [100] axes display a girdle in the foliation plane. The distribution of [001] display a single maximum in all samples except for sample NMS032 where [001] displays girdle in the foliation plane (Figure V.11).

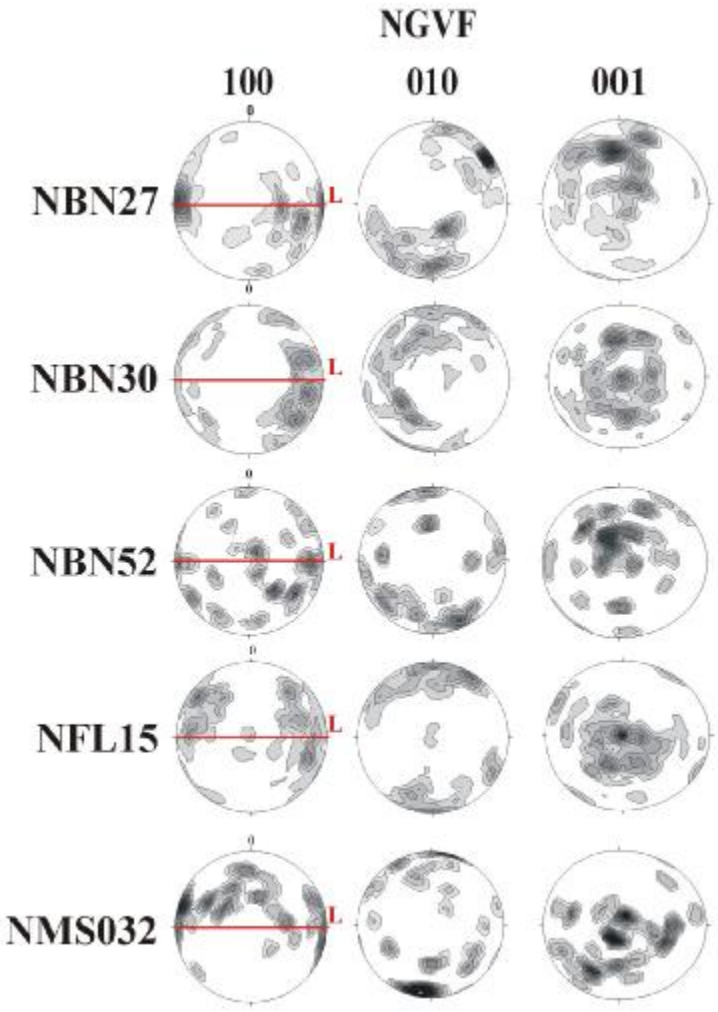

Figure V.11 Stereograms of olivine orientations in five xenoliths from the NGVF. 100 grains were analyzed in each sample, except for NMS032 (35 grains). Red line denotes orientation of macroscopic foliation or compositional banding; L – macroscopic lineation. Lower hemisphere, equal area projection. Data contoured at 1, 2, 3,… times uniform distribution.

The [010] axes in all cases display scattered distribution with a weak maximum perpendicular to the foliation and the lineation, but strong girdles towards the lineation [100] clearly occur. No obvious differences between the orientation of rare olivine porphyroclasts and the recrystallized grains have been observed. It should be stated, however that in NMS032 only 35 grains were analyzed. Such olivine orientation patterns are attributed to the activation of a single slip system (010)[100] during intracrystalline deformation (e.g., Carter and Avé Lallemant, 1970) in case of ((NBN27, NBN30, NBN52, NFL15) and the activation of multiple slip systems is suggested for NMS032.

The orientation of olivine grains in the dunite band around a Cr-diopside vein of NBN 27 was also studied. Orientations do not differ significantly from that of olivines from the wall rock peridotite.

ETBVF

All the six xenoliths selected for detailed study were analyzed with the U-stage (Table V.1). In the porphyroclastic xenoliths (LGR09 and BG15) orientation of both porphyroclasts and recrystallized grains was analyzed. The [100] of olivines (both porphyroclasts and neoblasts) displays a single maximum at the lineation in the foliation plane (Figure V.12). The [010] axes cluster at high angles to the lineation and also to the foliation plane (almost perpendicular). Finally [001] shows a marked maximum at high angles to the lineation in the foliation plane. A partial girdle of [100] towards [010] and also one of [010] towards [100]. Note, however, that due to geometric reasons only about 30 olivine orientations could be measured in sample BG15, nevertheless olivines still display remarkably strong LPO (Figure V.12).

In contrary to the porphyroclastic xenoliths, in those samples with mylonitic textures only the orientation of (porphyro-) clasts could be analyzed with the U-stage. The orientation of the recrystallized grains, due to their ultrafine grain size could not be resolved with U-stage. To obtain orientation data from the recrystallized grains the application of more advanced techniques (e.g., EBSD) would be required. Only a small number of olivine clasts (~15 in each sample) could be analyzed in the mylonites, because of the U-stage geometry and the relatively low number of olivine porphyroclasts. Nevertheless, considerable LPO of the clasts can still be resolved (Figure V.13). The orientations of crystal axes generally display multiple maximums, however one dominant direction is always present. It is remarkable that the dominant [100] maximum is always oblique to the macroscopic lineation (Figure V.13). The [010] axes (the dominant ones) plot at high angles to the lineation and the

foliation, however, the obliquity n this case is still remarkable. In most of the cases [001] plots at high angles to the lineation in the foliation plane. However, in one case (LGR03-04) the [001] axes form a remarkable partial girdle towards [010].

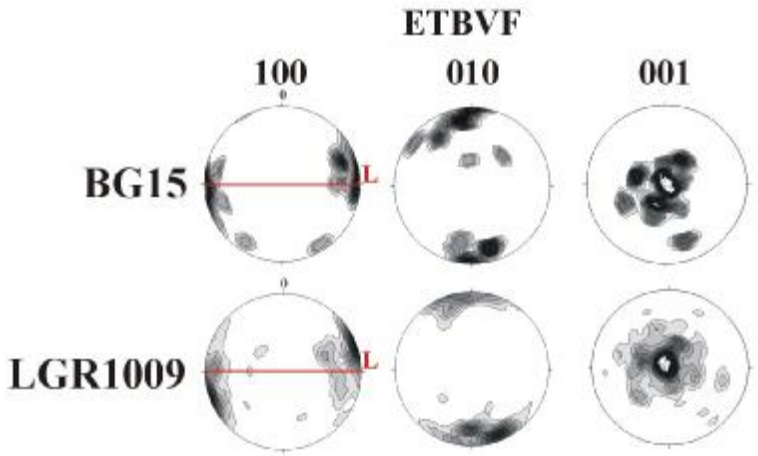

Figure V.12 Stereograms of olivine orientations in two xenoliths from the ETBVF. 35 grains and 100 grains were analyzed in lherzolite BG15 and LGR09, respectively. Note point maximum in the orientation of mineral axes. Red line denotes orientation of macroscopic foliation or compositional banding; L – macroscopic lineation. Lower hemisphere, equal area projection. Data contoured at 1, 2, 3,… times uniform distribution.

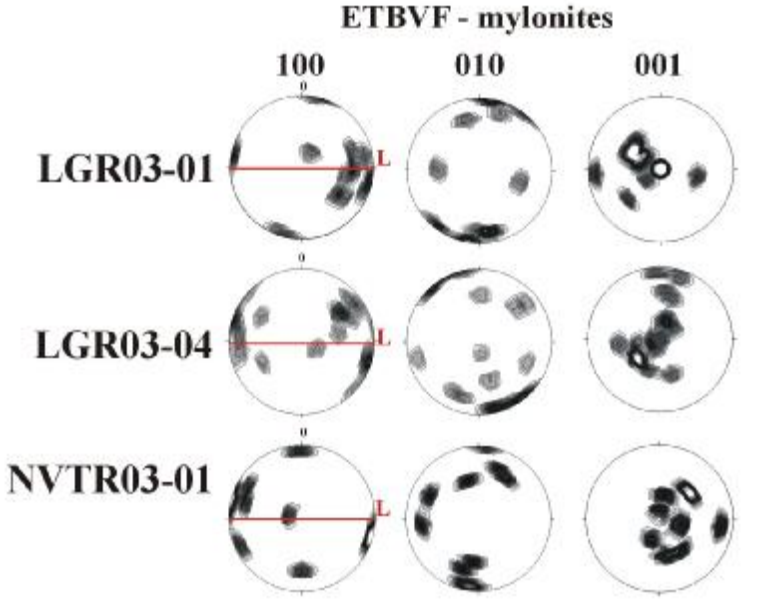

Figure V.13 Stereograms of olivine orientations in three mylonite xenoliths from the ETBVF. 15 grains were analyzed in each sample. Note weak point maximum in the orientation of mineral axes probably due to very low number of grains analyzed (see text for details). Red line denotes orientation of macroscopic foliation or compositional banding; L – macroscopic lineation. Lower hemisphere, equal area projection. Data contoured at 1, 2, 3,… times uniform distribution.

One protogranular sample (BG18) was also studied in details. Although the number of analyzed grains, due to coarse grain size and U-stage geometry, was low (35) the orientations are pronounced. Olivine orientations in the specific sample show similar distribution to those in the other ones from the ETBVF (Figure V.14).

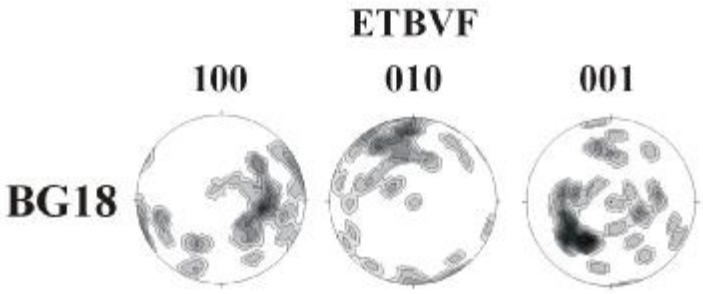

Figure V.14 Stereogram of olivine orientations in xenolith BG18 from the ETBVF. 35 grains were analyzed in the sample. Note point maximum in the orientation of mineral axes. Note that orientation patterns could not be fixed to external reference frame (macroscopic lineation, foliation). Lower hemisphere, equal area projection. Data contoured at 1, 2, 3,… times uniform distribution.

V.2 Misorientation analysis

The distribution of rotation angles (misorientations) and the orientation of the rotation axes provide information on the type of recrystallization and deformation mechanism operating in the mantle section represented by the studied xenoliths. Subgrain rotation (dynamic) recrystallization leads to the breakdown of large porphyroclasts into smaller grains, which largely preserve the crystallographic orientation of the original grain. This process is reflected in the small rotation angle between the lattices of the porphyroclasts and recrystallized grains. In the misorientation analysis crystallographic relations between neighboring olivine grains is established. The crystallographic relation between two neighboring grains, expressed in terms of rotation axis (common in the two grains) rotation was calculated (Randle, 1992; Fliervoet et al., 1999)*.

Angular relations between adjacent grains are expressed with respect to each other irrespective of any external reference frame (e.g., foliation, lineation, compositional banding). Generally the method is applied to clarify geometric relations between adjacent porphyroclasts and recrystallized grains (e.g., Dijkstra, 2002), i.e., subgrain–parental grain relation. Its geometric meaning is not clear in equigranular samples where considerable degree of static recrystallization and grain growth took place. In fact, adjacent grains now observed were not necessarily neighbors (no subgrain–parental grain relation) during or at the

final stages of deformation. Nevertheless, misorientation analysis in some special tabular equigranular xenoliths (Hidas et al., in prep.) was indeed preformed (see later in this chapter).

Eight representative samples from the LHPVF (GC03-06, GC03-10) and the BBHVF (Szba1, Szb28, Szbd-9, Szbd-13, Szbd-15 and Szgk03-01) were selected for misorientation analysis. The selected samples from the two region represent the main deformed fabric and textural types occurring in the xenolith locations. In the misorientation analysis crystallographic relations between neighboring olivine grains is established. The crystallographic relation between two neighboring grains, expressed in terms of rotation axis (common in the two grains) rotation was calculated (Randle, 1992; Fliervoet et al., 1999).

---

*Misorientation analysis mathematical methodology (Randle, 1992; Faul and Fitzgerald, 1999)

Misorientation between adjacent grains is expressed in terms of rotation axis-angle pairs, where the rotation axis is defined as a mutual direction that has the same (Miller) indices in both grains. One of the grains is taken as the fixed reference frame, though rotation required to bring crystallographic axes into coinsidence with the axes of the reference grains defines the misorientation angle.

Step 1) The orthonormal set of normalized crystal directions (in case of U-stage measurements crystal axes are automatically normalized) is transposed onto an external reference frame. Rotation matrix ($\mathbf{R_{total}}$) rotation required to transpose the pattern matrix onto the fixed external frame is determined. The transposition requires 3 subsequent rotations $\mathbf{R_z}$ then $\mathbf{R_y}$ and finally $\mathbf{R_x}$ ($\mathbf{R_{total}}=\mathbf{R_z}\mathbf{R_y}\mathbf{R_x}$) that are the rotations around the axes of the fixed reference frame.

$$R_z=\begin{pmatrix}\cos g & -\sin g & 0\\ \sin g & \cos g & 0\\ 0 & 0 & 1\end{pmatrix}\quad Ry=\begin{pmatrix}\cos b & 0 & \sin b\\ 0 & 1 & 0\\ -\sin b & 0 & \cos b\end{pmatrix}\quad Rx=\begin{pmatrix}1 & 0 & 0\\ 0 & \cos a & -\sin a\\ 0 & \sin a & \cos a\end{pmatrix}$$

where α, β and γ are the rotation angles required to transpose the normalized mineral axes onto the external reference frame. $\mathbf{R_{total}}$ is essentially the orientation matrix (**O**) of the grains in case of U-stage measurements.

Step 2) When the orientation matrix of two adjacent grains is determined the misorientation (**M**) matrix describing rotation of one subgrain onto the other is produced:

$$M = O_1^{-1}O_2$$

M describes the misorientation in the external reference co-ordinates. Rotation axis and angle can now be calculated:

Rotation axis V[uvw]: $u=M_{32}-M_{23}$ $v=M_{13}-M_{31}$ $w=M_{21}-M_{12}$

Misorientation angle (Θ) $\cos\Theta=\dfrac{M_{11}+M_{22}+M_{33}-1}{2}$

The resulting orientation of the rotation axis is common in both grains.

Step 3) Because olivine is orthorhombic, each grain can be indexed in four equivalent ways resulting in 16 axis-angle pairs. The axis-angle pairs are multiplied by the symmetry matrices

$$\begin{pmatrix}1 & 0 & 0\\ 0 & 1 & 0\\ 0 & 0 & 1\end{pmatrix}\quad\begin{pmatrix}1 & 0 & 0\\ 0 & -1 & 0\\ 0 & 0 & -1\end{pmatrix}\quad\begin{pmatrix}-1 & 0 & 0\\ 0 & 1 & 0\\ 0 & 0 & -1\end{pmatrix}\quad\begin{pmatrix}-1 & 0 & 0\\ 0 & -1 & 0\\ 0 & 0 & 1\end{pmatrix}$$

the rotation axis-angle pair with the smallest misorientation angle is selected

Step 4) Finally, rotation axis is multiplied by the **L** matrix ($\mathbf{VL^{-1}}$) containing lattice constants of forsteritic olivines to normalize axes back to the orthorhombic coordinate system:

$$\mathbf{L^{-1}}=\begin{pmatrix}4.767 & 0 & 0\\ 0 & 10.239 & 0\\ 0 & 0 & 6.003\end{pmatrix}$$

Misorientation distribution of all studied samples display significantly large number of small misorientations with respect to random distribution. It means that more grains have small misorientations (>60 degrees) with respect to their neighbors than would be expected from the fabric (stereograms).

Rotation axes are represented in crystal co-ordinate system. These plots are often referred to in the literature as inverse pole figures (e.g., Mercier and Nicolas, 1975). Those misorientation axes were plotted that significantly exceeded random distribution. Although, it should be noted that the error in the measurements of the orientation of olivine crystals by universal stage is ~5^{o}. The error in the orientation of rotation axis can be much larger (up to tens of degrees) especially in the case of small rotation angles (Fliervoet at al., 1999; Dijkstra et al., 2002).

LHPVF

Stereographic projection of olivine crystal axes orientation distribution of the two selected samples (GC03-06 and GC03-10) already suggests that markedly different deformation occurred within these two studied xenoliths. Nevertheless, the high abundance of low angle misorientation of adjacent subgrains with respect to random distribution (Figure V.15,16) suggests that subgrain rotation recrystallization was the dominant recrystallization process occurring in the mantle sections represented by the two mantle fragments.

GC03-06

Misorientation angle distribution in the sample (Figure V.15a) shows that grain boundaries with small misorientations are significantly more frequent in two angle ranges (10-30^{o} and 50-60^{o}), than expected from the olivine axis orientation (Figure V.3). This indicates that subgrain rotation has been an important process in the development of the observed microstructure. The rotation axes of low rotation angle (10-30^{o}) grain boundaries have a preferred orientation close to the olivine [b]-axis extending toward the [a]-axis (Figure V.15b). This type of distribution is indicative of slip systems (001)[100], (100)[001] slip and twist walls in (010) (Zhang et al., 2000; De Kloe, 2001). The distribution of rotation axes of somewhat higher rotation angles (50-60^{o}) is more scattered (Figure V.15c). A weak preference close to [a]-, [b]- and [c]-axes is observed.

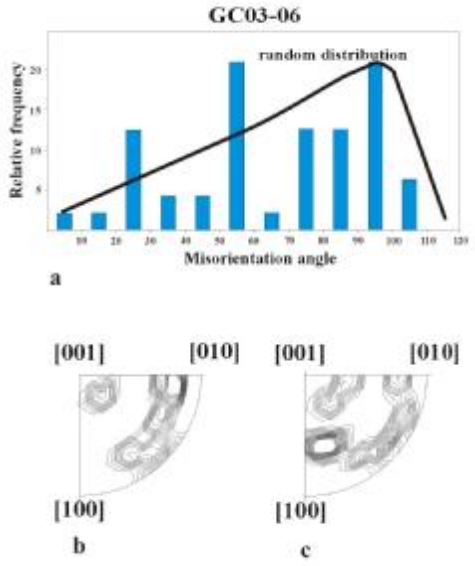

Figure V.15 Misorientation analysis of xenolith GC03-06 from the LHPVF. The distribution of misorientation angles between neighboring olivine grains is compared to misorientation angles between olivine grains of hypothetical sample with random orientation distribution. a) significantly more misorientations occur between 20 and 30° and between 50 and 60° than expected from the fabric. Inverse pole figures for olivines with rotation axes of grain pairs with b) 10-30° and c) 50-60° misorientations. For methodology see Randle (1992), Fliervoet et al. (1999).

GC03-10

The distribution of misorientation angles in the sample shows marked deviancy from random distribution at 10-40° and 50-70° angle ranges (Figure V.16a). Low rotation angles show a preferred distribution close to the [c]-axis indicating the important contribution of (010)[100] slip system. Rotation axes of the high misorientation angle grain boundaries show a weak preference close to the [b]-axis, however most of them plot further away from low-symmetry orientations (Figure V.16bc), which is imposed by symmetry related restrictions (Fliervoet et al., 1999).

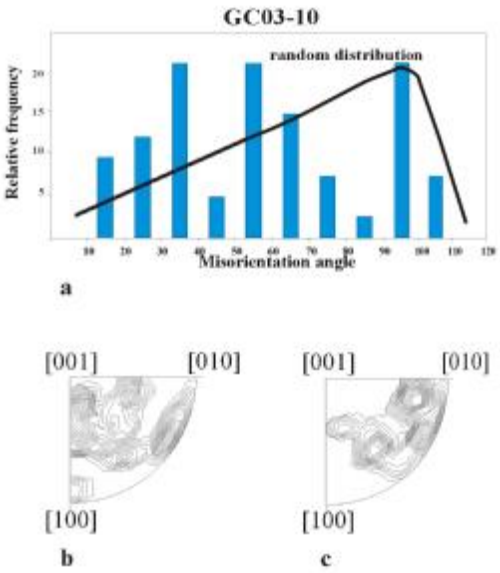

Figure V.16 Misorientation analysis of xenolith GC03-10 from the LHPVF. The distribution of misorientation angles between neighboring olivine grains is compared to misorientation angles between olivine grains of hypothetical sample with random orientation distribution. a) significantly more misorientations occur between 10 and 40° and between 50 and 70° than expected from the fabric. Inverse pole figures for olivines with rotation axes of grain pairs with b) 10-40° and c) 50-70° misorientations. For methodology see Randle (1992), Fliervoet et al. (1999).

BBHVF

Six samples from the BBHVF have been selected form misorientation analysis. Three of these xenoliths (Szba1, Szbd-15 and Szgk03-01) are very similar tabular equigranular lherzolites studied in details by Hidas et al, (submitted). These three samples show analogous olivine and orthopyroxene preferred orientations. The other three xenoliths (Szb28, Szbd-9 and Szbd-13) represent the main orientation patterns occurring in the BBHVF.

Szba1, Szbd-15, Szgk03-01

Misorientations and rotation axes, as expected for these three xenoliths are quite similar. Significantly higher ratio of low angle grain boundaries occur than random distribution and indicate that subgrain rotation was the dominant process in the formation of these textural types (Figure V.17). Rotation axes of low angle misorientation grain boundaries (10-30^{o}) show a preferred orientation close to the [c]-axis and [b]-axis reflecting that the slip systems active during deformation were the (010)[100] and (100)[001] slip and twist walls in (010), respectively (Zhang et al., 2000; De Kloe, 2001; Figure V.17b). The rotation axes of higher angle grain boundaries (not present in Szgk03-01) show a preference close to the [b]-axis tending towards the [a]-axis and plotting further away from low symmetry orientations (Figure V.17c).

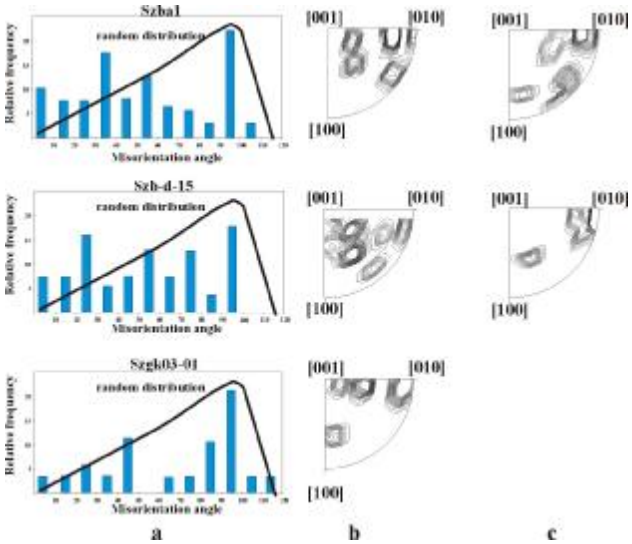

Figure V.17 Misorientation analysis of the three selected xenoliths (Szba1, Szbd-15 and Szgk03-01) from the BBHVF. The distribution of misorientation angles between neighboring olivine grains is compared to misorientation angles between olivine grains of hypothetical sample with random orientation distribution. a) significantly more misorientations occur between 0 and 40^{o} and between 50 and 60^{o} for Szba1; 0 and 30^{o} and between 50 and 60^{o} for Szbd-15; and 0 and 30 and between 40 and 50 for Szgk03-01 than expected from the fabrics. Inverse pole figures for olivines with rotation axes of grain pairs with b) small and c) high misorientations, respectively. For methodology see Randle (1992), Fliervoet et al. (1999).

Szb28

The distribution of misorientations in the samples shows marked deviancy from the random distribution at low angles (10-30°; Figure V.18a). However, it is likely that subgrain rotation was the main microfabric forming process. Rotation angles of the low misorientation angle grain boundaries cluster at [c]- and [b]-axes indicating slip systems (010)[100] and (100)[001] (Zhang et al., 2000) and twist walls in (010) (De Kloe, 2001) to be active during deformation (Figure V.18b).

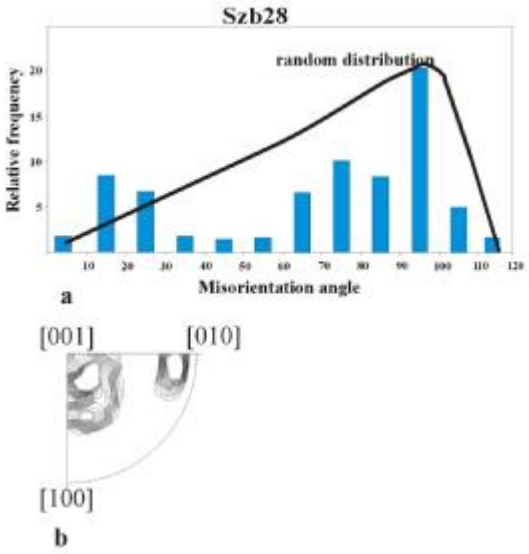

Figure V.18 Misorientation analysis of xenolith Szb28 from the BBHVF. The distribution of misorientation angles between neighboring olivine grains is compared to misorientation angles between olivine grains of hypothetical sample with random orientation distribution. a) significantly more misorientations occur between 10 and 30° than expected from the fabric. Inverse pole figures for olivines with rotation axes of grain pairs with b) 10-30° misorientations. For methodology see Randle (1992), Fliervoet et al. (1999).

Szbd-9

The sample has unique olivine axis orientations with respect to the other xenoliths studied. Significantly higher ratio of low (10-30°) and medium (40-60°) misorientation angle grain boundaries are present with respect to random distribution (Figure V.19a). The low angel misorientation grain boundary axes show a preferred orientation close to [c]-axis tending towards [a]-axis and also a weak preference at [b]-axis (Figure V.19b) indicating the dominance of (010)[100] slip system. At higher angles remarkable difference to all other misorientation distribution is observed. Rotation axes tend to plot close to the [a]-axis (Figure V.19c). Rotations at ~60° around the [a]-axis of olivine are in accordance with a twinning system in olivine (~t Hart, 1978).

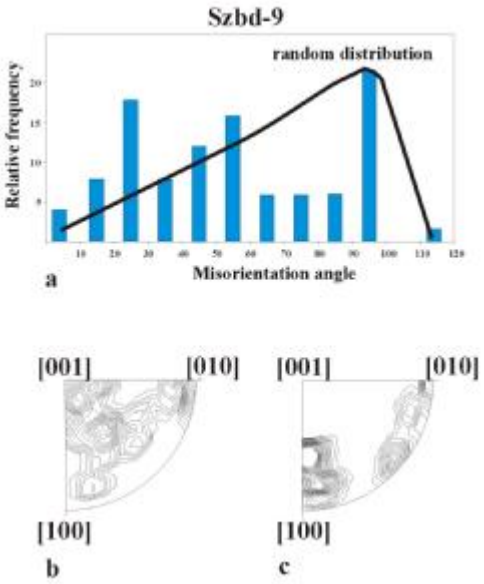

Figure V.19 Misorientation analysis of xenolith Szbd-9 from the BBHVF. The distribution of misorientation angles between neighboring olivine grains is compared to misorientation angles between olivine grains of hypothetical sample with random orientation distribution. a) significantly more misorientations occur between 10 and 30^{o} and between 40 and 60^{o} than expected from the fabric. Inverse pole figures for olivines with rotation axes of grain pairs with b) 10-30^{o} and c) 40-60^{o} misorientations. For methodology see Randle (1992), Fliervoet et al. (1999).

Szbd-13

The protogranular sample with strong point maximum distribution of olivine crystal axes was also studied. The abundance of low angle grain boundary rotation axes between 10-30 degrees is significantly higher than that of random distribution (Figure V.20a). Rotation axes in the inverse pole Figures plot close to the [c] axis suggesting the predominance of (010)[100] slip system during intracrystalline slip (Figure V.20b).

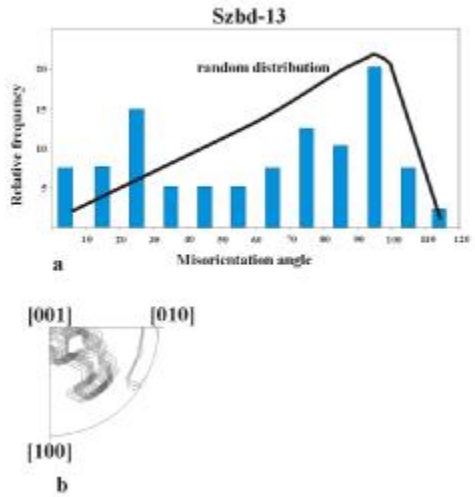

Figure V.20 Misorientation analysis of xenolith Szbd-13 from the BBHVF. The distribution of misorientation angles between neighboring olivine grains is compared to misorientation angles between olivine grains of hypothetical sample with random orientation distribution. a) significantly more misorientations occur between 10 and 30^{o} than expected from the fabric. Inverse pole figures for olivines with rotation axes of grain pairs with b) 10-30^{o} misorientations. For methodology see Randle (1992), Fliervoet et al. (1999).

VI. Major, trace element and isotope geochemistry of the sub-continental lithospheric mantle of the Intra-Carpathian Basin System

Geochemical feature is among the best and most intensively studied characters of the subcontinental lithospheric mantle in the Intra-Carpathian Basin System. The main aim of this chapter is to position the xenoliths, which were analyzed in detail with respect to their textural and microstructural characteristics, in geochemical dimensions of the framework of upper mantle peridotite suite of the Intra-Carpathian Basin System. Most of the data used derives from a huge set of high quality major, trace element and isotopic data from scientific literature of the last decade. Additional geochemical analyses were only carried out on those mantle xenoliths with specific textural types where no chemical data were available.

Major element composition of constituent mineral phases was carried out, using Microprobe analyses were carried out using a JEOL Superprobe JXA-8600 WDS at the Department of Earth Sciences, University of Florence and University of Bristol For the analyses in Florence, an accelerating voltage of 15 kV was used, with a 10 nA sample current and a beam diameter of 5 microns was used. Counting times were 20 seconds for each element. In both laboratories natural and synthetic standards were employed for the analyses, and the method of Bence & Albee (1968) was applied for correction.

However, it should be emphasized that geochemical characterization of the lithospheric mantle beneath the Intra-Carpathian Basin System is not the goal of the thesis.

Upper mantle xenoliths originating from the sub-continental lithospheric mantle were extensively analyzed in the region. Chemical analyses were preformed on bulk rock major and trace elements. In situ measurements on constituent phases on major and trace elements were also carried out on hundreds of samples. In some cases, mostly in more recent studies, radiogenic and stable isotopes were also analyzed. The sufficient number of chemical analyses carried out in the region elucidates the nature and sometimes also the relative timing of various geochemical processes.

VI.1 Major element composition of peridotite xenoliths in the Intra-Carpathian Basin System

Major element composition of the mantle xenoliths is the best studied and understood geochemical character of upper mantle peridotite fragments worldwide. Concentration and abundance of major elements comprising the 99 percent of the rocks studied are essentially an important and considerable factor for the mantle fragments analyzed. The depletion of one specific group of major elements, often referred to as basaltic major elements (Al, Ti, Na, Ca, Fe, (Si)) is primarily attributed to partial melting events within the subcontinental lithospheric mantle during its evolution. This first order variance in the geochemical characteristics of the upper mantle xenoliths was recognized already early in the history of xenolith studies (e.g., Frey and Green, 1974; Frey and Prinz, 1978). This variance is also observed in massifs and ophiolites and thus should be treated as a general character of the subcontinental lithospheric mantle. Moreover, changing rock textures, indicative of the deformation state of the mantle section they have been derived from (see Chapter III. for details), shows significant relations to major element composition of the studied mantle rocks (e.g., Downes et al., 1992).

Bulk rock major element composition, the first available geochemical analysis in the history of xenolith studies, is a powerful and widely used tool in geochemical characterization of the mantle derived rocks. The method clearly indicates negative correlation of all basaltic major elements with Mg compatible element in mantle rocks (e.g., Downes et al., 2001). Whereas, in case of Cr, also a very compatible element in mantle rocks, a clear positive correlation is observed (e.g., Frey and Green, 1974; Frey and Prinz, 1978).

Bulk rock major element compositions however, are influenced by two factors: 1) the modal composition of the mantle rocks, i.e., the abundance and volume ratio of constituent mineral phases, and 2) the chemical compositions of the constituent mineral phases. The volume ratio of the constituent phases is easily considered through basic petrographic analysis of the mantle rocks. Major elements in constituent mineral phases, because of their different crystal structures behave distinctly in mantle processes. The potential of the analysis of single mineral phases of mantle rocks, thus enables a finer resolution of the physico-chemical processes occurring in the mantle.

Olivines, the dominant mineral phases in peridotitic mantle rocks are Fe-Mg silicates. Despite their relative barrenness in chemical components, olivine Mg-numbers ($Mg^{2+}/Mg^{2+}+Fe^{2+}$) are sensitive and widely used tools to characterize the depleted nature of the mantle section they were derived from (e.g., Zheng et al., 2001). Systematic analysis of large number of olivines from different xenolith locations clearly showed systematic difference between Achean lithosphere (characterized by olivine mg-numbers >94) and Phanerozoic lithosphere with olivine mg-numbers generally lower than 91 (Zheng et al., 2001). Olivine mg-numbers are also indicative of deformation state of the mantle (e.g., Szabó et al., 1995a). In accordance with bulk rock major element composition, undeformed (protogranular) xenoliths exhibit lower mg-numbers compared to those with deformed ones.

Major element compositions of orthopyroxenes, that in most of the cases appear in considerable volume ratios in the mantle derived peridotites world wide, generally follow the composition variance of olivines, although orthopyroxenes generally show slightly higher mg-numbers than co-existing olivines (e.g., Szabó et al., 1995a). Orthopyroxenes are mostly Fe-Mg silicates, their Al_2O_3 CaO and Na_2O concentrations may be considerable and sometimes applied in their geochemical characterization. Basaltic elements within the orthopyroxenes generally display negative correlation with MgO. Orthopyroxenes from the undeformed samples are characterized by higher abundance of basaltic element together with lower MgO concentrations, whereas more deformed and recrystallized xenoliths contain orthopyroxenes depleted in Al_2O_3, CaO and Na_2O and relatively enriched in MgO (e.g., Szabó et al., 1995a).

Clinopyroxenes, common constituents in peridotitic upper mantle, are among the most sensitive minerals to indicate various physico-chemical processes occurring in the mantle. Their crystal structures can accommodate several elements that cannot be incorporated into other common mantle phases. Thereby both major and trace element composition of clinopyroxene provide valuable information on the processes that affected the mantle portion represented by the xenolith studied. High chromium content in clinopyroxenes of mantle derived xenoliths is one of the major characteristic features of rocks derived from the lherzolitic xenolith suite, addressed as type-I (Frey and Green, 1974; Frey and Prinz, 1978) and often referred to as Cr-diopside suite. These xenoliths are characterized by relatively high Cr clinopyroxenes (~1 wt%) and are believed to represent a mantle portion, which is the residuum after

partial melting event(s) and the extraction of basaltic melts (Frey and Green, 1974; Frey and Prinz, 1978). Basaltic major elements in the clinopyroxenes (e.g., Ti, Al, Na, (Fe)) generally show negative correlation, whereas Cr frequently displays marked positive correlation with Mg. Clinopyroxene compositions, similarly to olivine and orthopyroxene also act sensitively to mantle deformation.

The only common non-silicates in the shallow subcontinental lithospheric mantle are spinels. Besides being the main Al container, spinels in the Cr-diopside suite may also exhibit high Cr-contents. In fact cr-numbers (Cr/Cr+Al) of spinels are effective indicators of partial melting and depletion. Forsterite (Fo) content of olivines and cr-number of spinels was used by Arai (1994) to construct the olivine-spinel mantle array (OSMA), which is believed to represent the path for partial melting and the extraction of basaltic melts in the mantle. Cr-number of spinels with Na_2O concentration of clinopyroxenes is also capable of demonstrating partial melting. Moreover, Xu et al. (1998, 2003) suggests that such plots may also able to show metasomatic effects occurring as additional Na_2O in clinopyroxenes, with respect to cr-number in spinels.

Detailed description of major element composition of peridotitic mantle xenoliths will be given based on xenolith locations, mostly relying on high quality data from the literature. Where necessary, own measurements on xenoliths analyzed texturally and microstructurally in detail were also preformed and will be treated similarly data from the literature. Tables (Table VI.1-5) summarizing geochemical compositions of analyzed phases only contain own analyses. Other data shown will only be referred. The order of xenolith locations is similar to that given in earlier chapters.

SBVF

Xenoliths studied from the SBVF are dominantly protogranular (virtually undeformed) spinel lherzolites with the rare occurrence porphyroclastic lherzolites and protogranular-porphyroclastic harzburgites, probably of secondary origin. Bulk major element composition of the rocks, studied by Vaselli et al (1996) reflects a rather undepleted character with relatively low MgO (average ~39-40 wt%) and relatively high concentration of basaltic major elements. In contrary, harzburgites

display depletion in basaltic major elements with respect to MgO (~45 wt%) (Vaselli et al., 1996).

As expected similar characteristics are observed when turning to individual mineral compositions. The mg-numbers of olivines analyzed by Kurat et al. (1991), Downes et al. (1992), Vaselli et al. (1996) and Embey-Isztin et al. (2001) are in the range of 0.85-0.92, with an average for the spinel lherzolites around 0.88 and somewhat higher (~0.91) for the harzburgites. Due to low abundance of more deformed textural types, confirmed by high number of detailed studies (Kurat et al., 1991; Downes et al., 1992; Vaselli et al., 1996, Embey Isztin et al., 2001), no apparent correlation between xenolith texture and olivine mg-number could be demonstrated.

Samples selected for detailed microstructural analysis (Kf4, Kf5 and Kpfs17 analyzed earlier by Vaselli et al. (1996)) and one sample analyzed earlier (Kf3; Falus et al., 2000), all spinel lherzolites, exhibit mg-numbers (Table VI.1) similar to the earlier studied lherzolites from the xenolith location (Kapfenstein). Similar results arise for orthopyroxene compositions (Table VI.1).

Clinopyroxenes, from the SBVF, the most sensitive mineral-phase for physico-chemical changes, also reflect quite monotonous character as demonstrated by earlier geochemical studies (e.g., Embey-Isztin et al., 2001). Most of the compositions plot to high-Na high-Al field of the Na vs. Al plot (Figure VI.1). Cation number of Na in the clinopyroxene is around or generally slightly above 0.1, whereas Al is in the range of 0.25-0.30 (Figure VI.1; Table VI.1).

Composition of clinopyroxenes in the selected lherzolites falls within the same high-Na high-Al field as the majority of clinopyroxene compositions earlier analyzed, although clinopyroxenes in Kf3 display somewhat lower Na content (cat no.~0.04; Table VI.1). Some harzburgites define a trend towards the low-Na low-Al part of the Na vs. Al diagram with cation numbers of Na and Al down to 0.05 and 0.1, respectively (Figure VI.1).

Geochemical studies demonstrated that spinel compositions (namely cr-number) cover a wide range from very low (0.04) to unusually high (0.59) values in the xenoliths. Lherzolites, as expected are generally characterized by low cr-numbers (max. 0.26), whereas high cr-numbers are characteristic for the harzburgites (Table VI.1). Although some of the harzburgites reflect low cr-numbers (0.10-0.12). Cr-numbers of the selected lherzolites (Kf3, Kf4, Kf5, Kf17) lies within the composition range defined by the other lherzolites from the xenolith location (Table VI.1).

Sample	Kf4				Kf5				Kf3				Kf17			
Texture	pr/po				po				pr				pr			
Mineral	cpx	opx	sp	ol	cpx	opx	sp	ol	cpx	opx	sp	ol	cpx	opx	sp	ol
Element																
SiO_2	50.8	54.4	0.12	40.6	52.2	54.3	0.16	41.2	51.7	55.0	0.02	41.1	51.4	55.0	0.06	41.2
TiO_2	0.57	0.16	0.1	na.	0.3	0.11	0.13	na.	0.65	0.15	0.11	bd.	0.70	0.17	0.16	bd.
Al_2O_3	7.61	5.13	56.7	na.	6.45	4.41	49.7	na.	7.33	4.99	59.1	0.03	7.33	4.81	59.2	0.02
Cr_2O_3	0.76	0.32	8.74	0.02	0.99	0.52	16.1	0.03	0.70	0.32	8.01	0.01	0.67	0.23	7.99	0.01
FeO	3.78	6.55	4.58	10.4	2.9	5.71	4.31	8.96	3.13	6.66	11.1	10.3	3.03	6.68	11.3	10.5
MnO	0.12	0.11	8.28	0.16	0.1	0.14	8.19	0.1	0.09	0.14	0.07	0.16	0.11	0.12	0.06	0.17
NiO	0.02	0.05	0.1	0.32	0.04	0.1	0.2	0.27	na.	na.	0.37	0.34	na.	na.	0.38	0.38
MgO	15.0	32.2	0.4	49.3	15.2	33.19	0.28	50.3	15.1	32.7	21.2	49.2	14.9	32.9	21.3	49.2
CaO	19.0	0.9	21.3	na.	19.4	0.82	20.5	na.	19.9	0.75	na.	0.06	19.7	0.70	na.	0.06
Na_2O	1.65	na.	na.	0.08	1.68	na.	na.	0.08	0.58	0.04	na.	na.	1.75	0.11	na.	na.
Total	99.34	99.80	100.30	100.91	99.30	99.32	99.60	100.94	99.08	100.79	99.92	101.25	99.60	100.83	100.46	101.52
Al-cn.	0.33				0.28				0.32				0.32			
Na-cn.	0.12				0.12				0.04				0.12			
mg# Mg/Mg+Fe	0.88	0.90	0.82	0.89	0.90	0.91	0.82	0.91	0.90	0.90	0.77	0.90	0.90	0.90	0.77	0.89
cr# Cr/Cr+Al			0.09				0.18				0.08				0.08	
Fo%				88.88				90.50				89.02				88.78

Table VI.1 Composition of constituent phases of mantle xenoliths from the SBVF in wt%. Al-ca – cation number of Al; Na-ca cation number of Na; mg# - mg number; cr# - cr-number; Fo% - forsterite mol%; cpx – clinopyroxene; opx – orthopyroxene; sp – spinel; ol – olivine; na. – not analyzed; bd. – below detection limit. Data from Vaselli et al. (1996); Falus et al. (2000).

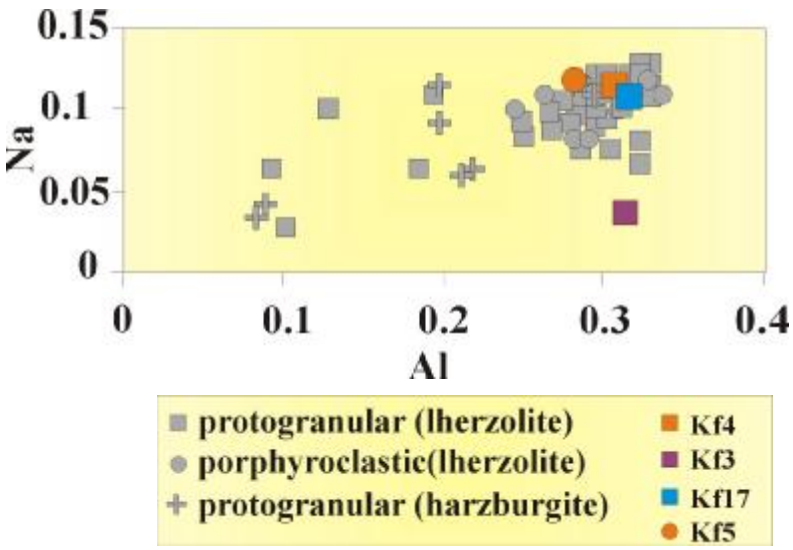

Figure VI.1 Al vs. Na (cation number normalized to 6 oxygens) diagram of clinopyroxenes in mantle peridotites from the SBVF with respect to xenolith texture. Samples, selected for detailed microstructural analysis are highlighted. Data from Kurat et al. (1991), Vaselli et al. (1996), Falus et al. (2000), Embey-Isztin et al. (2001).

Olivine and spinel compositions of earlier studied xenoliths and those selected for detailed analysis were plotted on OSMA-diagram (Figure VI.2). All compositions fall within the array suggested by Arai (1994) to represent mantle depletion processes. Most of the xenolith compositions, including those selected for detailed study fall below or close to the line indicating 20% partial melting as already shown by Szabó et al. (1995a). Some of the harzburgites, however, fall above the 20% partial melting line (Figure VI.2).

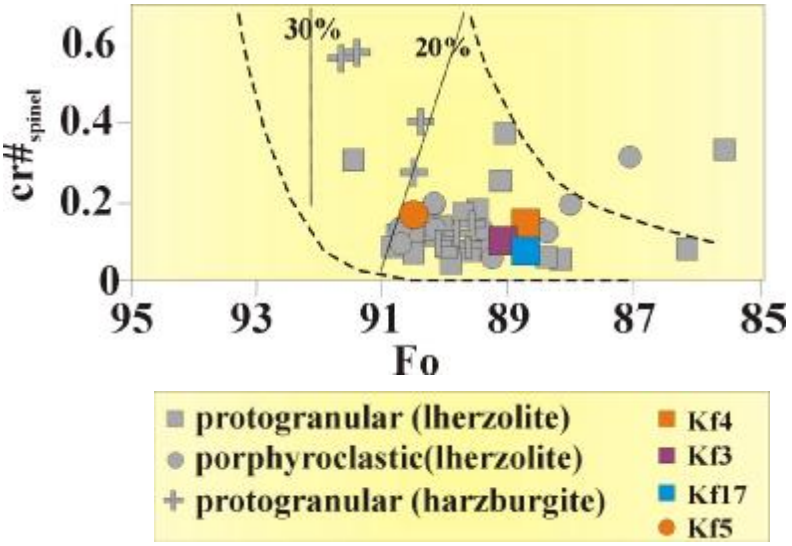

Figure VI.2 Fo vs. $cr\#_{spinel}$ diagram (OSMA; Arai, 1994) of mantle peridotites from the SBVF with respect to xenolith texture. Note reverse order of Fo. Samples, selected for detailed microstructural analysis are highlighted. Also, dotted lines indicate the extent of partial melting (20%-30%). Data from Kurat et al. (1991), Vaselli et al. (1996), Falus et al. (2000), Embey-Isztin et al. (2001).

The diagram of spinel cr-number vs. Na_2O in clinopyroxene was first used by Xu et al. (1998, 2003) to demonstrate, whether a peridotite followed normal depletion or has experienced some kind of metasomatism. Plotting SBVF compositions (Figure VI.3) indicate that most of the peridotites from earlier geochemical studies, and most of those selected for detailed study follow the normal depletion trend of the plot (Figure VI.3), and only rare deviancy towards higher Na_2O contents is observed. Samples falling off the normal depletion trend are mostly the harzburgites and rare porphyroclastic lherzolite xenoliths like sample Kf5 selected for detailed study (Figure VI.3).

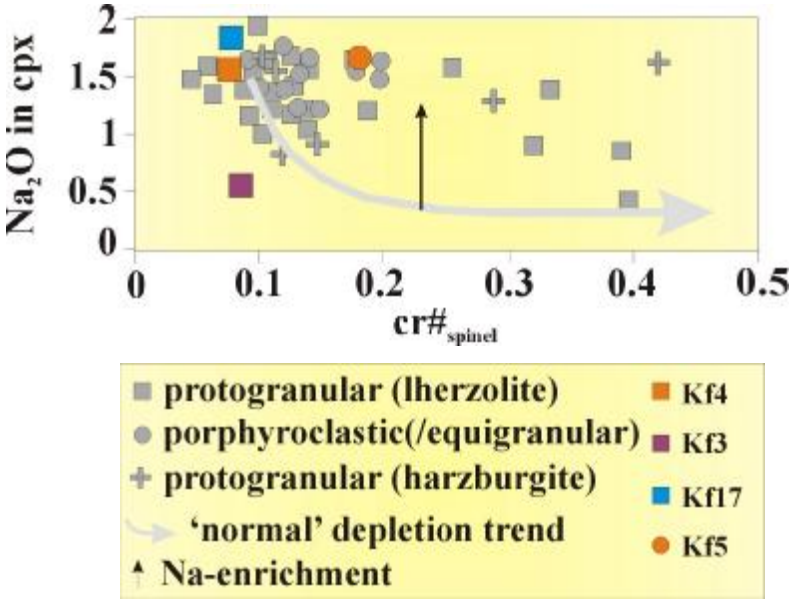

Figure VI.3 Na_2O (wt%) in clinopyroxene vs. $cr\#_{spinel}$ diagram (Xu et al., 2003) of mantle peridotites from the SBVF with respect to xenolith texture. Samples, selected for detailed microstructural analysis are highlighted. Area surrounded dashed line shows 'normal' depletion trend. Data from Kurat et al. (1991), Vaselli et al. (1996), Falus et al. (2000), Embey-Isztin et al. (2001).

LHPVF

Basalts rising from the deep mantle (e.g., Harangi, 2001) sampled xenoliths from the protogranular mantle only scarcely in the LHPVF. Although some were described by Kurat et al., (1991), their geochemical characteristics are poorly studied. In fact the most abundant textural type among mantle xenoliths is porphyroclastic, whereas equigranular and secondary recrystallized xenoliths are also found (e.g., Kurat et al., 1991; Szabó et al., 1995b).

Geochemical studies (Kurat et al., 1991; Downes et al., 1992; Szabó et al., 1995b; Embey-Isztin et al., 2001) showed that major element bulk composition of the xenoliths does not show remarkable variability. MgO is in the range of 38-45 wt% and shows a weak negative correlation with basaltic major elements.

Mineral chemistry of samples from the LHPVF as demonstrated by detailed geochemical analysis (e.g., Szabó et al., 1995b) considerably differs from that of the SBVF. Clinopyroxene compositions on the Al vs. Na plot (Figure VI.4, Table VI.2) clearly indicate a strong positive correlation. Porphyroclastic compositions plot to the

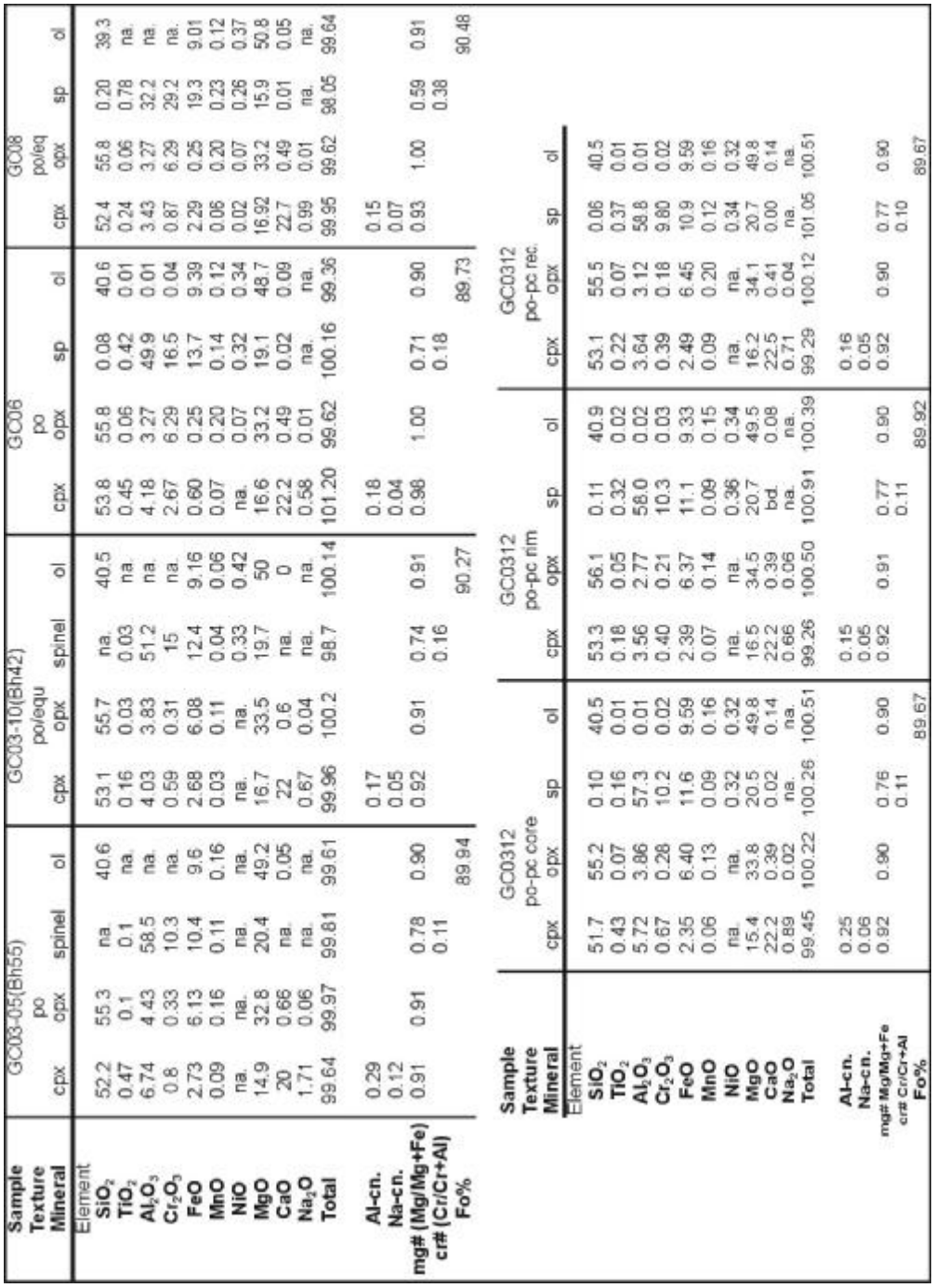

Sample	GC03-05(Bh55)				GC03-10(Bh42)				GC06				GC08			
Texture		po			po/equ				po				po/eq			
Mineral	cpx	opx	spinel	ol	cpx	opx	spinel	ol	cpx	opx	sp	ol	cpx	opx	sp	ol
Element																
SiO_2	52.2	55.3	na.	40.6	53.1	55.7	na.	40.5	53.8	55.8	0.08	40.6	52.4	55.8	0.20	39.3
TiO_2	0.47	0.1	0.1	na.	0.16	0.03	0.03	na.	0.45	0.06	0.42	0.01	0.24	0.06	0.78	na.
Al_2O_3	6.74	4.43	58.5	na.	4.03	3.83	51.2	na.	4.18	3.27	49.9	0.01	3.43	3.27	32.2	na.
Cr_2O_3	0.8	0.33	10.3	na.	0.59	0.31	15	na.	2.67	6.29	16.5	0.04	0.87	6.29	29.2	na.
FeO	2.73	6.13	10.4	9.6	2.68	6.08	12.4	9.16	0.60	0.25	13.7	9.39	2.29	0.25	19.3	9.01
MnO	0.09	0.16	0.11	0.16	0.03	0.11	0.04	0.06	0.07	0.20	0.14	0.12	0.06	0.20	0.23	0.12
NiO	na.	na.	na.	na.	na.	na.	0.33	0.42	na.	0.07	0.32	0.34	0.02	0.07	0.26	0.37
MgO	14.9	32.8	20.4	49.2	16.7	33.5	19.7	50	16.6	33.2	19.1	48.7	16.92	33.2	15.9	50.8
CaO	20	0.66	na.	0.05	22	0.6	na.	0	22.2	0.49	0.02	0.09	22.7	0.49	0.01	0.05
Na_2O	1.71	0.06	na.	na.	0.67	0.04	na.	na.	0.58	0.01	na.	na.	0.99	0.01	na.	na.
Total	99.64	99.97	99.81	99.61	99.96	100.2	98.7	100.14	101.20	99.62	100.16	99.36	99.95	99.62	98.05	99.64
Al-cn.	0.29				0.17				0.18				0.15			
Na-cn.	0.12				0.05				0.04				0.07			
mg# (Mg/Mg+Fe)	0.91	0.91	0.78	0.90	0.92	0.91	0.74	0.91	0.96	1.00	0.71	0.90	0.93	1.00	0.59	0.91
cr# (Cr/Cr+Al)			0.11				0.16				0.18				0.38	
Fo%				89.94				90.27				89.73				90.48

Sample	GC0312				GC0312				GC0312				GC0312			
Texture	po-pc core				po-pc rim								po-pc rec.			
Mineral	cpx	opx	sp	ol	cpx	opx	sp	ol	cpx	opx	sp	ol	cpx	opx	sp	ol
Element																
SiO_2	51.7	55.2	0.10	40.5	53.3	56.1	0.11	40.9					53.1	55.5	0.06	40.5
TiO_2	0.43	0.07	0.16	0.01	0.18	0.05	0.32	0.02					0.22	0.07	0.37	0.01
Al_2O_3	5.72	3.86	57.3	0.01	3.56	2.77	58.0	0.02					3.64	3.12	58.8	0.01
Cr_2O_3	0.67	0.28	10.2	0.02	0.40	0.21	10.3	0.03					0.39	0.18	9.80	0.02
FeO	2.35	6.40	11.6	9.59	2.39	6.37	11.1	9.33					2.49	6.45	10.9	9.59
MnO	0.06	0.13	0.09	0.16	0.07	0.14	0.09	0.15					0.09	0.20	0.12	0.16
NiO	na.	na.	0.32	0.32	na.	na.	0.36	0.34					na.	na.	0.34	0.32
MgO	15.4	33.8	20.5	49.8	16.5	34.5	20.7	49.5					16.2	34.1	20.7	49.8
CaO	22.2	0.39	0.02	0.14	22.2	0.39	bd.	0.08					22.5	0.41	0.00	0.14
Na_2O	0.89	0.02	na.	na.	0.66	0.06	na.	na.					0.71	0.04	na.	na.
Total	99.45	100.22	100.26	100.51	99.26	100.50	100.91	100.39					99.29	100.12	101.05	100.51
Al-cn.	0.25				0.15								0.16			
Na-cn.	0.06				0.05								0.05			
mg# Mg/Mg+Fe	0.92	0.90	0.76	0.90	0.92	0.91	0.77	0.90					0.92	0.90	0.77	0.90
cr# Cr/Cr+Al			0.11				0.11								0.10	
Fo%				89.67				89.92								89.67

Continued on next page

Sample	Gko07				Gko07				GC0306				GC0306			
Texture	po-pc core				po-pc rim				po-pc core				po-pc rim			
Mineral	cpx	opx	sp	ol	cpx	opx	sp	ol	cpx	opx	sp	ol	cpx	opx	sp	ol
Element																
SiO_2	51.6	55.9	0.03	40.4	51.8	56.1	bd.	40.2	50.7	54.6	0.02	40.1	51.4	56.2	bd.	39.7
TiO_2	0.22	bd.	0.16	bd.	0.34	0.04	0.06	bd.	0.59	0.13	0.04	bd.	0.34	0.05	0.04	0.01
Al_2O_3	6.24	2.55	25.3	bd.	4.79	2.67	30.0	bd.	6.54	4.58	57.4	bd.	4.94	3.19	58.0	0.02
Cr_2O_3	1.97	0.45	38.1	bd.	1.40	0.56	35.9	bd.	0.84	0.43	10.8	bd.	0.70	0.19	10.6	0.01
FeO	3.36	6.02	19.2	9.13	3.27	5.89	17.0	8.82	2.68	6.48	11.9	9.67	2.67	6.41	11.5	9.92
MnO	0.07	0.14	0.19	0.12	0.09	0.17	0.17	0.16	0.09	0.15	0.09	0.12	0.08	0.18	0.15	0.12
NiO	na.	na.	0.23	0.35	na.	na.	0.18	0.38	0.04	0.06	na.	0.29	0.04	0.09	0.40	0.41
MgO	15.9	33.7	15.1	49.8	17.3	33.7	16.0	49.8	15.0	33.3	19.8	49.1	15.8	33.7	20.5	49.4
CaO	19.2	0.82	0.02	0.09	19.2	0.91	bd.	0.11	21.7	0.46	bd.	0.02	22.1	0.50	bd.	0.12
Na_2O	1.23	0.08	na.	na.	0.88	0.03	na.	na.	0.95	0.06	na.	na.	0.99	0.02	na.	na.
Total	99.72	99.58	98.34	99.85	98.97	100.09	99.30	99.55	99.09	100.25	100.07	99.28	99.02	100.59	101.19	99.69
Al-cn.	0.27								0.28				0.21			
Na-cn.	0.09				0.21				0.07				0.07			
mg# Mg/Mg+Fe	0.89	0.91	0.58	0.91	0.06											
cr# Cr/Cr+Al			0.50		0.90	0.91	0.63	0.91	0.91	0.90	0.75	0.90	0.91	0.90	0.76	0.90
Fo%				90.16			0.45				0.11				0.11	
								90.36				89.66				89.27

Table VI.2 Composition of constituent phases of mantle xenoliths from the LHPVF in wt%. Al-ca – cation number of Al; Na-ca cation number of Na; mg# - mg number; cr# - cr-number; Fo% - forsterite mol%; cpx – clinopyroxene; opx – orthopyroxene; sp – spinel; ol – olivine; na. – not analyzed; bd. – below detection limit; pc – porphyroclast; rec. – recrystallized grains. Note porphyroclast core-rim-recrystallized grain relations. Some data from Szabó et al. (1995b).

high-Na and high-Al segment of the diagram (Figure VI.4) reaching typical values of 0.1-0.15 and 0.25-0.33 respectively, whereas secondary recrystallized xenoliths, which are in fact harzburgites have low Al (0.06) and extremely low Na content (>0.01). Equigranular samples fall in between these compositions.

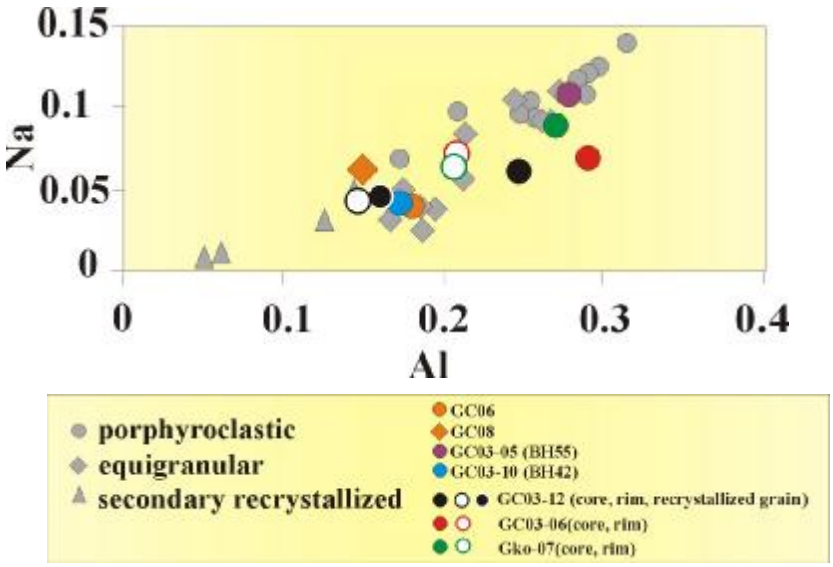

Figure VI.4 Al vs. Na (cation number normalized to 6 oxygens) diagram of clinopyroxenes in mantle peridotites from the LHPVF with respect to xenolith texture. Samples, selected for detailed microstructural analysis are highlighted. Note porphyroclast-recrystallized grain pairs connected with solid line. Some data from Downes et al. (1992), Szabó et al. (1995b), Embey-Isztin et al. (2001).

Those samples selected for detailed microstructural analysis (GC06, GC03-06, GC03-12 and GC03-10 petrographically similar to BH42 of Szabó et al., 1995b; GC03-05 similar to BH55 of Szabó et al., 1995b) do not deviate from the trend displayed by the other xenoliths (Figure V.4) and plot to intermediate Al and Na compositions. It is however remarkable that clinopyroxene porphyroclast (analyzed in GC03-06, GC03-12, Gko-07) all reflect depletion in Al towards the rims, whereas changes in Na content are not so significant (Figure VI.4; Table VI.2). Similar zoning in clinopyroxene porphyroclasts (regarding Al) was also described by Embey-Isztin et al., 2001).

Olivine mg-numbers (~Fo) are also variable ranging from 89 for some of the porphyroclastic xenoliths to values as high as 92 for the recrystallized samples as shown by early geochemical studies (e.g., Szabó et al., 1995b). Most of the samples

plot below or on the 20% partial melting line on the OSMA-diagram (Figure VI.5) however, one secondary recrystallized sample plots well above this line close to the 30% partial melting (Figure VI.5).

Selected samples all plot below or on the 20% partial melting line (Figure VI.5) together with the majority of samples analyzed earlier in the literature. Core-rim pairs of porphyroclast reflect negligible difference in both olivine mg-numbers and spinel cr-numbers (Figure VI.5; Table VI.2).

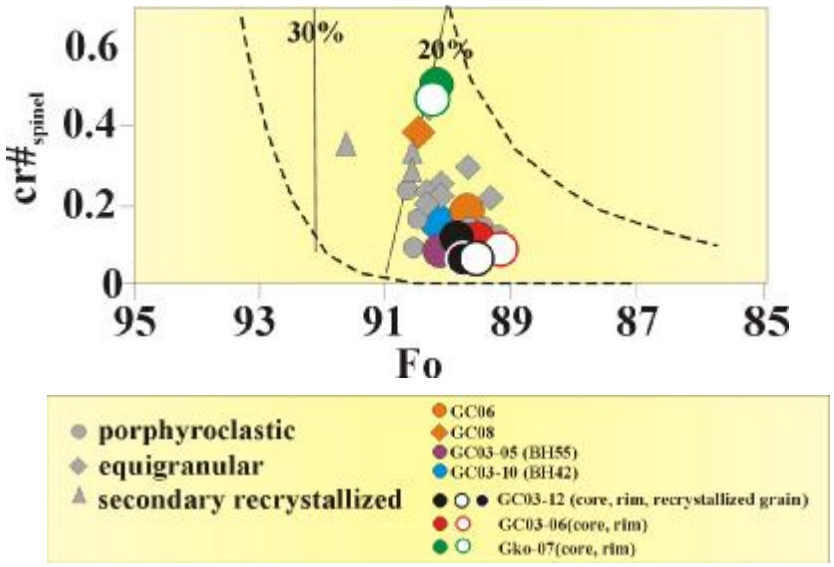

Figure VI.5 Fo vs. $cr\#_{spinel}$ diagram (OSMA; Arai, 1994) of mantle peridotites from the LHPVF with respect to xenolith texture. Note reverse order of Fo. Samples, selected for detailed microstructural analysis are highlighted. Note porphyroclast-recrystallized grain pairs. Also, dotted lines indicate the extent of partial melting (20%-30%). Data from Downes et al. (1992), Szabó et al. (1995b), Embey-Isztin et al. (2001).

Cr-number of spinels analyzed in earlier studies ranges between 0.1-0.5 also showing marked relation with xenolith textures. Two trends can be distinguished on the spinel cr-number vs. Na_2O in clinopyroxene diagram (Figure VI.6). One trend unambiguously follows the normal depletion trend (Xu et al., 1998, 2003), whereas the other trend almost plotting on a straight line indicates considerable Na_2O enrichment.

Samples GC06, GC03-06, GC03-12, GC03-05 and GC03-10 fall on the normal depletion trend, whereas GC08 and Gko07 show Na_2O enrichment (Figure

VI.6). Core-rim pairs display similar compositions except for Gko07, where significant decrease in both Na_2O in clinopyroxene and cr-number of spinel is observed towards the rims.

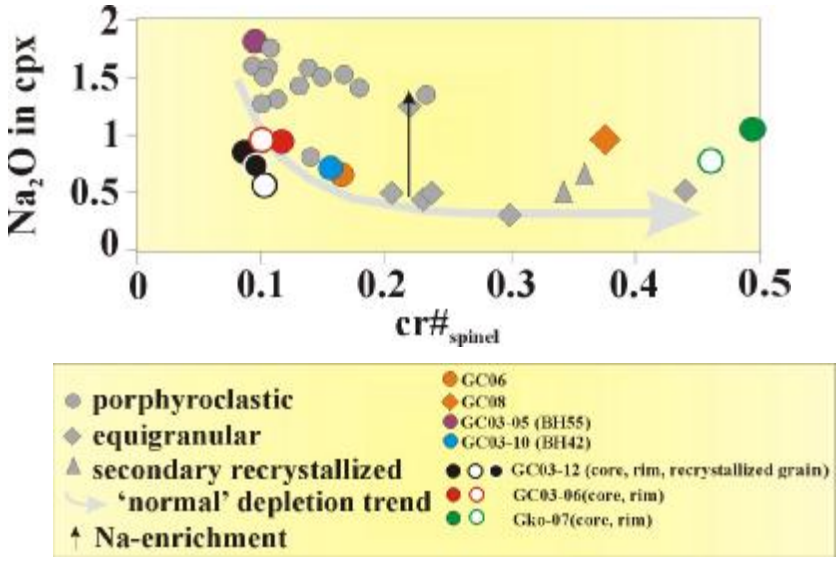

Figure VI.6 Na_2O (wt%) in clinopyroxene vs. $cr\#_{spinel}$ diagram (Xu et al., 2003) of mantle peridotites from the LHPVF with respect to xenolith texture. Samples, selected for detailed microstructural analysis are highlighted. Note porphyroclast-recrystallized grain pairs. Area surrounded dashed line shows 'normal' depletion trend. Data from Downes et al. (1992), Szabó et al. (1995b), Embey-Isztin et al. (2001).

BBHVF

Most of the xenoliths selected from detailed textural analysis originate from the BBHVF, the xenolith location which was probably the most extensively studied xenolith location among those of the Intra-Carpathian Basin System (e.g., Embey-Isztin et al., 1976; 1984, 1989, 2001; Downes et al., 1992; Bali et al., 2001). The xenolith location provides a large variety of xenolith textural types covering a large field of geochemical compositions.

Major element bulk compositions of xenoliths analyzed in earlier geochemical studies (e.g., Embey-Isztin et al., 1976; 1984, 1989, 2001; Downes et al., 1992; Bali et al., 2001), similarly to other xenolith locations display MgO contents between 38-46 wt%, and negative correlation with basaltic major elements.

Mineral compositions of the mantle-derived xenoliths cover a large field of the analyzed interval. Clinopyroxene compositions show a continuous trend from the undepleted high Al (0.35) and Na (0.13) contents (Figure VI.7), related to protogranular and porphyroclastic xenoliths to very depleted Al and Na compositions (0.07 and 0.02, respectively; Figure VI.7).

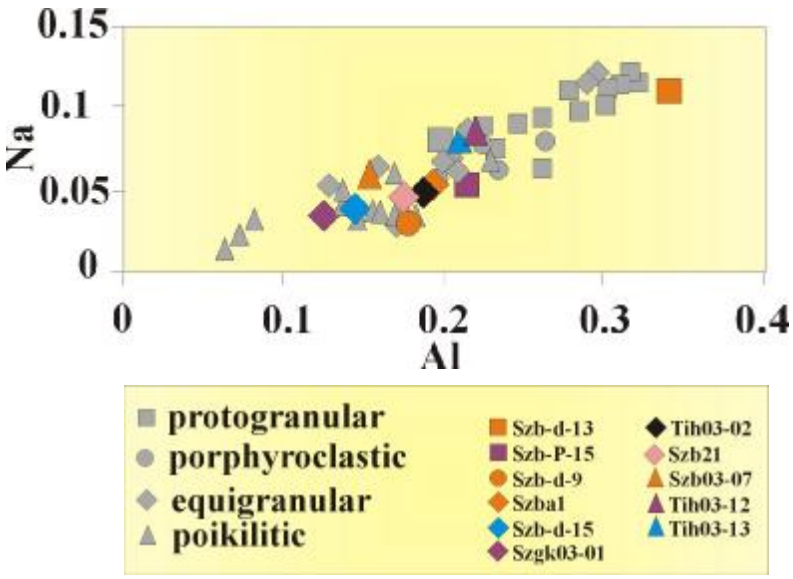

Figure VI.7 Al vs. Na (cation number normalized to 6 oxygens) diagram of clinopyroxenes in mantle peridotites from the BBHVF with respect to xenolith texture. Samples, selected for detailed microstructural analysis are highlighted. Some data from Downes et al. (1992), Embey-Isztin et al. (2001), Bali et al. (submitted).

Samples selected for detailed textural analysis cover the full spectrum of compositions. Szbd-13, a protogranular xenolith shows high Al (0.34) and considerably high Na (0.11) compositions (Figure VI.7, Table VI.3). The other selected protogranular (Szbp-15) and the porphyroclastic xenolith (Szbd-9) display intermediate compositions, Szbd-9 being more depleted in both Al (0.18) and Na (0.03), whereas Szbp-15 displays more fertile compositions (Al-0.23, Na 0.06) (Table VI.3). Equigranular samples (Szba1, Szbd-15, Szgk03-01, Tih03-02 and Szb21) plot to the more depleted end of the Na vs. Al plot (Figure VI.7).

Sample	Szba1				Trh03-02				Trh03-12				Trh03-13			
Texture		tab-equ			mos-equ				poik				poik			
Mineral	cpx	opx	sp	ol	cpx	opx	sp	ol	cpx	opx	sp	ol	cpx	opx	sp	ol
Element																
SiO_2	51.4	54.9	0.05	40.4	52.6	55.9	0.02	40.4	51.6	55.9	0.03	40.4	52.6	56.1	na.	40.4
TiO_2	0.10	0.04	0.07	bd.	0.13	0.04	0.15	bd.	0.22	0	0.16	bd.	0.21	0.05	0.06	bd.
Al_2O_3	4.59	3.84	44.7	bd.	4.44	2.41	33.0	0.04	6.24	2.55	25.3	bd.	5.26	2.93	30.0	0.04
Cr_2O_3	1.08	0.52	22.5	bd.	1.08	0.35	31.9	bd.	1.97	0.45	38.1	bd.	1.31	0.58	35.9	bd.
FeO	2.58	5.16	11.10	8.35	4.24	8.37	20.8	10.1	3.36	6.02	19.2	9.13	3.81	6.20	17.0	9.00
MnO	0.12	0.12	0.14	0.14	0.11	0.18	0.16	0.14	0.07	0.14	0.19	0.12	0.12	0.13	0.17	0.14
NiO	na.	na.	0.32	0.36	na.	na.	0.09	na.	na.	na.	na.	0.35	na.	na.	0.18	na.
MgO	17.0	34.0	19.2	50.1	16.4	33.04	15.0	49.9	15.9	33.7	0.23	49.79	16.6	33.4	16.0	49.9
CaO	20.8	0.92	0.00	0.08	20.3	0.77	0.00	0.09	19.2	0.82	15.1	0.09	19.8	0.89	na.	0.09
Na_2O	0.94	0.07	0.00	na.	0.72	0.09	0.00	na.	1.23	0.08	0.02	na.	1.16	0.08	0.00	na.
Total	98.6	99.6	98.1	99.4	100.05	101.18	101.15	100.74	99.72	99.58	98.34	99.85	100.86	100.36	99.30	99.60
Al-cn.	0.20				0.19				0.27				0.22			
Na-cn.	0.07				0.05				0.09				0.08			
mg# Mg/Mg+Fe	0.92	0.92	0.76	0.91	0.87	0.88	0.56	0.90	0.89	0.91	0.02	0.91	0.89	0.91	0.63	0.91
cr# Cr/Cr+Al			0.25				0.39				0.50				0.45	
Fo%				91.46				89.78				90.68				90.83

Sample	Szbp-15				Szbd-9				Szbd-13				Szb03-07			
Texture		pr			po				pr				poik			
Mineral	cpx	opx	sp	ol	cpx	opx	sp	ol	cpx	opx	sp	ol	cpx	opx	sp	ol
Element																
SiO_2	52.8	54.6	0.00	41.2	51.6	55.4	0.03	40.6	51.1	53.7	0.09	40.1	54.2	56.6	0.05	41.2
TiO_2	0.08	0.04	0.11	bd.	0.42	0.175	0.63	na.	0.58	0.15	0.19	bd.	0.06	0.02	0.07	0.02
Al_2O_3	5.42	4.55	47.3	0.01	4.11	3.57	36.7	na.	7.98	5.75	59.1	bd.	4.02	3.17	35.1	0.03
Cr_2O_3	1.12	0.67	21.4	0.03	1.1	0.71	30.3	na.	0.71	0.43	8.80	bd.	1.26	0.53	32.0	0.04
FeO	2.37	5.73	10.4	8.95	2.49	5.39	12.7	8.28	3.38	6.43	10.9	9.99	2.58	4.82	15.21	7.71
MnO	0.10	0.14	0.12	0.15	0.09	0.125	0.11	0.12	0.12	0.17	0.06	0.13	0.15	0.13	0.14	0.11
NiO	na.	na.	0.29	0.33	na.	na.	0.24	0.31	na.	na.	0.36	0.31	na.	na.	na.	na.
MgO	16.8	32.7	19.3	49.3	17.3	33.2	17.8	50.0	15.6	31.6	20.7	48.7	16.9	33.3	16.6	49.2
CaO	19.7	1.15	0.00	0.11	20.9	1.045	0.00	0.09	17.9	1.07	0.00	0.12	20.8	0.85	0.01	0.08
Na_2O	0.93	0.09	na.	na.	0.46	0.05	na.	na.	1.61	0.18	na.	na.	0.88	0.45	na.	na.
Total	99.35	99.66	98.90	100.01	98.44	99.72	98.43	99.41	99.01	99.42	100.23	99.34	100.87	99.83	99.25	98.48
Al-cn.	0.23				0.18				0.34				0.17			
Na-cn.	0.06				0.03				0.11				0.06			
mg# Mg/Mg+Fe	0.93	0.91	0.77	0.91	0.93	0.92	0.71	0.92	0.89	0.90	0.77	0.90	0.92	0.92	0.66	0.92
cr# Cr/Cr+Al			0.23				0.36				0.09				0.38	
Fo%				90.76				91.51				89.70				91.93

Continued on next page

Sample	Szbd-15				Szgk03-01				Szb21*			
Texture	tab-equ				tab-equ				mos-equ			
Mineral	cpx	opx	sp	ol	cpx	opx	sp	ol	cpx	opx	sp	ol
Element												
SiO_2	53.2	56.0	0.03	41.5	53.3	57.1	0.05	41.3	52.0	55.0	na.	41.0
TiO_2	0.18	0.05	0.09	bd.	0.04	0.01	0.05	0.01	0.25	0.03	0.08	na.
Al_2O_3	3.99	3.75	52.8	0.04	2.89	2.66	32.9	0.04	4.48	4.12	55.4	na.
Cr_2O_3	0.49	0.38	15.0	bd.	0.92	0.59	35.0	0.04	0.66	0.31	11.8	na.
FeO	2.52	5.86	12.0	9.05	2.24	5.21	14.0	8.25	2.92	6.74	12.4	10.4
MnO	0.09	0.14	0.13	0.17	0.10	0.13	0.15	0.12	0.00	0.08	0.07	0.20
NiO	na.	na.	0.31	0.37	na.	na.	0.20	0.36	na.	na.	0.34	0.35
MgO	16.8	33.4	19.8	50.0	17.5	34.3	17.1	50.5	16.6	32.9	19.9	49.0
CaO	22.3	0.63	0.01	0.05	21.8	0.85	na.	0.09	21.8	0.71	na.	0.08
Na_2O	0.43	0.01	na.	na.	0.51	0.05	na.	na.	0.77	0.08	na.	na.
Total	99.94	100.24	100.18	101.14	99.35	100.86	99.42	100.74	99.41	99.97	99.98	101.07
Al-cn.	0.17				0.12				0.19			
Na-cn.	0.03				0.04				0.05			
mg# Mg/Mg+Fe	0.92	0.91	0.75	0.91	0.93	0.92	0.69	0.92	0.91	0.90	0.74	0.89
cr# Cr/Cr+Al			0.16				0.42				0.13	
Fo%				90.79				91.62				89.34

Table VI.3 Composition of constituent phases of mantle xenoliths from the BBHVF in wt%. Al-ca – cation number of Al; Na-ca cation number of Na; mg# - mg number; cr# - cr-number; Fo% - forsterite mol%; cpx – clinopyroxene; opx – orthopyroxene; sp – spinel; ol – olivine; na. – not analyzed; bd. – below detection limit.

The Al contents of the studied equigranular xenoliths range between 0.12-0.1, whereas Na content ranges from 0.03 to 0.07 (Table VI.3). Clinopyroxenes in the poikilitic samples (Szb03-07, Tih03-12 and Tih03-13) show somewhat higher Al (0.17-0.26) and Na (0.06-0.08) contents compared to other poikilitic samples in the region (Table VI.3). This may indicate weaker depletion or stronger metasomatic effects in these studied xenoliths.

Olivine mg-numbers of earlier geochemical studies (e.g., Embey-Isztin et al., 2001) also display large variance from "fertile" values of 0.89 to highly "depleted" values of 0.92. Fo-contents plotted against cr-number of spinels on the OSMA-diagram indicate that most of the xenoliths plot below or close to the 20% partial melting line (Figure VI.8). However some of the samples, even those displaying protogranular or porphyroclastic textures, plot above the 20% partial melting line. Some poikilitic samples fall close to the 30% partial melting line (Figure VI.8).

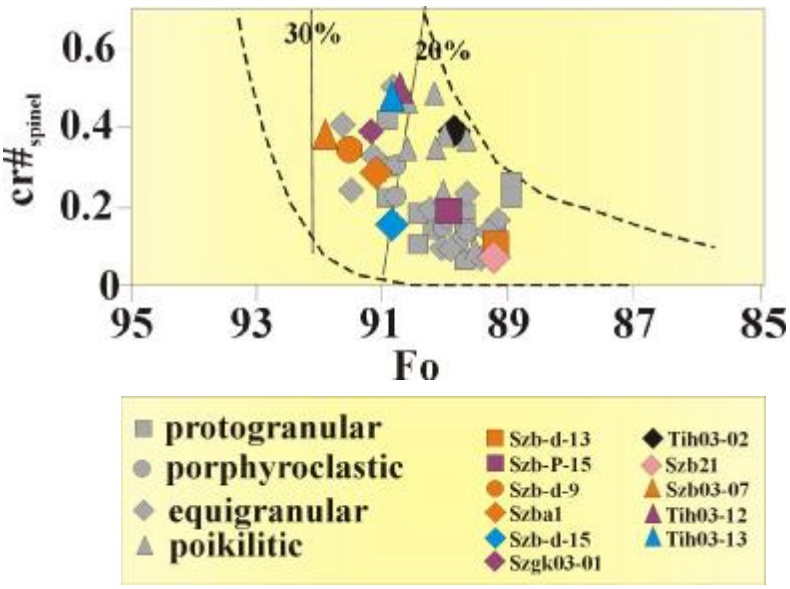

Figure VI.8 Fo vs. $cr\#_{spinel}$ diagram (OSMA; Arai, 1994) of mantle peridotites from the BBHVF with respect to xenolith texture. Note reverse order of Fo. Samples, selected for detailed microstructural analysis are highlighted. Also, dotted lines indicate the extent of partial melting (20%-30%). Some data from Downes et al. (1992), Embey-Isztin et al. (2001), Bali et al. (submitted).

Szbd-13 as expected, falls below the 20% partial melting line in the undepleted field of the diagram together with most of the protogranular xenoliths analyzed earlier. Szbp-15 and Szbd-9 display high Fo contents and plot in the more

depleted field of the OSMA (Figure VI.8). The selected equigranular samples similarly to those analyzed in earlier geochemical studies (e.g., Embey-Isztin et al., 2001) cover wide range from low Fo-content (89) low cr-numbers (0.12) to high Fo content (0.92) high cr-numbers (0.42) (Table VI.3). Samples with poikilitic textures exhibit high Fo content (91-92) and high cr-numbers (0.38-0.5) (Table VI.3) and all plot in the depleted field of OSMA (Figure VI.8).

Compositions, plotted on the Na_2O in clinopyroxene vs. cr-number in spinel diagram, in most of the cases indicate considerable deviance (Na-enrichment) from the 'normal' depletion trend in xenoliths from earlier geochemical studies (e.g., Szabó et al., 1995b). Xenoliths of all textural types show Na_2O enrichment (Figure VI.9).

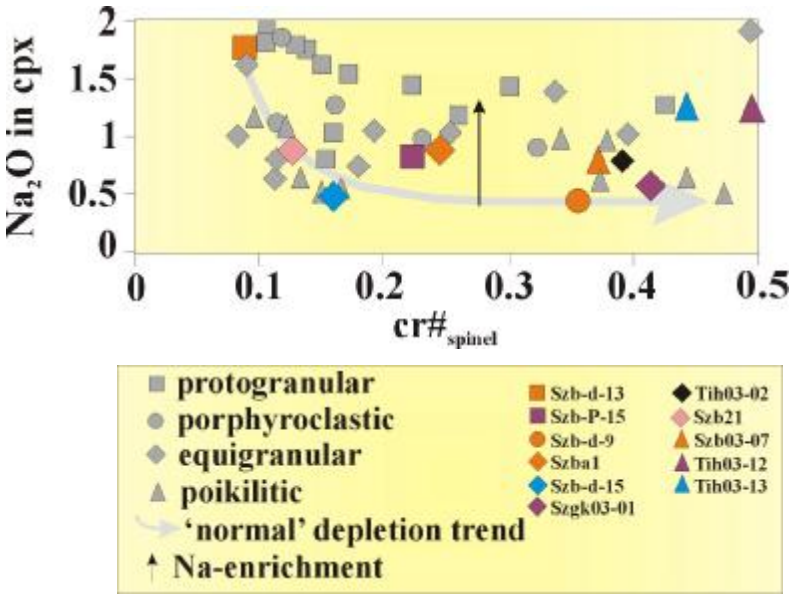

Figure VI.9 Na_2O (wt%) in clinopyroxene vs. $cr\#_{spinel}$ diagram (Xu et al., 2003) of mantle peridotites from the BBHVF with respect to xenolith texture. Samples, selected for detailed microstructural analysis are highlighted. Area surrounded dashed line shows 'normal' depletion trend. Some data from Downes et al. (1992), Embey-Isztin et al. (2001), Bali et al. (submitted).

The selected samples show variable characters, Szbd-13 plots to the higher end (low cr-number, high Na_2O-content) of the normal depletion trend. Szbd-9 compositions follow the 'normal' depletion trend, whereas Szbp-15 displays marked addition of Na_2O (Figure VI.9). All selected equigranular samples follow the 'normal' depletion trend. Only Tih03-02 displays Na_2O enrichment (Figure VI.9). Poikilitic

xenoliths exhibit marked Na_2O enrichment with respect to the 'normal' depletion trend (Figure VI.9).

NGVF

Mantle xenoliths from the NGVF are derived from several xenolith locations that are located along a more or less north-south line. Remarkable textural variance is observed from north to south. Xenoliths derived from the northern part of the volcanic field exhibit protogranular/porphyroclastic textures, whereas more to the south, towards the center of the Intra-Carpathian Basin System the predominance of porphyroclastic/ equigranular textures is observed (Szabó and Taylor, 1994 Konecny et al., 1995).

Major element bulk compositions of the peridotite xenoliths as demonstrated by Szabó and Taylor (1994), similarly to other xenolith locations show MgO contents from 39 to 44 wt%. Basaltic major elements display marked negative correlation with the MgO content (Szabó and Taylor, 1994).

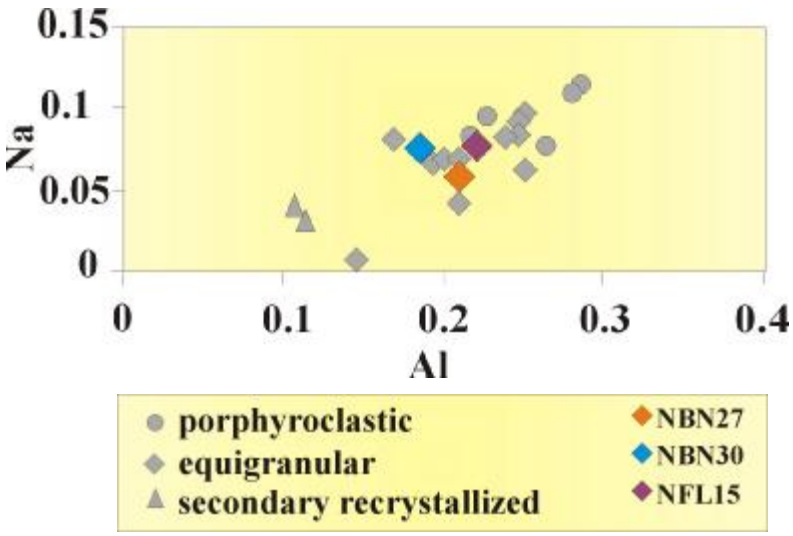

Figure VI.10 Al vs. Na (cation number normalized to 6 oxygens) diagram of clinopyroxenes in mantle peridotites from the NGVF with respect to xenolith texture. Samples, selected for detailed microstructural analysis are highlighted. Data from Szabó and Taylor (1994) and Konecny et al. (1995).

Remarkable positive correlation is observed between Na and Al content of clinopyroxene compositions analyzed by earlier geochemical studies (Szabó and Taylor, 1994; Figure VI.10). Al contents fall in a narrower range than in other xenolith locations (0-3-0.1), whereas Na contents display high variability. As in other locations, xenoliths with the least deformed texture plot to the fertile part (Al and Na rich) of the diagram whereas, secondary recrystallized ones are characterized by low Al and Na contents (Figure VI.10).

Selected samples (NBN27, NBN30 and NFL15) represent intermediate Al and Na values (0.22-0.17 and 0.0-0.08, respectively). Composition of the selected samples coincides with that of equigranular xenoliths studied by Szabó and Taylor (1994) and Konecny et al (1995).

Olivine ~Fo-contents are relatively low (87-90), whereas cr-numbers of spinels are also generally below 0.3 in the xenoliths analyzed earlier by Szabó and Taylor (1994). Samples on the OSMA-diagram generally plot below or close to the 20% partial melting line (Figure VI.11). Although, some exceptions, displaying high cr-numbers up to 0.4 also occur (Table VI.4).

Sample	NBN27				NBN30				NFL15			
Texture	mos-equ				mos-equ				mos-equ			
Mineral	cpx	opx	sp	ol	cpx	opx	sp	ol	cpx	opx	sp	ol
Element												
SiO_2	51.9	55.2		40.5	52.6	56.0		40.8	51.7	54.7		40.1
TiO_2	0.4	0.09	0.41	na.	0.08	0.03	0.09	na.	0.3	0.08	0.08	na.
Al_2O_3	4.9	3.76	51.3	na.	3.93	2.51	34.7	na.	5.1	3.95	50.0	na.
Cr_2O_3	0.63	0.36	14.3	na.	1.28	0.47	33	na.	0.8	0.35	18.0	na.
FeO	2.94	6.32	13.1	10.2	2.49	5.81	14.1	8.94	3.36	7.63	14.5	11.7
MnO	0.08	0.14	0.12	0.15	0.08	0.14	0.14	0.13	0.11	0.18	0.14	0.19
NiO	na.	na.	0.27	0.33	na.	na.	0.19	0.33	na.	na.	0.34	0.37
MgO	16.7	33.1	18.8	48.7	16.3	33.8	16.4	49.6	15.7	32.0	17.8	47.3
CaO	21.2	0.68	na.	0.1	21.5	0.72	na.	0.1	21.1	0.73	na.	0.07
Na_2O	0.82	0.04	na.	na.	1.09	0.05	na.	na.	1.1	0.08	na.	na.
Total	99.57	99.69	98.3	99.98	99.35	99.53	98.62	99.9	99.27	99.7	100.86	99.73
Al-cn.	0.21				0.04				0.22			
Na-cn.	0.06				0.08				0.08			
mg# Mg/Mg+Fe	0.91	0.90	0.72	0.89	0.92	0.91	0.67	0.91	0.89	0.88	0.69	0.88
cr# Cr/Cr+Al			0.16				0.39				0.19	
Fo%				88.95				90.29				87.25

Table VI.4 Composition of constituent phases of mantle xenoliths from the NGVF in wt%. Al-ca – cation number of Al; Na-ca cation number of Na; mg# - mg number; cr# - cr-number; Fo% - forsterite mol%; cpx – clinopyroxene; opx – orthopyroxene; sp – spinel; ol – olivine; na. – not analyzed; bd. – below detection limit. Data from Szabó and Taylor (1994).

The selected samples plot in remarkably different points of the Fo vs. spinel cr-number plot. The sample NBN27 has low Fo content (89) and relatively low cr-numbers (0.16) and plots in the undepleted segment of the OSMA. NBN30, however displays higher Fo content (90) and cr-numbers and plots on the 20% partial melting line. Whereas, NFL15 displays high cr-number (0.24) with respect to Fo in olivine (88) and plots somewhat outside the OSMA (Figure VI.11, Table VI.4) due to metasomatism.

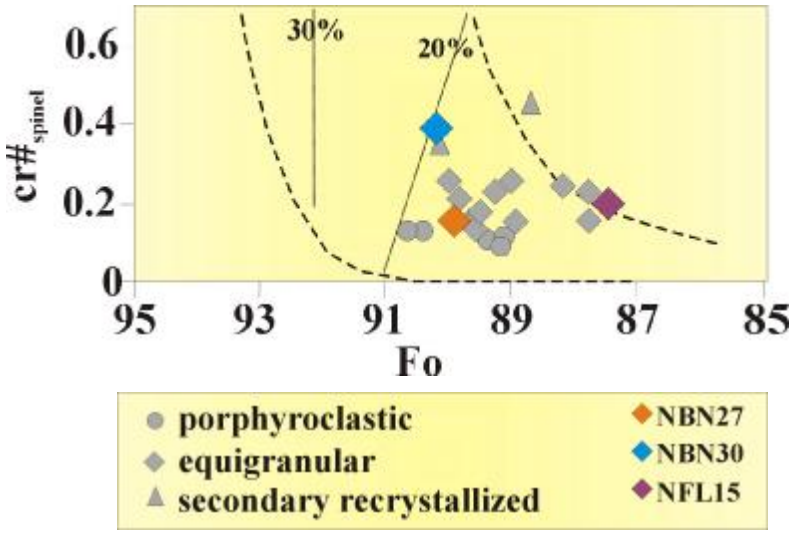

Figure VI.11 Fo vs. $cr\#_{spinel}$ diagram (OSMA; Arai, 1994) of mantle peridotites from the NGVF with respect to xenolith texture. Note reverse order of Fo. Samples, selected for detailed microstructural analysis are highlighted. Also, dotted lines indicate the extent of partial melting (20%-30%). Data from Szabó and Taylor (1994) and Konecny et al. (1995).

The Na_2O in clinopyroxene vs. spinel cr-number diagram (Figure VI.12) shows quite similar distribution to that of LHPVF (Figure VI.6). However, most of the samples deviate from the 'normal' depletion trend (Figure VI.12). Nevertheless, xenoliths with the most undeformed texture follow the 'normal' depletion trend and plot to the fertile end (high Na_2O; low cr-number) of the diagram (Figure VI.12).

Among the studied samples only NBN 27 follows the 'normal' depletion trend (Figure VI.12), whereas the two other samples show marked enrichment in Na_2O in clinopyroxene with respect to cr-number of co-existing spinel.

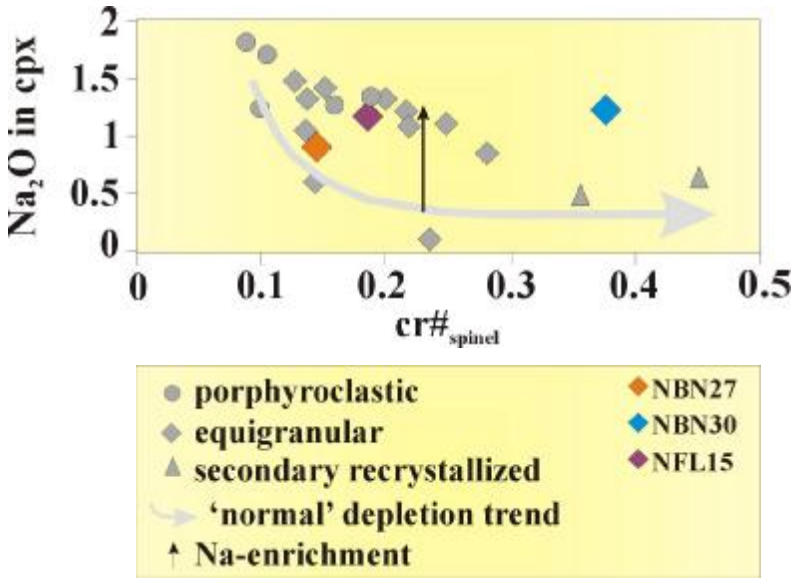

Figure VI.12 Na_2O (wt%) in clinopyroxene vs. $cr\#_{spinel}$ diagram (Xu et al., 2003) of mantle peridotites from the NGVF with respect to xenolith texture. Samples, selected for detailed microstructural analysis are highlighted. Area surrounded dashed line shows 'normal' depletion trend. Data from Szabó and Taylor (1994) and Konecny et al. (1995).

ETBVF

Compositions of mantle xenoliths of the ETBVF are of particular importance because they are the only alkali basalt hosted xenoliths representing the upper mantle of the TISZIA microplate (Figure II.3); all other samples are derived from the upper mantle of the ALCAPA microplate (e.g., Csontos, 1995; Figure II.3).

Major element bulk composition of the upper mantle xenoliths from the ETBVF is similar to all other xenolith locations studied. MgO content of the peridotitic samples varies from 39 wt% in the most fertile lherzolites to 45 wt% in the most depleted harzburgites (Vaselli et al., 1995). The strong negative correlation between basaltic major elements and MgO is clearly observed.

Turning to clinopyroxene compositions, Na and Al contents display a much narrower distribution (0.13 and 0.31, respectively) compared to other xenolith locations (Figure VI.13). Clinopyroxene of the only harzburgite, however plots to the depleted part (low Na, low Al) of the diagram (Figure VI.13).

Sample	Bg18*				Bg15*				Lgr09*				Lgr09*			
Texture	Pr				fol				fol				fol			
Mineral	cpx	opx	sp	ol	cpx	opx	sp	ol	cpx	opx	sp	ol	cpx	opx	sp	ol
Element																
SiO_2	50.9	54.2	0.19	40.6	51.0	55.0	0.14	40.7	51.8	56.4	0.16	41.1	53.9	56.6	0.16	41.3
TiO_2	0.42	0.11	0.21	0.03	0.36	0.11	0.11	0.03	0.49	0.10	0.02	0.06	0.38	0.13	0.02	na.
Al_2O_3	6.85	5.37	53.4	0.01	6.24	4.22	56.7	0.02	7.39	2.82	na.	na.	4.22	2.71	57.6	na.
Cr_2O_3	1.07	0.56	14.0	0.05	0.85	0.33	10.6	0.01	0.91	0.22	10.3	0.07	0.43	0.19	10.3	0.01
FeO	3.17	6.00	11.1	9.26	2.72	6.22	11.2	9.52	2.36	6.40	11.0	9.59	2.59	6.17	11.0	9.63
MnO	0.07	0.14	0.07	0.11	0.06	0.15	0.10	0.14	0.10	0.07	0.08	0.06	0.10	0.08	0.08	na.
NiO	0.11	0.05	0.37	0.39	0.06	0.08	0.39	0.46	na.	na.	0.19	0.32	0.20	0.16	0.19	0.17
MgO	15.7	31.9	20.4	48.5	15.1	32.8	20.4	48.6	14.0	33.0	20.4	48.3	15.4	33.3	20.4	48.2
CaO	19.9	1.06	na.	0.28	21.9	0.66	na.	0.06	21.0	0.46	na.	0.08	21.3	0.42	na.	na.
Na_2O	1.58	na.	na.	na.	1.21	na.	na.	na.	1.96	na.	na.	na.	1.39	na.	na.	na.
Total	99.70	99.37	99.73	99.20	99.47	99.60	99.57	99.53	99.93	99.44	99.68	99.53	99.91	99.76	99.68	99.31
Al-cn.	0.29				0.27				0.32				0.18			
Na-cn.	0.11				0.09				0.14				0.10			
mg# Mg/Mg+Fe	0.90	0.90	0.77	0.90	0.91	0.90	0.76	0.90	0.91	0.90	0.77	0.90	0.91	0.91	0.77	0.90
cr# Cr/Cr+Al			0.15				0.11				0.11				0.11	
Fo%				89.55				89.50				89.55				89.78

Sample	Rk99				Rk99			
Texture	myl-pc core				myl-pc rim			
Mineral	cpx	opx	sp	ol	cpx	opx	sp	ol
Element								
SiO_2	50.7	54.9	0.02	41.3	49.4	55.1	0.06	41.0
TiO_2	0.67	0.09	0.05	0.01	0.91	0.08	0.06	0.01
Al_2O_3	7.19	3.30	56.1	bd.	5.10	3.40	55.6	bd.
Cr_2O_3	0.91	0.19	9.70	0.01	1.17	0.33	9.15	0.03
FeO	2.41	6.71	11.2	10.74	2.84	6.52	10.9	10.31
MnO	0.08	0.12	0.11	0.16	0.11	0.16	0.13	0.14
NiO	0.05	0.02	0.34	0.41	0.03	0.04	0.43	0.37
MgO	14.0	33.3	20.5	47.7	16.1	33.3	20.8	48.7
CaO	21.1	0.39	bd.	0.04	20.4	0.50	0.02	0.03
Na_2O	1.86	0.04	0.01	0.00	1.10	0.04	0.00	0.00
Total	98.96	99.04	97.97	100.38	97.16	99.48	97.09	100.63
Al-cn.	0.31				0.23			
Na-cn.	0.13				0.08			
mg# Mg/Mg+Fe	0.91	0.90	0.77	0.89	0.91	0.90	0.77	0.89
cr# Cr/Cr+Al			0.10				0.10	
Fo%				88.23				88.92

Continued on next page

Sample	LGR0301				LGR0301				LGR0301			
Texture	myl-pc core				myl-pc rim				myl - rec			
Mineral	cpx	opx	sp	ol	cpx	opx	sp	ol	cpx	opx	sp	ol
Element												
SiO_2	51.2	54.4	0.08	40.7	52.8	55.6	0.02	40.3	52.7	55.9	0.05	40.6
TiO_2	0.49	0.13	0.03	bd.	0.21	0.06	0.06	0.02	0.24	0.05	0.03	bd.
Al_2O_3	6.27	5.66	57.1	bd.	3.46	3.16	56.9	0.02	3.78	2.63	56.8	bd.
Cr_2O_3	0.75	0.55	11.4	bd.	0.43	0.36	11.0	0.00	0.50	0.14	11.0	0.02
FeO	2.41	6.26	12.2	9.46	2.53	6.05	11.8	9.35	2.55	6.21	11.8	9.33
MnO	0.06	0.17	0.12	0.18	0.06	0.18	0.08	0.17	0.09	0.16	0.10	0.13
NiO	na.	na.	0.31	0.34	0.00	0.00	0.37	0.27			0.32	0.36
MgO	15.2	32.7	19.4	49.9	16.5	33.7	19.6	49.6	16.4	34.1	19.4	49.6
CaO	21.6	0.41	bd.	0.03	22.5	0.44	bd.	0.02	22.6	0.43	0.01	0.04
Na_2O	0.99	0.03	na.	na.	0.70	bd.	na.	na.	0.67	bd.	na.	na.
Total	99.02	100.32	100.65	100.69	99.24	99.49	99.82	99.69	99.55	99.57	99.41	100.10
Al-cn.	0.27				0.15				0.16			
Na-cn.	0.07				0.05				0.05			
mg# Mg/Mg+Fe	0.92	0.90	0.74	0.90	0.92	0.91	0.75	0.90	0.92	0.91	0.75	0.90
cr# Cr/Cr+Al			0.12				0.11				0.11	
Fo%				89.91				90.03				89.97

Sample	NVTR0301				NVTR0301				NVTR0301			
Texture	myl -pc core				myl -pc rim				myl - rec			
Mineral	cpx	opx	sp	ol	cpx	opx	sp	ol	cpx	opx	sp	ol
Element												
SiO_2	50.9	54.1	0.08	40.4	52.1	55.0	0.06	40.6	52.7	56.1	0.03	40.9
TiO_2	0.52	0.12	0.05	bd.	0.32	0.05	0.01	bd.	0.37	0.05	0.05	bd.
Al_2O_3	6.89	5.32	58.0	0.02	4.58	3.85	58.9	0.03	4.90	3.01	60.1	0.01
Cr_2O_3	0.73	0.39	9.44	0.00	0.57	0.23	9.69	0.02	0.36	0.16	8.20	bd.
FeO	2.69	6.60	11.7	10.1	2.52	6.48	11.6	10.5	2.67	6.53	11.7	9.90
MnO	0.10	0.15	0.10	0.14	0.05	0.15	0.10	0.11	0.10	0.16	0.12	0.12
NiO			0.39	0.34	na.	na.	0.39	0.42	na.	na.	0.40	0.34
MgO	14.9	32.3	19.4	49.10	16.0	33.1	19.6	49.7	15.9	33.7	19.9	49.3
CaO	21.9	0.42	bd.	0.06	22.3	0.43	bd.	0.04	21.7	0.45	0.02	0.07
Na_2O	0.93	0.03	na.	na.	0.67	0.04	na.	na.	1.02	0.01	na.	na.
Total	99.53	99.36	99.12	100.20	99.09	99.34	100.31	101.41	99.59	100.16	100.49	100.66
Al-cn.	0.30				0.20				0.21			
Na-cn.	0.07				0.05				0.07			
mg# Mg/Mg+Fe	0.91	0.90	0.75	0.90	0.92	0.90	0.75	0.89	0.91	0.90	0.75	0.90
cr# Cr/Cr+Al			0.10				0.10				0.08	
Fo%				89.16				88.92				89.40

Table VI.5 Composition of constituent phases of mantle xenoliths from the ETBVF in wt%. Al-ca – cation number of Al; Na-ca cation number of Na; mg# - mg number; cr# - cr-number; Fo% - forsterite mol%; cpx – clinopyroxene; opx – orthopyroxene; sp – spinel; ol – olivine; na. – not analyzed; bd. – below detection limit; pc – porphyroclast; myl – mylonite. Some data from Vaselli et al. (1995).

Selected samples (BG15, BG18, LGR09) exhibit Al contents around 0.2 and Na around 0.1 (TableVI.5; Figure VI.13). A systematic variance in both Al and Na content of clinopyroxene porphyroclast cores, rims and neoblasts is observed in the mylonitic xenoliths (Rk99/04; LGR03-01 and NVTR03-01; Figure VI.13; Table VI.5). Porphyroclast cores in all cases display high Al values around 0.3, whereas neoblasts and even more intensively porphyroclast rims show depletion in Al to values around 0.15-0.2. Similarly, Na content also shows a remarkable depletion towards the rims and the neoblasts (from 0.07 to 0.05; Table VI.5).

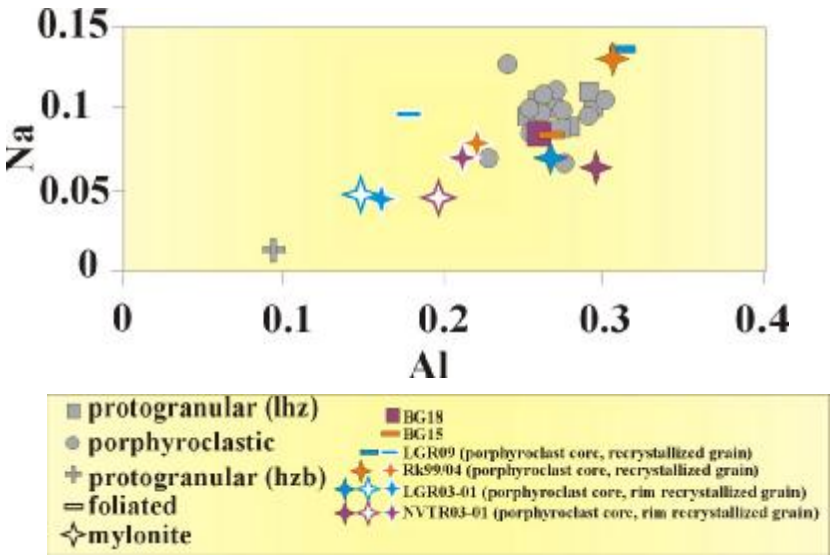

Figure VI.13 Al vs. Na (cation number normalized to 6 oxygens) diagram of clinopyroxenes in mantle peridotites from the ETBVF with respect to xenolith texture. Samples, selected for detailed microstructural analysis are highlighted. Note porphyroclast-recrystallized grain pairs in mylonitic xenoliths. Some data from Vaselli et al. (1995).

Samples from the ETBVF generally plot well below the 20% partial melting line of the OSMA-diagram in those samples earlier analyzed in geochemical studies (Vaselli et al., 1995; Figure VI.14), having low Fo-content in olivine (86-90) together with low cr-numbers in spinel (below 0.2). The only exception is a harzburgite, exhibiting relatively high Fo content (90) and cr-number (0.35). This composition plots just above the 20% partial melting line (Figure VI.14).

The selected samples (including the mylonites) plot in the low Fo low cr field. Moreover, porphyroclast cores, rims and neoblasts exhibit practically similar Fo and cr values (Figure VI.14; Table VI.5).

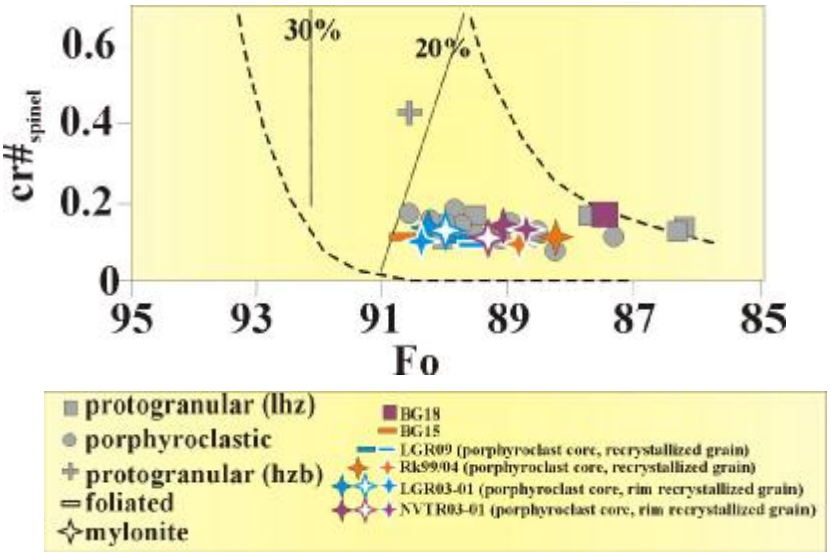

Figure VI.14 Fo vs. $cr\#_{spinel}$ diagram (OSMA; Arai, 1994) of mantle peridotites from the ETBVF with respect to xenolith texture. Note reverse order of Fo. Samples, selected for detailed microstructural analysis are highlighted. Note porphyroclast-recrystallized grain pairs in mylonitic xenoliths. Also, dotted lines indicate the extent of partial melting (20%-30%). Some data from Vaselli et al. (1995).

Distribution of samples on the Na_2O in clinopyroxene vs. spinel cr-number diagram differs significantly from that observed in the other xenolith locations (Figure VI.15). All xenoliths, plot to the uppermost part (high Na_2O-low cr-number) of the normal depletion trend, regardless of their texture. They all exhibit high Na_2O content (generally above 1 wt%) together with low cr-numbers (Table VI.5). Only one sample, the harzburgite displays evidence for Na_2O enrichment (Figure VI.15).

Samples selected for detailed analysis also plot to the high Na_2O-low cr-number part of the plot. The depletion of Na_2O in the mylonites from the porphyroclast cores towards the rims and the neoblasts is clearly shown on the diagram (Figure VI.15).

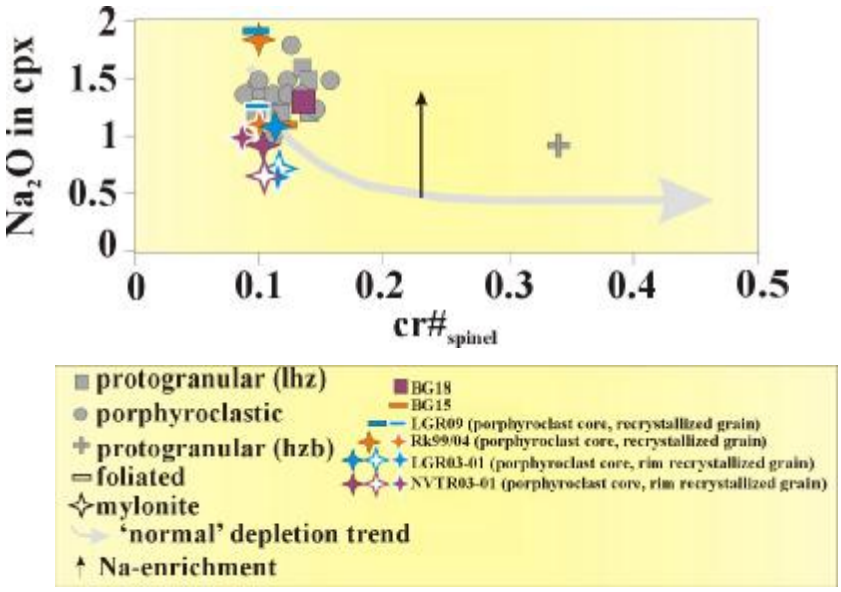

Figure VI.15 Na_2O (wt%) in clinopyroxene vs. $cr\#_{spinel}$ diagram (Xu et al., 2003) of mantle peridotites from the ETBVF with respect to xenolith texture. Samples, selected for detailed microstructural analysis are highlighted. Note porphyroclast-recrystallized grain pairs in mylonitic xenoliths. Area surrounded dashed line shows 'normal' depletion trend. Some data from Vaselli et al. (1995).

VI.2 Modal metasomatism: its effects on major element composition of the upper mantle

Although the analysis of metasomatic phases in the peridotitic upper mantle fragments is not the major goal of the thesis, it is necessary to summarize its main aspects and features. Detailed discussion of the significance of these phases is given in several papers (e.g., Vaselli et al., 1995, 1996; Szabó et al., 1995 and submitted; Bali et al., 2002).

Besides the so-called "dry" peridotite phases, hydrous minerals may also occur in the mantle. These phases are the principal H_2O containers of the mantle and are basically responsible for the average 0.5 wt% H_2O present in the mantle. They are believed to represent metasomatic processes occurring in the subcrustal realm. Among hydrous phases, amphibole is the most common in the subcontinental lithospheric mantle although phlogopitic mica also occurs. Amphiboles, besides clinpyroxenes, generally incorporate basaltic major elements and are hosts for several incompatible trace elements.

Pargasitic and kearsutitic amphiboles and phlogopitic micas occur as modal metasomatic minerals in both peridotite and pyroxenite xenoliths from the Intra-Carpathian Basin System. Amphiboles, occurring as interstitial phases, veins and selvages, are more common than phlogopites. In spite of the significant textural variation of amphibole, they display moderate variation in major element composition. All amphiboles from the NGVF, LHPVF, SBVF and ETBVF are pargasites, whereas BBHVF amphiboles show wide compositional range, where Mg-hastingsite and kaersutite also can be found (Figure VI.16). The occurrence of amphiboles in the SBVF and ETBVF shows weak preference to textural types, presumably because of the low variability textures in these regions. Nevertheless, amphiboles in the xenoliths from the central portion of the basin show strong preference to the most strongly deformed and recrystallized rocks. They are practically absent from protogranular and porphyroclastic xenoliths in these locations (Szabó et al., submitted).

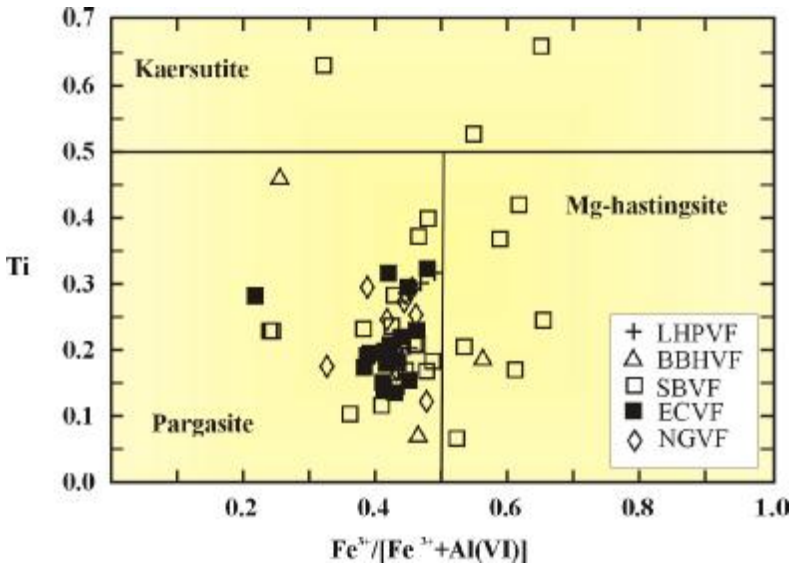

Figure VI.16 $Fe^{3+}/[Fe^{3+}+Al(VI)]$ vs. Ti for amphiboles in upper mantle xenoliths from the Intra-Carpathian Basin System. Data source for SBVF: Vannucci et al., 1994; Vaselli et al., 1996; Bali et al., submitted; for LHPVF: Szabó et al., 1995a; for BBHVF: Embey-Isztin, 1976; Bali et al., 2002; for NGVF: Szabó and Taylor, 1994; for ETBVF: Zanetti et al., 1995; Vaselli et al., 1995; Szabó et al., submitted). The fields of pargasite, Mg-hastingsite and kaersutite are taken after Leake (1978). Values of Fe^{3+} were calculated using equation of Droop (1987).

An indirect evidence for the presence of hydrous metasomatic phases is the occurrence of melt pockets in peridotite xenoliths. These small melted and partially crystallized pockets are suggested to be related to melting and breakdown of metasomatic amphiboles (e.g., Bali et al., 2002). These amphiboles often went through mantle processes as they became source materials for the subsequent silicate melt pocket formation (e.g., Bali et al., submitted). In the LHPVF, BBHVF and NGVF xenoliths melt pockets can be considered to be common although minor constituents of mantle xenoliths. They contain assemblages of glass, ±clinopyroxene, ±olivine, ±spinel, ±plagioclase, ±carbonate, ±sulfide and ±apatite. Their size is similar to those of the other mantle minerals in the xenoliths. Melt pockets occur dominantly in deformed and recrystallized xenoliths. It has been demonstrated that the melting of mantle amphibole (and coexisting clinopyroxene) played a significant role in the formation of the melt pockets even in those cases when the amphibole was completely missing in the assemblage of the studied xenolith (Bali et al., submitted; Bali, 2004).

VI.3 Incompatible trace elements in the peridotite xenoliths of the Intra-Carpathian Basin System

Some of the trace elements are effective indicators of lithospheric mantle processes such as depletion and enrichment. Rare earth elements are among the most frequently used trace elements in peridotitic rocks that are successfully applied in this manner. Rare earth elements are incompatible with the anhydrous spinel peridotite, being the most common rock type in the shallow sub-continental lithospheric mantle. Partial melting, thus the removal of basaltic component from the mantle, strongly affects their relative abundances (McDonough and Frey, 1989). Light rare earth elements (LREE) are more incompatible than heavy rare earth elements (HREE) and thus will become strongly depleted in the refractory mantle during partial melting and the extraction of basaltic elements. Xenoliths, being fertile in basaltic major elements, also reflect LREE depleted character (Downes, 2001). Enrichment processes, related to interaction of depleted mantle wall rock with percolating fluids and melts, generally results in strong enrichment of LREE with respect to HREE. These enrichment processes are generally associated with depletion in basaltic major elements (e.g., Frey and Green, 1974). The enrichment processes are believed to occur due to

chromatographic fractionation (Bodinier et al., 1990), thus the evidence for the effect of enrichment is mostly observed close to melt veins and diminishes with distance (e.g., Szabó et al. 1995b, Vaselli et al., 1995).

Clinopyroxene, one of the constituent phases of mantle peridotites, is the mineral phase, which accommodates rare earth elements in the highest concentration. Rare earth element concentration in clinopyroxenes is about 7 times higher than in the bulk rock (Downes, 2001). Therefore, rare earth concentrations of the clinopyroxene (in dry peridotites) controls bulk rock rare earth geochemistry. Consequently, rare earth composition of mantle xenoliths is sufficiently described analyzing the composition of clinopyroxenes.

Rare earth elements of clinopyroxenes in the Intra-Carpathian Basin System mantle xenoliths, hosted in Neogene alkali basalts, have been extensively studied. Significant correlation between texture, i.e., deformation state of the mantle xenolith and chondrite-normalized rare earth element pattern has been observed in the samples. Protogranular and some of the porphyroclastic xenoliths display LREE depleted patterns with low La/Nd (<0.5) and also low Sm/Yb (< 1) ratios. In contrast, deformed and recrystallized (equigranular) xenoliths generally display high La/Nd and moderate Sm/Yb ratios (Downes, 2001). This concentration distribution is frequently observed in other xenolith locations, e.g., Massif Central (Downes and Dupuy, 1987; Zangana et al., 1997). Amphiboles are also hosts for rare earth elements. Their rare earth element pattern, being interstitial or vein amphibole varies between LREE depleted and LREE enriched character, respectively (e.g., Vaselli et al., 1995). Rare earth pattern of vein amphiboles closely reflects the enriched nature of the host alkali basalts (e.g., Downes and Vaselli, 1995). Depleted characters for interstitial amphiboles may be due to re-equilibration with the wall rock peridotite or continuous depletion of migrating fluids due to wall-rock fluid interaction (e.g., Szabó et al., 1995b).

Concentration of other trace elements, such as large ion lithophile elements (LILE), i.e., Rb Sr, Ba, etc. and high field strength elements (HFSE), i.e., Zr, Hf, Nb, etc. also bear with significant importance in tracking the evolution and reconstructing various chemical processes occurring in the sub-continental lithospheric mantle. LILE-elements, being strongly incompatible to the peridotititic material, strongly favor partitioning into partial melts of the upper mantle. Thus, chondrite normalized trace element patterns of upper mantle material, which followed the ‘normal’

depletion trend, would exhibit negative anomalies of these elements. Subduction-related percolating fluids and silicate melts, for instance, derived by low degree partial melting and are thus enriched in LILE elements, would consequently cause enrichment in the depleted peridotitic material, resulting in strong positive Rb, Sr, Ba, U, etc. anomalies. In contrary, in such cases the HFSE elements will show negative anomalies due to their weak solubility in aqueous fluids. HFSE elements tend to partition in carbonatitic melts and often display positive anomalies in asthenosphere-derived partial melts (Downes, 2001).

Xenoliths depleted in basaltic major elements and have high mg-numbers generally display LREE enriched patterns (e.g., Downes et al., 1992). This indicates metasomatism of the upper mantle material by REE enriched percolating fluids. HFS elements, although their analysis is very scarce, generally show negative correlation with increasing mg-numbers (e.g., Vaselli et al., 1996). This indicates their depletion associated with the partial melting and mobilization of basaltic elements (Embey-Isztin et al. 2001b; Dobosi, 2003).

VI.4 Radiogenic isotope composition of the peridotite xenoliths from the Pannonian Basin

Radiogenic isotopes, studied in mantle derived xenoliths worldwide. Radiogenic isotopes not only indicate depletion and enrichment processes in the mantle, but are also capable of giving age data related to large scale processes, mostly partial melting that affected lithospheric mantle. Three isotopic systems are widely used for upper mantle material (Rb-Sr; Sm-Nd, Pb-Pb), although recently the application of Re-Os isotopic system is getting more and more widespread. Isotopic compositions are mostly retrieved from separated and leached clinopyroxene.

Sr and Nd isotope compositions from the Pannonian Basin xenoliths were analyzed by several studies (e.g., Downes et al., 1992; Vaselli et al., 1995, 1996). These works revealed that $^{87}Sr/^{86}Sr$ ratios vary between depleted 0.70307 and enriched 0.70523 values, whereas $^{143}Nd/^{144}Nd$ falls between enriched 0.513341 and depleted 0.512733 (Downes et al., 1992; Vaselli et al., 1995, 1996). Most of the xenoliths studied in the literature fall between depleted MORB compositions and the Bulk Earth value (e.g., Downes et al., 1992). Some of the studied samples plot in the field of host alkali basalts, whereas others show similarities with Bulk Earth (Figure

VI.17). Similarly to major and trace element compositions, Sr and Nd isotope compositions display strong correlation with the state of deformation (i.e., xenolith texture). Protogranular samples representing virtually undeformed mantle portion reflect the most depleted nature showing high $^{143}Nd/^{144}Nd$ and low $^{87}Sr/^{86}Sr$ ratios and falling in, or close to the MORB field (Vaselli et al., 1995; Downes and Vaselli, 1995; Figure VI.17). In contrary, deformed xenoliths generally show more enriched character (high $^{87}Sr/^{86}Sr$ and low $^{143}Nd/^{144}Nd$ ratios) falling close either to host alkali basalts or Bulk Earth. The Nd isochron indicates (not shown) that depletion, efficiently changing Nd isotopic compositions of the upper mantle beneath the Intra-Carpathian Basin System occurred ~1 Ga before recent times (e.g., Downes et al., 1992; Vaselli et al., 1995; Embey-Isztin et al., 2001b).

The Pb isotope system, although, the number of analyses carried out is much lower than on Sr-Nd isotopes, indicates mixing between depleted mantle material, low in radiogenic Pb and a plume component with more radiogenic Pb (Rosenbaum et al., 1997). Some rare Intra-Carpathian Basin System samples also indicate a subducted sediment component (Wilson et al., 1997).

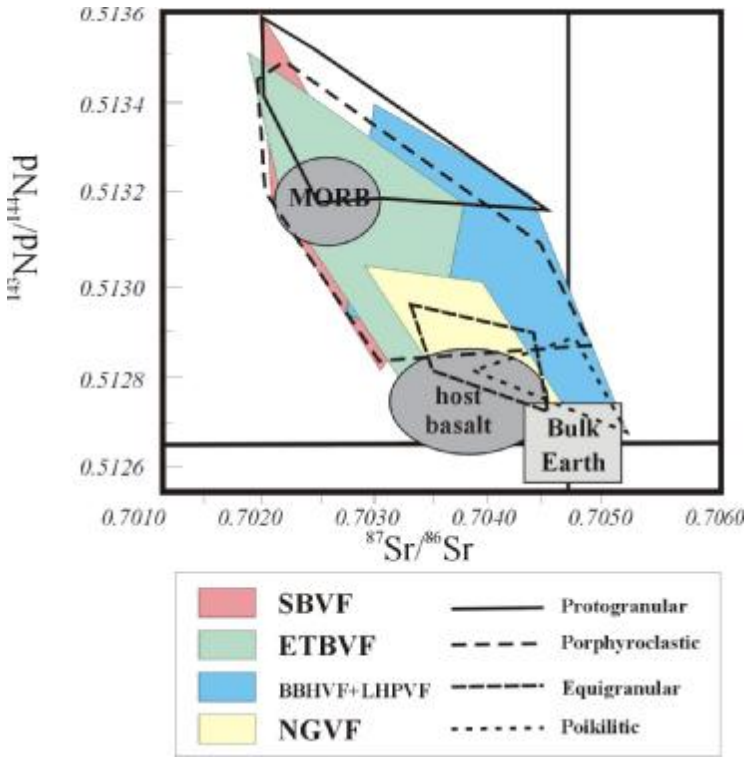

Figure VI.17 $^{143}Nd/^{144}Nd$ vs. $^{87}Sr/^{86}Sr$ isotope ranges for peridotitic mantle xenoliths from the Intra-Carpathian Basin System from leached clinopyroxenes with respect to xenolith location and texture. Isotopic data of the SBVF from Vaselli et al. (1996) and Bali et al. (submitted); LHPVF and BBHVF from Downes et al. (1992); NGVF from Szabó et al. (unpublished); ETBVF from Vaselli et al. (1995); isotopic range of 'host basalt' from Salters et al. (1988). MORB and Bulk Earth values are also indicated, data from Hart (1984).

VII. Physical conditions in the upper mantle beneath the Intra-Carpathian Basin System

Peridotite xenoliths derived from the upper mantle not only provide information on the chemical composition of the mantle (see Chapter VI.), but they also offer a unique opportunity to study physical conditions (temperature, oxygen fugacity and pressure) characterizing the subcontinental lithospheric mantle. Moreover, geochemical features (depletion and enrichment processes) could be correlated with the estimated physical conditions.

This chapter summarizes geothermometric and oxygen fugacity estimations carried out on peridotitic xenoliths analyzed in the last few decades. The aim of this chapter is twofold: 1) to construct a coherent picture of the thermal state and oxygen fugacity of the upper mantle beneath the Pannonian Basin system and to explore the relation of deformation state of the represented upper mantle to the estimated equilibrium temperatures and oxygen fugacity; 2) to trace the reliance between estimated equilibrium temperatures, oxygen fugacity and the geochemical variation in the peridotite xenoliths. Equilibrium pressure estimations will not be covered due to large uncertainties in the methods and the lack of adequate paleogeobarometer in the spinel lherzolite field. However, petrographic evidence of earlier high-pressure phases and their information on the evolution of the physical state of the mantle will be discussed in Chapter VIII.

VII.1 Paleogeothermometry

Most of the geothermometers used to estimate crystallization temperatures of mineral assemblages assume chemical equilibrium between co-existing phases. This is generally the starting condition for most of the thermometers. The main theoretical basis of these thermometers is the exchange or transfer reactions between coexisting minerals. In reliable thermometers these reactions are mostly temperature dependent and largely independent on pressure. The applicability and effectiveness of thermometers can be shown if a certain exchange or transfer reaction is both available for simple and complex systems (e.g., Brey and Köhler, 1990).

In the following section the thermometer most frequently used in the spinel lherzolite environment (Brey and Köhler, 1990) will be treated in detail. The effect of

chemical compositions will also be tested and a coherent picture of the thermal state of the mantle using the most reliable geothermometer will be given.

Two-pyroxene thermometer

The two-pyroxene thermometer of Brey and Köhler (1990) was constructed using experimental results in the simple CMS (Calcium-Magnesium-Silicon) system. The system was mathematically treated with valid thermodynamic solution models for mixing properties of coexisting pyroxenes. Empirical models (Bertrand and Mercier, 1985; Finnerty and Boyd, 1987) served as a basis for the empirical barometer. Moreover, additional non-ideality parameters for clinopyroxene were also needed to reproduce very well experimental results obtained in the CMS system. The simple system used for thermobarometric calibration is useful because it is less susceptible to analytical errors due to fewer fitted parameters.

Brey and Köhler (1990) found that $(\ln K_D)^2$ of the transfer reaction of En(opx) = En(cpx) is linearly dependent on inverse temperature, where

$$K_D = (1\text{-}Ca^{M1})^{cpx}/(1\text{-}Ca^{M2})^{opx} \quad (1)$$

This linear relation, in contrary to curved relation between $\ln K_D$ and inverse temperatures, enables treating the CMS system as entirely ideal (Brey and Köhler, 1990). Similar relation was found in the experiments (Brey and Köhler, 1990) on natural systems.

The following equation was found to give appropriate results in natural systems:

$$T = [23058 + 38.4P]/[14.12 + (\ln K_D^*)^2] \quad (2)$$

This equation reproduces experimental data to ± 16 ^oC (1σ) in natural systems. The equation is based on the assumption that the occurrence of Ca is restricted to the M2 site of the pyroxenes and that Mg in the M1 site of clinopyroxene equals to that of Mg in the M1 site of orthopyroxene. Although in natural systems, instead of K_D K_D^* term is used, because of necessary Na correction (see later).

The assumption of equal Mg on M1 sites in both pyroxenes is not entirely fulfilled in the CMAS (Calcium-Magnesium-Aluminum-Silicon) system because of Mg-Al interaction on the M1 site in both pyroxenes. Therefore, interaction between the two pyroxenes may not be treated as ideal. This non-ideal behavior results in larger errors of temperature estimations (60 ^oC – 1σ). Nevertheless, ideal behavior is

found again in the CMASCr (Calcium-Magnesium-Aluminum-Silicon-Chromium) system (Brey and Köhler, 1990). It seems likely that Cr-Ca cross-site interactions counterbalance Ca-Al interactions (Nickel, 1989). Thus, the behavior of the system can be treated ideal.

As mentioned above for natural systems, correction for Na is necessary, using the following equation constructed on theoretical basis:

$$Ca^* = Ca^{M2}/(1-Na^{M2}) \quad (3)$$

and K_D (1) changes to

$$K_D^* = (1-Ca^*)^{cpx}/(1-Ca^*)^{opx} \quad (4)$$

The importance and effectiveness of Na correction was shown by Mori and Green (1978). This correction enabled quite good reproduction of experimental temperatures.

The effect of Al is counterbalanced by Cr and the correction for Na is also included in the equation for natural systems. The only element which causes deviation from equation 2 is Fe. The presence of Fe creates strong decrease in Ca in the clinopyroxenes, whereas the Ca content of coexisting orthopyroxenes slightly increases (Davidson and Lindsley, 1985). With the Fe correction for natural systems, the following equation reproduces best experimental conditions:

$$T_{BKN} = \frac{23664 + (24.9 + 126.3 \cdot (X_{Fe}^{cpx})P}{13.38 + (\ln K_D^*)^2 + 11.59 \cdot (X_{Fe}^{opx})}, \quad (5)$$

where T is in kelvin, P in kilobars (Brey and Köhler, 1990). The thermometer reproduces experimental temperatures to ± 15°C (1σ). The equation has the advantage that it does not show systematic dependence either on temperature or pressure or compositional parameters. Moreover, the equation can be applied to wide range of compositions from virtually Fe free compositions of pyroxenes down to mg-numbers of 89 and even to mg-numbers of 85-80 with minimal errors (Brey and Köhler, 1990).

All equilibrium temperatures were estimated at 10 and 25 kbar confining pressures, also to test pressure dependence of the thermometer. Different pressures resulted in ~30°C (≈2σ) difference between lower and higher pressures. This encouraged the author to represent temperature data of the lower pressure estimation (see results given below)

VII.2 Oxygen fugacity (oxygen barometry)

The highly heterogeneous nature of the oxidation state of peridotitic upper mantle is well known and was recognized in several studies (e.g., Ballhaus et al., 1990; Ballhaus, 1993). The variance is large that differences in oxygen fugacity within the mantle may reach 4 orders of magnitude. The oxidation state of a specific mantle section (or domain) is a fundamental physical property, which among others influences the pressure and temperature position of the mantle solidus and also the composition of the mantle derived melts and fluids. Moreover, it may also influence a large number of geophysical properties and even the deformation characteristics of the mantle (e.g., Taylor and Green, 1987).

Spinel, a common phase in mantle derived material carries valuable information on the oxidation state of the mantle represented by the studied sample. Spinel is the only common mantle phase in spinel lherzolites which, due to its crystal structure may contain considerable amounts of Fe^{3+} besides Fe^{2+}(e.g., Ballhaus et al., 1990). The oxygen barometer of Ballhaus et al. (1991), which is a widely used technique for mantle materials, uses the following redox reaction:

Fayalite + O_2 = **M**agnetite + **Q**uartz (FMQ)

These parameters are gained from the sample analyzing both olivine and spinel compositions. Independent pressure and temperature estimates are also required to solve the oxygen barometry equation of Ballhaus et al (1990):

$$\Delta \log(f_{O_2})^{FMQ} = 0.27 + 2505/T - 400P/T - 6\log(X_{Fe}^{ol}) - 3200(1 - X_{Fe}^{ol})^2/T$$
$$+ 2\log(X_{Fe^{2+}}^{sp}) + 4\log(X_{Fe^{3+}}^{sp}) + 2630(X_{Al}^{sp})^2/T$$

where P is in GPa, T in K, $X_{Fe^{3+}}^{sp}$ and X_{Al}^{sp} the $Fe^{3+}/\sum R^{3+}$ and $Al/\sum R^{3+}$ ratios in spinel and X_{Fe}^{ol} and $X_{Fe^{2+}}^{sp}$ the ($Fe^{2+}/(Fe^{2+}$ + Mg) ratios in olivine and spinel, respectively.

Samples studied in this work and those from the literature dealing with peridotite xenoliths from the Intra-Carpathian Basin System (Downes et al., 1992; Szabó and Taylor, 1994; Szabó et al., 1995a; Vaselli et al., 1995, 1996; Embey-Isztin et al., 2000) were plotted in oxygen fugacity vs. temperature diagram (Figure VII.1-5). Variables for the equation were taken from measured chemical compositions, pressure was assumed to be constant (1 GPa) for all samples, whereas equilibrium temperatures used in the equation were calculated according to the method of Brey

and Köhler (1990; T_{BKN}) see details above. It is noteworthy that using 1 GPa for all samples generates an error in the estimations. The effect of pressure on oxygen fugacity was also tested. The result is a decrease of $\Delta\log fO_2$ (FMQ) by 0.015-0.2 units for 0.1 GPa. Typical values for $\Delta\log fO_2$ (FMQ) in materials derived from the sub-continental lithospheric mantle are between FMQ 1 to FMQ-2 (e.g., Ballhaus, 1993). It is strongly suggested that the increase of $\Delta\log fO_2$ (FMQ) is controlled by water rich subduction related oxidizing fluids (e.g., Ballhaus, 1993). Nevertheless, the depletion process of the mantle may also control oxygen fugacity, because depleted peridotites are poorer in Fe than fertile ones, and the buffer capacity of Fe^{2+} is much lower (Ballhaus, 1993).

Thermal and oxidation state of the upper mantle beneath the Intra-Carpathian Basin System will be reviewed according to the earlier chapters. Noted that temperature and oxygen fugacity values were estimated for 1 GPa.

VII.3 Temperature and oxygen fugacity of the peridotite xenoliths

SBVF

Mantle xenoliths from the Styrian Basin Volcanic Field display a relatively narrow range in equilibrium temperatures and adjoining oxygen fugacity values. Equilibrium temperatures range from almost 1200 ^{o}C to temperatures somewhat above 900 ^{o}C (Table V.1, Figure VII.1). Oxygen fugacity values, although cover a range between –1.5 - 1.25 (FMQ), they generally fall above the FMQ buffer regardless of xenolith texture (Figure VII.1). Although the variability in textures is quite restricted in the region. Slight negative correlation of oxygen fugacity with increasing temperature is observed. Similar results were obtained from MORB samples by Ballhaus (1990). Porphyroclastic xenoliths seem to have somewhat lower equilibrium temperatures than protogranular ones (940-1080; 910-1180 ^{o}C, respectively). However this difference is not significant. Even less pronounced difference is observed in oxygen fugacities (Table V.1, VII.1, Figure VII.1).

Samples selected for detailed microstructural study display values coinciding with equilibrium temperatures and oxygen fugacity values of xenoliths earlier studied. Equilibrium temperature is the highest (1130 ^{o}C) for sample Kf3, whereas the lowest temperatures for Kpfs17 are still above 1000 ^{o}C (1015 ^{o}C). The oxygen fugacity

values, similarly to those earlier studied (e.g., Vaselli et al., 1996) fall close to the QFM buffer (Table V.1, VII.1)

Location	SBVF			
Sample	Kf3	Kf4	Kf5	Kf17
Texture	pr	pr/po	po	pr
$T_{B\&K}$	1128	1076	1057	1014
• $\log fO_2$	-0.5	0.37	0.43	-0.37

Table VII.1 T – equilibrium temperature and $\Delta\log fO_2$ – oxygen fugacity estimated for mantle xenoliths from the SBVF using the method of Brey and Köhler (1990) and Ballhaus et al. (1990), respectively. Data from Vaselli et al. (1996).

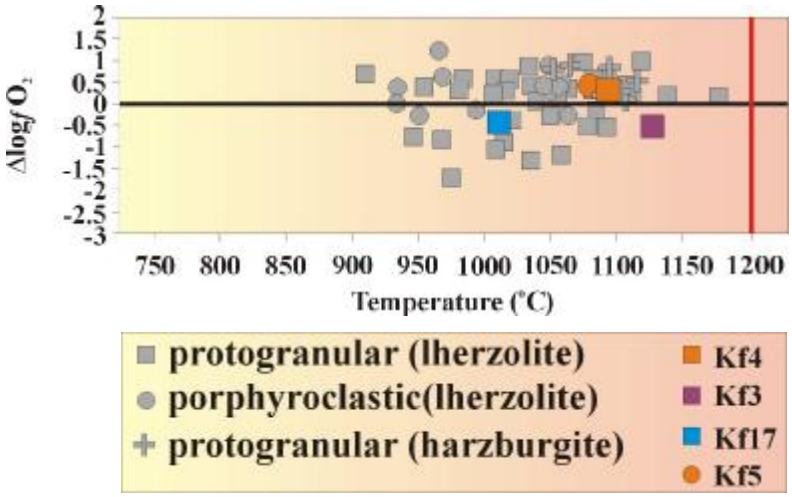

Figure VII.1 Equilibrium temperature vs. Δoxygen fugacity (ΔFMQ) diagram for mantle peridotites from the SBVF with respect to xenolith textures. Samples selected for detailed microstructural study are highlighted. Equilibrium temperatures were calculated using the method of Brey and Köhler (1990), oxygen fugacity according to Ballhaus et al. (1990). Horizontal black line denotes FMQ-0, vertical red line at 1200 °C indicates 'recent' realistic maximum temperature for the lithosphere in the region. Data from Kurat et al. (1991), Vaselli et al. (1996), Falus et al. (2000), Embey-Isztin et al. (2001).

Textural connection to the oxygen fugacity is more clearly observed on the oxygen fugacity vs. cr-number of spinel diagram (Figure VII.2). Xenoliths with protogranular textures generally plot to the low ΔFMQ, low cr-number end of the diagram. Harzburgites with protogranular texture (supposedly of secondary origin) are found on the high end of the plot (Figure VII.2).

Selected samples, with the exception of Kf5, display low cr-numbers (~0.08, 0.17, respectively) with variable oxygen fugacity values (-0.49-0.43).

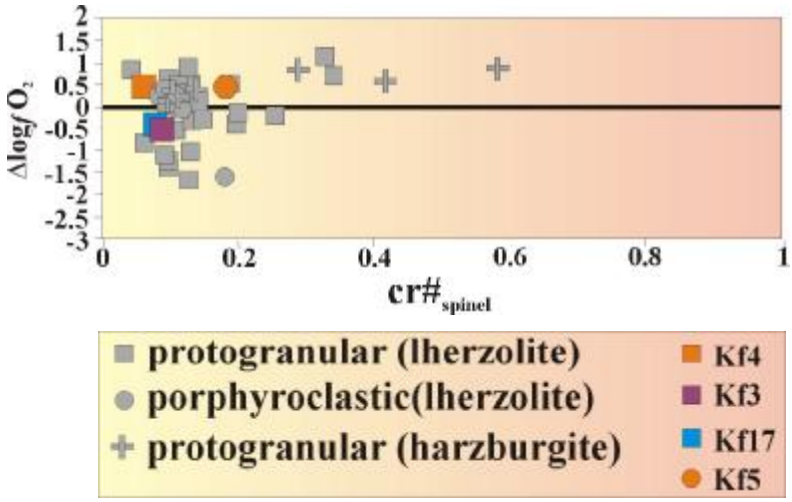

Figure VII.2 $Cr\#_{spinel}$ vs. Δoxygen fugacity (ΔFMQ) diagram for mantle peridotites from the SBVF with respect to xenolith textures. Samples selected for detailed microstructural study are highlighted. Oxygen fugacity calculated according to Ballhaus et al. (1990). Horizontal black line denotes FMQ-0. Data from Kurat et al. (1991), Vaselli et al. (1996), Falus et al. (2000), Embey-Isztin et al. (2001).

LHPVF

Mantle xenoliths from the LHPVF have porphyroclastic to secondary recrystallized textures. Equilibrium temperatures are somewhat lower than those estimated for the SBVF samples. For most of the xenoliths it is below 1000 ^{o}C down to around 800 ^{o}C (Table V.1; Figure VII.3). However, some of them fall close to 1150 ^{o}C (Table V.1; Figure VII.3). Oxygen fugacity values are remarkably lower than those observed for SBVF going down to FMQ –2. Significant correlation between xenolith textures and estimated equilibrium temperatures is observed (Table V.1; Figure VII.3). Porphyroclastic xenoliths plot to the high temperature-low oxygen fugacity part of the diagram, whereas secondary recrystallized xenoliths display low temperature and high oxygen fugacity (Table V.1, VII.2; Figure VII.3). Although some exceptions (Gko07) do occur, a marked negative correlation between equilibrium temperature and ΔFMQ is observed. Similar distribution was found for MORB samples (Ballhaus, 1990).

Location	LHPVF										
Sample	GC03-05(BH55)	GC03-10 (BH42)	GC06	GC08	Gko07	Gko07	GC03-06	GC03-06	GC03-12	GC03-12	GC03-12
Texture	po	po/equ	po	po/equ	po/equ	po/equ	po	po	po	po	po
					pc-core	pc-rim	pc-core	pc-rim	pc-core	pc-rim	rec
$T_{B\&K}$	995	960	960	788	1125	1148	902	823	857	920	864
• logfO_2	-3.24	0.19	-0.03	1.41	1.17	0.75	-1.42	-0.68	-0.45	-1.2	-1.67

Table VII.2 T – equilibrium temperature and $\Delta \log fO_2$ – oxygen fugacity estimated for mantle xenoliths from the LHPVF using the method of Brey and Köhler (1990) and Ballhaus et al. (1990), respectively. Note core-rim-recrystallized grain relations. pc – porphyroclast; rec – recrystallized grain. Some data from Szabó et al. (1995b).

Selected samples follow the main temperature-oxygen fugacity trend. The highest temperatures among the studied xenoliths are observed in xenolith GC03-05 (similar to Bh55 of Szabó and Taylor, 1994) (1000 °C) with the exception of Gko07 (~1150 °C). No clear relation between temperature and oxygen fugacity of core-rim-recrystallized grain was observed (Table V.1, VII.2; Figure VII.3).

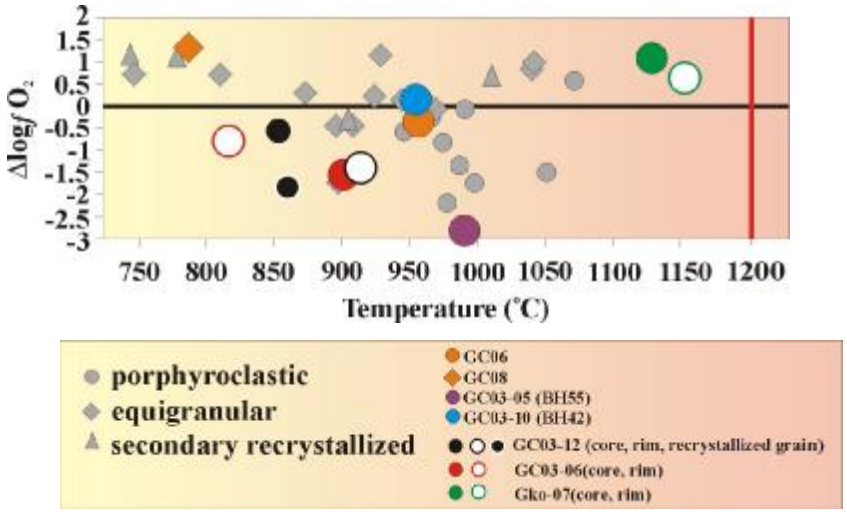

Figure VII.3 Equilibrium temperature vs. Δoxygen fugacity (ΔFMQ) diagram for mantle peridotites from the LHPVF with respect to xenolith textures. Samples selected for detailed microstructural study are highlighted. Note porphyroclast core-rim-recrystallized grain groups. Equilibrium temperatures were calculated using the method of Brey and Köhler (1990), oxygen fugacity according to Ballhaus et al. (1990). Horizontal black line denotes FMQ-0, vertical red line at 1200 °C indicates 'recent' realistic maximum temperature for the lithosphere in the region. Some data from Downes et al. (1992), Szabó et al. (1995b), Embey-Isztin et al. (2001).

The relation of textures to oxygen fugacity and cr-numbers is also clear. Less deformed samples, plot to the low $\Delta \log fO_2$ (FMQ) low cr-number end of the diagram,

whereas secondary recrystallized grains are found on the high cr-number-high $\Delta \log fO_2$ end of the plot (Figure VII.4).

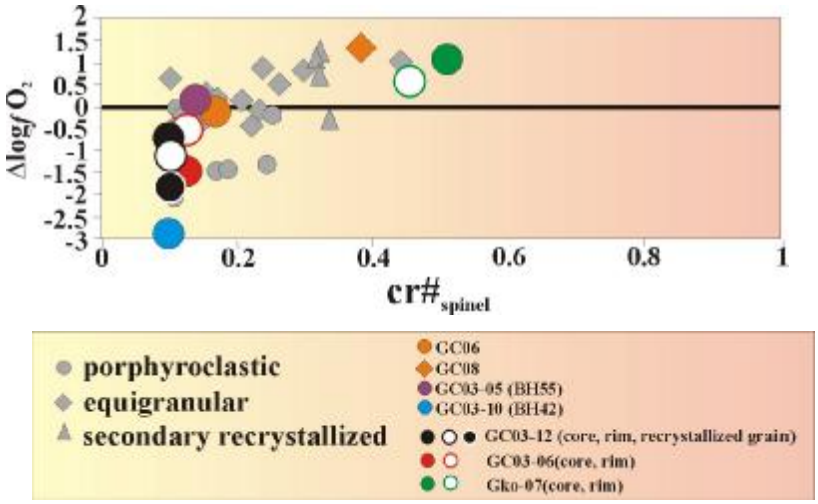

Figure VII.4 $Cr\#_{spinel}$ vs. Δoxygen fugacity (ΔFMQ) diagram for mantle peridotites from the LHPVF with respect to xenolith textures. Samples selected for detailed microstructural study are highlighted. Note porphyroclast core-rim-recrystallized grain groups. Oxygen fugacity calculated according to Ballhaus et al. (1990). Horizontal black line denotes FMQ-0. Some data from Downes et al. (1992), Szabó et al. (1995b), Embey-Isztin et al. (2001).

BBHVF

The xenolith locations of BBHVF provide the widest range of xenolith textures in the region. In fact, estimated equilibrium temperatures display the widest range from 830 to 1200 ^{o}C (Table V.1, VII.3, Figure VII.5). Despite the high variability in equilibrium temperatures, oxygen fugacity values fall in a narrow range (FMQ-1.5- 1) typical of samples derived from young subcontinantal lithospheric mantle (Ballhaus, 1993). Marked negative correlation between equilibrium temperatures and ΔFMQ-values similarly to xenoliths from the LHPVF. Clear relation between xenolith textures and temperature-oxygen fugacity values was observed (Table V.1, Figure VII.5). Similarly to LHPVF, undeformed xenoliths plot to the high temperature-low oxygen fugacity part of the diagram, whereas with increasing deformation and recrystallization xenoliths display continuously lower temperature and higher oxygen fugacity (Table V.1, VII.3, Figure VII.5).

Location	BBHVF										
Sample	Szbd-13	Szbp-15	Szbd-9	Szba1	Szbd-15	Szgk03-01	Szb21	Tih03-02	Szb03-07	Tih03-12	Tih03-13
Texture	pr	pr	pr	tab-equ	tab-equ	tab-equ	mos-equ	mos-equ	poik	poik	poik
$T_{B\&K}$	1154	1128	1070	1017	978	1009	940	1071	1093	1125	1100
• logfO_2	-2.19	-2.21	-0.55	-0.49	-0.38	0.09	-0.55	0.96	-0.24	0.09	0.67

Table VII.3 T – equilibrium temperature and $\Delta\log fO_2$ – oxygen fugacity estimated for mantle xenoliths from the BBHVF using the method of Brey and Köhler (1990) and Ballhaus et al. (1990), respectively. Data of Szb21 from Bali et al. (submitted).

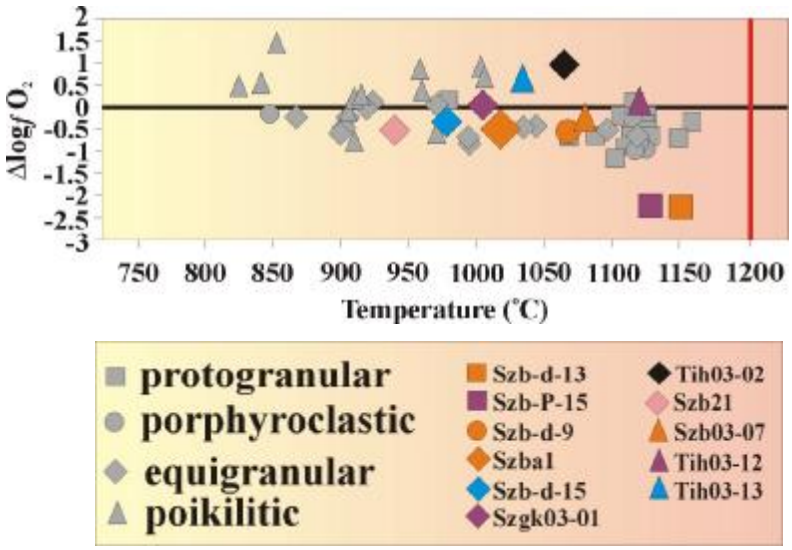

Figure VII.5 Equilibrium temperature vs. Δoxygen fugacity (ΔFMQ) diagram for mantle peridotites from the BBHVF with respect to xenolith textures. Samples selected for detailed microstructural study are highlighted. Equilibrium temperatures were calculated using the method of Brey and Köhler (1990), oxygen fugacity according to Ballhaus et al. (1990). Horizontal black line denotes FMQ-0, vertical red line at 1200 °C indicates 'recent' realistic maximum temperature for the lithosphere in the region. Some data from Downes et al. (1992), Embey-Isztin et al. (2001), Bali et al. (submitted).

Selected samples generally follow the temperature-oxygen fugacity trend of xenoliths earlier studied (e.g., Embey-Isztin et al., 2001). Protogranular samples like Szbd-13 and Szbp-15 display high equilibrium temperatures (~1150 °C) and low oxygen fugacity with typical values around QFM-2.5. Selected porphyroclastic and equigranular xenoliths follow plot to lower equilibrium temperature and higher oxygen fugacity. However, poikilitic samples from Tihany (Tih03-12, -13) reflect high equilibrium temperature (~1100°C) together with high oxygen fugacity values (~ΔFMQ 0.4).

The relation of textures to oxygen fugacity and cr-numbers is also clear. Less deformed samples plot to the low ΔFMQ low cr-number end of the diagram, whereas secondary recrystallized grains are found on the high end of the plot (Figure VII.6).

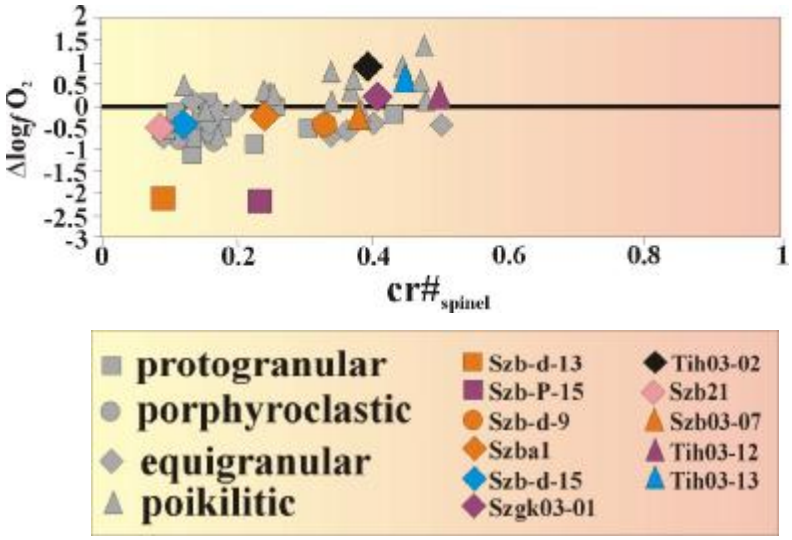

Figure VII.6 Cr#$_{spinel}$ vs. Δoxygen fugacity (ΔFMQ) diagram for mantle peridotites from the BBHVF with respect to xenolith textures. Samples selected for detailed microstructural study are highlighted. Oxygen fugacity calculated according to Ballhaus et al. (1990). Horizontal black line denotes FMQ-0. Some data from Downes et al. (1992), Embey-Isztin et al. (2001), Bali et al. (submitted).

A relation of textures to oxygen fugacity in the selected samples is also clearly observed. The least deformed samples display plot to the low cr-number-low Δlog$f$O$_2$ portion of the diagram, whereas equigranular, poikilitic xenoliths exhibit high cr-number-high Δlog$f$O$_2$ values.

NGVF

In contrast to other xenolith locations of the Intra-Carpathian Basin system, samples from the NGVF cluster in a narrow temperature (~1000-900^{o}C) and oxygen fugacity range (ΔFMQ-1.5-0). No significant difference between porphyroclastic and equigranular samples was observed (Figure VII.7). However, secondary recrystallized xenoliths, similarly to the other xenolith locations reflect low equilibrium temperatures and high oxygen fugacity (Table V.1, VII.4; Figure VII.7). No clear relation between the temperature and oxygen fugacity values is observed.

Location	NGVF		
Sample	NBN27	NBN30	NFL15
Texture	equ	equ	equ
$T_{B\&K}$	1004	919	939
• logfO_2	-0.45	-0.5	-1.02

Table VII.4 T – equilibrium temperature and ΔlogfO_2 – oxygen fugacity estimated for mantle xenoliths from the NGVF using the method of Brey and Köhler (1990) and Ballhaus et al. (1990), respectively. Data from Szabó and Taylor (1994).

Selected samples (NBN27, NBN30 and NFL15), all equigranular plot well within the field defined by other equigranular xenoliths of the volcanic field (920-1000 ^{o}C; ΔFMQ-1- -0.4; Table V.1, VII.4; Figure VII.7).

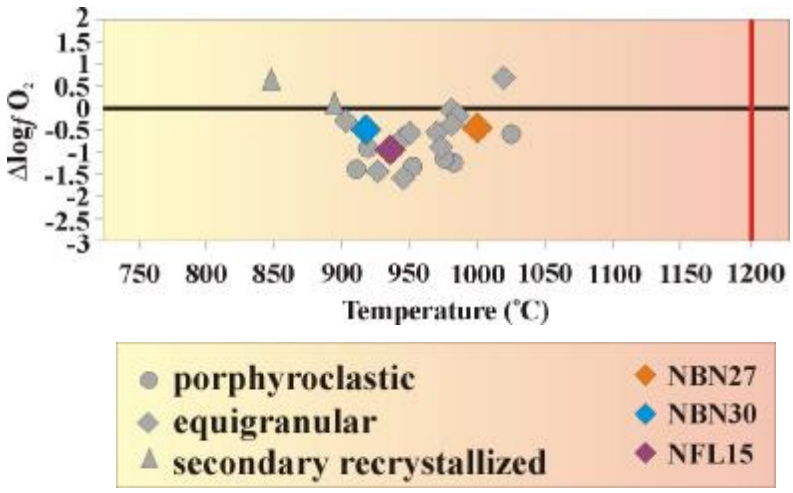

Figure VII.7 Equilibrium temperature vs. Δoxygen fugacity (ΔFMQ) diagram for mantle peridotites from the NGVF with respect to xenolith textures. Samples selected for detailed microstructural study are highlighted. Equilibrium temperatures were calculated using the method of Brey and Köhler (1990), oxygen fugacity according to Ballhaus et al. (1990). Horizontal black line denotes FMQ-0, vertical red line at 1200 ^{o}C indicates 'recent' realistic maximum temperature for the lithosphere in the region. Data from Szabó and Taylor (1994) and Konecny et al (1995).

Despite the lack of any remarkable correlation in the T vs. ΔFMQ plot (Figure VII.7), the oxygen fugacity vs. cr-numbers plot clearly defines a strong trend. Similarly to all other locations, the texturally most primitive xenoliths plot to the low ΔFMQ low cr-number end of the diagram, whereas with increasing deformation and recrystallization, samples tend to display higher oxygen fugacity higher cr-number

defining a marked positive correlation of cr-numbers and ΔFMQ (Table V.1, VII.4; Figure VII.8). Selected xenoliths do not deviate from this defined trend.

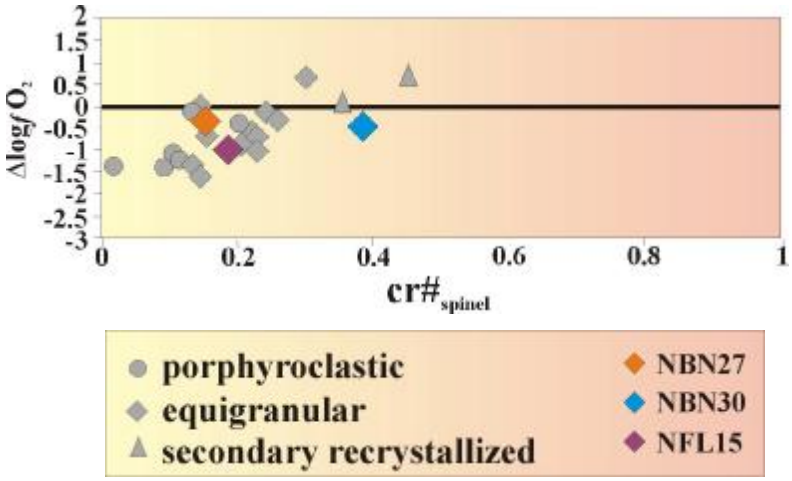

Figure VII.8 $Cr\#_{spinel}$ vs. Δoxygen fugacity (ΔFMQ) diagram for mantle peridotites from the NGVF with respect to xenolith textures. Samples selected for detailed microstructural study are highlighted. Oxygen fugacity calculated according to Ballhaus et al. (1990). Horizontal black line denotes FMQ-0. Data from Szabó and Taylor (1994) and Konecny et al (1995).

ETBVF

Mantle xenoliths from the ETBVF, similarly to those of SBVF represent relatively low textural variability. Peridotitic samples derived from the region are mostly protogranular or porphyroclastic (addressed as "foliated"). Nevertheless, some rare xenoliths with mylonitic textures (described in detail in Chapter V. and Falus et al. in prep.) are also found. Equilibrium temperatures are low (750-1030 ^{o}C) and oxygen fugacity values displayed are also relatively low compared to the other xenolith locations (ΔFMQ-2.5- 1; generally close to or below FMQ). A remarkable positive correlation between equilibrium temperatures and oxygen fugacity values is observed (Table V.1, VII.5; Figure VII.9). Xenoliths with undeformed texture display the highest equilibrium temperatures and highest oxygen fugacity values, whereas with more intense recrystallization xenoliths tend to display lower oxygen fugacity and equilibrium temperature values (Figure VII.9). Such trends were found in old lithospheric material (Ballhaus, 1993).

Location	ETBVF											
Sample	BG18	BG15	LGR09	LGR09	Rk99/04	Rk99/04	LGR03-01	LGR03-01	LGR-03-01	NVTR03-01	NVTR03-01	NVTR03-01
Texture	pr	fol	fol pc	myl rec	myl pc	myl rec.	myl pc-core	myl pc-rim	myl rec	myl pc-core	myl pc-rim	myl rec
$T_{B\&K}$	1024	805	785	899	707	971	908	857	864	886	893	920
• $\log fO_2$	-0.76	-0.6	-1.22	-1.38	-0.05	0.05	-1.6	-1.09	-1.51	-1.98	-2.63	-1.78

Table VII.5 T – equilibrium temperature and $\Delta \log fO_2$ – oxygen fugacity estimated for mantle xenoliths from the LHPVF using the method of Brey and Köhler (1990) and Ballhaus et al. (1990), respectively. Note core-rim-recrystallized grain relations. pc – porphyroclast; rec – recrystallized grain. Some data from Vaselli et al. (1995).

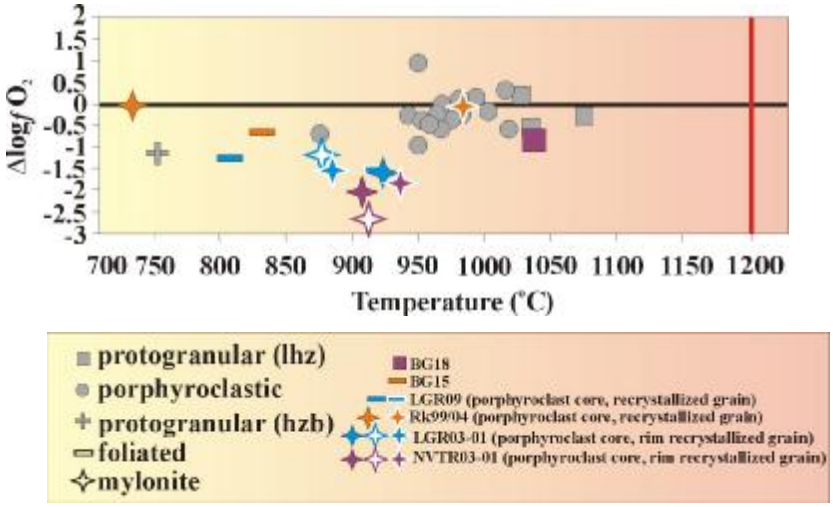

Figure VII.9 Equilibrium temperature vs. Δoxygen fugacity (ΔFMQ) diagram for mantle peridotites from the ETBVF with respect to xenolith textures. Samples selected for detailed microstructural study are highlighted. Note core-rim-recrystallized grain groups for foliated and mylonitic xenoliths. Equilibrium temperatures were calculated using the method of Brey and Köhler (1990), oxygen fugacity according to Ballhaus et al. (1990). Horizontal black line denotes FMQ-0, vertical red line at 1200 ^{o}C indicates 'recent' realistic maximum temperature for the lithosphere in the region. Some data from Vaselli et al. (1995). Note, xenoliths with protogranular/porphyroclastic textures plot to the higher ΔFMQ part of the diagram.

Most of the selected samples follow the overall trend defined by the mantle xenoliths earlier studied (Vaselli et al., 1995). At the joint occurrence of porphyroclasts and recrystallized grains, equilibrium temperatures and oxygen fugacity values of the different grain generations were analyzed. With the exception of a mylonite (LGR03-01), recrystallized grains reflect remarkably higher equilibrium temperatures (30-200 ^{o}C; Table V.1, VII.5, Figure VII.9) with only minor differences (~0.5) in oxygen fugacity with respect to porphyroclasts.

The selected samples also follow the steep trend defined by xenoliths earlier studied. Difference in porphyroclasts and neoblasts in the selected samples is only controlled by minor variance in the ΔFMQ values (Table V.1, VII.5).

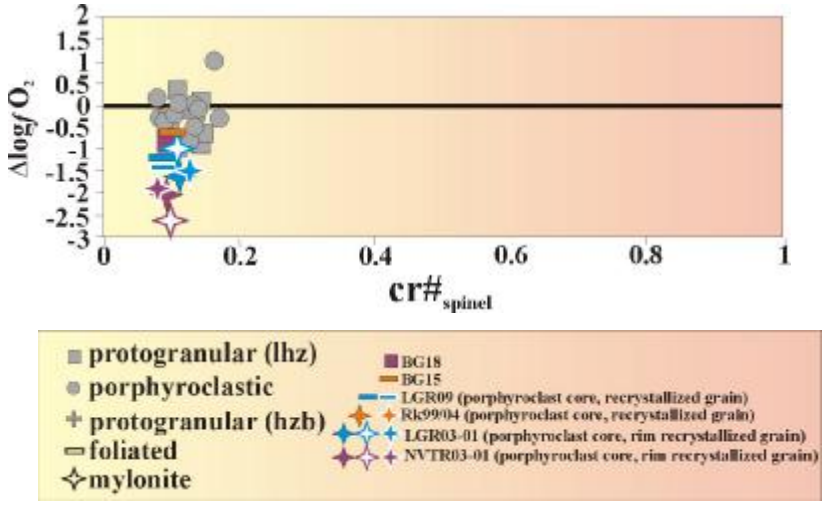

Figure VII.10 $Cr\#_{spinel}$ vs. Δoxygen fugacity (ΔFMQ) diagram for mantle peridotites from the ETBVF with respect to xenolith textures. Samples selected for detailed microstructural study are highlighted. Note core-rim-recrystallized grain groups for foliated and mylonitic xenoliths. Oxygen fugacity calculated according to Ballhaus et al. (1990). Horizontal black line denotes FMQ-0. Some data from Vaselli et al. (1995).

VIII. Discussion

VIII.1 The effect of annealing on olivine fabrics

Most of the mantle derived xenoliths world wide undoubtedly experienced to some extent certain static recrystallization and annealing. Petrographic evidence for such processes are straight, gently curved grain boundaries and the lack of subgrains and undulouse extinction in the crystals (Passchier and Trouw, 1995). Static grain growth is also evidenced by abundant triple junctions. Peridotitic upper mantle fragments, displaying such textural features, are often addressed as equigranular texture (e.g., Mercier an Nicolas, 1975). It is widely accepted that annealing and static recrystallization is a thermally induced process (Lloyd et al., 1997), however, the presence of migrating fluids and/or melts may also assist or at least influence the recrystallization process. Thus, annealing may take place *in situ* in the mantle after the cessation of deformation if mantle temperatures are high enough (>800-900 ^{o}C) (e.g., Harte et al., 1977; Mercier an Nicolas, 1975). On the other hand, a subsequent thermal and geochemical impulse related to rising of hot asthenospheric material, as demonstrated for mantle material of various origins (Van der Wal and Bodonier, 1996, Vauchez and Garrido, 2001, Xu et al., 2003), may also result in annealing and static recrystallization. Finally, transport of mantle xenoliths in their host magmas may also reside in static recrystallization as suggested for some kimberlite-hosted xenoliths (Mercier, 1979).

Annealing, as displayed by their textural characteristics, is a distinctive process in the lithospheric upper mantle represented by most of the xenoliths from the central part of the Intra-Carpathian Basin System. It is strongly suggested that annealing was related to asthenospheric upwelling, which was the most intensive beneath the central portion of the basin (Huismans, 2001). It is thus a relevant question how lattice preferred orientation (LPO) of olivines formed during deformation, predating annealing, survive static recrystallization.

Detailed fabric analysis was carried out on peridotite massifs, ophiolites and mantle xenoliths that have experienced intensive static recrystallization due to intense interaction with (hot) asthenospheric material observed both in their textural and geochemical characteristics (Van der Wal and Bodonier, 1996, Vauchez and Garrido,

2001; Xu et al., 2003; Vauchez and Tommasi, 2003). These studies clearly demonstrated that original lattice preferred orientations are well preserved after static recrystallization. Effect of the presence of migrating fluids during annealing was also discussed in these studies. Samples that have undergone the most percolation of migrating melts/fluids, geochemical modification by these fluids and the precipitation of new phases observed display very weak olivine LPO, whereas those showing moderate geochemical modification display only slight changes in olivine LPO (Vauchez and Tommasi, 2003).

Studied xenoliths from the Intra-Carpathian Basin System all exhibit weak to strong LPO. The decisiveness of LPOs is suggested to be dependent on the number of olivine grains analyzed but also is believed to be influenced by annealing and static recrystallization. To test the influence of the number of olivines analyzed in the decisiveness of experienced LPO olivine orientations were selected randomly from two xenoliths with relatively strong LPO (Figure VIII.1). Results clearly show that marked difference from the original patterns (100 olivines) only resides at very low projected orientations (~10). Above this critical number, only minor changes with respect to the projection of 100 grains are observed. This suggests that in xenoliths, displaying weak fabric, either olivine patterns were originally weak or they were modified during annealing and static recrystallization. Most of the weak LPOs are related to equigranular or poikilitic xenoliths (e.g., Szbd-10, Szba2, Tih03-02, Szb03-07, Szbd-8, GC03-05; Figure V.5, 10). Some of these xenoliths (Szbd-8) still contain orthopyroxene porphyroclasts with lobated grain boundaries (Figure IV.9), displaying textural indication of percolating reactive melts during annealing and static recrystallization. Similar textural features in ophiolites were described by Dijkstra et al. (2002). These studies demonstrated that the specific occurrence of lobated orthopyroxene porphyroclasts is a strong sign for the migration and interaction of reactive melts. Intensive reaction of peridotite wall rock with percolating melts may indeed change and reset original lattice preferred orientation in mantle xenoliths (e.g., Vauchez and Tommasi, 2003).

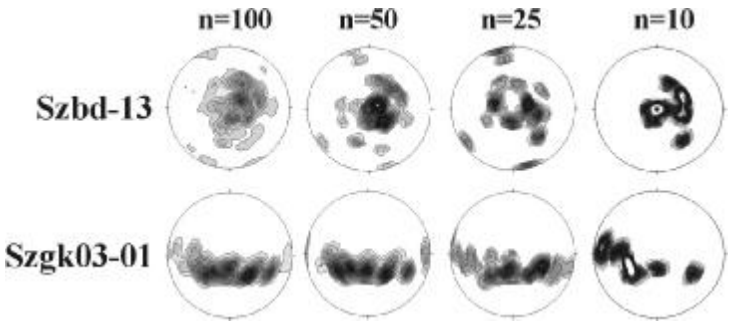

Figure VIII.1 Olivine [001] orientation patterns in two samples from the BBHVF (Szgk03-01) and the ETBVF (LGR09). The orientation patterns contain 100-10 olivine [001] orientations randomly selected from the database. Note, that significant deviance from the pattern of 100 grains only occurs at n=10. Lower hemisphere, equal area projection. Data contoured at 1, 2, 3,… times uniform distribution

However, it seems that recrystallization was not intense enough to fully erase lattice preferred orientations. Weak to strong lattice preferred orientation in all selected xenoliths was clearly observed. Orientation distribution of olivine axes in samples with weak lattice preferred orientation shows a strong scatter on these plots. However, a systematic girdle of olivine [100]-axes toward [010]-axes is clearly observed in all cases (e.g., Figure V.10). This feature is not related to any known slip system in olivine. Girdle of [100]- and [010]-axes, at least partly, is attributed to dynamic recrystallization and progressive misorientation (Tommasi et al., 2000). Although, probably annealing and static recrystallization may have remarkable influence on the observed pattern. In fact, similar patterns, though more pronounced were found in xenoliths from Kaapval craton (Tommasi et al., 2000). This could mean that deformation/recrystallization processes that drive the development of such specific orientation patterns are confined to rigid the lithosphere.

An important question arises whether or not the systematic occurrence of girdles of [100]- and [010]-axes are in any way related to the presence of percolating melts? Anisotropy of melt distribution and the resulting anisotropy in the permeability of mantle rocks is enhanced by lattice preferred orientation of constituent mineral phases, primarily olivine. Basaltic melts preferably wet (010) faces of olivine (e.g., Waff and Faul, 1992; Daines and Kohlstedt, 1997) because the liquid/solid interfacial energies are the lowest on this face (Waff an Faul, 1992). It is possible that static recrystallization was dominated by the minimization of melt/solid interfacial

energies. This resulted in the crystallization of neoblasts with specific orientations that contribute to the systematic changes in the lattice preferred orientation..

VIII.2 Relation between equilibrium temperatures and deformation patterns

Equilibrium temperatures of basalt hosted mantle fragments can be estimated using major element compositions of constituent mineral phases (see Chapter VII. for details; e.g., Brey and Köhler, 1990). These equilibrium temperatures are believed to represent thermal state of the lithospheric mantle at the instance they were sampled by the host alkali basalts (e.g., Szabó et al., 1995a). Nevertheless, equilibrium temperatures estimated for xenoliths are applicable for relative comparison at least for samples derived from the same volcanic vent.

The estimated equilibrium temperatures are suggested to provide information on the relative position of mantle portions represented by the xenoliths within one xenolith location. Thus, higher equilibrium temperatures (e.g., protogranular xenoliths from the BBHVF) represent deeper mantle portions, whereas lower equilibrium temperatures of equigranular xenoliths from the same location are characteristic for shallower mantle sections. Although, it must be noted that the estimation of equilibrium temperatures by the thermometer applied for the selected samples (Brey and Köhler, 1990) is based on solid state element diffusion, grain size also has a marked effect on the resulting temperatures. This is because the closure temperature of diffusion is among other factors strongly dependent on grain-size (Dodson, 1973; Spear, 1993). Nevertheless, the deviations in equilibrium temperatures related to grain size differences are believed not to have influenced the equilibrium temperatures reasonably.

A comparison of deformation fabrics and related equilibrium temperatures was only carried out at xenolith locations where the olivines in the studied xenoliths displayed variable LPOs. Moreover, sufficient number of deformed xenoliths was available for a detailed textural study. Based on these limiting criteria the samples from only four of the five principal xenolith locations (LHPVF, BBHVF, NGVF and ETBVF) were selected for further analysis.

Xenoliths with high temperature deformation (slip on the (010)[100] system)

Orientation patterns from the selected xenolith localities can be classified into three major groups. The first group, which is present in all four localities is the one where olivine axis orientations display point maximum distributions parallel to the macroscopic lineation in the foliation plane (olivine [100]-axes), perpendicular to the lineation in the foliation plane (olivine [001]-axes) and perpendicular to both the foliation plane and the lineation (olivine [010]-axes) (Figure V.2, 3, 6, 11, 12), all with high multiples of uniform distribution. This type of distribution is frequently observed in deformed mantle rocks world wide (e.g., Mercier and Nicolas, 1975; Van der Wal and Bodonier, 1996; Dijkstra et al., 2001). The orientation distribution corresponds to dislocation creep deformation (intracrystalline glide) on the high temperature (>1000 ^{o}C) (010)[100] slip system (e.g., Carter and Avé Lallemant, 1970). Misorientation analysis of these samples, namely Szbd-13 (Figure V.20) from the BBHVF and GC03-10 (Figure V.16) of LHPVF shows that rotation axes of low angle grain boundaries cluster close to [001]-axis and also suggests for slip on the (010)[100] slip system. The mantle xenoliths that exhibit this specific orientation pattern from the LHPVF, BBHVF (central portion) reflect the highest equilibrium temperatures among xenoliths from the xenolith locations (Figure VII.3, 5). Moreover, these high-T xenoliths also display low oxygen fugacity values (Table VII.2, 3; Figure VII.3, 4, 5, 6). The studied NGVF samples, however, reflect olivine orientation pattern, which suggests high temperature dislocation creep in the (010)[100] slip system. These xenoliths exhibit various but generally relatively low equilibrium temperatures (1000-900 ^{o}C) and oxygen fugacity values close to the QFM buffer (Figure VII.7). Similarly, xenoliths from the ETBVF with olivine LPOs indicating slip on the (010)[100] slip system all exhibit the lowest equilibrium temperatures (800-900^{o}C), and oxygen fugacity values (Figure VII.9). It is more than interesting that ETBVF samples all reflect low equilibrium temperature values with respect to other xenolith locations of the Intra-Carpathian Basin System. This feature is most likely related to the peripheral position of the ETBVF within the studied region, however their different origin (TISZA-microplate) with respect to other xenolith locations (ALCAPA-microplate) in the Intra-Carpathian Basin System should be noted (e.g., Csontos, 1995; Figure II.1). It is possible that the lithospheric mantle of the TISZA-block had a different evolution from that of the ALCAPA, reflected in the difference in their thermal (and oxidation) state (Figure VII.9, 10).

Xenoliths with deformation on multiple slip systems

The second type of olivine LPO is characterized by strong point maximum of olivine [010]-axes perpendicular to the foliation, whereas [100]- and [001]-axes exhibit girdles around the foliation plane. The [010] and [001]-axes display high multiples of uniform distribution, whereas [100] axes show low- intermediate values. This type of orientation pattern is solely observed in xenoliths from the LHPVF and BBHVF (Figure V.4, 7, 8), whereas only one weak indication for this orientation type was found among the NGVF xenoliths (Figure V.11; NMS032).

Olivines in xenoliths displaying such orientation distributions are only rarely reported in natural samples (e.g., Mercier and Nicolas, 1975; Tommasi et al., 2000; Dijkstra, 2001), however, do occur in high-T-p experimental runs (e.g., Zhang et al., 2000). Misorientation analysis of these samples clearly indicates a double maximum distribution of rotation axes of low misorentation angle grain boundaries plotting close to the [001]- and the [010]-axis, however, girdles of these axes are also observed. This distribution pattern suggests that beside the (010)[100] slip system, other slip systems, most probably the (100)[001] (Zhang et al., 2000) and probably the activation of olivine [100]&[001] with twist walls in the (010) plane (e.g., Darot and Gueguen, 1981) cannot be excluded. Some of the xenoliths analyzed exhibit tabular equigranular texture (Szba1, Szbd-15, Szgk03-01) with relatively coarse grain size, indicating static grain growth, which may have significantly changed original parental grain-subgrain relations. Nevertheless, misorientation pattern of these xenoliths (Figure V.17) is quite similar to those that have presumably preserved "original" grain-grain relations (e.g., GC03-06, Figure V.15; Szb28, Figure V.18).

Some simple shear experiments succeeded to reproduce such fabrics in recrystallized grains (Zhang et al., 2000). The development of these orientations in the experiments is suggested to be related to a switch from shear geometry controlled lattice preferred orientation to a stress controlled one (Zhang et al., 2000). In this case instead of [100]-axes aligning parallel to the shear direction, [010]-axes cluster subparallel to the maximum stress (σ_1). However, in these rocks significant difference occurs between the orientation of porphyroclasts and recrystallized grains, which is not true for the studied samples from the Intra-Carpathian Basin System. In fact, recrystallized grains and porphyroclasts display similar orientation distribution

(Figure VIII.2ab) implying that subgrain rotation, although present, did not affect LPOs. Similar orientation patterns in natural samples were interpreted to have formed in a deformation regime having a remarkable flattening component (e.g., Dijkstra, 2001). Alternatively, the development of such LPOs might be related to multi-stage deformation when remarkable strain and fabric development is superimposed by another deformation also with considerable strain but with a maximum strain/stress/flow axes at large angles (sub-perpendicular) to the earlier one. Simply because of geometric reasons (i.e., Schmid-factor; see Chapter III. for details) this should result in the activation and considerable contribution of slip systems normally not being important in accommodating intracrystalline deformation.

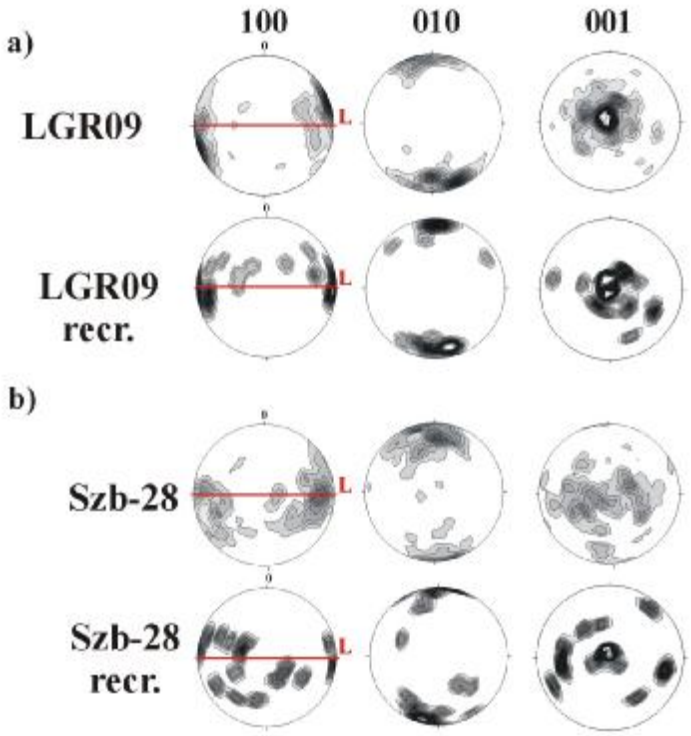

Figure VIII.2 Olivine orientation patterns of two xenoliths from the ETBVF (LGR09) and the BBHVF (Szb28). The orientation of recrystallized grains is shown separately from that of the whole orientation distribution. Note similarities between two types of distributions in both samples. In both cases n=100 for the whole orientation patterns and n=25 for recrystallized grains (recr.). Horizontal red line denotes orientation of macroscopic foliation or compositional banding; L – macroscopic lineation. Lower hemisphere, equal area projection. Data contoured at 1, 2, 3,… times uniform distribution.

These samples, although displaying very different textures in LHPVF and BBHVF, all exhibit low equilibrium temperatures ~900 and ~1000^{o}C, respectively.

This low temperature corresponds to the results of Zhang et al (2000), who demonstrated the activation of multiple slip systems at low temperatures and low strains. It is also remarkable that this orientation distribution shows a strong preference to tabular equigranular xenoliths in the BBHVF (Table V.3). However, some porphyroclastic and mosaic equigranular xenoliths also display similar olivine LPO (Table V.3, Figure V.7). Xenoliths from the LHPVF with this specific LPO are all porphyroclastic showing no or just subordinate annealing and static recrystallization. This feature implies that tabular equigranular xenoliths from the BBHVF represent LPOs of real deformation events and are not the consequence of static recrystallization. This implies that static recrystallization responsible for the formation of tabular equigranular textures is a young process following major basin forming events beneath the studied region.

Xenoliths with deformation on the {0kl}[100] slip system

Olivines in some rare xenoliths from the BBHVF and LHPVF exhibit distinct olivine patterns from the other two described above. Olivine [100]-axes show a point maximum distribution parallel to the lineation in the foliation plane, whereas [010]- and [001]-axes exhibit girdles perpendicular to the foliation (Figure V.5, 9). This orientation pattern suggests that deformation occurred on the {0kl}[100] slip system (Carter and Avé Lallemant, 1970). Mantle peridotites with similar orientation distribution pattern are often observed (e.g., Van der Wal, 1993; Dijkstra, 2001). Moreover, the rotation axes distribution of low angle misorientation grain boundaries in the studied sample displays quite similar pattern to rocks Dijkstra (2001) studied. Equilibrium temperature of the xenolith with the specific orientation pattern is intermediate (~1070^{o}C) between the high temperature xenoliths displaying evidence for (010)[100] slip and those indicating significant contribution of (100)[001] slip and [100]&[001] slip with twist walls in (010).

A clear relation between deformation pattern and equilibrium temperatures (depth of origin) is only observed in the xenoliths from the BBHVF and LHPVF. The lack of this systematic in the other xenolith locations could also be related to low variance in xenolith textures (SBVF, ETBVF) or low number of xenoliths analyzed (NGVF). It should be noted, however, that sample NBN52 from the NGVF also displayed tabular equigranular texture, but orientation patterns are similar to others of the NGVF.

Cataclasites and mylonites

Xenoliths showing evidence of extremely localized deformation are also found among xenoliths from the Intra-Carpathian Basin System. Such xenoliths are rare and two textural groups were identified: 1) Cataclasites from the BBHVF (Falus et al., 2004) and 2) mylonites from the ETBVF (Falus et al., in prep.). Cataclasites are suggested to form in very late stages of the evolution of the Intra-Carpathian Basin System, and are related to mantle earthquakes associated with alkali basaltic volcanism (Falus et al., 2004). The development of mylonites is suggested to be more complex and is related to major basin forming processes. These kind of textures (rather than fabrics) in mantle rocks are attributed to low temperature (<800^{o}C) localized plastic deformation (e.g., Vissers et al., 1997). The mechanism that drives shear localization is the grain size reduction related to dynamic recrystallization in the dislocation creep regime during ongoing deformation (e.g., Van der Wal, 1993). At a certain stage of deformation where the grain size reaches a critically low value a switch in the deformation mechanism, accommodating deformation from grain size insensitive (dislocation creep) to grain size sensitive (GSS) creep (i.e., diffusion creep) occurs (Van der Wal et al., 1993; Vissers et al., 1997; Dijkstra et al., 2002).

Localization in the mylonites and also the cataclasites is believed to be associated with melt infiltration (Falus et al., 2004), evidenced by interstitial glass (Figure VIII.3). Porphyroclasts in the mylonites exhibit strong shape preferred orientation, i.e., they are elongated subparallel to the foliation. Weak indication of lattice preferred orientation in the mylonites is also observed (Figure V.13). However, the low number of porphyroclasts (n<20) measured indicates that orientation data should be handled with care. Equilibrium temperatures of porphyroclast cores in the mylonites (Rk99/00; NVTR03-01 and LGR03-01) in all cases exhibit low-very low equilibrium temperatures (750-900^{o}C; Figure VII.9). Rim of the porphyroclasts and recrystallized matrix grains in the mylonites generally indicate higher temperature (830-980 ^{o}C), suggesting that during deformation thermal conditions have remarkably changed (+30-100^{o}C). This temperature elevation is

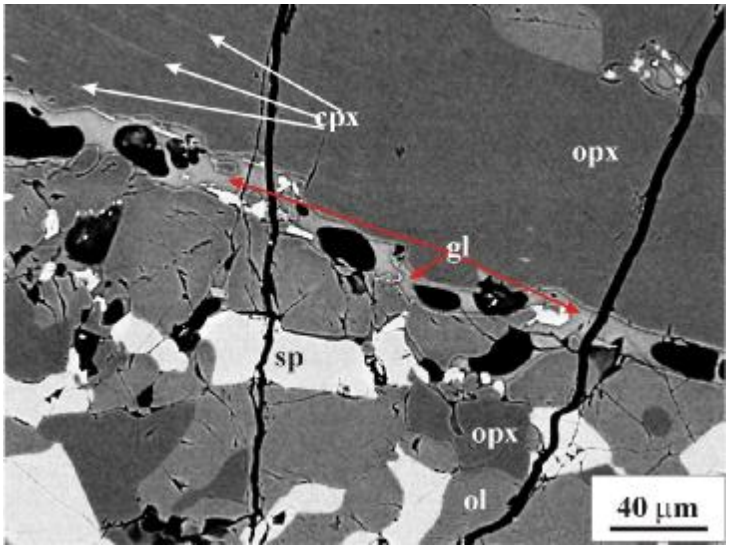

Figure VIII.3 Mylonitic xenolith from the ETBVF (LGR03-01). Infiltration of glass is observed along an orthopyroxene porphyroclast, which displays elongated shape. The orthopyroxene porphyroclast contains clinopyroxene exsolution lamellae and is surrounded by recrystallized olivine orthopyroxene and spinel. ol-olivine; opx-orthopyroxene; sp-spinel, cpx-clinopyroxene; gl-glass; SEM image.

attributed either to shear heating or the infiltration of melts or both. Taking into consideration the position of the ETBVF, being close to the subducting European slab (Figure 2 in Chalot-Prat and Girbacea, 2000), it is not senseless to account for shearing related to the motion of the subducting slab as demonstrated by Peacock (1992). However, the traceable changes in oxygen fugacity in the mylonite porphyroclasts and matrix (Figure VII.9) presume some kind of interaction of peridotitic wall rock with infiltrating melts.

Recrystallized olivine grain size was used to estimate differential stress driving the formation of mylonites using paleopiezometric methods (e.g., Avé Lallemant et al., 1980; Karato et al. 1980; Van der Wal, 1993). Grain size of the recrystallized olivines was determined applying image analysis on digital SEM images. Minimum grain sizes were found in sample NVTR03-01 (30-40 microns). This grain size corresponds to differential stress ~100 MPa, which seems realistic for supra subduction shear zone environment (e.g., Peacock, 1992). Even higher differential stress (~150 MPa) is suggested to have operated in case of the cataclasites displaying average recrystallized grain size (10-20 microns). These latter ones, as

demonstrated by Falus et al. (2004) are suggested to be related to deep-seated earthquakes.

VIII.3 The evidence and quantification of lithospheric thinning during basin formation

There is no doubt that the formation of the Intra-Carpathian Basin System had considerable effect on the lithospheric upper mantle. Geophysical studies already in the 1950s and early 1960s suggested that the asthenosphere beneath the region is in an anomalously high position (e.g., Stegena, 1974). Structural geological studies (e.g., Csontos, 1995; Tari and Horváth, 1995; Fodor et al., 1999; Tari et al., 1999) and subsidence modeling (e.g., Royden et al., 1983; Huismans et al, 2001) demonstrated that thinning of the lithosphere was significant (β~1.5-2) and that in the central potion of the basin the lithospheric mantle thinning was significantly larger (γ~2-6) than that of the crust.

Petrographic evidence for the lithospheric thinning was also provided by several xenolith studies. Reaction products of pressure dependent phase transformations (i.e., breakdown of garnet) in lower crust (Török, 1995; Dégi and Török, 2004) and upper mantle (Falus et al., 2000) material were used to quantify the thinning, i.e., decrease in pressure. Thinning of the crust in the central portion of the Pannonian Basin was found to be around 15 km (Török, 1995, Dégi and Török, 2004), whereas the thinning in the lithosphere could reach 40-60 km (Falus et al., 2000), estimated for the marginal portions of the basin system.

Pyroxene-spinel symplectites occurring in some of the xenoliths from the LHPVF (Figure IV.6) are also suggested to be the breakdown products of garnet (Falus et al., in prep.). The bulk composition of these clusters (Table VIII.1) with coexisting orthopyroxene and clinopyroxene porphyroclasts, both containing exsolution lamellae (Figure IV.3, 4, respectively), could be used to obtain more precise estimates on the physical conditions (pressure and temperature) of an earlier state of the lithosphere before the thinning and the formation of the Intra-Carpathian Basin System with respect to estimates of Falus et al. (2000). The expected reason for the higher precision lies within the relative intact composition of symplectite compared to pyroxene-spinel clusters of the ETBVF and SBVF, that clearly recrystallized and to some rate have reached equilibrium with the host minerals. The

preservation of exsolution lamellae in the orthopyroxene and clinopyroxene porphyroclasts also indicates low diffusion rates operating in these rocks. Moreover, temperature values representing the garnet peridotitic environment can also be directly estimated using the recalculated pyroxene compositions with the application of the Brey and Köhler thermometer (1990).

The former garnet exhibits high pyrope content (~72 mol%), in accordance with garnet composition derived from the garnet peridotite xenolith suite (Cox et al., 1987). Temperatures estimated for the recalculated pyroxene compositions reflect temperatures around (1050^{o}C). Whereas, those temperatures estimated for rims of the porphyroclasts, believed to represent equilibrium thermal state after deformation and recrystallization are around 830^{o}C. Pressure estimates, using the barometer of Nickel and Green (1985). The barometer provides pressure values between 28-31 kbar (corresponding to ~90 km depth) for garnet and recalculated orthopyroxene pairs.

Geophysical soundings (seismic and magnetotelluric), analyzing the lithospheric thickness of the Intra-Carpathian Basin System indicate ~80 km thick lithosphere beneath the LHPVF (e.g., Horváth et al., 1993; Ádám, 1996 and references therein; Figure II.3). Temperatures at the base of the lithosphere at this depth, corresponding to heat flow (~80mW/m^2) values measured for the LHPVF (Dövényi, 1988) are around 1100-1150 ^{o}C. Temperature values of 830^{o}C from the same area and identical geothermal gradient reflect mantle depth around 50 km (15-17 kbar). This implies that the mantle material, now containing pyroxene spinel symplectites, suffered decompression in the scale of 10-15 kbar (30-45 km). Somewhat higher values were established for pyroxene spinel clusters from the marginal portion of the basin (Falus et al., 2000), most probably due to diffusion and reequilibration of cluster minerals with their host. Nevertheless, decrease in pressure, i.e. thinning is considerable and is within the same scale in both central regions and edges. This indicates that considerable mantle thinning (30-50 km) is a general, overall feature characteristic for the whole of the lithospheric mantle of the Intra-Carpathian Basin System, which are proved by petrographic tools.

	constituent phases of the symplectite				calculated gt. composition		
	Mineral	opx	cpx	sp			
	Element					wt%	
	SiO_2	55.8	52.8	0.17		42.0	
	TiO_2	0.04	0.19	0.04		0.07	
	Al_2O_3	3.68	4.46	60.2		16.7	
	Cr_2O_3	0.23	0.39	8.11		2.06	
	FeO	6.66	2.83	10.7		6.74	
	MnO	0.15	0.07	0.11		0.12	
	NiO	0.05	0.04	3.77		0.90	
	MgO	33.8	16.4	18.1		26.3	
	CaO	0.48	22.2	0.04		4.83	
	Na_2O	0.05	0.87	0.00		0.21	
	ZnO	na.	na.	0.15		0.03	
	Total	100.9	100.3	101.4			
	vol%*	56.66	21.61	21.29	Pyr%	72.00	
	density	3.3	3.18	3.6	And%	12.66	
	host-opx	host-cpx	host-sp	sp-in-cpx		recalc. opx	recalc. cpx
SiO_2	54.6	50.7	0.01	bd.	**SiO_2**	54.3	49.4
TiO_2	0.13	0.59	0.04	0.06	**TiO_2**	0.15	0.57
Al_2O_3	4.58	6.54	57.7	58.6	**Al_2O_3**	4.64	8.36
Cr_2O_3	0.43	0.84	10.7	9.25	**Cr_2O_3**	0.45	1.19
FeO	6.48	2.68	11.7	10.7	**FeO**	6.21	3.01
MnO	0.15	0.09	0.12	0.14	**MnO**	0.14	0.09
NiO	0.06	0.04	0.40	na.	**NiO**	0.06	0.05
MgO	33.3	14.99	20.2	20.5	**MgO**	32.1	15.3
CaO	0.46	21.7	0.00	0.07	**CaO**	1.88	21.1
Na_2O	0.06	0.95	na.	na.	**Na_2O**	0.12	0.93
Total	100.25	99.09	100.83	99.42			
cpx-in-opx vol%		6.64					
sp-in-cpx vol%				3.13			

recent	T_{BK}=	~900 °C
original	T_{BK}=	1050 °C
original	P_{NG}=	28-31 Kbar

Table VIII.1 Composition of mineral phases in the symplectite of sample GC03-06 from the LHPVF. Bulk composition of symplectite is also shown. vol%* - volumetric percentage of minerals. Pyr – pyrope content; And – andradite content (mol%). host-opx – host orthopyroxene next to the symplectite; host-cpx – host clinopyroxene next to the symplectite; host-sp – host spinel next to the symplectite; sp-in-cpx – spinel inclusions in clinopyroxene. recalc. opx – recalculated orthopyroxene compositions together with clinopyroxene lamellae; recalc cpx – recalculated clinopyroxene compositions together with spinel inclusions. T_{BK} – equilibrium temperature applying the method of Brey and Köhler (1990); P_{NG} – calculated pressure for garnet-recalculated orthopyroxene pairs using the method of Nickel and Green (1985); recent – values calculated using equilibrium mineral assemblage, original - values calculated using recalculated mineral assemblage.

VIII.4 An attempt to understand relation between deformation state and geochemical nature of the lithospheric mantle

Major element compositions, a well studied character of upper mantle peridotite xenoliths within the Intra-Carpathian Basin System (e.g., Kurat et al., 1991; Downes et al., 1992; Szabó and Taylor, 1994; Szabó et al., 1995a; Vaselli et al., 1995,1996; Dobosi et al., 1999; Embey-Isztin et al., 2001; Dobosi, 2003). It is clear that significant relation between major element composition and xenolith textures is observed. It is suggested that depletion of mantle rocks in basaltic major elements, a first order geochemical process in the mantle, is dominantly related to partial melting. Basaltic melts produced are extracted and a residuum depleted in basaltic elements is left (Frey and Green, 1974).

In the LHPVF, BBHVF, NGVF and ETBVF locations the most intensively recrystallized xenoliths, displaying porphyroclastic, equigranular and secondary recrystallized textures, reflect a depleted character in basaltic major elements (Figure VI.1-15). Whereas, protogranular and protogranular/porphyroclastic xenoliths exhibit fertile compositions and they are relatively rich in basaltic major elements (e.g., Kurat et al., 1991; Vaselli et al., 1995, 1996). However, xenoliths from the SBVF, probably because of their minor textural variability, do not follow this trend. Harzburgites, for example, reflecting the most depleted major element characteristics display protogranular/porphyroclastic texture. This suggests that these textures are either of secondary origin or partial melting and deformation are not necessarily associated processes. Another possible explanation for such discrepancy is the reaction of peridotite wall rock with percolating melts/fluids. Clear evidence for such processes are represented in ophiolites (e.g., Kelemen et al., 1992; Dijkstra et al., 2002), as well as mantle xenoliths (Xu et al., 2003). In all cases asthenosphere derived melts reacted with peridotitic clinopyroxene and/or orthopyroxene and precipitated olivines

pyroxene + low-Si melt **à** olivine + high-Si melt

resulting in an overall depletion of basaltic major elements. The occurrence of similar textural features in the xenoliths from the LHPVF, BBHVF and NGVF (Figure V.9) implies that depletion related to solid-liquid reaction was an operating, but probably not a dominant process in the subcontinental lithospheric mantle beneath the studied region.

Similar results are obtained from the trace element (focusing mostly on the REE in clinopyroxene) composition of the mantle peridotites. The ratio between chondrite-normalized Ce and Yb, indicative (to first approximation) of depletion/enrichment of light REE with respect to heavy REE was plotted against cr-number of spinels (Figure VIII.4). It should be noted that enrichment of LREE with respect to HREE does not necessarily mean absolute REE enrichment. Chen et al. (2001) demonstrated that cr-numbers in clinopyroxenes from mantle xenoliths of Hannuoba (China) show negative correlation with bulk REE content of the clinopyroxene. Simultaneously normalized Ce/Yb ratios display positive correlation with increasing cr-numbers. Nevertheless, data for xenoliths from the five xenolith locations of the Intra-Carpathian Basin System were plotted, mostly using data from the literature (e.g., Downes et al., 1992; Szabó et al., 1995b; Vaselli et al., 1995, 1996). Xenoliths from the LHPVF, BBHVF and ETBVF two clear trends could be distinguished (Figure VIII.4). The first trend shows a clear positive correlation between the chondrite normalized Ce/Yb ratios (also observed for xenoliths from the SBVF) and cr-number in spinel. Textures of the xenoliths following this trend are mainly the more deformed ones within the locations. These samples are believed to represent mantle domains that went through partial melting and then subsequent metasomatism. The metasomatizing melts reacted with the peridotite rock resulting in continuous depletion in basaltic major elements and simultaneous enrichment in incompatible trace elements. Xenoliths of the other trend reflect large variance in cr-numbers with normalized Ce/Yb values close to 1. It is believed that this trend may reflect the partial melting without subsequent metasomatism. Xenoliths with the least deformed textures within the locations fall in this group.

The existing relation between xenolith texture, major and trace element composition is clear. Probably the most remarkable feature among those observed is that secondary recrystallized xenoliths from the LHPVF and poikilitic xenoliths from the BBHVF reflect similarly high normalized Ce/Yb in clinopyroxene ratios and high cr-number in spinel (Figure VIII.4). However, what are those factors that assure relation between these various physico-chemical processes? *It seems very likely, that elastic strain energy stored in the deformed minerals may be one of the parameters, which has the capability of linking physical and chemical processes in the mantle*.

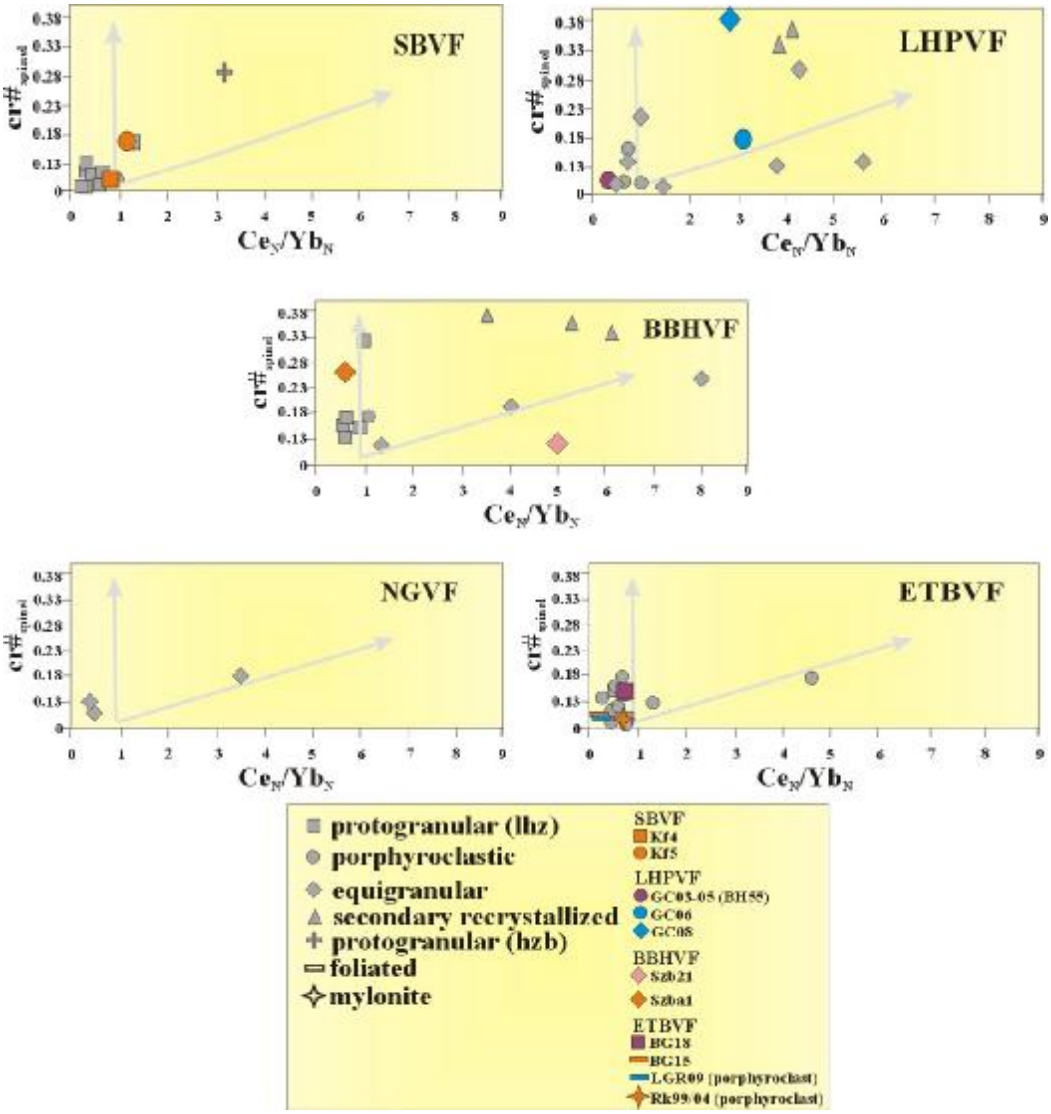

Figure VIII.4 Ce_N/Yb_N vs. cr-number of spinel diagram for separated clinopyroxenes from xenoliths of the Intra-Carpathian Basin System with respect to texture. Xenoliths selected for detailed microstructural study are highlighted. Note two trends indicated by the gray arrows. Vertical arrow denotes depletion, whereas subhorizontal one indicates enrichment with synchronous reaction with host basaltic magma. Data from Vaselli et al. (1996), Dobosi et al. (1999) – SBVF; Szabó et al. (1995b) – LHPVF; Downes et al. (1992), Bali et al. (submitted), own measurements BBHVF; Vaselli et al. (1995) – ETBVF.

Recrystallization, earlier believed to be an isochemical process (e.g., Mercier and Nicolas, 1975), is controlled by temperature (e.g., Lloyd et al., 1997) and the attempt of the crystals to minimize their elastic strain energy (~dislocation density) of the crystals (Passchier and Trouw, 1995). If these two parameters are the only factors to

control recrystallization the mantle with higher temperatures would display more intensive recrystallization than that in lower temperature. This, however, is not the full case. It seems likely that the intensity of recrystallization (both dynamic and static) is also influenced by the presence of interstitial fluids/melts (e.g., Bussod and Christie, 1991; Passchier and Trouw, 1995; Xu et al., 2003). In the relation of the Intra-Carpathian Basin System this means that in the "shallower" mantle portions an infiltrating melt could trigger recrystallization. This is because minerals in the mantle portion probably have higher dislocation density (elastic strain energy) due to deformation in variable stress fields and lower temperatures, where recovery processes are operating much slower. In addition, the infiltrating melt/fluid may react (and generally does) with the peridotite resulting in a continued depletion of the mantle in basaltic major elements. However, synchronously recrystallizing clinopyroxene grains could easily incorporate some of the trace elements from the infiltrating melt/fluid and thus could reflect a strongly metasomatized (generally LREE-enriched) character. The relation of geochemical characteristics and xenolith texture is thus not the consequence of a single process but is the result of superimposed physico-chemical processes in the mantle.

Several models deal with the migration of fluids/melts in the mantle. One end-member of the studies suggests that melt migration in the mantle is solely connected to migration in veins (Bodinier et al., 1990), similarly to that observed in peridotite massifs. Melt migration related to veins is undoubtedly a process that occurs in the mantle beneath the Intra-Carpathian Basin System evidenced among others by amphibole, clinopyroxenite veins (e.g., Embey-Isztin 1976,1986; Szabó and Taylor, 1994; Vaselli et al., 1995; Dobosi, 2003; Bali et al., submitted.). However, the capacity of such vein to produce overall metasomatism in the upper mantle is limited. Studies in peridotite massifs (Bodinier et al., 1990) and mantle xenoliths (e.g., Vaselli et al., 1995) demonstrate, that traceable geochemical effects are only observed in the very close vicinity of the melt veins (few cm or maximum meters). It is unlikely that metasomatism would only be related to such veins. This would either mean a shallow upper mantle penetrated by infinite melt veins, which is not supported by the xenolith record of the Intra-Carpathian Basin System and is also not realistic rheologically or the metasomatized xenoliths studied derive from the vicinity of the melt veins. The strong relation between texture (deformation and recrystallization state), equilibrium temperature and geochemical character of the studied xenoliths

contradicts with metasomatism being only a 2-D process. Downes (1990) suggested that melt migration and metasomatism are strongly related to shear zones. Although this approach enables migrating melts/fluids to metasomatize a large volume of deformed rocks, still it does not give proper explanation for the strong relation of equilibrium temperatures with chemistry and recrystallization state. The other end-member of the fluid migration models is the reactive porous melt flow (e.g., Ionov et al., 2002). In this case no melt vein or crack is required as a source and melts can migrate along grain boundaries continuously equilibrating with the peridotite. As a result chromatographic fractionation occurs during reactive porous melt flow, which produces a variety of enrichment patterns in a single event. Moreover, a full 3-D metasomatism is achieved. The source of melt/fluid should be mostly the asthenosphere. In this case, however xenoliths with higher equilibrium temperatures (representing deeper mantle portions) should reflect a stronger metasomatic effect.

The realistic picture that relates geochemical characteristics with xenolith texture and equilibrium temperatures should incorporate metasomatism related to both end-member migration processes. Furthermore, internal recrystallization habitude, related to elastic strain energy should also be accounted for.

VIII.5 Mantle deformation: its role and correspondence to the formation of the Intra-Carpathian Basin System

Large-scale tectonic processes are controlled or at least strongly influenced by the nature of the asthenosphere and lithospheric mantle. The physico-chemical state of these geospheres has remarkable effect on i.e., plate motion, their tectonic interaction, partial melting, melt migration and volcanism, etc.

Formation of the Intra-Carpathian Basin System, occurring in early-middle Miocene times (e.g., Kázmér and Kovács, 1985; Csontos et al., 1992; Fodor et al., 1999), is related to the subduction of European oceanic lithosphere beneath the African Plate resulting in the collision of the European continent and the Apulian microplate (Figure I.1). The collision was followed by extrusion, subduction rollback, extension and probably even active upwelling of the asthenosphere (e.g., Horváth et al., 1993; Huismans et al., 2001, and references therein). These young processes, however, were not dramatic to be alone responsible for the formation of the subcontinental lithosphere beneath the Intra-Carpathian Basin System. The formation

of the lithospheric root is more likely related to early partial melting and continental crust formation events, indicated also by Nd-model ages (~ 1Ga; Vaselli et al., 1995). All other processes up to the time of sampling by their host alkali basalts including the major tectonic event of the Intra-Carpathian Basin System formation superimposed on the early lithospheric structures and influenced the physical and chemical state of the mantle.

It is evident to start the description of the evolution of the lithospheric mantle beneath the region with a magmatectonic process producing the mass of the now observed subcontinental lithospheric mantle. Although the Intra-Carpathian Basin System is composed of two main lithospheric units (e.g., Csontos, 1995), there is no indication to suggest remarkably different genesis for the lithospheric root of the two units (e.g., similar Nd-model ages; Downes et al., 1992; Vaselli et al. 1995). This major lithosphere forming process, although temporally weakly constrained, is suggested to be a single scale process as was shown for cratons (Gaul et al., 2000, and references therein) and is believed to be responsible for high (~1 Ga) model ages observed for mantle xenoliths from the studied basin. Moreover, the large-scale trend of basaltic major element compositions, showing systematic depletion towards shallower levels of the mantle and modal variance from clinopyroxene-rich compositions to clinopyroxene poor occurrences, are also the consequence of this old episode of lithospheric root formation.

Such features are observed world wide in the subcontinental lithosphere (e.g., Gaul et al., 2000) and similar phenomenon are described from suboceanic mantle diapirs (Godard et al., 2000). This geodynamic process was described and modeled by McKenzie (1984). In the model the mechanism is described as the effect of progressively greater degree of partial melting and melt extraction from fertile upper mantle at shallower depth due to adiabatic decompression followed by the compaction of the melting column.

The resulting lithospheric “root” (for both mega blocks, being separated at this time of the evolution) of the "proto" lithosphere beneath the Intra-Carpathian Basin System reflects systematic depletion in basaltic major elements towards the shallower mantle levels. The microstructure of the lithosphere at this stage is uncertain. Whether this structure was preserved during further evolution of the lithospheric mantle is unclear. It is, however, clear that fluids and melts mostly derived from the asthenosphere and tectonic events continuously evolved the composition of the

lithospheric mantle similarly to the process described by Gaul et al. (2000) who studied xenolith occurrences worldwide. Besides geochemical changes, the structure of both lithospheric units is suggested to have occurred. The effect of migrating fluids and melts in the lithosphere was clearly demonstrated by Vauchez and Tommasi (2003) on Tanzanian xenoliths.

The next episode in the evolution of the subcontinental lithosphere beneath the region, which definitely had a marked and temporally well-constrained effect on lithospheric mantle, is the formation of the Intra-Carpathian Basin System (Figure VIII.5a). The tectonic episode resulted in thinning of the lithospheric mantle with a factor of 1.5-2 (e.g., Royden et al., 1983; Huismans, 2001) in NE-SW and later E-W directions (e.g., Fodor et al., 1999; Figure VIII.5a). In the Miocene, at the time of basin formation, the two lithospheric units were already physically interlocked resulting in similar physico-chemical effects within the two units. Garnet symplectites, and pyroxene-spinel clusters found in lower crust (e.g., Török, 1995; Dégi and Török, 2004) and mantle derived material (Figure IV.5), Falus et al., 2000; Falus et al., in prep) are solid petrographic evidence for the thinning. Moreover, their high instability suggests that the formation of these symplectites/clusters is a young process related to basin formation.

The basin formation affected the geochemical characteristics of the lithospheric mantle. Thinning and the proposed active mantle upwelling could have caused partial melting in the lithospheric mantle, resulting in further depletion of basaltic major and incompatible trace elements. An extremely strong petrographic evidence for this process could be the occurrence of melt pockets in the xenoliths of the LHPVF, BBHVF and NGVF (e.g., Szabó et al., 1996; Bali et al., 2002; Bali et al., submitted). The vitalization of metasomatic melt/fluid migration related to mantle upwelling and subduction is clear (e.g., Downes et al., 1992; Wilson et al., 1997). Migrating of these melts/fluids is documented by trace element and radiogenic isotopic composition of clinopyroxenes (e.g., Downes et al., 1992; Wilson et al., 1997) and the presence of metasomatic amphiboles (Szabó et al., 1995a; Vaselli et al., 1995, 1996), as well as of interstitial glass (Bali et al., submitted). Moreover, lobated pyroxene porphyroclasts (Figure IV.9) from the Bakony—Balaton Highland Volcanic Field in strongly annealed equigranular mantle xenoliths can be taken as a clear textural evidence for the migration of reactive melts similar to those described by Kelemen et al. (1992) and Dijkstra et al. (2002) from ophiolitic mantle rocks. These

melts through their pyroxene-consuming reactions may have also contributed to the depletion of the upper mantle in basaltic major elements.

Changes in texture and microstructure of the upper mantle in relation to the formation of the Intra-Carpathian Basin System were significant. Fabrics observed in the mantle xenoliths are presumably dominantly the consequence of this tectonic episode, although the preservation of earlier deformation signatures especially in the shallower mantle portion cannot be excluded.

The major rift phase was followed by a thermal cooling phase (Figure VIII.5b) during the Late Miocene (e.g., Royden and Horváth, 1988). During the thermal cooling phase addition of asthenosphere to the bottom of the lithosphere is suggested (Horváth et al., 1988). Sampling of the upper mantle by ascending basaltic magmas occurred during this phase.

Olivine orientation patterns in deformed xenoliths derived from the marginal portions of the basin system (NGVF and ETBVF), irrespective of their depth of origin, texture and geochemical characteristics suggest that deformation was accommodated by intracrystalline slip dominantly on a single slip system (010)[100] (see Chapter V.; Figure V.11-14). It is widely accepted that olivine [100] and subordinately [001] align subparallel to maximum strain axes (e.g., Carter and Avé Lallemant, 1970). Experimental results of co-axial deformation and uniaxial compression have come up with similar results (e.g., Carter and Avé Lallemant, 1970). In the Intra-Carpathian Basin System it is thus evident to assume that maximum strain orientations are subhorizontal coinciding with maximum elongation observed in the crust, conveniently σ_1 (the maximum stress) is dominantly vertical. Moreover, the deformation is suggested to have affected the whole lithospheric section. The symmetry of the olivine orientation patterns indicates that the deformation was either coaxial or large enough to extinguish fabric asymmetry as a result of simple shear (e.g, Tommasi et al., 2000). The systematic variance in olivine orientation patterns in deformed xenoliths from the LHPVF and BBHVF with respect to depth of origin is an unambiguous feature (Figure VIII.5b). Olivines in xenoliths derived from the deep lithospheric mantle, displaying the most primitive compositions and texture, always display decisive symmetric fabrics indicating that deformation was coaxial in a constant stress field and was accommodated by intracrystalline slip

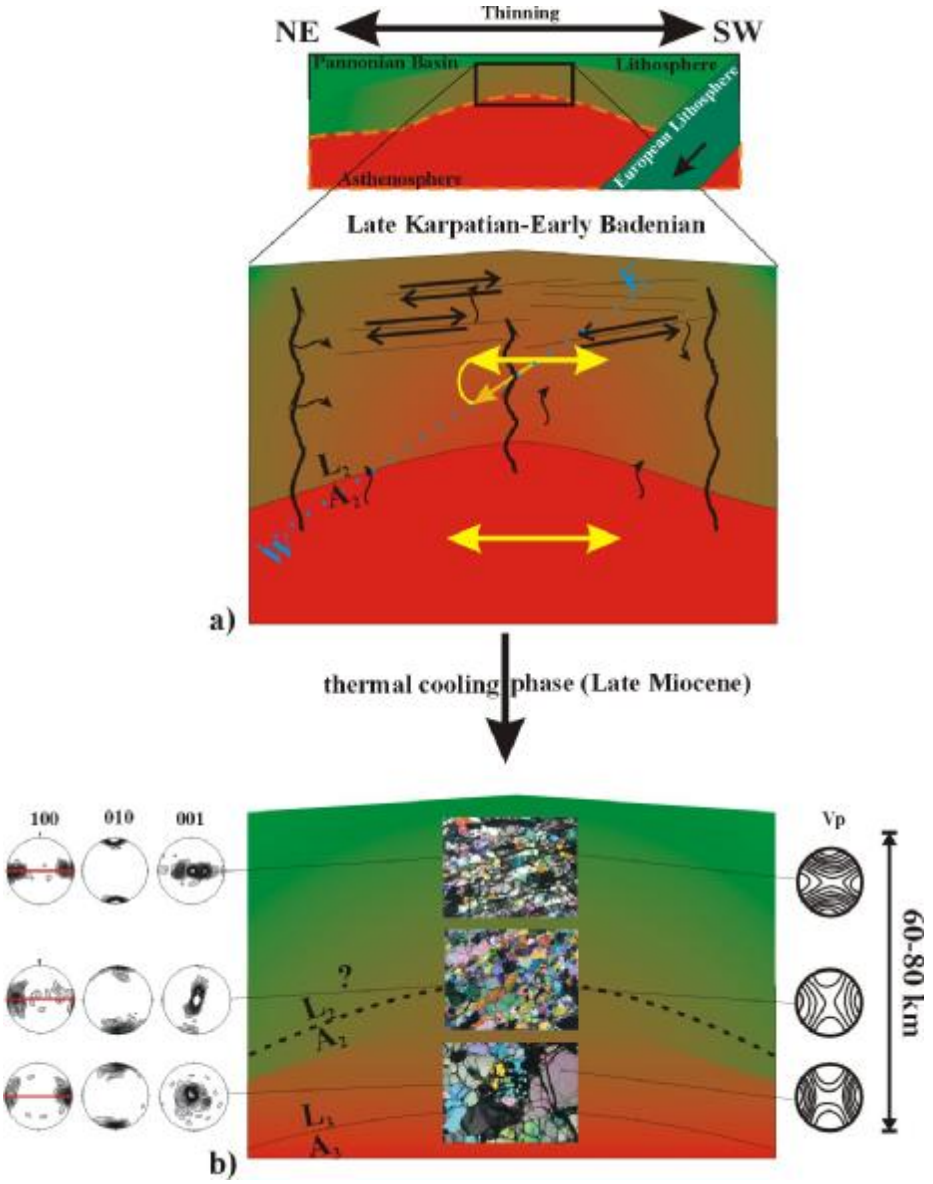

Figure VIII.5 Simplified evolution of the lithospheric mantle beneath the Intra-Carpathian Basin System. a) Thinning of the lithosphere during extension and the formation of the Intra-Carpathian Basin System ~17-14 Ma. Yellow arrows denote major extension directions (NE-SW), whereas orange arrow at large angles to the yellow indicates a switch in extension directions from NE-SW to E-W (e.g., Fodor et al., 1999), which affected only the lithosphere but not the asthenosphere. Note reheating of the lithosphere. Shear zones (D), cracks (solid lines) and magmatic conduits (vertical sinuous lines) are indicated as possible source for metasomatism (sinuous arrows). L_2/A_2 denotes lithosphere/asthenosphere boundary after thinning and mantle upwelling. b) state of the lithosphere beneath the region during sampling by basalts. L_3/A_3 denotes recent lithosphere/asthenosphere boundary (60-80 km; e.g., Horváth, 1993; Lenkey, 1999) beneath the region. Characteristic textural type "end members" with lattice preferred orientation and predicted V_P speed distribution (V_p distribution from Ben Ismail and Mainprice, 1998).

on a single slip system (010)[100] (e.g., Figure V.3,6) as Carter and Avé Lallemant (1970) stated. Those samples derived from shallower depths (Figure VII.5b) always reflect the activation of multiple slip systems (e.g., (010)[100]; (010)[001] and (010) twist walls [100]&[001]) (Figure V.8) also described by Zhang et al. (2000) in experimentally deformed olivines. Xenoliths displaying such olivine fabrics show contrasting textural and compositional features in the LHPVF and BBHVF (Figure II.2,4, respectively), which indicate that static recrystallization and possibly related geochemical modification is a process subsequent to the deformation. These orientation patterns are indicative of flattening as Dijkstra, 2001 pointed out for ophiolitic mantle material or could be related to multiple extension directions.

Rotation of stress fields is a recognized phenomenon during the formation of the Intra-Carpathian Basin System (e.g., Csontos, 1995; Fodor et al., 1999; Huismans et al., 2002). Fabric analysis of upper mantle xenoliths suggests that rotation of the stress fields may have affected deformation of the shallow upper mantle. The presence of mantle portions with different orientation patterns (Figure VIII.5b), where the shallower mantle portion evidence flattening and the deeper reflect a constant stress field imply two possibilities of the formation of these mantle portions. They may indicate 1) the stress field responsible for flattening decays with depth; or 2) that the stratigraphically higher portion of the upper mantle suffered a deformation in a stress field characterizing the lithosphere, assuming that it was originally part of the lithosphere before and during the basin formation, whereas the deeper mantle section was deformed by asthenospheric flow and was attached to the lithosphere during cooling after the cessation of deformation in the Late Miocene. This latter explanation is supported by several thermal and subsidence models (Horváth et al., 1988; Huismans et al., 2001), however gradual increase in the manifestation of undulating stress regime with decreasing depth cannot be excluded. Moreover, at higher temperatures subgrain rotation recrystallization, resulting in strong olivine fabrics displaying activation of the (010)[100] slip system, is more active (e.g., Zhang et al. 2000). This feature could have played role in the observed fabric distribution (Figure VIII.5b), however significant recrystallization is not supported by petrographic and geochemical observations.

Irrespective of the origin of mantle sections with olivines, being the largest volume of mineral constituent in the lithospheric mantle and displaying distinct lattice preferred orientations, it is beyond question that the lithospheric mantle beneath the

Intra-Carpathian Basin System is structurally anisotropic. This anisotropy is the consequence of the development strong fabric and is almost certainly associated with the basin forming tectonic processes. It is a reasonable assumption to suggest that the anisotropy is subhorizontal coinciding with maximum strain axis (roughly NE-SW) observed in the Intra-Carpathian Basin System. An extreme mantle domain showing this anisotropy could be the occurrence of tabular equigranular xenoliths (Szba1, Szbd-15 and Sgk03-01; Figure III.5; V.8) from two xenolith locations (20 km apart) of the BBHVF. These mantle fragments display similar lattice preferred orientation, misorientation pattern and exhibit the same equilibrium temperature (Figure VII.5). Their occurrence implies that structural domains (~20-30 km horizontal dimension) with similar anisotropy might be present in the subcontinental lithosphere, at least in the central portion of the Intra-Carpathian Basin System (Hidas et al., submitted).

Structural anisotropy, besides producing detectable modification in the propagation of seismic waves (e.g., Ribe, 1992), but also influences the migration of percolating fluids and melts (e.g., Waff and Faul, 1992). Basaltic melts, preferably wet (010) crystal faces of olivine due to achieved minimal interfacial energies (e.g., Waff and Faul, 1992). In mantle segments that exhibit strong lattice preferred orientation this results in favorable percolation directions of the infiltrating melt, parallel to olivine (010). Regarding the anisotropy of the mantle beneath the Intra-Carpathian Basin System, (010) faces being subhorizontal (Figure VIII.6a) this suggests that the migration of melts/fluids is dominantly subhorizontal. Moreover, in the shallower parts of the lithospheric mantle beneath the region, where flattening dominated, the anisotropic effect is even more pronounced. Note that (010) faces in this portion of the mantle remain subhorizontal (Figure VIII.6b). Vertical motion is only achieved where (010) faces are subvertical or the migrating fluids can segregate from the peridotitic matrix (e.g., cracks, veins; Figure VIII.6b). Where the segregation cannot take place, melts/fluids are retained in the mantle exerting intensive geochemical modification/reaction and static recrystallizing effects on the deformed peridotite producing equigranular, secondary recrystallized and, probably at very intensive melt/solid interaction, poikilitic xenoliths. This feature provides clear connection of textural and trace element geochemical features observed for the xenoliths. The melts finally crystallize as subhorizontal magmatic bodies. This effect might be one of the factors, which causes the abundant occurrence of cumulate bodies at the vicinity of the MOHO (Embey-Isztin et al., 1993; Kovács et al., 2004).

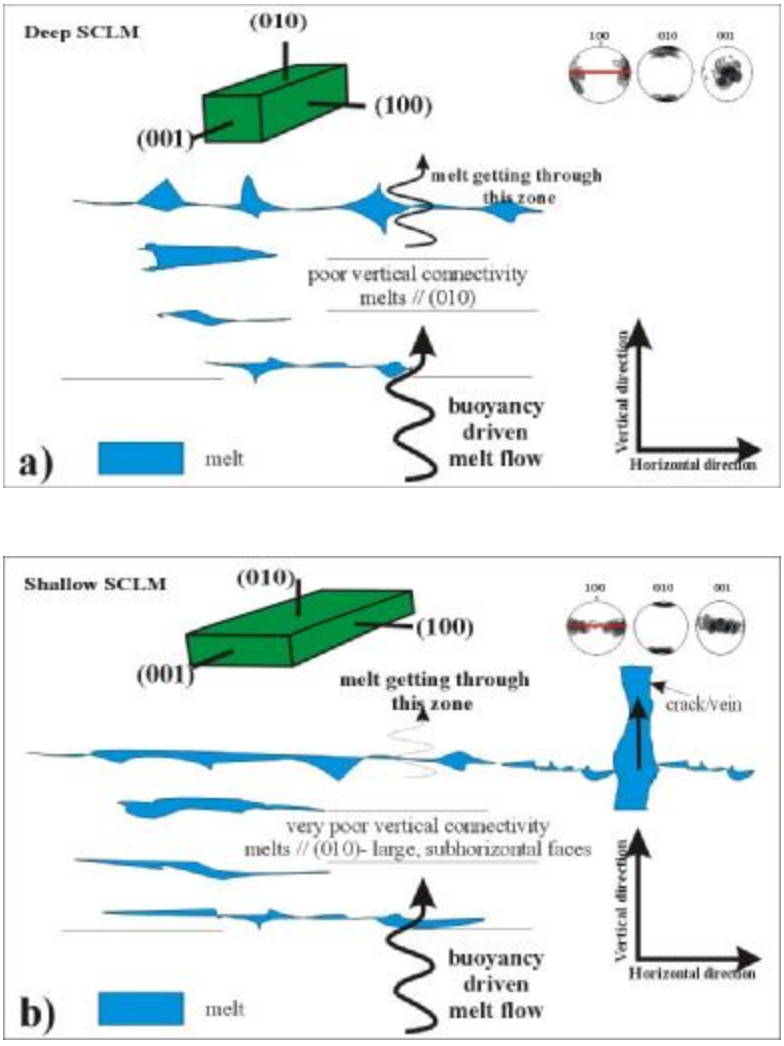

Figure VIII.6 Differences in vertical and horizontal permeability due to changes in lattice preferred orientation of olivine; a) point maximum distribution of olivine axes, slip system (010)[100]; b) girdle of [100] and [001] in the foliation plane. Note very weak vertical connectivity in case of *b*.

VIII.6 Perspectives - seismic anisotropy: a method for studying deformation fabrics in the mantle

The existence of seismic anisotropy in the upper mantle is a well known and recently well studied phenomenon world wide (e.g., Anderson, 1961; Artemieva et al., 2002, and references therein). Seismic anisotropy observed in the mantle is commonly attributed to the elastic anisotropy of volumetrically dominant phases olivine and orthopyroxene and the strong statistical alignment of their crystal axes or lattice-preferred orientation (e.g., Nicolas and Christensen, 1987; Karato, 1992). The

crystallographic basis for this phenomenon resides from the anisotropic nature of olivine and orthopyroxene crystals. Where seismic waves (P- and S-waves) travel through an elastically anisotropic medium they are split into two orthogonally polarized waves traveling at different velocities. Measurements of the splitting of the seismic waves provide information on the anisotropy of the mantle that can be used to unravel the structure and flow pattern of the upper mantle (e.g. Silver, 1996). However, some studies demonstrated that the preferred orientation of melt pockets also contributes to (e.g., Jousselin and Mainprice, 1997) or diminishes (e.g., Holtzmann et al., 2003) seismic anisotropy.

Seismic studies have been carried out in several geodynamic settings, from Archean-Precambrian cratons (e.g., Artemieva and Mooney, 2001), Phanerozoic orogens (e.g., Montagner, 1994), rift basins (e.g., Soedjatmiko and Christensen, 2000) and recent plate tectonics (e.g., Chen et al., 2001). There are also some scarce studies from the surroundings of the Intra-Carpathian Basin System (e.g., Dricker et al., 1999, and references therein). These soundings studied the anisotropy pattern beneath the mountain belts surrounding the region. The observations as expected (e.g., Vauchez et al., 1997) displayed orogen-parallel seismic anisotropy. Seismic anisotropy measurements within the Pannonian Basin are fully absent from the scientific literature. Nevertheless, an attempt to predict character of detectable seismic anisotropy, using orientation distribution patterns experienced in mantle xenoliths, is made in the following section. Note an assumption that anisotropy features in mantle xenolith fabrics coincide with macroscopic deformation observed in the Intra-Carpathian Basin System is made.

The upper mantle beneath the marginal portions of the Intra-Carpathian Basin System should reflect marked anisotropy (Figure VIII.7a), mainly in the eastern and northern region, suggested by strong olivine fabrics with point maximum distributions (Figure V.3, 6, 11). A further study in the NGVF is needed to assure the presence or the absence of xenoliths representing the flattening component in the shallow upper mantle (Figure V.11). Moreover, shear zones observed in the xenoliths from the ETBVF are suggested to appear even on seismic reflection profiles. In fact, reflective horizons in the Békés Basin (Posgay et al., 1995) may also evidence similar features. Seismic anisotropy in the central portion of the Intra-Carpathian Basin System is believed to depend on the mantle depth sounded by the analysis. Shallower mantle portions, suggested to be the part of the lithosphere during basin formation, should

reflect weak horizontal anisotropy (Figure VIII.7b) due to the scattered subhorizontal distribution of olivine [100]-axes (fast wave propagation direction). However deeper horizons of the mantle, which were originally part of the asthenosphere and were only attached to the lithosphere during cooling after the formation of the Intra-Carpathian Basin System, should reflect marked horizontal anisotropy (Figure VIII. 7a).

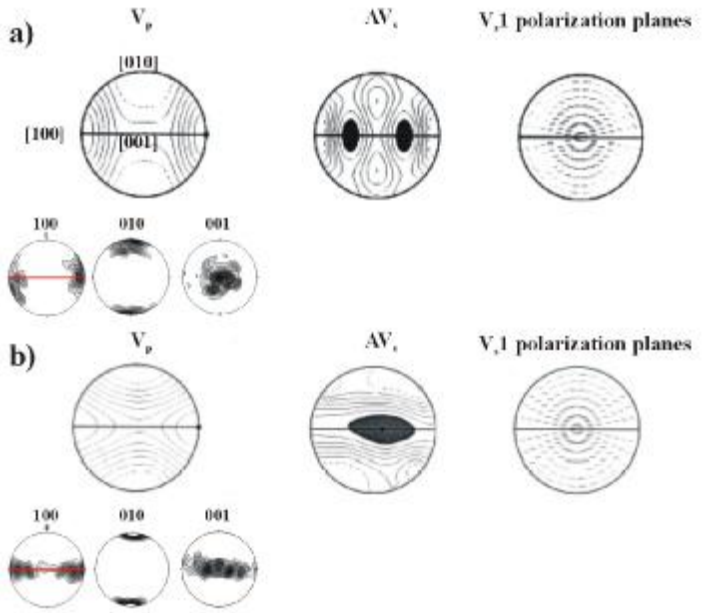

Figure VIII.7 Seismic properties of the characteristic LPO patterns (a), (010)[100] slip system (b), (010)[100] + slip systems (001)[100], (100)[001] slip and twist walls in (010) (Zhang et al., 2000; De Kloe, 2001). The dispersion of the [100] axes reduces the P-waves seismic anisotropy and the [001] axes orientation has an important effect on the shear wave splitting patterns. Figure after Ben Ismail and Mainprice (1998).

Detailed petrographic and fabric analysis of upper mantle peridotite xenoliths provides valuable information on the evolution of the Intra-Carpathian Basin System. Results obtained from this study synthesized with high-quality geochemical data elucidate interrelations of mantle processes and offer answers to some of the so far unanswerable questions.

Conclusions

1) Formation of the Intra-Carpathian Basin System was the consequence of Alpine collision, subsequent extrusion, subduction and rollback of the European oceanic lithosphere beneath the African plate.
2) The Intra-Carpathian Basin System is constituted of two main lithospheric units (ALCAPA and TISZA) with different pre-Miocene history, but with similar tectonic/structural/geodynamic and geochemical evolution after their docking in early Miocene times.
3) Basin formation was associated with deformation and geochemical modification of the lithospheric mantle.
4) Equilibrium temperatures of mantle xenoliths are suggested to represent their relative stratigraphic position within the lithospheric mantle, i.e., higher equilibrium temperatures represent deeper portion of the lithospheric mantle.
5) Systematic variance in the depletion of basaltic major elements with decreasing depth (decreasing equilibrium temperatures) is believed to be the consequence of more superimposed mantle processes:
    - ancient depletion related to increasing partial melting during adiabatic decompression and mantle upwelling associated with continental crust formation,
    - reaction of the peridotite with migrating melts/fluids, resulting in pyroxene breakdown and olivine precipitation.
6) Enrichment, mostly observed in the composition of incompatible trace elements was subsequent to the ancient depletion. Migration of metasomatic fluids occurred along veins, shear zones, but melt percolation along grain boundaries could have also been an important feature in the overall metasomatism of the shallower part of the upper mantle.
7) Deformation features observed in the lithospheric mantle beneath the region are mostly attributed to the formation of the Intra-Carpathian Basin System., although the preservation of older deformation features cannot be excluded.
8) The formation of the Intra-Carpathian Basin System was associated with considerable lithosphere thinning evidenced by garnet symplectites from the SBVF, ETBVF and LHPVF and granulitic xenoliths from the BBHVF. According to geobarometric estimations the lithosphere before basin formation was at least 40-50 km thicker, than at recent times.
9) Olivine orientation distribution in the mantle xenoliths, despite relatively low number studied, imply that deformation in the mantle beneath the northern and eastern marginal

portions of the basin system was dominantly accommodated by intracrystalline slip on the (010)[100] slip system regardless of equilibrium temperatures.

10) Conversely deformation in the xenoliths from the central portion of the Intra-Carpathian Basin System displays clear relation to equilibrium temperatures (~ depth of origin). Xenoliths from the deep lithospheric mantle display evidence for intracrystalline slip on the (010)[100] slip system, whereas those from the shallow mantle display clear evidence for the activation of multiple slip systems beside the (010)[100], most likely the (100)[001] slip system and the occurrence of twist walls on the (010). It is strongly suggested that this remarkable feature is a consequence of deformation in different stress regimes with respect to mantle depth. In the shallow mantle deformation was characterized by considerable flattening, also recognized in surface processes. Whereas, the deep lithosphere deformed by asthenospheric flow and was only attached to the bottom of the lithosphere after cooling and the cessation of deformation.
11) Mylonites among the xenoliths of the ETBVF are unique features. Localization of deformation is attributed to melt infiltration. The driving force for deformation is suggested to be related to the proximity of the subducting slab.
12) The development of annealed and statically recrystallized textures is the consequence of young processes associated with the heating of the asthenospheric upwelling and melt/fluid percolation, triggering subgrain rotation, static recrystallization and grain growth. However, the effect of static recrystallization on developed mantle fabric is suggested to be subordinate.
13) The remarkable anisotropy observed in the fabric of mantle xenoliths should have considerable effect on the migration of fluids and melts. In fact, it could be an important factor in controlling the spatial distribution of the surface manifestation of magmatic activity.
14) Anisotropy features and the evidence for the occurrence of structural domains within the subcontinental lithospheric mantle beneath the Intra-Carpathian Basin System by the fabric analysis of deformed mantle xenoliths implies that these features should be detectable, as they are world wide, by seismic sounding methods. The mutual application microstructural and geochemical analysis together with geophysical methods could reveal the nature of the upper mantle in regions where the volcanic activity did not sample these portions of the lithosphere. Moreover, this way of the research would significantly contribute to the understanding of basin formation, associated deformation and melt/fluid migration processes.

References

Anderson DL (1961) Elastic wave propagation in layered anisotropic media. J Geophys Res, **66**, 2953-2963.

Arai S (1994) Compositional variation of olivine-chromian spinel in Mg-rich magmas as a guide to their residual spinel peridotites. J. Volcanol Geotherm Res, **59**, 279–293.

Artemieva IM, Mooney WD (2001) Thermal thickness and evolution of Precambrian lithosphere: A global study. J Geophys Res, **106**, 16387-16414.

Artemieva IM, Mooney WD, Perchuc E, Thybo H (2002) Processes of lithosphere evolution: new evidence on the structure of the continental crust and uppermost mantle. Tectonophysics, **358**, 1-15.

Avé Lallemant HG, Carter NL (1970) Syntectonic recrystallization of olivine and modes of flow in the upper mantle. Bull Geol Soc Am, **81**, 2203-2220.

Avé Lallement HG, Mercier HG, Carter NL, Ross JV (1980) Rheology of the upper mantle: inference from peridotite xenoliths, Tectonophysics, **70**, 85-113.

Ádám A (1978) Geothermal effects in the formation of electrically conducting zones and temperature distribution in the Earth. Phys Earth Planet Inter, **17**, 21-28.

Ádám A, Szarka L, Prácser E, Varga G (1996): Mantle plumes or EM distortions in the Pannonian Basin? (Inversion of the deep magnetotelluric (MT) soundings along the Pannonian Geotraverse). Geophys Transactions, **40**, 45-78.

Babuška V, Plomerová J, Pajdušák P (1988) Lithosphere-Asthenosphere in central Europe. Models derived from P residuals, In: Proceedings of the 4th EGT Workshop. The Upper Mantle, Commission of the European Communities, European Science Foundation, 37-48.

Bada G (1999) Cenozoic stress field evolution in the Pannonian Basin and surrounding orogens. PhD Thesis, Vrije Universiteit Amsterdam 204 pp.

Bali E, Szabó Cs, Vaselli O, Török K (2001) The significance of carbonate-bearing and carbonate-free silicate melt pockets in the upper mantle: a case study on Szentbékkálla ultramafic xenoliths, Bakony - Balaton Highland Volcanic Field. Földtani Közlöny (Bull Geol Soc Hung), **131**, 415-442. (in Hungarian with English abstract).

Bali E, Szabó Cs, Vaselli O, Török K (2002) Significance of Silicate Melt Pockets in Upper Mantle Xenoliths from the Bakony–Balaton Highland Volcanic Field, Western Hungary. Lithos, **61**, 79-102.

Bali E (2004) Fluid/melt – wall-rock interaction in the uppermantle beneath the central Pannonian basin. PhD thesis. Eötvös University, Department of Petrology and Geochemistry, pp. 160.

Bali E, Szabó Cs, Vaselli O, Zanetti A, Downes H, Thirlwall MF (2004) Two stages of metasomatism in the subcontinental lithospheric mantle beneath the Styrian basin (Eastern Austria/Northern Slovenia): Geochemical and textural evidence from peridotite and pyroxenite xenoliths. (submitted)

Balla Z (1984) The Carpathian loop and the Pannonian basin. A kinematic analysis. Geophys. Transactions, **30,** 313-353.

Balla Z (1988) Clockwise paleomagnetic rotations in the Alps in the light of the structural pattern of the Transdanubian Range (Hungary). Tectonophysics, **145**, 277-292.

Ballhaus C, Berry RF, Green DH (1990) Oxygen fugacity controls in the Earth's upper mantle. Nature **348,** 437 – 440.

Ballhaus C (1993) Redox states of lithosphereic and asthenospheric upper mantle Contrib. Mineral. Petrol., **114,** 331-348.

Balogh K, Árva-Sós E, Pécskay Z, Ravasz-Baranyai L (1986) K/Ar dating of Post-Sarmatian alkali basaltic rocks in Hungary. Acta Miner-Petr, Szeged **28**, 75-84.

Balogh K, Ebner F, Ravasz Cs with contribution by Herrmann P, Lobitzer H, Solti, G, (1994) K/Ar Alter tertiare Vulkanite der südstlichen Steiermark und südlichen Burgenlands. In: Jubilaumschrift 20 Jahre geologische Zusammenarbeit Österreich-Ungarn (Lobitzer H, Császár G Daurer A Eds.), Geologische Bundesanstalt, **2**, 55-72.

Bence, AE, Albee, AL (1968): Empirical correction factors for the electron microanalysis of silicates and oxides. Journal of Geology, **76,** 382-403.

Ben Ismail W, Mainprice D (1998) An olivine fabric database: an overview of upper mantle fabrics and seismic anisotropy. Tectonophysics, **296**, 145-157

Bertrand P, Mercier JCC (1985) The mutual solubility of coexisting ortho- andclinopyroxene: toward an absolute geothermometer for the natural system? Earth Planet Sci Lett, **76**, 109-122.

Bodinier JL, Vasseur G, Vernieres J, Dupuy C, Fabries J (1990) Mechanisms of mantle metasomatism: geochemical evidence from Lherz orogenic peridotite. J Petrol, **31**, 59 7-628.

Bouillier AM, Nicolas A (1973) Texture of peridotite nodules from kimberlite at Mothae, Thaba Putsoa and Kimberley. In: Nixon PH (Ed) Lesotho Kimberlites, pp. 55-66.

Brey, GP, Köhler TP (1990) Geothermobarometry in four phase lherzolites II. New thermobarometers and practical assessment of existing thermobarometers. Journal of Petrology. **31,** 1353-1378.

Bulau JR, Waff HS, Tyburczy JA (1979) Mechanical and thermodynamic constraints on fluid distribution in partial melts. J Geophys Res, **84**, 6102-6108.

Burke K, Sengör AMC (1986) Tectonic escape in the evolution of the continental crust. In: Barazangi, M. and Brown, L., (Eds), Reflection seismology: a global perspective. Geodynamics Series, **14**, 41-53.

Bussod Y, Christie JM (1991) Textural development and melt topology in spinel lherzolite experimetally deformed at hypersolidus conditions. J Petr, Special lherzolite issue, 17-39.

Carter NL, Avé Lallemant HG (1970) High temperature flow of dunite and peridotite. Bull Geol Soc Am, **81**, 2181-2202.

Chalot-Prat F, Girbacea R (2000) Partial Delamination of Continental Mantle Lithosphere, Uplift-related Crust-Mantle Decoupling, Volcanism and Basin Formation: a new model for the Pliocene-Quaternary evolution of the southern East-Carpathians, Romania. Tectonophysics, **327**, 83-107.

Chen S, O`Reilly SY, Zhou X, William LG, Zhang G, Sun M, Feng J, Zhang M, (2001) Thermal and petrological structure of the lithosphere beneath Hannouba, Sino-Korean Craton, China: evidence from xenoliths. Lithos. **56,** 267-301.

Christensen NI (1984) The magnitude, symmetry, and origin of upper mantle anisotropy based on fabric anlysis of ultramafic tectonites. Geophys. J. R. Astron. Soc. **76**, 89-112.

Ciulavu D, Bertotti G, Andreissen P, Cloetingh SAPL, Dinu C, Huismans R, Sanders C (1994) Tectonics of the Transylvanian Basin. Rom J Tect Reg Geol, **75**, 7-8.

Cooper RF, Kohlstedt DL (1982) Interfacial energies in the olivine-basalt system. In: High-Pressure Research in Geophysics, Adv Earth Planet Sci (Akimoto S, Manghnani MH, Eds), Center for academic publications Japan, Tokyo, **12**, pp. 217-228.

Cox KG, Smith MR, Beswetherick S (1987). Textural studies of garnet lherzolites: evidence of exsolution origin from high-temperature harzburgites. In: Nixon PH (Ed.) Mantle Xenoliths. Wiley, Chichester, pp. 537 – 550.

Csontos L, Nagymarosy A, Horváth F, Kovac M (1992) Tertiary evolution of the Intra-Carpathian area: a model. Tectonophysics, **208**, 221-241.

Csontos, L (1995) Tertiary tectonic evolution of the Intra-Carpathian area: a review. Acta Vulcanologica, **7 (2)**, 1-13.

Csontos L, Nagymarosy A (1998) The Mid-Hungarian line: a zone of repeated tectonic inversions. Tectonophysics. **297,** 51-71.

Csontos L, Benkovics L, Bergerat F, Mansy JL, Wórum, G (2002) Tertiary deformation history from faulting analysis and seismic section study in a former European Tethyan margin (the Mecsek-Villány area, SW Hungary) Tectonophysics **357,** 81-102.

Daines MJ, Kohlstedt DL (1997) Influence of deformation on melt topology in peridotites. J. Geophys. Res., **102**, 10257-10271.

Darot M. Gueguen Y (1981) High-temperature creep of forsterite single crystals. J. Geophys. Res., **86,** 6219-6234.

Davidson JB, Lindsey DH (1985) Thermodynamic analysis of quadrilateral pyroxenes, Part II. Contrib Miner Petrol, **91**, 390-404.

Dégi J, Török K (2004) Petrographic evidence of crustal thinning in Bakony-Balaton Highland Volcanic Field. Hungarian Geophysics (in press)

De Kloe, P.A. (2001) Deformation mechanisms and melt nano-structures in experimentally deformed olivine-orthopyroxene rocks with low melt fractions. Geologica Ultraiectina, pp. 201.

Dewey J (1988) Extensional collapse of orogens. Tectonics, **7**, 1123-1139.

Dijkstra AH (2001) Deformation and melt in natural mantle rocks: The Hilti massif (Oman) and the Othris massif (Greece). PhD Thesis, pp. 164.

Dijkstra AH, Drury MR, Vissers RLM, Newman J (2002) On the role of melt-rock reaction in mantle shear zone formation in the Othris Peridotite Massif (Greece) - J Struct Geol, **24**, 1431-1450.

Dobosi G., Kurat G., Jenner G.A., Brandstätter F (1999): Cryptic metasomatism in the upper mantle beneath Southeastern Austria: a Laser Ablation Microprobe - ICP - MS study. Mineral Petrol, **67**, 143-161

Dobosi, G. (2003): The geochemistry of upper mantle and lower crust based on the xenoliths of alkaline basalts based mainly on Carpthian basin samples. (A felsőköpeny és az alsókéreg

geokémiája a bázisos vulkanitok és xenolitjainak vizsgálata alapján – elsősorban a Kárpát-medence példáján) D.Sc. thesis, Hungarian Academy of Science, pp. **294**. In Hungarian

Dodson MH (1973) Closure temperature in cooling geochronological and petrological systems. Contrib Mineral Petrol, **40,** 259-274.

Downes H, Dupuy C (1987) Textual, isotopic and REE variation in spinel peridoditic xenoliths, Massif Central, France. Earth Planet Sci Lett, **82**, 121-135.

Downes H (1990) Shear zones in the upper mantle-relation between geochemical environment and deformation in the mantle peridotites. Geology, **8**, 374-377.

Downes, H., Embey-Isztin, A,Thirlwall, MF (1992) Petrology and geochemistry of spinel peridotite xenoliths from the western Pannonian Basin (Hungary): evidence for an association between enrichment and texture in the upper mantle. Contrib Mineral Petrol, **109**, 340–354.

Downes H, Vaselli O (1995) The lithosphereic mantle beneath the Carparthian-Pannonian Region: a review of trace element and isotopic evidence from ultramafic xenoliths. Acta Vulcanologica. **7 (2).** 219-231.

Downes H, Seghedi I, Szakacs A, Dobosi G, James DE, Vaselli O, Rigby IJ, Rex D, Pecskay Z. (1995) Petrology and geochemistry of Late Tertiary/ Quaternary mafic alkaline volcanism in Romania. Lithos, **34**, 65-81.-

Downes H (2001) Formation and modification of the shallow sub-continental lithospheric mantle: a review of geochemical evidence from ultramafic xenolith suites and tectonically emplaced ultramafic massifs of western and central Europe. J Petrol, **42**, 233-250.

Dövényi P, Horváth F. (1988) Review of temperature, thermal conductivity and heat flow data for the Pannonian Basin. In: The Pannonian Basin, a Study in Basin Evolution (Royden LH, Horváth F, Eds.),. The American Association of Petroleum Geologists Bulletine, **68**, 195-233.

Dricker I, Vinnik L, Roeker S, Makeyeva L (1999), Upper-mantle flow in Eastern Europe: Geophys Res Lett **26**, 1219–1222.

Droop GTR (1987) A general equation for estimating Fe^{3+} concentration in ferromagnesian silicates and oxides from microprobe analyses, using stochimetric criteria. Mineral. Mag. **51,** 431-435.

Durham WB and Goetze C (1977) Plastic flow of oriented single crystals of olivine-2- observations and interpretations of the dislocation structures. J Geophys Res, **82**, 5755-5770.

Embey-Isztin, A. (1976) Amphibolite/lherzolite composite xenolith from Szigliget, north of the Lake Balaton, Hungary. Earth Planet Sci Lett, **31**, 297–304.

Embey-Isztin, A. (1984) Texture types and their relative frequencies in ultramafic and mafic xenoliths in alkali basalts and implications for magmatic processes within the mantle. Ann. Hist. Nat. Mus. Hung., **70**, 27-44.

Embey-Isztin A, Scharbert HG, Dietrich H, Poultidis H (1989) Petrology and geochemistry of peridotite xenoliths in alkali basalts from the Transdanubian Volcanic Region, West Hungary. J. Petrol., **30**, 79-105.

Embey-Isztin, A., Downes, H., James, D.E., Upton, B.G.J., Dobosi, G., Ingram, G., Harmon, R.S. & Scharbert, H. G. (1993) The petrogenesis of Pliocene alkaline volcanic rocks from the Pannonian Basin, Eastern Central Europe. Journal of Petrology,, **34,** 317-343.

Embey-Isztin A, Dobosi G (1995) Source mantle characteristics beneath the Carpathian-Pannonian Region: a review of trace element and isotopic evidence from Pliocene to Quaternary alkali basalts. Acta Vulcanol. **7**, 155-166.

Embey-Isztin A, Dobosi G, Altherr R and Meyer H-P. (2001a) Thermal evolution of the lithosphere beneath the western Pannonian Basin: evidence from deep-seated xenoliths. Tectonophysics **331**, 285-306.

Embey-Isztin, A., Dobosi, G. & Downes, H. (2001b) Geochemical characterization of the Pannonian Basin mantle lithosphere and asthenosphere: an overview. Acta Geol Hung, **44**, 2001 2-3, 259-280.

Falus Gy, Drury MR, van Roermund HLM, Szabo Cs (2004) Magmatism Related Localized Deformation in the Mantle: a Case Study. Contrib Mineral Petrol, **146**, 493-505.

Falus Gy, Szabó Cs, Vaselli O (2000) Mantle upwelling within the Pannonian Basin: evidence from xenolith lithology and mineral chemistry. Terra Nova, **12**, 295-302.

Faul UH, FitzGerald JD (1999) Grain Misorientations in Partially Molten Olivine Aggregates: An Electron Backscatter Diffraction Study. Phys Chem Min., **26**, 187-197.

Finnerty AA, Boyd FR (1984) Thermobarometry for garnet peridotites: basis for determination of thermal and compositional structure of the upper mantle. In: Nixon PH (Ed.) Mantle xenoliths. New York: John Wiley.

Fliervoet TF, Drury MR, Chopra PN (1999) Crystallographic preferred orientations and misorientations in some olivine rocks deformed by diffusion or dislocation creep. Tectonophysics, **303**,1-27.

Fodor L, Csontos L, Bada G, Györfi I, Benkovics L (1999) Tertiary tectonic evolution of the Pannonian basin system and neighbouring orogens: a new synthesis of paleostress data. In: Durand B, Jolivet L, Hortváth F, Séranne M (Eds): The Mediterranean basins: Tertiary extension within the Alpine orogen. Geological Society, London. Spec publ., **156**, 295-334.

Fodor L, Magyari A, Kázmér M, Fogarasi A (1992) Gravity-flow dominated sedimentation on the Buda slope - A sedimentary record of continental escape of the Bakony Unit (SW-Hungary). Geol. Rundsch., **81**, 695-716.

Frey FA, Green DH (1974) The mineralogy, geochemistry and origin of lherzolite inclusions in Victorian basanites. Geochim. Chosmochim. Acta., **38**, 1023-1059.

Frey FA, Prinz M (1978) Ultramafic inclusions from San Carlos, Arizona; petrologic and geochemical data bearing on their petrogenesis. Earth. Planet. Sci. Lett., **38**, 129-178.

Gaul OF, Griffin WL, O'Reilly SY, Pearson NJ (2000) Mapping olivine composition in the lithospheric mantle, Earth Planet Sci Lett, **182**, 223-235.

Géczy B (1973) Plate tectonics and paleogeography in the East-Mediterranean Mesozoic. Acta Geol Hung, **27**, 379-389.

Géczy B (1984) Provicialism of Jurassic ammonites: examples from Hungarian faunas. Acta Geol Hung, **27, 3-4:** 379-389.

Godard M, Jousselin D, Bodinier JL (2000) Relationships between geochemistry and structure beneath a paleo-spreading centre: A study of the mantle section in the Oman Ophiolite, Earth Planet Sci Lett,**180,** 133-148.

Györfi I, Csontos L (1994) Structural evolution of SE Hungary and Neogene basins of the Apuseni Mountains (Romania). Rom J Tect Reg Geol, **75**, 19-20.

Harangi R, Harangi Sz (1995) Volcanological study of the Neogene basaltic volcano of Sághegy (Little Hungarian Plain Volcanic, Western Hungary). Acta Vulcanologica. **7 (2).** 173-189.

Harangi Sz, Wilson M, Tonarini S (1995) Petrogenesis of Neogene potassic volcanic rocks in the Pannonian Basin. Acta Vulcanol, **7 (2)**, 125-134.

Harangi Sz, Downes H (2000) Contrasting origins of Neogene calc-alkaline volcanic suites in the Charpathian-Pannonian region, Eastern-Central Europe. Journal of Conference Abstracts, **5,** p. 484.

Harangi Sz. (2001) Neogene to Quaternary Volcanism of the Carpathian-Pannonian Region - a review. Acta Geol Hung, **44**, 223-258.

Hart SR (1984) A large isotopic anomaly in the Southern Hemisphere mantle. Nature, **309,** 753-757.

Harte B (1977) Rock nomenclature with particular relation to deformation and recrystallization textures in olivine-bearing xenoliths. J Geol, **85**, 279-288.

Hawkesworth CJ, Gallagher K, Hergt JM, McDermott F (1995) Destructive Plate Margin Magmatism - Geochemistry and Melt Generation. Lithos, **33**, 169-188.

Hidas K, Falus Gy, Szabó Cs (2004) Orthopyroxene and olivine fabrics: indicators of alternating stress field during the formation of the Pannonian Basin. (submitted to Tectonophysics)

Holtzman BK, Groebner NJ, Zimmerman ME, Ginsberg SB, Kohlstedt DL (2003) Deformation-driven melt segregation in partially molten rocks. Geochem Geophys Geosyst, (in press)

Horváth F, Royden L (1981) Mechanism for the formation of the intra-Carpathian basins: a review. Earth Evol Sci, **1**, 307-316.

Horváth F, Dövényi P, Szalay Á, Royden LH (1988) Subsidence, thermal and maturation history of the Great Hungarian Plain. In: Royden LH, Horváth F (Eds) The Pannonian Basin, a study in basin evolution, Bull Amer Assoc Petrol Geol, **45**, 355-372.

Horváth F (1993) Towards a mechanical model for the formation of the Pannonian basin. Tectonophysics, **226**, 333-357.

Horváth F (1995) Phases of compression during the evolution of the Pannonian basin and its bearing on hydrocarbon exploration. Mar Petrol Geol, **12**, 837-844.

Horváth F, Cloetingh SAPL (1996) Stress-induced late stage subsidence anomalies in the Pannonian Basin. Tectonophysics, **266**, 287–300.

Huismans RS, Podladchikov YY, Cloetingh S (2001) Dynamic modelling of the transition from passive to active rifting: Application to the Pannonian basin. Tectonics, **20**, 1021-1039.

Ibrmajer I, Tomek Č, Koráb T, Dvořáková L (1994) Deep reflection seismic profiling in Czechoslovakia – the ČESLOKORP (Czechoslovak crustal reflection profiling project). In: Bucha V Blížkovský M (Eds) Crustal Structure of the Bohemian Massif and the West Carpathians. Springer, Berlin, Heidelberg, New York and Praha, 21-44.

Ionov DA, Bodinier JL, Mukasa SB, Zannetti A (2002) Mechanisms and sources of mantle metasomatism: major and trace element composition of peridotite xenoliths from Spitsbergen in the context of theoretical modeling. J Petrol, **43**, 2219-2259.

Ishii K, Sawaguchi T (2002) Lattice- and shape-preferred orientation of orthopyroxene porphyroclasts in peridotites: an application of two-dimensional numerical modeling. Journal of Structural Geology, 517-530.

Ji S; Wang Z; Wirth R (2001) Bulk flow strength of forsterite-entstatite composites as a function of forsterite content. Tectonophysics, **341**, 69-93

Jousselin D, Mainprice D (1998) Melt topology and seismic anisotropy in mantle peridotites of the Oman ophiolite. Earth Planet Sci Lett, **164**: 553-568.

Karato, SI, Toriumi M, Fujii T (1980) Dynamic recrystallization of olivine single crystals during high-temperature creep. Geophys Res Lett, **7**, 649-652.

Karato SI (1992) On the Lehmann discontinuity. Geophys Res Let, **9**, 2255-2258.

Kázmér M, Kovács S (1985) Permian-Paleogene paleogeography along the eastern part of the Insubric-Periadriatic lineament system: evidence for the continental escape of the Bakony-Drauzug unit. Acta Geol Hung, **28**, 71-84.

Kelemen PB, Dick HJB, Quick JE (1992) Formation of harzburgites by pervasive melt/rock reaction in the upper mantle. Nature, **358**, 635-641.

Kovác M, Král J, Márton E, Plasienka D, Uher P, (1994) Alpine uplift history of the Central Western Carpathians: geochronological, paleomagnetic, sedimentary and structural data. Geol Carpathica, **45**, 83-97.

Kovács I, Zajacz Z, Szabó Cs (2004): History of the Lithosphere Beneath the Nógrád-Gömör Volcanic Field (N-Hungary/S-Slovakia). Tectonophysics, (in press)

Konecny V, Lexa J, Balogh K, Konecny P (1995) Alkali basalt volcanism in Shouthern Slovakia: volcanic forms and time evolution. Acta Vulcanologica. **7 (2)** 167-173.

Kurat G, Embey-Isztin A, Karcher A, Scharbert H (1991) The upper mantle beneath Kapfenstein and the Transdanubian Volcanic Region, E-Austria and W Hungary: A comparison. Miner Petrol, **44**, 21-38.

Leake BE (1978) Nomenclature of amphiboles. Am Mineral, **63**, 1023-1052.

Lenkey L (1999) Geothermics of the Pannonian basin and its bearing on the tectonics of basin evolution Amsterdam Vrije Univ, 215 p.

Lloyd GE, Farmer AB, Mainprice D (1997) Misorientation analysis and orientation of subgrain and grain boundaries. Tectonophysics. **279**, 55-78.

Mainprice D, Nicolas A (1989) Development of shape and lattice preferred orientations: application to the seismic anisotropy of the lower crust. J Struct Geol, **11**, 175-189.

Márton E, Márton P (1978) The difference between the paleomagnetic pole positions of the Mesozoic from the Transdanubian Central Range and Villány Mts. respectively. Magyar Geofizika, **19**, 129-136.

Márton E, Márton P (1996) Large scale rotation in North Hungary during the Neogene as indicated by paleomagnetic data. In: Morris A, Tarling DH (Eds) Paleomagnetism and tectonics of the Mediterranean Region. Geological Society London, Special Publications, **105**, 153-173.

McDonough WF, Frey FA (1989) Rare Earth Elements in Upper Mantle Rocks. In: Lipin BR, McKay GA (Eds.) Geochemistry and Mineralogy of Rare Earth Elements, Reviews in Mineralogy, **21**, 99-145.

McKenzie D (1984) The generation and compaction of partially molten rock. J Petrol, **25**, 713-765.

Mercier,J-CC. Nicolas A (1975). Textures and fabrics of upper-mantle peridotites as illustrated by xenoliths from basalts. J Petrol, **6**, 454-487.

Mercier JCC (1979) Peridotite xenoliths and the dynamics of kimberlite intrusions. In: Boyd FR, Meyer HGA (Eds.) The mantle sample: Inclusions in kimberlites and other volcanics. Washington : Am. Geophys. Union, pp. 197-212.

Montagner JP (1994) Can seismology tell us anything about convection in the mantle? Rev Geophys, **32**, 115–137.

Mori T, Green DH (1978) Laboratory duplication of phase equlibria observed in natural garnet lherzolites. J Geol, **86.** 83-97.

Németh K, Martin U (1999) Large hydrovolcanic fi eld in the Pannonian Basin: general characteristics of the Bakony—Balaton Highland Volcanic Field, Hungary. Acta Vulcanol, **11**, 271-282.

Nickel KG, Green DH (1985) Empirical geothermobarometry for garnet peridotites and implications for the nature of the lithosphere, kimberlites and diamonds. Earth Planet Sci Lett, **73**, 158-170.

Nickel KG (1989) Garnet-pyroxene equlibria in the system SMACCr (SiO_2-MgO-Al_2O_3-CaO-Cr_2O_3): the Cr-geobaromether. Proc. 4th Int. Kimberlite Conf., Autr. J. Earth Sci.

Nicolas A, Christensen NI (1987). Formation of anisotropy in upper mantle peridotites - a review. In Fuchs K, Froidevaux C (Eds) Composition, Structure and Dynamics of the Lithosphere-Asthenosphere System (Geodynamics Series), **16**, 111-123.

Passchier CW Trouw RAJ (1995) Microtectonics. Springer Verlag. 283 pp.

Peacock SM (1992) Blueschist-facies metamorphism, shear heating, and P-T-t paths in subduction shear zones. J Geophys Res, **97**, 17693-17707.

Pécskay Z, Lexa J, Szakács A, Balogh K, Seghedi I, Konecny V, Kovács M, Márton E, Kaliciak M, Széky-Fux V, Póka T, Gyarmati P, Edelstein O, Rosu E, Zec B (1995) Space and time distribution of Neogene-Quaternary volcanism in the Carpatho-Pannonian Region. Acta Vulcanol, 7, 15-28.

Pike NJE, Schwartzman EC (1977) Classification of textures in ultramafic xenoliths. J Geol, **85**, 49-61.

Posgay K, Albu I, Hegedűs E, Tímár Z (1990) Deep seismic investigations along the Pannonian Geotraverse. Acta Geod Geophys Mont Hung, **25**, 267-277.

Posgay K, Bodoki T, Hegedűs E, Kovácsvölgyi S, Lenkey L, Szafián P, Takács E, Tímár Z, Varga G (1995) Asthenospheric structure beneath a Neogen Basin in suotheast Hungary. In: Interplay of extension and compression in basin formation Techtonophysics, **252**, 467-484.

Randle V (1992) Microtexture determination and its applications (London: Institute of Materials). pp.174

Ratschbacher L, Frisch W, Linzer H-G, Marle O (1991) Lateral extrusion in the Eastern Alps, part 2: Structural analysis. Tectonics, **10**, 257-271.

Ribe NM (1992) On the relation between seismic anisotropy and finite strain, J *Geophys. Res.*, **97**, 8737–8747.

Ross JV, Avé Lallement HG, Carter NL (1980) Stress dependence of recrystallized-grain and subgrain size in olivine. Tectonophysics, **70**, 39-61.

Royden LH, Horváth F, Nagymarosy A, Stegena L (1983) Evolution of the Pannonian basin system: 2. Subsidence and thermal history. Tectonics, **2**, : 91-137.

Royden LH, and Horváth F (1988) The Pannonian Basin, a Study in basin evolution. Amer Assoc Petr Geol Mem, **45,** 394 pp.

Rosenbaum JM, Wilson M, Downes H (1997) Multiple enrichment of the Carpathian-Pannonian mantle: Pb-Sr-Nd isotope and trace element constraints. J Geophys Res - Solid Earth. **102 (B7)**, 14947-14961.

Sacchi M, Horváth F, Magyari O (1999) Role of unconformity-bounded units in stratigraphy of continental record: a case study from the late Miocene of Western Pannonian Basin, Hungary. In: Durand B, Jolivet L, Horváth F, Séranne M (Eds) The Mediterranian Basins: Tertiary extension within the Alpine Orogen. Geological Society Special Publications, **156**, 357-390.

Salters JM, Hart SR, Panthó G (1988): Origin of late Cenozoic volcanic rocks of the Carpathian arc, Hungary. In: Royden, L.H., Horvath, F. (Eds), The Pannonian basin. A study in basin evolution. AAPG Mem., **45,** 279-292.

Silver PG (1996) Seismic anisotropy beneath the continents: Probing the depths of geology. Ann Rev Earth Planet Sci, **24**, 385-432.

Smith D (1976) The origin and interpretation of spinel-pyroxene clusters in peridotite. J Geol, **85**, 476-482.

Soedjatmiko B, Christensen NI (2000) Seismic anisotropy under extended crust: evidence from upper mantle xenoliths, Cima Volcanic Field, California. Tectonophysics, **321**, 279-296.

Spakman W (1990) Images of the upper mantle of central Europe and the Mediterranean, Terra Nova, **2**, 542-553.

Spear FS (1993) Metamorphic phase equilibria and pressure-temperature-time paths. Mineralogical Society of America Monograph, 79 pp.

Stegena L (1974) Geothermics and tectogenesis in the Pannonian Basin. Acta Geol Hung, **18**, 257-266.

Stegena L, Géczy B, Horváth F (1975) Late Cenozoic evolution of the Pannonian basin. Tectonophysics, **26**, 71-90.

Suhr G (1993) Evaluation of upper mantle microstructures in the Table Mountain massif (Bay of Islands ophiolite). J Struct Geol, **15**, 1273-1292.

Szabó Cs., Harangi Sz., Csontos L. (1992) Review of Neogene and Quaternary volcanism of the Carpathian-Pannonian region. Tectonophysics, **208**, 243-256

Szabó Cs, Taylor LA (1994) Mantle petrology and geochemistry beneath Nógrád-Gömör Volcanic Field, Carpathian-Pannonian Region. Inter Geol Rev, **36**, 328-358.

Szabó Cs, Harangi Sz, Vaselli O, Downes H, (1995a) Temperature and oxygen fugacity in peridotite xenoliths from the Carpathian-Pannonian Region. Acta Vulcanol, **7**, 231-239.

Szabó Cs, Vaselli O, Vanucci R, Bottazzi, P, Ottolini L, Coradossi N, Kubovics I (1995b) Ultramafic xenoliths from the Little Hungarian Plain (Western Hungary): a petrologic and geochemical study. Acta Vulcanol, **7**, 249-263.

Szabó Cs., Bodnar RJ, Sobolev AV (1996) Metasomatism associated with subduction-related, volatile-rich silicate melt in the upper mantle beneath the Nógrád-Gömör Volcanic Field, Northern Hungary/Southern Slovakia: Evidence for silicate melt inclusions. Eur J Mineral, **8,** 881-899.

Szabó Cs, Falus Gy, Zajacz Z, Kovács I, Bali E (2004): Composition and Evolution of Lithosphere beneath the Carpathian-Pannonian Region: a review. Tectonophysics, (in press)

Szafián P, Horváth F, Cloetingh, SAPL (1997) Gravity constraints on the crustal structure and slab evolution along a Trans-carpathian transect. Tectonophysics, **272**, 233-247.

Szakács A, Segedhi I (1995) The Calimani-Gurghiu-Hargitha volvanic chain, East Carpathians, Romania: volcanological features. Acta Vulcanol, **7 (2)**, 145-155.

Szakács A, Zelenka T, Márton E, Pécskay Z, Póka T Seghedi I (1998) Miocene acidic explosive volcanism in the Bükk Foreland, Hungary: Identifying eruptive sequences and searching for source locations. Acta Geol Hung, **41**, 413-435.

Széky-Fux V, Pécskay Z (1991) A Fruska Gora hegység harmadkori vulkanizmusa és a vulkanizmus K-Ar radiogén kora Acta Geogr. Debr **28**, 203-215.

Szente, I. (1995): Bivalvia from the Bathonian (Middle Jurassic) of the Mecsek Mts, Hungary. Annales Univ Sci Budapest, Sect Geol, **30**, 93-109; 221-224.

T'Hart J (1978) The structural morphology of olivine I. A qualitative derivation. Canad Mineral, **16**, 175-186.

Tari G, Báldi T, Báldi-Beke M (1993) Paleogene ratroarc flexural basin beneath the Neogene Pannonian Basin: a geodynamic model. Tectonophysics, **226**, 433-455.

Tari, G. (1994) Alpine tectonics of the Pannonian Basin. Ph.D. Thesis, Rice University, Houston, 501 pp.

Tari G, Horváth F (1995) Middle Miocene extensional collapse in the Alpine-Pannonian transition zone. In: F. Horváth, G. Tari and Cs. Bokor (Editors), Extensional collapse of the Alpine orogene and hydrocarbon prospects in the basement and basin fill of the western Pannonian Basin. AAPG International Conference and Exhibition, Nice, France, Guidebook to fieldtrip. **No. 6**, Hungary: 75-105.

Tari G, Dövényi P, Dunkl I, Horváth F, Lenkey L, Stefanescu M, Szafián P, Tóth T (1999): Lithospheric structure of the Pannonian basin derived from seismic, gravity and geothermal data. In: Durand B, Jolivet L, Hortváth F, Séranne M (Eds): The Mediterranean basins: Tertiary extension within the Alpine orogen. Geological Society, London. Spec publ, **156**, 215-250.

Tapponier P, Molnar P (1976): Slip line field and large scale continental tectonics. Nature, **264**,319-324.

Taylor, W.R. and Green, D.H. (1987) Measurement of reduced peridotite-C–O –H solidus and implication s for redox melting of the mantle. Nature, **332**, 349-352.

Thompson RN, Gibson SA (1991) Subcontinental mantle plumes, hot spots and preexisting thin spots. J Geophys Res, **148**, 973-977.

Thompson RN, Leat P, Dickin A, Morrison MA, Hendry G, Gibson S (1989) Strongly potassic mafic magmas from lithospheric mantle sources during continental extension and heating: evidence from Miocene minettes of northwest Colorado, U.S.A. Earth Planet Sci Lett, **98**, 139-153.

Tommasi A, Mainprice D, Canova G, Chastel Y (2000) Viscoplastic self-consistent and equilibrium-based modeling of olivine lattice preferred orientations. Implications for the upper mantle seismic anisotropy. Journal of Geophysical Research, **105**, 7893-7908.

Tommasi A, Vauchez A (2001) Continental rifting parallel to ancient collisional belts: An effect of the mechanical anisotropy of the lithospheric mantle. Earth Planet Sci Lett, **185:** 199-210.

Toramaru A, Fujii N, (1986) Connectivity of melt phase in a partially molten peridotite. Journal of Geophysical Research, **91**, 9239–9252.

Török K (1995) Garnet breakdown reaction and fluid inclusions in a garnet clinopyroxenite xenolith from Szentbékkálla (Balaton Highland, W-Hungary). Acta Vulcanol, **7 (2)**, 285-290.

Trepied L, Doukhan JC, Paquet J (1980) Subgrain boundaries in quartz: theoretical analysis and microscopic observations. Phys Chem Miner, **5**, 201-218.

Urai JL, (1983) Water assisted dynamic recrystallization and weakening in polycrystalline bischofite. Tectonophysics **96,** 125-127

Vakarcs G, Vail PR, Tari G, Pogácsás Gy, Mattick RE, Szabó A (1994) Third-order Miocene-Pliocene depositional sequences in the prograding delta complex of the Pannonian basin. Tectonophysics, **240**, 81–106.

Van der Wal D (1993). Deformation processes in Mantle Peridotites: with emphasis on the Ronda peridotite of SW Spain. Univ. Utretch, pp. 180.

Van der Wal D, Bodinier JL. (1996). Origin of the recrystallization front in the Ronda peridotite by km-scale pervasive porous melt flow. Contrib Mineral Petrol **122,** 387–405.

Vannucci R, Ottolini L, Botazzi P, Downes H, Dupuy C (1994) INAA, IDMS and SIMS comparative REE investigations of clinopyroxenes from mantle xenoliths with different textures. Chem Geol, **118,** 85-108.

Vaselli O, Downes H, Thirlwall M, Dobosi G, Coradossi N, Seghedi I, Szakacs A, Vannucci R (1995) Ultramafic Xenoliths in Plio-Pleistocene alkali basalts from the Eastern Transylvanian Basin: depleted mantle enriched by vein metasomatism. J Petrol, **36**, 23-53

Vaselli O, Downes H, Thirlwall MF, Vannucci R, Coradossi N (1996) Spinel-peridotite xenoliths from Kapfenstein, (Graz Basin, Eastern Austria): a geochemical and petrological study. Mineral Petrol, **57**, 23-50.

Vauchez A, Barruol G, Tommasi A (1997) Why do continents break-up parallel to ancient orogenic belts? Terra Nova, **9**, 62-66.

Vauchez A, Garrido CJ (2001) Seismic properties of an asthenospherized lithospheric mantle: constraints from lattice preferred orientations in peridotite from the Ronda massif. Earth Planet Sci Lett, **192**, 235-249.

Vauchez A, Tommasi A (2003) Plume-lithosphere interaction: effects on the seismic anisotropy of the lithospheric mantle. Geophys Res Abs, **5**, 11450.

Vissers RLM, Drury MR, Newman J, Fliervoet TF (1997) Mylonitic deformation in upper mantle peridotites of the North Pyrenean Zone (S France): implications for strength and strain localization in the lithosphere - Tectonophysics, **279**, 303-325.

Vörös A. (1993) Jurassic microplate movements and brachiopod migrations in the western part of the Tethys. - Palaeogeogr, Palaeoclimatol, Palaeoecol, **100**, 125-145.

Waff HS, Faul UH (1992) Effects of Crystalline Anisotropy on Fluid Distribution in Ultramafic Partial Melts, J Geophys Res, **97**, 9003-9014.

Weertman J, Weertman JR (1964). Elementary Dislocation Theory. Macmillan, New York. pp. 213.

Wenk HR, Christie JM (1991) Comments on the interpretation of deformation textures in rocks. J Stuct Geol, **13**, 1091-1110.

Wenk HR, Tomé C (1999). Simulation of Deformation and recrystallization of olivine deformed in simple shear. J Geophys Res, **104**, 25513-25527.

Wilson M, Rosenbaum JM, Downes H (1997). Multiple enrichment of the Pannonian-Carpathian Mantle: Pb-Sr-Nd isotope and REE constraints. J Geophys Res, **102**, 14947-14961.

Xu YG,. Menzies MA, Bodinier JL, Bedini RM, Vroon P, Mercier JCC (1998).:Melt percolation and reaction atop a plume: evidence from thepoikiloblastic peridotite xenoliths from Borne (Massif Central,France) Contrib Mineral Petrol, **132,** 65-84.

Xu YG, Menzies MA, Matthew F, Huang XL, Liu Y, Chen XM (2003) "Reactive" harzburgites from Huinan, NE China: Products of the lithosphere-asthenosphere interaction during lithospheric thinning? Geochimica et Cosmochimica Acta, **Vol. 67**, No. 3, pp. 487-505

Zanetti A, Vannucci R, Oberti R, Dobosi G (1995) Trace element composition and crystal chemistry of mantle amphiboles from the Carpatho - Pannonian Region. Acta Vulcanol. **7 (2),** 265-276.

Zangana NA, Downes H, Thirlwall MF, Marriner GF, Bea F (999) Geochemical variation in peridotite xenoliths and their constituent clinopyroxenes from Ray Pic (French Massif Central): implications for the composition of the shallow lithospheric mantle. Chem Geol, **153**, 11-35.

Zentai L (1996) http://lazarus.elte.hu/hun/dolgozo/zentail.htm

Zhang S, Karato S, Fitz Gerald JD, Faul UH, Zhou Y (2000) Simple shear deformation of olivine aggregates, Tectonophysics, **316**, 133-152.

Zheng JP, O'Reilly SY, Griffin WL, Lu F, Zhang M**,** Pearson NJ (2001). Relict refractory mantle beneath the eastern North China block: significance for lithosphere evolution. Lithos, **57**, 43-66.

http://www.msm.cam.ac.uk/doitpoms/tlplib/BD4/slip_geometry.php

Acknowledgements

I am grateful for the careful supervision of Csaba Szabó, who guided me throughout the whole Ph.D. work and beyond. I owe great thanks to Orlando Vaselli for his help with EPMA analysis at the University of Florence. I also acknowledge the support of the European Community Access to Research Infrastructure action of the Improving Human Potential Programme, contract HPRI-CT-1999-00008 awarded to Prof. B. J. Wood (EU Geochemical Facility, University of Bristol).

I thank the financial support partially funding this work provided by the Hungarian National Scientific Foundation (OTKA) Grant T043686 to Cs. Szabó.

I acknowledge the following people for fruitful conversation: Kálmán Török, László Csontos, Antal Embey-Isztin, Gábor Dobosi, Tamás Weiszburg, Szabolcs Harangi, István Dódony, Martyn Drury, Hilary Downes, Theo Ntaflos, David Green. I also thank the technical support of Filippo Olmi, Kamilla Gál-Sólymos, Herman van Roermund and Angéla Baross Szőnyi.

I owe great thanks to Enikő Bali, István Kovács and Károly Hidas for their fantastic help during the preparation of the Ph.D. thesis and also for incredibly fruitful discussions, which largely helped me in the work.

I thank the help of those people who will stay anonymous, but without them the finishing of my work could not have been possible.

And last but most I thank the faithful help of my FAMILY, who always believed in the success of my Ph.D. work and were always patient with me. I also thank my Parents for their continuous enthusiastic support and reassurance.